



Title	Bonding mechanism of resistance element welding for robust lap joints of lightweight alloys and ultra-high strength steels
Author(s)	Baek, Seung Yeop
Citation	大阪大学, 2024, 博士論文
Version Type	VoR
URL	https://doi.org/10.18910/96098
rights	
Note	

The University of Osaka Institutional Knowledge Archive : OUKA

<https://ir.library.osaka-u.ac.jp/>

The University of Osaka

Doctoral Dissertation

Bonding mechanism of resistance element
welding for robust lap joints of lightweight
alloys and ultra-high strength steels

(軽量金属と超高強度鋼の抵抗エレメント溶接メカニズム解
明による重ね継手の高強度化)

SEUNG YEOP BAEK

December 2023

Graduate School of Engineering,
Osaka University

Contents

Chapter 1 General introduction	1
1.1 Materials for automotive body structures	1
1.2 Conventional welding process for structural materials	15
1.3 Dissimilar materials welding	23
1.4 Limitations of RSW with dissimilar materials (RSW: Resistance spot welding)	29
1.5 REW with dissimilar materials (REW: Resistance element welding)	30
1.6 The purpose and structure of this thesis	33
References	35
Chapter 2 Bonding mechanism of REW with Al/Ultra-high strength steel (UHSS)	44
2.1 Introduction	44
2.2 Experimental procedures	46
2.2.1 Materials and REW processes	46
2.2.2 Microstructure observations	48
2.2.3 Evaluation of mechanical properties	49
2.3 Results	50
2.3.1 Mechanical strength	50
2.3.2 Cross-sectional observations	52
2.3.2.1 Welding current of 3.5 kA and 4.5 kA	52
2.3.2.2 Welding current of 6.5 kA and 8.5 kA	56
2.3.2.3 Welding current of 10.5 kA and 12 kA	58
2.3.3 Microstructure observations	61
2.3.4 Microhardness distributions	64
2.3.5 Fracture characterizations	66
2.4 Discussion	69
2.4.1 Welding mechanism determining mechanical strength	69
2.4.2 Welding current influence on the microstructure developments	73
2.4.3 Microstructure and deformation influence on the tensile-shear behavior	77
2.4.4 Relation between fracture mode and Portevin–Le Chatelier effect	79
2.4.5 Comparison with Al/Fe joining candidate processes	82
2.5 Conclusions	84
References	87

Chapter 3 Microstructural and interface geometrical influence on the mechanical fatigue property of Al/UHSS lap joints using REW

	92
3.1 Introduction	92
3.2 Experimental procedures	93
3.3 Results	96
3.3.1 Welding morphologies	96
3.3.2 Microstructure investigations	98
3.3.2.1 Initial state of base materials	98
3.3.2.2 Welding interfaces	99
3.3.2.3 HAZ of AA5052	101
3.3.3 Mechanical behaviors	103
3.3.3.1 Tensile-shear tests	103
3.3.3.2 Fatigue endurance	105
3.3.4 Fractography	108
3.3.5 Fatigue crack propagations	118
3.4 Discussion	120
3.4.1 Microstructure developments	120
3.4.2 Microstructures influence on the fatigue strength	126
3.4.3 Geometrical effect for fatigue fracture modes	127
3.5 Conclusions	131
References	133

Chapter 4 Investigation of microstructural transition and fracture due to heat transfer in Al REWeld lap joints of Al/UHSS without heat affected zones

	137
4.1 Introduction	137
4.2 Experimental procedures	138
4.2.1 Al HAZ-less REW	138
4.2.2 Measurement of Al HAZ and fusion zone temperatures	140
4.2.3 Microstructural and mechanical characterizations	141
4.3 Results	142
4.3.1 Morphological characteristics of the welded joints	142
4.3.2 Microstructures of the welded joints	145
4.3.3 Mechanical behaviors	155

4.3.4 Fracture modes	163
4.4 Discussion	168
4.4.1 Temperature behaviors inside weld joints	168
4.4.2 Phase and texture formation	173
4.4.3 Mechanism of Al HAZ effects for enhancing the REW lap joints	182
4.5 Conclusions	187
References	190

Chapter 5 Effect of Mg remelting and mechanical hooks of steel on the mechanical and fatigue responses of REWed Mg/DP780 joints

	194
5.1 Introduction	194
5.2 Experimental procedures	196
5.2.1 Materials and REW processing	196
5.2.2 Mechanical testing	197
5.2.3 Microstructure characterizations	199
5.3 Results	201
5.3.1 Welding morphologies and its geometries	201
5.3.2 Microstructure investigations	204
5.3.2.1 As-received base materials	204
5.3.2.2 Welding interfaces	207
5.3.2.3 HAZ of AZ31B alloys	207
5.3.3 Mechanical properties	211
5.3.3.1 Hardness distributions	211
5.3.3.2 Tensile-shear properties	212
5.3.3.3 Fatigue performances	215
5.3.3.4 Fracture surfaces characterizations	217
5.4 Discussion	225
5.4.1 Phase transformation of S20C/DP780 welding interfaces	225
5.4.2 The mechanism for microstructures evolutions of AZ31B HAZ	229
5.4.3 Thermodynamic calculations of AZ31B HAZ	233
5.4.4 Microstructures determining mechanical properties in AZ31B	237
5.4.5 Mechanical factors determining the fracture mode	239
5.5 Conclusions	243
References	245

Chapter 6 Conclusions	252
List of publications	256
Acknowledgements	259

Chapter 1 General introduction

1.1 Materials for automotive body structures

Recently, higher environmental regulations have been required for automobiles. For example, improvements in fuel efficiency are underway to reduce CO₂ or greenhouse gas emissions. As a specific policy, the US Environmental Protection Agency (EPA) target to increase the proportion of electric vehicles to 67% by 2032[1]. From 2027 to 2032, vehicles must reduce CO₂, non-methane organic gas (NMOG), nitrogen oxides (NO_x), fine dust, and greenhouse gases (GHG) by an average of 13% per year. Accordingly, strong regulations are in progress to gradually strengthen regulations over six years to reduce pollutant emissions from new passenger cars and trucks by 56% by 2032 compared to the 2026[2].

In response to these regulations, the vehicle body lightweight structure is in the spotlight as a strategic solution for improving fuel economy and reducing CO₂ emissions. In particular, the weight reduction of vehicles is a key technology for the next generation of eco-friendly cars that can dramatically increase driving range[3]. As shown in Fig. 1-1, vehicle body weight continues to increase due to the increased use of high-strength materials and crash members and the increase in parts to support passenger convenience[4]. In particular, in the case of electric vehicles, the capacity of the battery system mounted on the vehicle increases along with improved battery efficiency. To improve the driving range of electric vehicles, the energy density of the battery must be increased, which means an increase in the weight of the battery system. As shown in Table. 1-1, it can be seen that electric vehicles with long driving ranges have relatively heavy batteries[5]. To effectively offset this, lightweighting is essential.

The weight reduction of the vehicle has the advantage of improving not only fuel efficiency but also various performances, as shown in Fig. 1-2. For example, if the weight of a 1,500kg passenger car is reduced by about 10%, fuel efficiency increases by 3.8% and acceleration performance increases by 8%. In addition, it is reported that the braking distance is reduced by 5%, exhaust gas emissions are reduced by 2.5-2.8%, and vehicle durability life is reported to be increased by 1.7 times. Therefore, the weight reduction of vehicles is one of the important challenges for reducing CO₂ emissions along with various advantages.

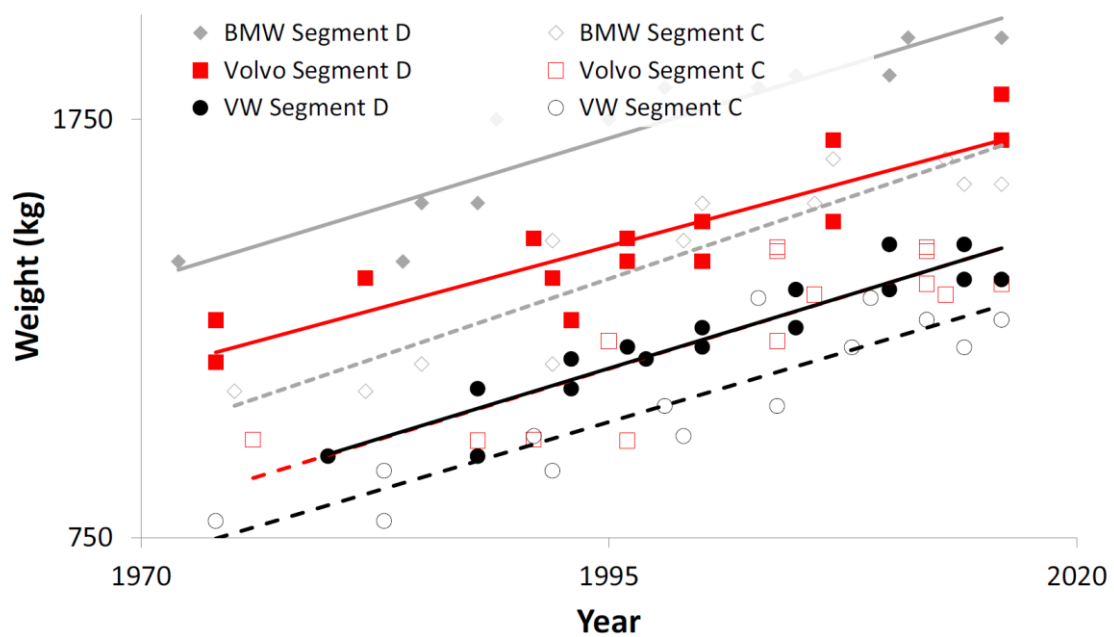


Fig. 1-1 The trend of weight increase of cars during the last decades[4].

Table. 1-1 Battery capacity, battery weight, total car weight, range on full battery of battery electric vehicles investigated[5].

Vehicle	Platform mass (kg)	Drivetrain type	Curb mass (kg)	Range (km)	Battery capacity (kWh)	Battery mass (kg)	Specific energy (Wh/kg)	Energy consumption (MJ/km)
BEVCM-0	1110	CM	1445	250	36.9	335	110	0.446
BEVCM-1	1110	CM	1685	400	63.3	575	110	0.479
BEVCM-2	1310	CM	1668	250	39.4	358	110	0.476
BEVCM-3	1310	CM	1924	400	67.5	614	110	0.510
BEVWM-0	1060	WM	1349	250	31.8	289	110	0.385
BEVWM-1	1060	WM	1551	400	54.0	491	110	0.409
BEVWM-2	1260	WM	1569	250	33.9	309	110	0.411
BEVWM-3	1260	WM	1784	400	57.6	524	110	0.435

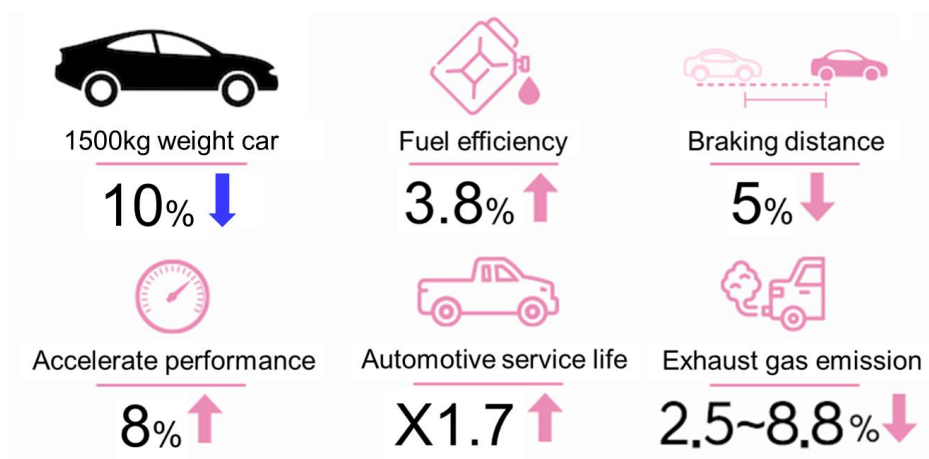


Fig. 1-2 Advantages of weight lightening the car body[6].

Typically, there are three ways to reduce the weight of a vehicle: structure, construction method, and material. First, lightweighting the BIW structure shown in Fig. 1-3 is a method of minimizing material use by implementing an optimized structure[7], which can minimize cost increases, but has limitations in innovative design changes and a limited scope of application. Second, lightweighting is a method of reducing material usage by processing existing materials more precisely. Although it

has the advantage of utilizing existing materials, large-scale facility investment is required. Lastly, lightweighting of materials is a method of replacing or partially combining existing steel materials with lightweight materials. Fig. 1-4 shows lightweighting according to the use of materials. Fig. 1-5 shows the lightweighting of the steel car body according to the application of lightweight materials. Among the various methods, the lightweight of the structure has limitations such as difficulty in design change, limited scope of application, and large-scale facility investment. For this reason, as shown in Fig. 1-6, recently, lightweighting of materials such as aluminum has attracted attention[8–10].

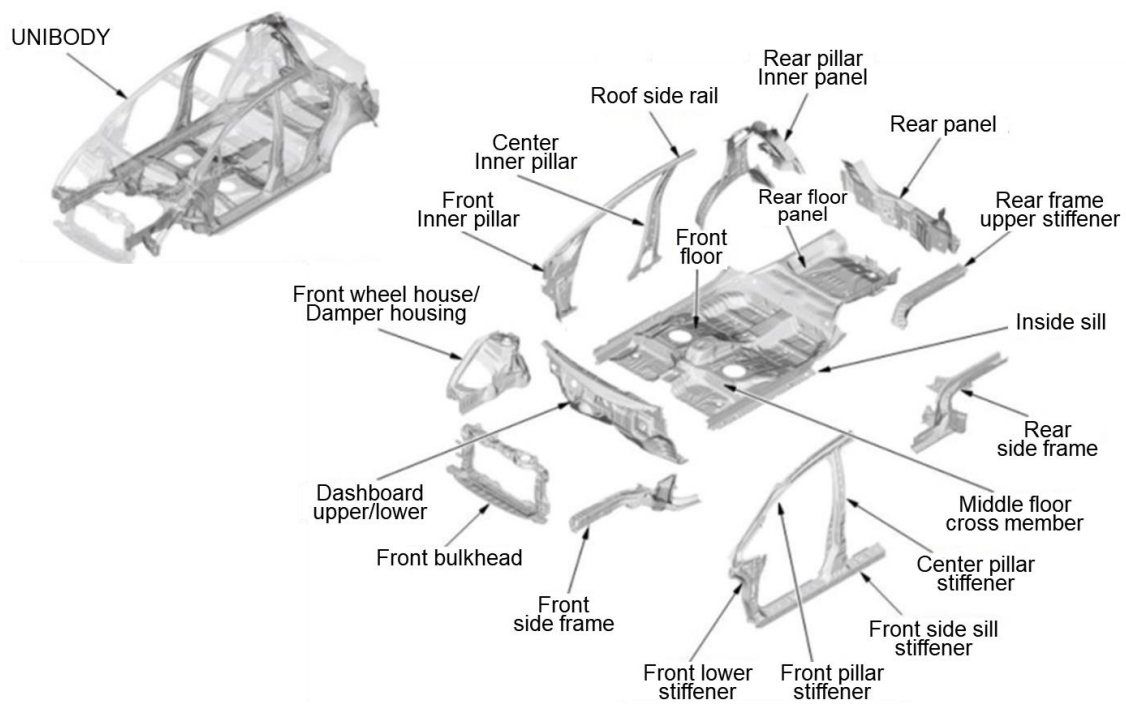


Fig. 1-3 Structure of car Body in white [7].

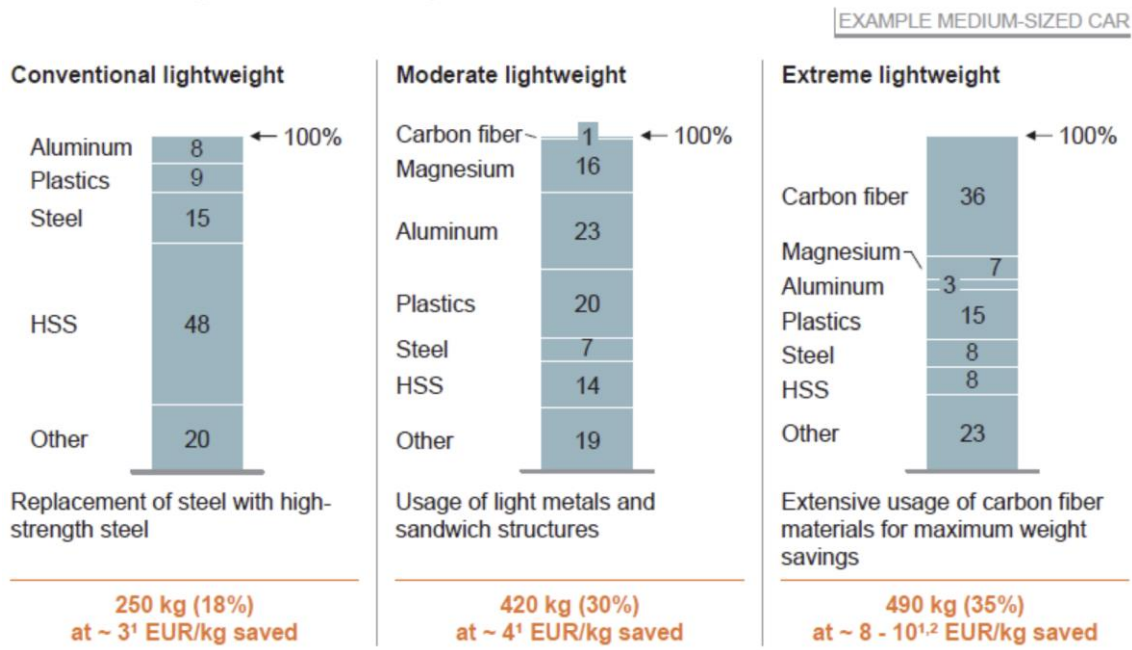


Fig. 1-4 Use of materials according to lightweight[8].

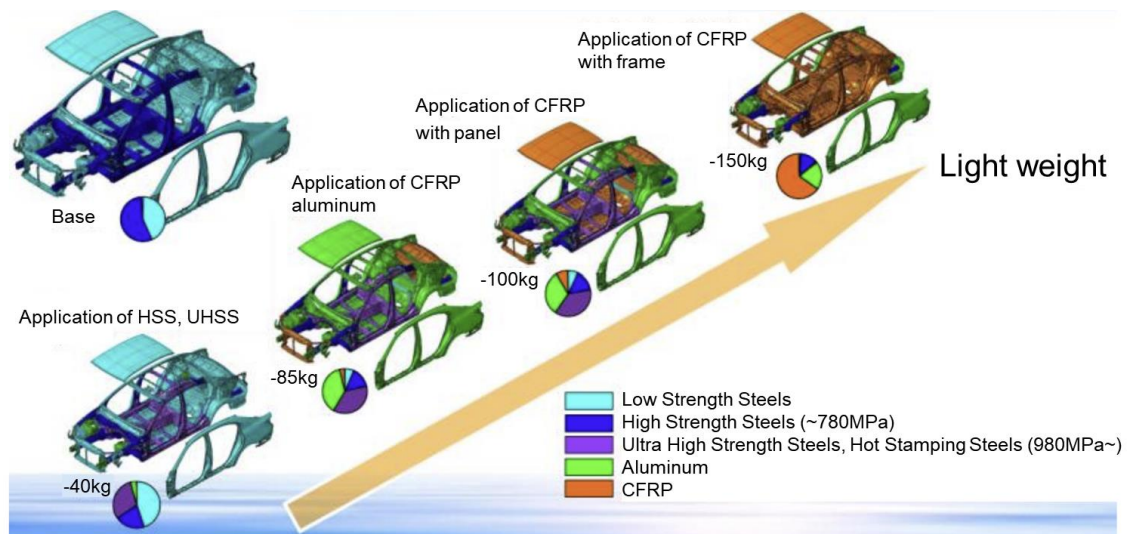


Fig. 1-5 View of light weighting for BIW[11].

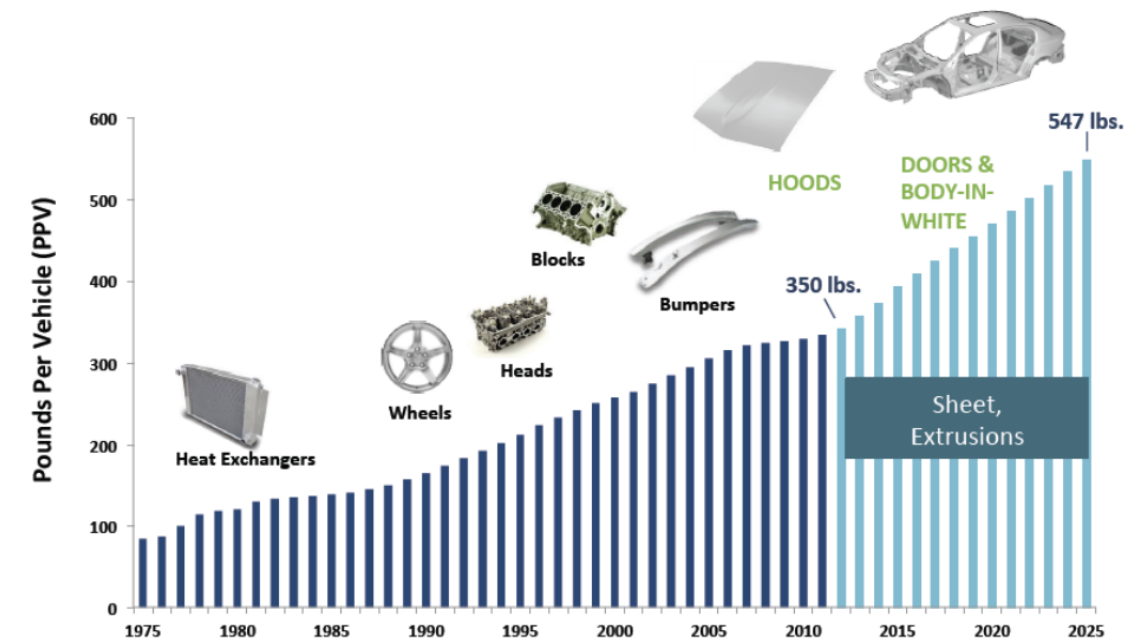


Fig. 1-6 Trend of automotive aluminum growth[9].

As the lightweighting of vehicles becomes a global trend in the automobile industry, the market share of steel, which was widely used as a structural material, is gradually being replaced by lightweight materials such as Al alloys, Mg alloys, composites, or carbon fibers[12,13]. The density of aluminum is 2.7g/cm^3 , which is about 1/3 lower than that of steel, resulting in a 35-40% weight reduction compared to existing steel materials[9]. By combining aluminum with other elements such as Cu, Mn, Si and Zn to form an alloy, it can provide superior corrosion resistance, electrical and thermal conductivity, and improved strength performance compared to structural steel. Aluminum alloys are classified into various four-digit series from 1000 to 9000, with each alloy designation corresponding to a specific composition, leading to a variety of automotive applications[14]. The applications and properties of aluminum alloys including car bodies are shown in Fig. 1-7 and Table. 1-2, respectively. For example, 1000 series aluminum alloys are commonly used in insulation and license plates due to

their excellent workability, surface finish, and highest corrosion resistance among all aluminum alloy series. 2000 series aluminum alloys containing the Cu element can achieve excellent properties even at somewhat higher or lower temperatures, so they are mainly used in automotive pistons, shock absorbers and valves. 5000 series aluminum alloys containing Mg elements are non-heat treated alloys and are widely used in body panels, including ship structures and fuel tanks, due to their excellent corrosion resistance and moldability. Unlike the strength improvement process through heat treatment that can be obtained from other aluminum alloys, strength can be increased using a work hardening process. Furthermore, 6000 series aluminum alloys using Mg and Si as basic alloy elements has high strength and excellent corrosion resistance, so they are applied to fenders, fillers, and frames of vehicles. In general, the car body is divided into inner and outer plates. The 5000 series aluminum, which has excellent formability, is used as the inner plate, and the 6000 series aluminum, which has excellent rigidity, is used for the exterior plate. The 7000 series is an alloy containing the Zn element and has the highest strength among existing aluminum alloys and is mainly used in aircraft and structures. Recently, it has been applied to electronic device frames such as mobile phones and laptops due to its excellent extrusion properties. In addition, it is a material that is reliable enough to be used as a missile component[15].

Magnesium has a density of 1.74g/cm^3 , making it the lightest structural alloy, less than 1/4 that of steel. Due to the combination of excellent specific strength and specific rigidity, magnesium and its alloys are automotive materials that can achieve excellent weight reduction. However, when magnesium is applied to a vehicle, galvanic corrosion, which is inevitably a problem, occurs at the joint with other parts, which can reduce the

durability of the vehicle[16]. Magnesium is used in various industries depending on its alloy composition, which is shown in Fig. 1-8. The magnesium alloy names A and Z refer to the composition of aluminum and zinc, respectively. The fundamental problem preventing widespread adoption of magnesium in automobiles is manufacturing. Compared to existing steel or aluminum, there is a lack of manufacturing technology experience, and low formability and high production cost. Nevertheless, as shown in Fig. 1-9, it is partially applied to aircraft industry, instrument panels, car steering wheels, engine cradles, and seats of high-end platforms. For this reason, as shown in Fig. 1-10, although magnesium is the lightest structural alloy with a density of about 1/3 of aluminum, its application to car bodies is limited compared to aluminum[17,18].

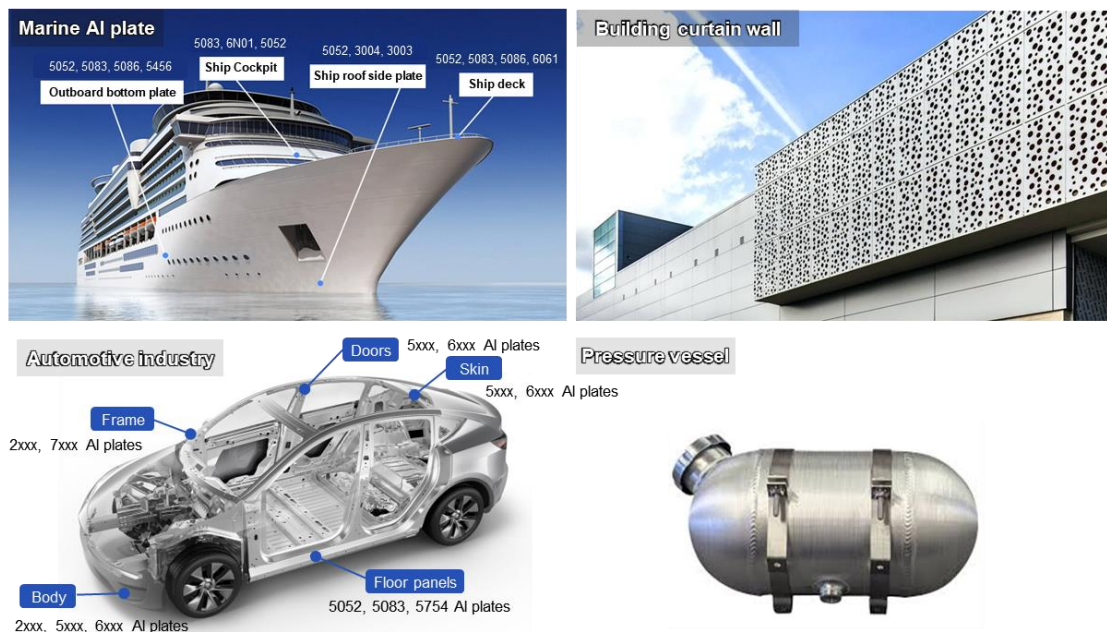


Fig. 1-7 The application of aluminum alloys in industry.

Table. 1-2 The application of aluminum alloys series in various industry.

Series	Main Alloying Elements	Main Characteristics	Example Applications
1xxx	~99% pure aluminum	High electrical and thermal conductivity, excellent corrosion resistance.	Electrical parts, food and chemical processing equipment.
2xxx	Copper	High strength-to-weight ratio, low corrosion resistance.	Truck wheels, suspension parts, aircraft fuselage, and wings.
3xxx	Manganese	Moderate strength and good workability.	General sheet work, recreation vehicles, electronics.
4xxx	Silicon	Low melting point and thermal expansion, high wear resistance.	Welding wire and brazing alloy, architectural applications, forgings.
5xxx	Magnesium	Moderate-to-high strength, good weldability, good corrosion resistance.	Appliances, automotive parts, marine components.
6xxx	Silicon and magnesium	Medium strength with good formability, weldability, machinability, and corrosion resistance.	Structural, aircraft and marine applications, architectural extrusions, recreational equipment.
7xxx	Zinc	Moderate-to-very high strength.	Airframe structures, mobile equipment, high-stress parts.

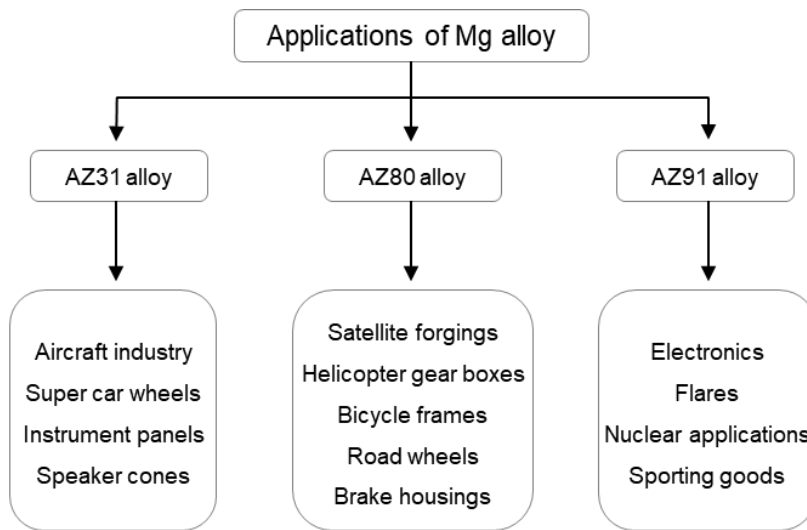


Fig. 1-8 Classification of magnesium alloys.

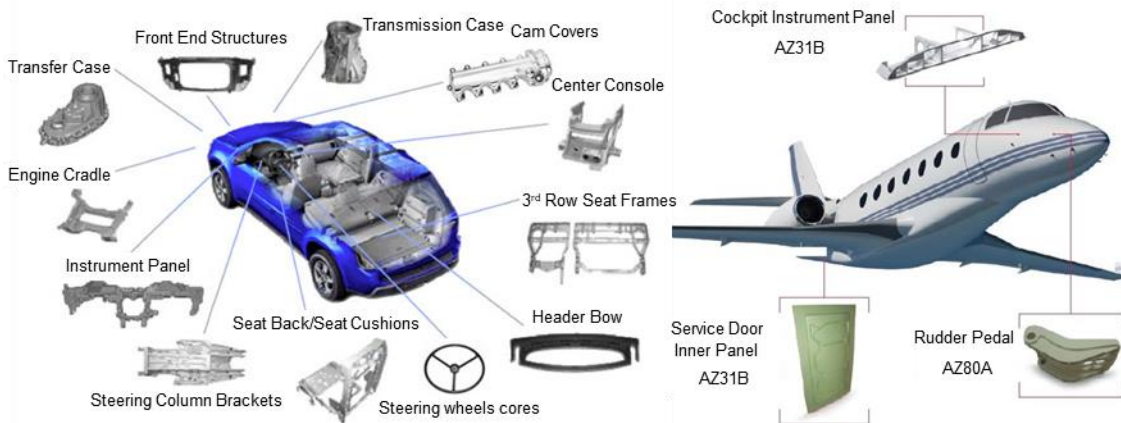


Fig. 1-9 The application of magnesium alloys in car and aircraft industry.

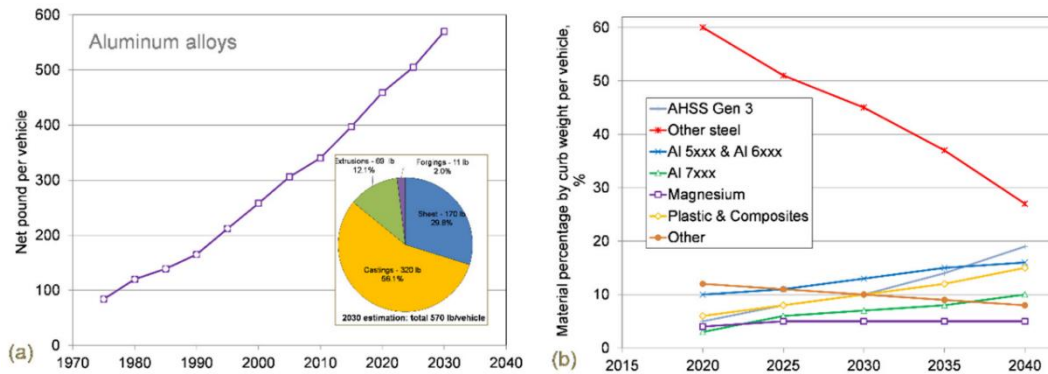


Fig. 1-10 Predicted contribution of automotive materials: (a) aluminum content growth in North America vehicle, (b) average vehicle structure material percentage [17].

Composite material refers to a material composed of two or more different materials. Here metal, ceramic or polymer materials can be used as the main base material. Compared to existing steel materials, most composite materials have high specific strength, light weight, and high resistance to corrosion[19]. Additionally, excellent fatigue strength, improved physical properties, and surface finish are the main advantages of composites. Generally, in the automobile industry, carbon fiber is used as a material for weight reduction[20]. CFRP, which is composed of carbon fiber, is an excellent material for lightweight design with vibration, fatigue, corrosion resistance, high specific strength, and crashworthiness. Recently, it has been applied to automobile roofs, floor panels, frames, and front and rear bumpers[21]. Although CFRP can achieve excellent weight reduction effects when applied to vehicles, high production costs are one of the major limitations of composite materials for widespread application. In addition, high-speed production is not possible and problems with recyclability and repairability are also challenges that must be resolved[22].

Steel has a wide range of characteristics, starting from a tensile strength of 200 MPa, are relatively low-cost compared to other materials, and have a well-established global supply chain. Automotive steel sheets are required to have various characteristics depending on the use, and the development meet these requirements has been underway. Types of steel include Dual phase (DP) steel, Complex phase (CP) steel, Martensite (MS) steel, Transformation induced plasticity (TRIP) steel, Twinning induced plasticity (TWIP) steel, Press hardening (PH) steel, and Boron steel. Steel materials are classified according to their strength and elongation characteristics and are shown in Fig. 1-11.

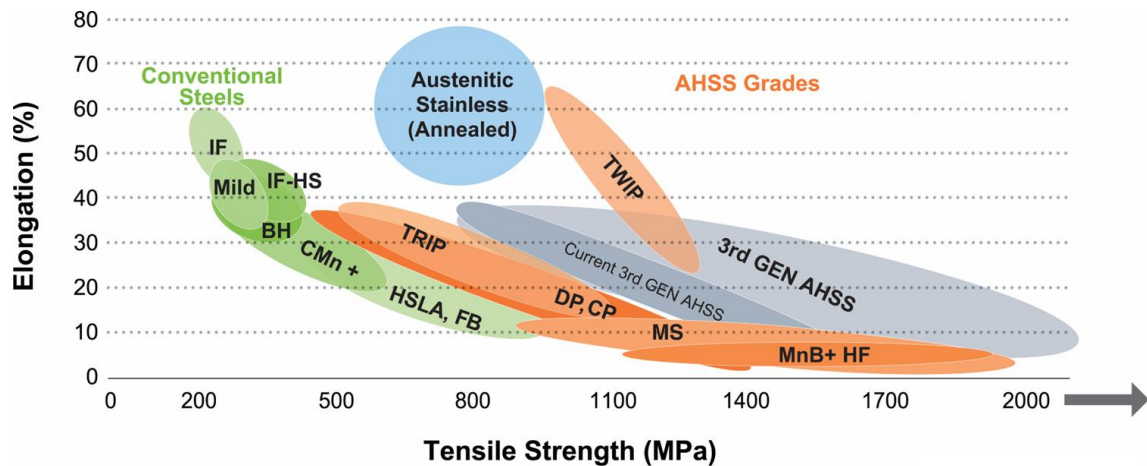


Fig. 1-11 Steel application trend of automotive industry[23].

The application of steel in the car body industry is divided according to the characteristics of the car body frame. As illustrated in Fig. 1-12, Body-in-white (BIW) is divided into a crumple zone and a safety zone. Generally, the front part is made of relatively low-strength material to absorb energy in the impact of a vehicle collision. In contrast, the space where passengers board requires safety, high-strength materials must be applied. Among the materials used in car bodies, SPFC steel is mainly used due to its high strength and improved formability. Because of its high strength, it is used in center pillars and door parts that require passenger safety, as shown in Fig. 1-13.

In general, as the strength of a steel plate increases, its ductility and its formability decreases. DP steel is a widely used high-strength steel to meet these requirements. As shown in Fig. 1-14, DP steel is a material that achieves a balance between strength and ductility by controlling the microstructure to form a dual-phase microstructure consisting of soft ferrite and hard martensite phases[24]. As illustrated in Fig. 1-15, it is also widely used in the automotive field because it can satisfy specific performance requirements such as crashworthiness[25]. DP steel, TRIP steel, etc. are the first generation Advanced high strength steel (AHSS), and TWIP steel, which has

improved formability by increasing the tensile strength to 700 MPa and elongation to over 40%, is the second generation AHSS. Meanwhile, in the case of TWIP steel, a large amount of expensive alloy elements such as Mn are added, and lower strength and ductility than TWIP steel may be required as needed. Recently, the 3rd generation AHSS, which has strength and ductility between the 1st and 2nd generation AHSS, is attracting attention[24,26].

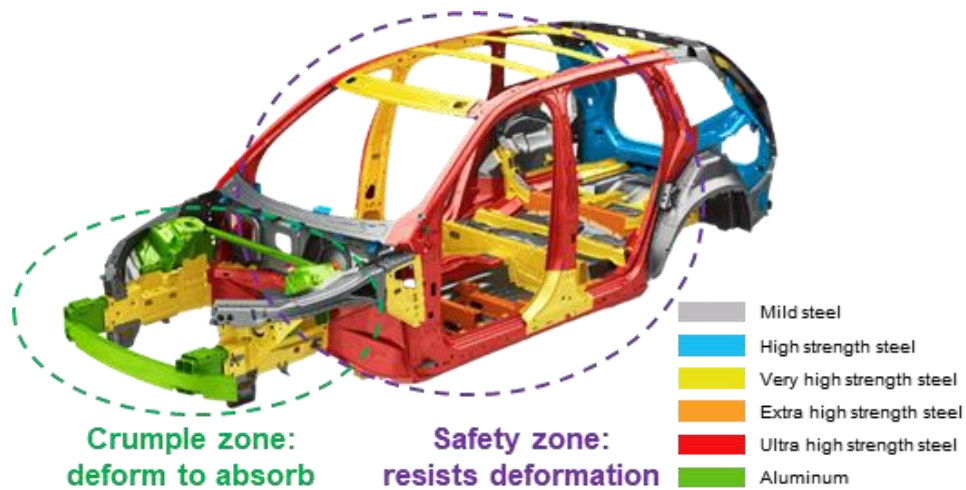


Fig. 1-12 Body in white of the all new XC90 and material application[27].



Fig. 1-13 SPFC steel applied to vehicle parts requiring safety.

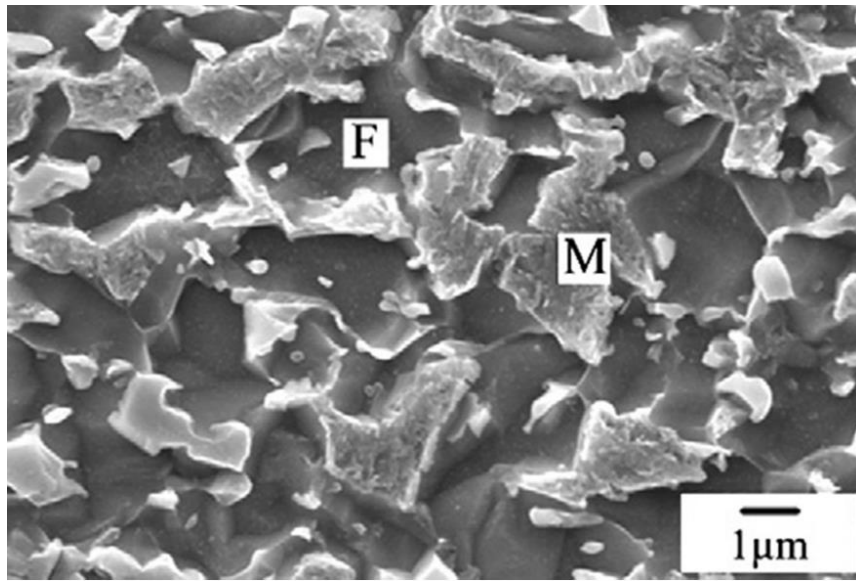


Fig. 1-14 Scanning electron image of a dual phase steel microstructure with ferrite(F) and martensite(M)[24].

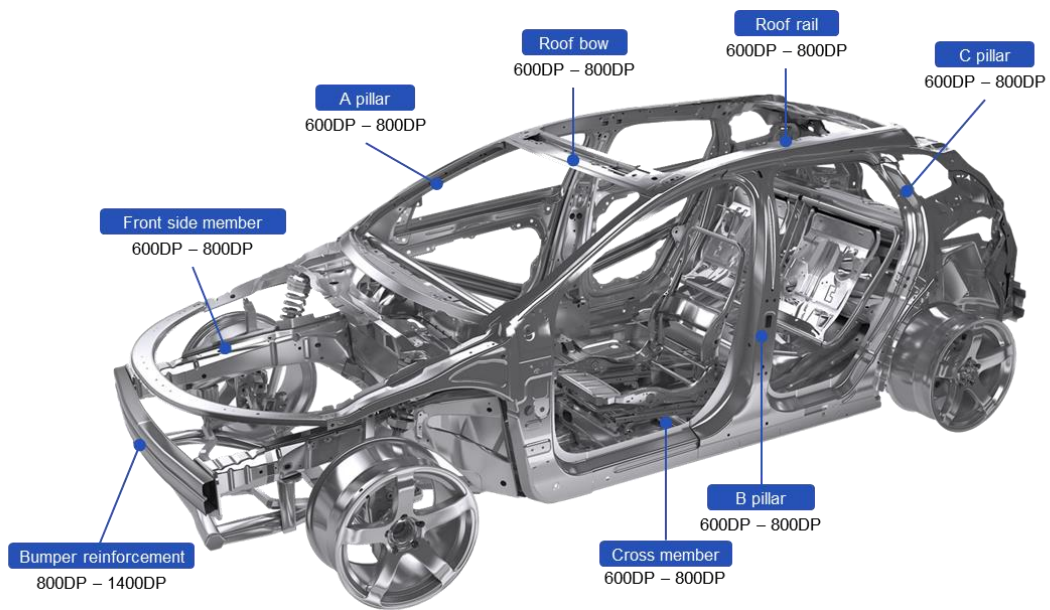


Fig. 1-15 Automotive applications for dual phase steels[28].

1.2 Conventional welding process for structural materials

To weld automotive structural materials, fusion welding, solid-state welding, mechanical fastening and adhesion are used. As shown in Fig. 1-16, representative fusion welding includes resistance welding, arc welding, and laser welding. Solid state welding includes friction stir welding (FSW), mechanical fastening includes SPR and FDS using rivets or screws, and adhesive bonding.

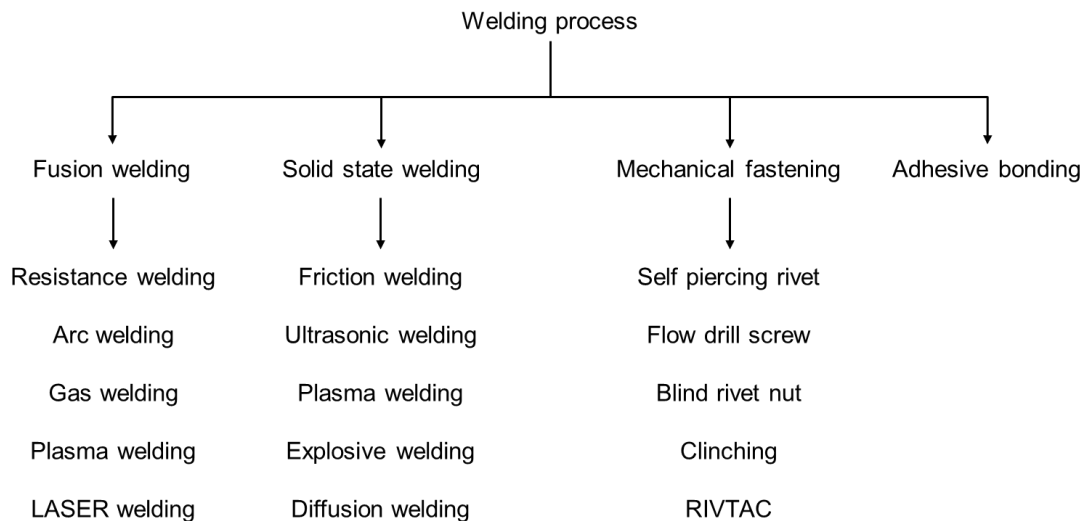


Fig. 1-8 Classification of welding process.

As shown in Fig. 1-17, resistance welding, which is fusion welding, contacts the base material and pressure it while applying an electric currents. Heat is generated by contact resistance and the resistivity of the metal itself. This is a method of joining by applying pressure when the base material is heated. In recent years, approximately 2,000 to 5,000 point of resistance spot welding have been applied in vehicle production [29].

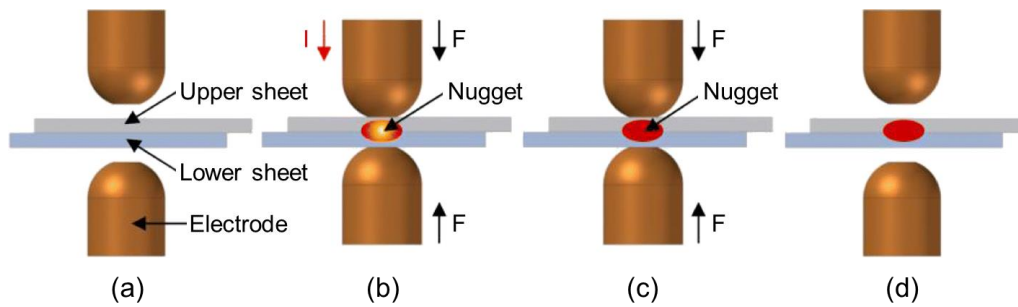


Fig. 1-9 Resistance spot welding process. (a)positioning, (b)application of pressing force and current, (c)cooling and post clamping, (d)retraction of electrodes[30].

Arc welding is a method of welding by generating an arc between the base material and a metal electrode to melt part of the base material and the welding electrode. There are three main types of arc welding: Shield metal arc welding (SMAW), Gas metal arc welding (GMAW), and Gas tungsten arc welding (GTAW). SMAW is a welding method in which the welding rod is held in a holder and an arc is generated directly on the base material, and the gas generated as the welding rod coating melts serves as a shield. It is mainly used for welding steel and is the cheapest welding method. GMAW, as shown in Fig. 1-18, is also called Metal inert gas (MIG) welding, Metal active gas (MAG) welding, CO₂ welding, and Flux cored arc welding (FCAW) welding. These are all welding methods that require filler metal, and depending on the method, it is necessary to be careful about spatter generation, rust, moisture, oil, etc. due to sensitivity to contamination of the base material. GTAW, also called tungsten inert gas (TIG) welding, is a method of welding by melting a tungsten welding rod. Inert gases such as argon and helium are used as shielding gases, and high quality and full-position welding is possible, but the work speed is slow and the parts and equipment are somewhat expensive.

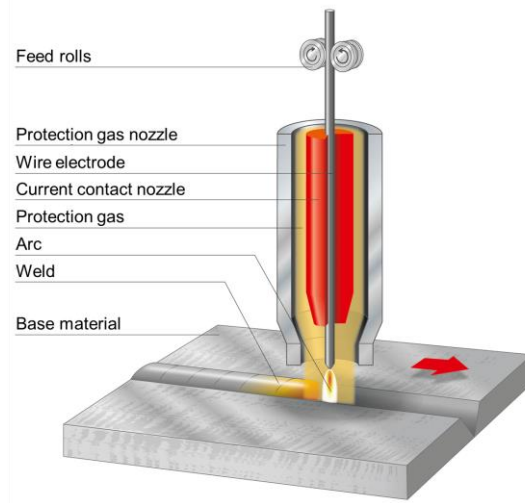


Fig. 1-10 Schematic illustration of GMAW[31].

A schematic illustration of laser welding is shown in Fig. 1-19. Laser welding focuses a beam on the welding material, which is absorbed by the surface of the object and converted into heat energy, causing local heating and melting. As the density of laser power increases, a key hole is formed due to evaporation or sublimation of the welding material, enabling deep penetration. Key hole welding is possible even on thick plates and a deep and narrow weld zone can be formed[32]. As shown in Fig. 1-20, laser welding is applied to the A pillar, B pillar, front rail, and rear rail of the car body[33].

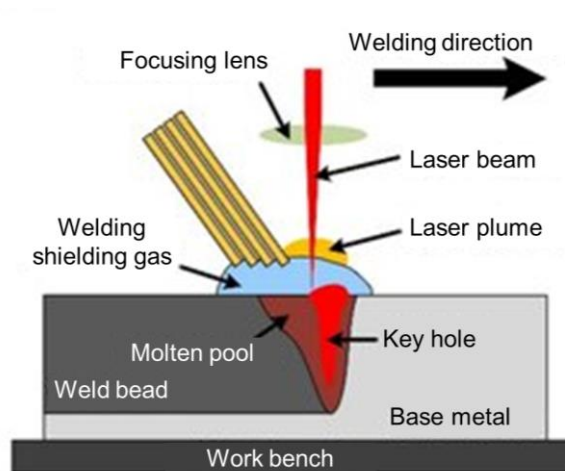


Fig. 1-11 Schematic illustration of Laser welding[32].

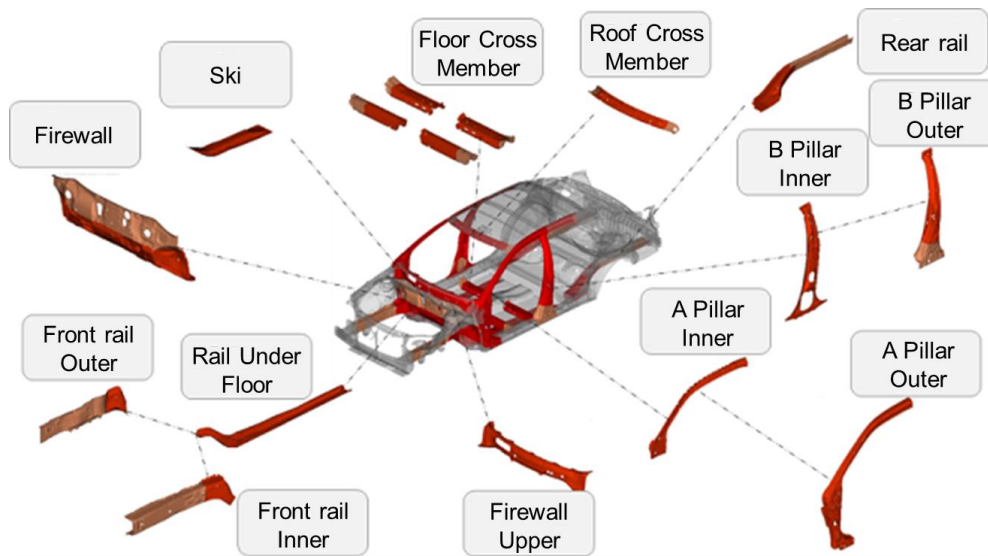


Fig. 1-20 Automotive parts with Laser welding[33].

The mechanical properties of the weld zone depend on its microstructure, which is determined by the chemical composition of the base material, welding conditions, and post-heat treatment. As the carbon content of structural steel increases, its weldability decreases, making it easy to defects such as overheating, undercooling, cold cracking, and porosity. Unlike fusion welding, solid state welding is a method of joining without melting the base material below the melting point, so these defects can be sufficiently suppressed. This joining process includes welding, which uses frictional heat generated by rotation at the interface. FSW involves joining using a tool with a threaded probe, is also widely applied to car bodies as a type of friction welding. FSW generates heat due to mutual friction with the tool when inserted into the material to be joined while rotating the tool at high speed. Welding is accomplished by mixing the material softened by this frictional heat with plastic flow by stirring the tool. The schematic diagram of FSW is shown in Fig. 1-21. Since welding is performed below the melting point of the base material, there is little deformation. As a result, excellent mechanical strength and

harmful gases are not generated, so it is characterized by being eco-friendly. As shown in Fig. 1-22, Honda applied FSW to the subframe of the Honda Accord for the first time in the world, reducing body weight by 25% and increasing rigidity by 20%[34].

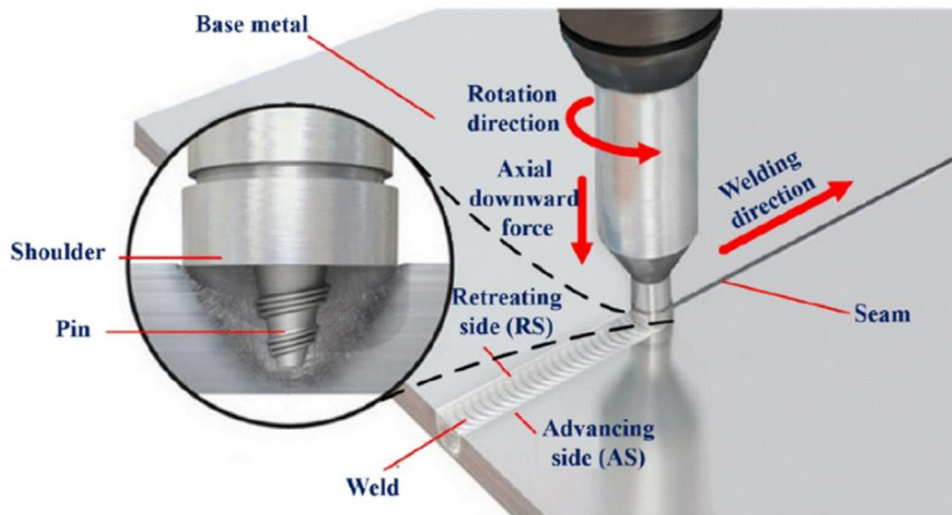


Fig. 1-21 Schematic image of friction stir welding process[35].

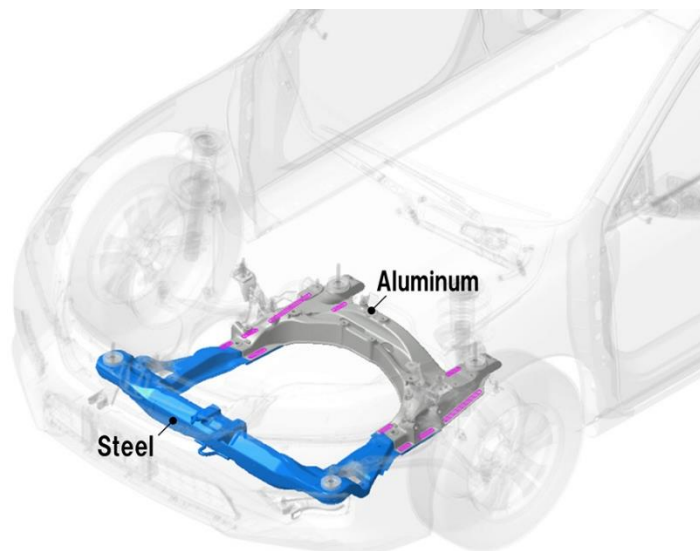


Fig. 1-22 FSW applied to Honda Accord subframe[34].

As the materials that make up the vehicle body become more diverse, new bonding technologies are being developed. When a metal and a polymer part need to be connected, the traditional welding method of inducing metal bonding between atoms has limitations. As a solution to this, mechanical fastening and adhesion, or a hybrid method combining them, are being used. Mechanical fastening does not cause thermal deformation and allows joining of materials with different strengths. In addition, it has the advantage of being eco friendly and enabling short processing and automation. Representative mechanical fastening methods include self-piercing rivet (SPR), flow drill screw (FDS), and clinching.

As shown in Fig. 1-23, SPR is a process of penetrating the upper plate and fastening the lower plate with plastic deformation based on forming. Pre hole is not required and the process is simple, so productivity is high and automation is easy. It can secure a joining strength equivalent to or greater than that of existing resistance spot welding, and is currently widely applied to the integration of car bodies with multiple materials. However, SPR, a forming-based mechanical joining, is partially applied to the dissimilar material process of non-ferrous metals and steel, but there are difficulties in piercing rivets in the case of high-strength steel. Additionally, there are problems such as reduced collision absorption capacity and galvanic corrosion. Fig. 1-24 shows automotive parts to which SPR can be applied.

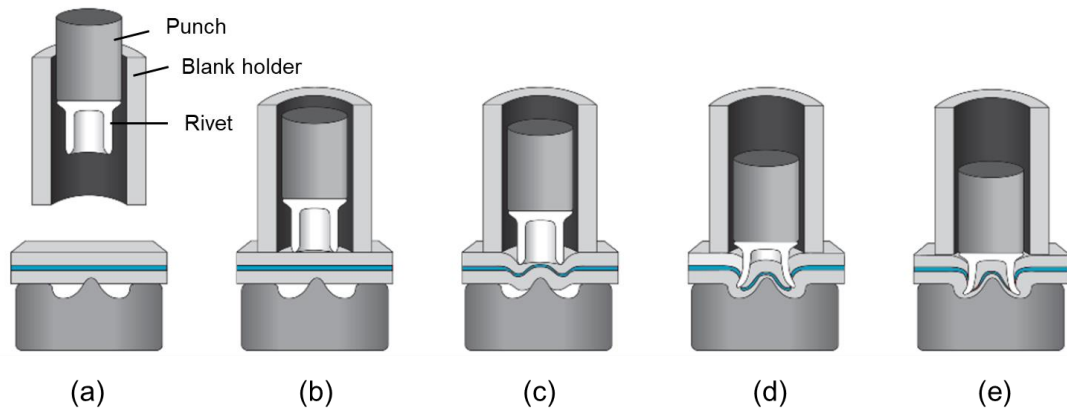


Fig. 1-23 Self piercing riveting process. (a)starting condition, (b)material clamped, (c)rivet penetration, (d)rivet insertion, (e)insertion complete[36].

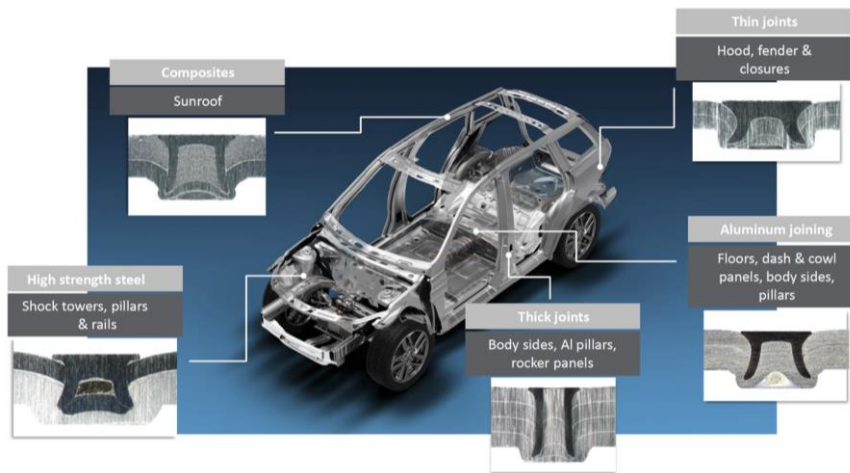


Fig. 1-24 Automotive parts applying self piercing rivet[36].

FDS is heated by a high-speed rotating screw pushing the plate down, and a hole is drilled to create a thread in the material. It is a fastening method in which the screw head contacts the top plate and final torque is applied to tighten the connection. The FDS process is shown in Fig. 1-25. Unlike SPR, which requires an upper rivet and a die to support the lower part, it has the feature that fastening is possible even in a closed cross-section structure. If the top plate is thick or high strength steel, it is difficult to penetrate the screw through the plate, so it is riveted by drilling a pre hole[37].

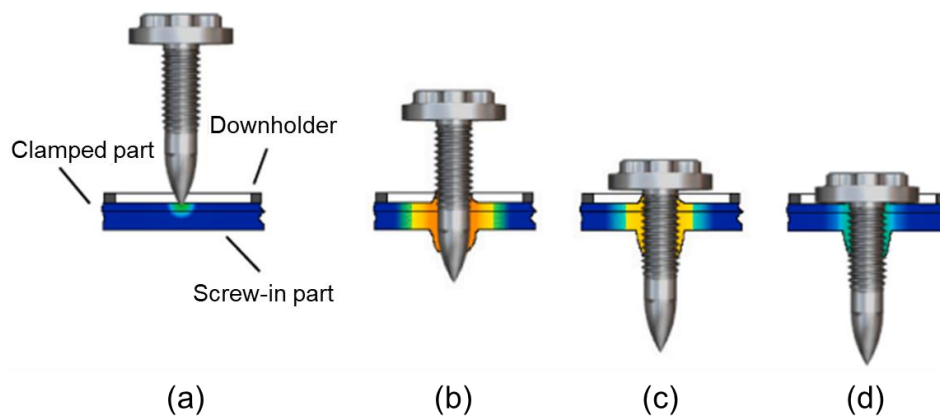


Fig. 1-25 Flow drill screw process. (a)positioning, (b)flow drilling, (c)screwing, (d)tightening[38].

As shown in Fig. 1-26, the clinching process is a method of mechanically fastening through forming-based plastic deformation of the upper and lower plates. The process is simple and short, resulting in high productivity and easy automation. In particular, unlike SPR or FDS joining, it is advantageous in terms of production costs because it does not require separate consumables such as rivets or screws. However, materials with low elongation, such as CFRP and ultra-high-strength steel (UHSS) cannot be applied. And the bonding strength has a lower disadvantage than other processes, so the scope of application is limited.

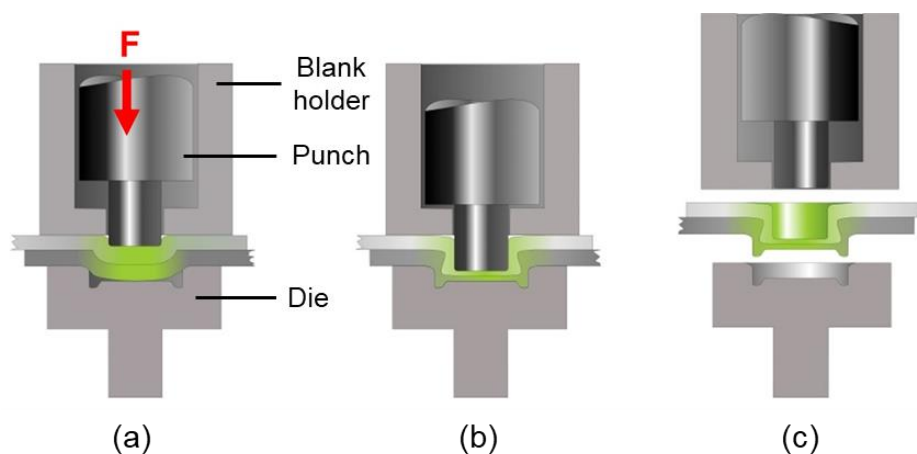


Fig. 1-26 Clinching process. (a)forming in die, (b)forming of interlock, (c)backstroke[39].

1.3 Dissimilar materials welding

As the materials that make up automobiles and other transportation devices change to non-ferrous or polymer materials, the corresponding bonding process must also be developed. As the safety standards required for vehicles become more stringent, the addition of reinforcing members causes an increase in weight. Steel materials are becoming increasingly high-strength and thinner, so it is important to secure processes for thin plate welding technology, and in the case of lightweight metals such as aluminum, it is necessary to develop joining or fastening technologies that can replace resistance spot welding. In particular, when replacing existing steel parts with lightweight metals such as aluminum, decision on joining and fastening technology for the connection with the existing steel part must be considered very important in terms of productivity and safety of the car body.

The various welding methods described above are also being considered for joining dissimilar metals such as steel and aluminum alloy. However, there are generally many problems in joining steel and aluminum by melting them with heat. Steel and aluminum are insoluble in each other and have different chemical and thermal properties (melting point, thermal expansion coefficient Fig. 1-27 shows the formation and growth of Fe-Al IMC layers during welding[40]. The high heat input of conventional fusion welding such as arc welding, spot welding, and laser welding causes a thick intermetallic compound (IMC) to form at the interface between steel and aluminum, which causes a decrease in strength[41,42]. Additionally, as shown in Fig. 1-28, traces of FeAl_3 and Fe_2Al_5 are shown through Transmission Electron Microscopy (TEM) observation[43]. IMC is formed at the interface due to the mutual diffusion of Al and Fe atoms. In general, the Fe_2Al_5 phase is considered the most dominant phase and can be

the origin of fracture due to its brittleness, but it is reported that the FeAl_3 and $\text{Fe}_4\text{Al}_{13}$ phases that can be found on the Al side are generally not problematic due to their ductility[40].

In addition, if aluminum HAZ softens due to heat generated during welding, the mechanical properties are reduced compared to the base material, which may cause fracture[44,45]. In particular, this phenomenon occurs in the Al6000 series, which is a heat treatment alloy material. It is reported that the artificial aging alloy is heated above the aging temperature during welding, and the precipitates deposited to secure strength are decomposed and coarsened. In addition, as shown in Fig. 1-29, the Al5000 series, which is a work hardening material, was softened in the HAZ area during resistance element welding, resulting in a decrease in hardness. Scholars reported that the softening of the non-heat treatment Al alloy welded joints is mainly caused by the coarse grain in the HAZ and the disappearance of the local cold work hardening effect of the welded joint[46]. Therefore, technology to use low heat input during welding is required to secure the strength of the HAZ[47,48].

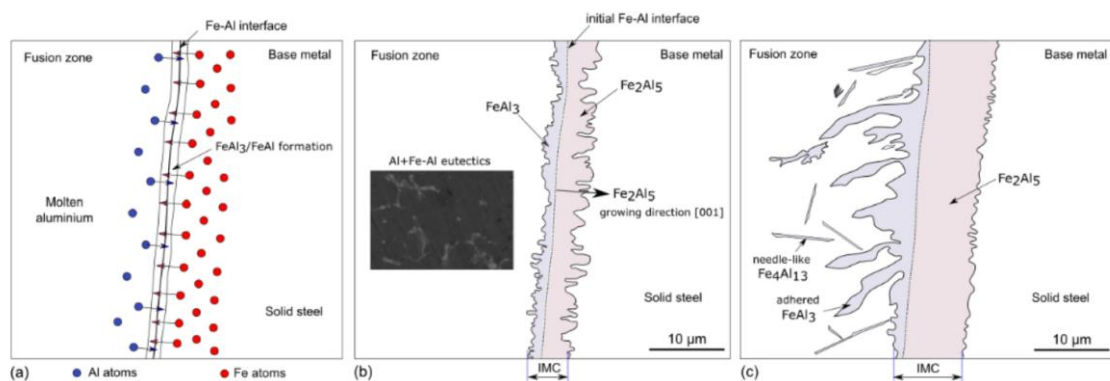


Fig. 1-12 Formation and growth of Fe-Al IMC layer during welding according to progress in weld thermal cycle: (a)initial formation of FeAl phases, (b) Fe_xAl_x phases during low heat input parameters and (c) Fe_xAl_x phases during high heat input[40].

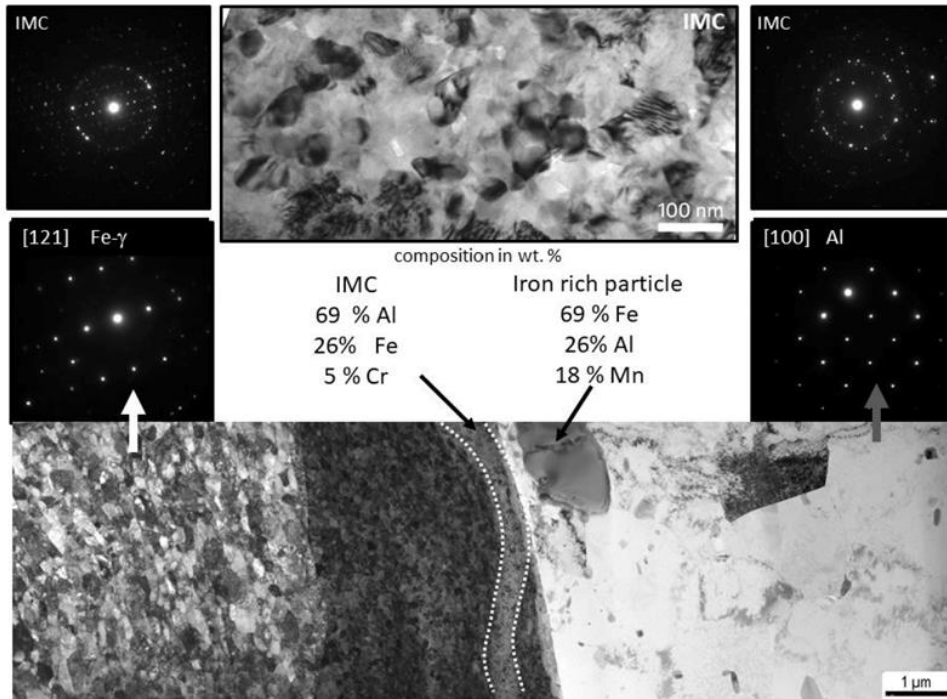


Fig. 1-13 Identification of the intermetallic compounds by Transmission Electron Microscopy (TEM) showing the presence of traces of Fe_2Al_5 and FeAl_2 [43].

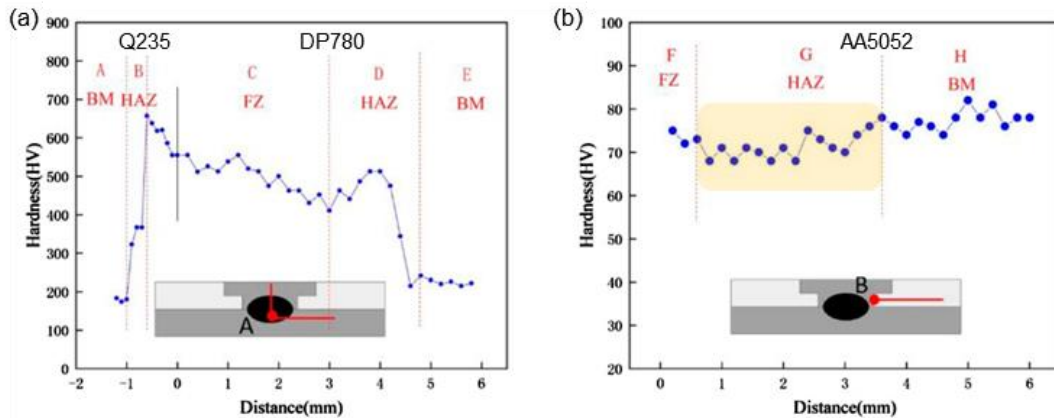


Fig. 1-29 Microhardness characteristics of the resistance element welding on (a) the steel side and (b) the aluminum side[46].

To compensate for these problems, mechanical bonding methods and hybrid bonding methods that combine them with adhesive are being used. Representative mechanical joining methods include the previously mentioned SPR, FDS, and clinching.

Unlike melt welding, there are no problems caused by strength reduction or softening of aluminum due to IMC caused by the heat generated during welding. It has the advantage of not requiring pre hole, and that the process is short and simple, resulting in high productivity and easy automation. However, in the case of the SPR process, which is a forming based mechanical joining, there is a limit to self-locking when applying ultra-high strength steel or CFRP over 800 MPa, and when the rivet penetrates the upper plate, it becomes thick or cracks due to insufficient strength. Furthermore, there are problems such as reduced collision absorption capacity and galvanic corrosion due to potential differences[49,50]. The clinching process is advantageous in terms of production cost because it does not require rivets, unlike the SPR process. However, it cannot be applied to materials with low elongation, and the joint strength is lower than other processes, so the scope of application is limited. In addition, in the FDS process, if the upper material is thick or high-strength steel, there is difficulty in forming holes through screws, and pre hole processing is essential[37].

Adhesive bonding is a method of permanently joining materials using organic adhesives such as epoxy and urethane. It has a high degree of freedom regarding materials and dimensions, and is advantageous for stress distribution by forming surface joints. However, since the adhesive is in a liquid state before hardening, it cannot maintain the shape of the structure, and after hardening, it is vulnerable to peeling stress and shows fracture behavior with little elongation. In addition, in a relatively high temperature and humidity environment, the deterioration rate due to moisture increases, resulting in a decrease in the strength of the joint[51,52]. Therefore, in the car body assembly process, adhesive bonding alone is not used, but a hybrid bonding method is used along with mechanical fastening. Due to the effectiveness of the

two joining methods, higher bonding strength can be achieved than each method alone. Additionally, the adhesive layer has a sealing effect that can prevent or reduce potential difference corrosion between different materials[37].

Table. 1-3 presents an overview progress through literature review on the strength development of Al-Steel lap joints by various bonding technologies. Among the various technologies, SPR as a mechanical joint technology for Fe/Al dissimilar materials are being actively conducted. SPR showed a higher maximum load value compared to other welding processes. However, in the case of high-strength steel, there is difficulty in penetrating the rivets of the upper plate, and a free hole machining process is required. Research on laser welding is also in progress, and is attracting attention as a high-quality, low-heat input welding technology. However, brittle fracture occurred at the weld zone due to the IMC layer, resulting in low displacement and limited load of 1700N. In the literature reviewed, the combination of mild steel and Al6061 joined by FSW, a solid-state bonding technology, showed a maximum load of 3607N. However, FSW has a fatal disadvantage in that traces of the tool remain even after processing.

Table. 1-3 Literature review of the mechanical strength of Al-Steel lap joints by various joining technologies.

Materials	Methods	Peak Load (N)	Displacement (mm)	Failure mode	Major defect	Ref
TWIP -Al5754	SPR	7430	2.66	Sheet pull-out	N/A	[53]
	Rivet drilling the top sheet	6360	2.26	Rivet failure	N/A	
	Kerb konus riveting	3070	1.87	Rivet pull-out	Hole	
TWIP -Al6111	SPR	6310	2.22	Rivet failure	N/A	
	Rivet drilling the top sheet	5810	2.06	Rivet failure	N/A	
	Kerb konus riveting	1740	1.22	Rivet pull-out	Hole	
DP590 -Al6061	LASER	1700	0.8	Weld joints	IMC(Brittle fracture)	[54]
AISI1008-Al1100	Resistance spot welding	1000	0.25	Interface failure and metal expulsion	IMC(Brittle+ Ductile)	[55]
SPCC -Al5083	Spot forge welding	3800	N/A	Base metal	No defects and cracks	[56]
DP600 -Al5754	Refill FSSW	4400	N/A	Interface	Kissing bond	[57]
Mild steel -Al6061	Flat spot FSW	3607	N/A	Plug fracture	Initial crack in the upper Al plate during the shear tensile tests	[58]
DP600 -Al5052	Resistance welding	4300	N/A	Interface	IMC	[59]
Q235-Al6061	Friction stir lap welding	2800	N/A	Joints (Necking+ Dimple -> Plastic fracture)	heterogeneous microstructure	[60]

1.4 Limitations of RSW with dissimilar materials (RSW: Resistance spot welding)

The RSW process is the most widely used joining process in existing steel car bodies due to its low cost and high efficiency. However, it is difficult to achieve a stable joint when joining dissimilar materials such as steel and aluminum using the existing RSW process due to differences in mechanical properties.

First, because the difference in thermal expansion coefficient between different materials is large, the expansion and contraction of each material becomes inconsistent during welding. As a result, local deformation and internal stress occur after forming the joint, affecting the dimensional accuracy of the vehicle body. In addition, the combination of internal stress and corrosion can reduce fatigue life[61,62].

Second, when joining dissimilar materials, hard and brittle IMC is easily created at the interface and dislocations are easy to accumulate, making bonding difficult. When a load is applied, cracks may occur in the IMC layer or at the interface between the IMC and the base material, causing fracture[40–42].

Third, because the electrochemical potential between different materials is different, a galvanic effect occurs when the two materials come into contact, causing the metal with a low potential to corrode. Fig. 1-30 shows the difference in corrosion depth caused by the potential difference between aluminum and steel. This is further accelerated in a salty and humid environment, greatly reducing the durability of the joint[16].

In addition, as mentioned earlier, HAZ generated from aluminum when steel and aluminum are bonded to dissimilar materials can be softened by heat, resulting in a weak part and a decrease in strength, thereby reducing the reliability of the structure[45,47,48,63]. Therefore, the above problems must be solved in the bonding of

dissimilar materials.

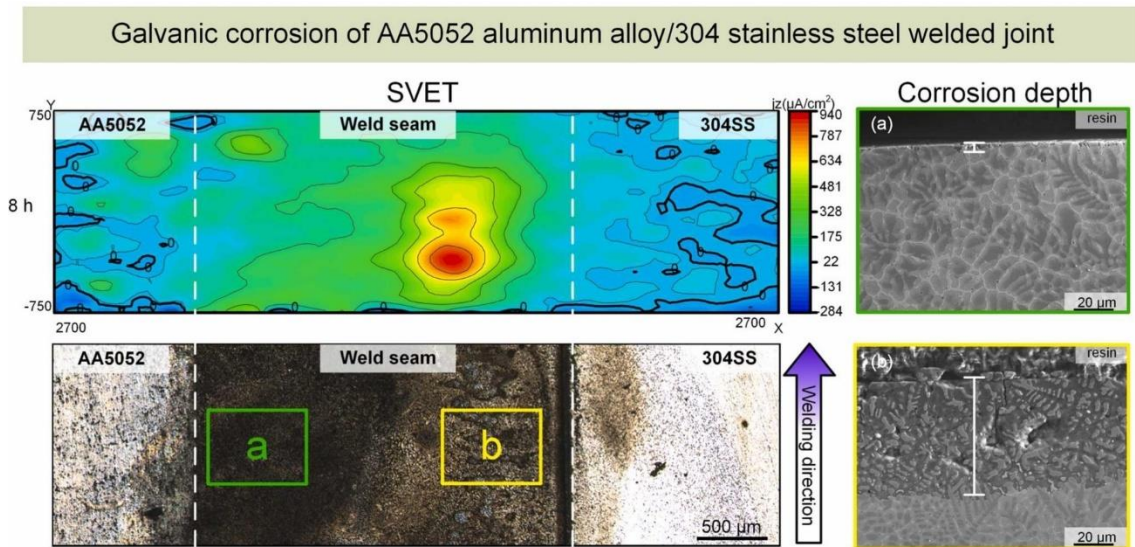


Fig. 1-30 Galvanic corrosion of dissimilar welded joint[16].

1.5 REW with dissimilar materials (REW: Resistance element welding)

In general, the most widely used welding method for vehicles is RSW, which has automation and high productivity. The REW process, a further development of the existing RSW process, can be defined as a new joining technology that joins dissimilar materials on the production line using the same joining technology as conventional steel parts[64–67]. REW can also be understood as a joining technology that combines mechanical and metallurgical joining and enables the expansion of boundaries for joining dissimilar material combinations.

Conventional RSW is still one of the most widely used joining processes in car body manufacturing. However, as mentioned above, there are various approaches to extend the heat-based joining process to address the challenges to enable joining of steel and aluminum alloys.

As shown in Fig. 1-31, the REW process is based on the application of steel elements in addition to the existing RSW process. In the first step, insert a rivet into the pre hole of the upper material or insert it at the same time as punching using a rivet. Soft materials such as aluminum are used as the upper material, and steel materials are used as the lower material. In the second step, welding is performed using upper and lower electrodes, similar to the existing RSW process. The heat generated by electrical resistance causes melting at the contact area between the steel elements and the lower steel, forming a melting zone. At this time, the electrode's pressing force, current, and energization time become the main process variables. By setting these variables, more compressive force can be applied to the weld. As a final process, the weld area is quickly cooled after welding due to the water cooling system of the electrode.

This REW process can prevent problems caused by dissimilar materials mentioned above by joining with a combination of steel elements and lower steel materials. Additionally, from an economic perspective, the existing car body assembly processes, RSW and REW, can be joined with the same spot welding equipment, providing significant cost advantages and savings.

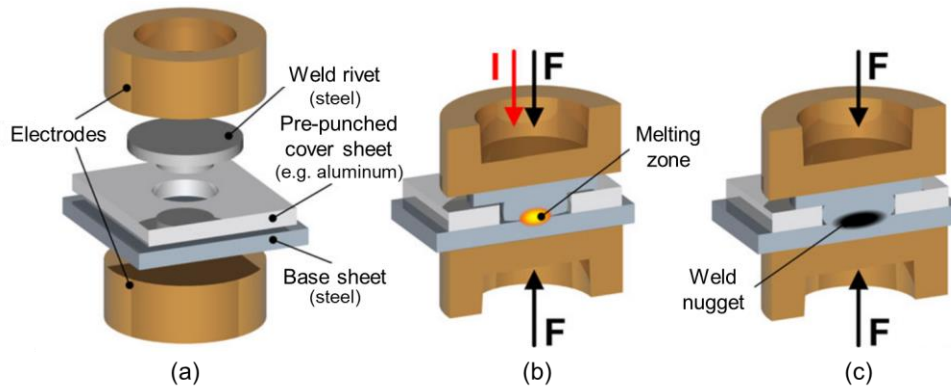


Fig. 1-31 Resistance welding process. (a)positioning, (b)welding, (c)riveting[68].

Mechanical fastening techniques such as SPR or clinching are commonly used to join materials with low strength and high ductility[69]. As shown in Fig. 1-32, the upper material was fractured because sufficient plastic deformation did not occur due to the high strength steel plate. Likewise, in the case of FDS thick or high strength steel, pre hole work is required on the upper plate, which increases working time[37]. Fig. 1-33 shows the BIW of an Audi A6 and presents joining possibilities and example joining operations by SPR and REW. All joints may not be or may be restrictively coupled by SPR, which is a mechanical fastening method. The use of REW can significantly improve the joining of these joints without limitation[70].

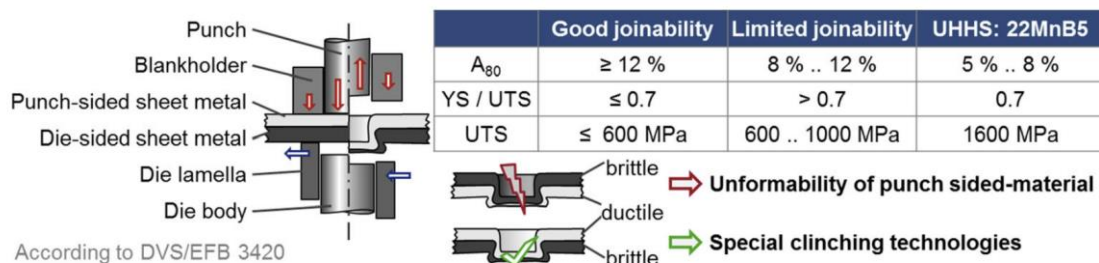


Fig. 1-32 Uniformability of punch sided-material due to the high strength by clinching[69].

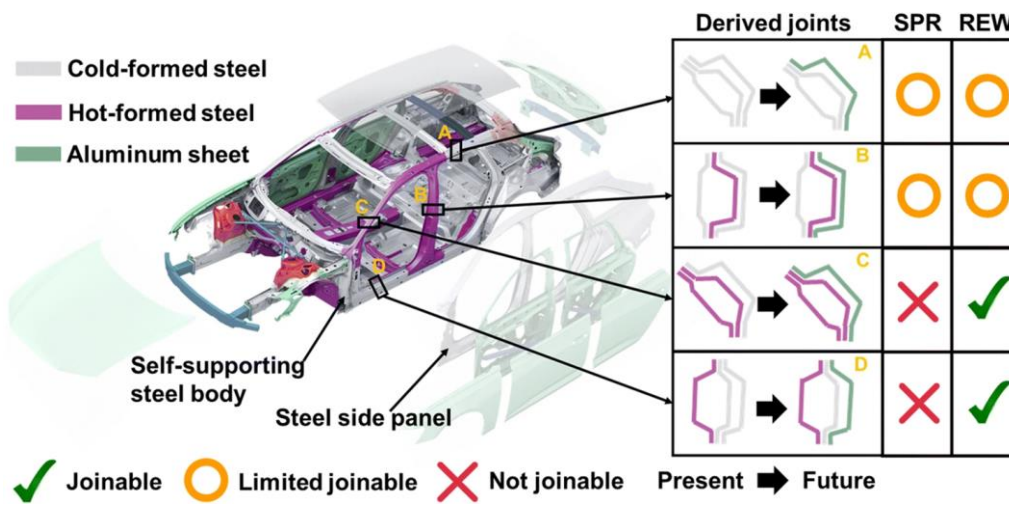


Fig. 1-33 steel body of the Audi A6 C8 utilizing a side panel made of steel, and the joinability of selected joints by SPR and REW[70].

1.6 The purpose and structure of this thesis

As mentioned earlier, environmental regulations are becoming more stringent. To respond to this, joining dissimilar materials such as steel and aluminum to lighten vehicle bodies, including transportation equipment, is essential. When applying dissimilar materials to the RSW welding process, which accounts for a significant portion of the car body assembly process considerably, various problems may occur as described in 1.4.1. Thermal-mechanical joining based on thermal and mechanical joining using elements was developed for REW[68], but it is not clear how the strength and fatigue performance of the weld shape change, how the microstructure phase deformation affects, and how the Al HAZ softened during welding affects.

Therefore, in this study, after quantitatively evaluating REW welded specimens of UHSS and lightweight alloys, differences in strength and fatigue performance were confirmed, and the relationship between joint shape and resulting performance and its

factors were verified. In order to more clarify the performance and relationship of the joint, microstructural analysis was deemed effective and was experimentally examined by combining histological analysis of the base material and joint. In addition, the heat generated during welding is experimentally measured, and the effect of the softened Al HAZ on the joint performance is to be revealed.

This thesis is consists of 6 chapters.

Chapter 1 gives the background and purpose of this study.

Chapter 2 presented the concept of REW process in joining Fe/Al for car body weight reduction and the mechanical strength characteristics of its lap joints.

In the chapter 3, the influence of microstructure and interface geometry on the mechanical fatigue properties of Fe/Al lap joints of REW was investigated experimentally and computationally.

In the chapter 4 present the fatigue fracture response and microstructure behavior of REWed by AZ31B magnesium alloy and dual phase (DP) 780 plates.

Chapter 5 shows by removing the HAZ of Al alloy, the Fe/Al lap joint properties are investigated, and the influence on the changed heat transfer path due to the HAZ-less system compared to existing REW is explained.

Chapter 6 summarized the main achievements of this research and described future application issues.

References

- [1] <https://www.fastmarkets.com/insights/us-aims-for-67-of-cars-to-be-evs-by-2032/>
n.d.
- [2] <https://www.epa.gov/regulations-emissions-vehicles-and-engines/regulations-green-house-gas-emissions-passenger-cars-and>. n.d.
- [3] Ferreira V, Merchán M, Egizabal P, García De Cortázar M, Irazustabarrena A, López-Sabirón AM, et al. Technical and environmental evaluation of a new high performance material based on magnesium alloy reinforced with submicrometre-sized TiC particles to develop automotive lightweight components and make transport sector more sustainable. *J Mater Res Technol* 2019;8:2549–64. <https://doi.org/10.1016/j.jmrt.2019.02.012>.
- [4] Molker H. Failure prediction of orthotropic Non-Crimp Fabric reinforced composite materials 2016:31.
- [5] Que Z, Wang S, Li W. Potential of Energy Saving and Emission Reduction of Battery Electric Vehicles with Two Type of Drivetrains in China. *Energy Procedia* 2015;75:2892–7. <https://doi.org/10.1016/j.egypro.2015.07.584>.
- [6] <https://www.hyundai.co.kr/story/CONT0000000000002975> n.d.
- [7] Automotive Body-in-White Manufacturing and Trends & Challenges to Ensure Dimensional Accuracy of Body Assemblies. 2023.
- [8] Emilsson E, Dahllöf L. Plastics in passenger cars A comparison over types and time. 2019. <https://doi.org/10.13140/RG.2.2.16313.93280>.
- [9] Zhang W, Xu J. Advanced lightweight materials for Automobiles: A review. *Mater Des* 2022;221:110994. <https://doi.org/10.1016/j.matdes.2022.110994>.
- [10] European Aluminium Association. Car body – Body structures. *Alum Automot Man*

2013;6:1–84.

- [11] Gene Liao Y. Topic 3: Lightweight Materials for Automotive Application. 2017 Summer Prof Dev Course Adv Automot Technol 2017:67.
- [12] Militzer M. Materials science: A synchrotron look at steel. *Science* (80–) 2002;298:975–6. <https://doi.org/10.1126/science.1078210>.
- [13] Kim SH, Kim H, Kim NJ. Brittle intermetallic compound makes ultrastrong low–density steel with large ductility. *Nature* 2015;518:77–9. <https://doi.org/10.1038/nature14144>.
- [14] J.G Kaufman, Introduction to aluminum alloys and tempers, ASM international 2000. n.d.
- [15] Rawal A, Kumar R, Saraswat H. Reviews on the Influences of Alloying elements on the Microstructure and Mechanical Properties of Aluminum Alloys and Aluminum Alloy Composites. *Int J Sci Res Publ* 2012;2:1–7.
- [16] Ma Y, Dong H, Li P, Wu B, Huang L, Zhang L, et al. Galvanic corrosion of AA5052/304SS welded joint with Zn–based filler metal in marine engineering. *Corros Sci* 2023;211:110912. <https://doi.org/10.1016/j.corsci.2022.110912>.
- [17] Czerwinski F. Current trends in automotive lightweighting strategies and materials. *Materials (Basel)* 2021;14. <https://doi.org/10.3390/ma14216631>.
- [18] Kim NJ. Critical Assessment 6: Magnesium sheet alloys: Viable alternatives to steels? *Mater Sci Technol (United Kingdom)* 2014;30:1925–8. <https://doi.org/10.1179/1743284714Y.0000000596>.
- [19] Kumar A, Lal S, Kumar S. Fabrication and characterization of A359/Al₂O₃ metal matrix composite using electromagnetic stir casting method. *J Mater Res Technol* 2013;2:250–4. <https://doi.org/10.1016/j.jmrt.2013.03.015>.

- [20] Singh H, Singh Brar G, Kumar H, Aggarwal V. A review on metal matrix composite for automobile applications. *Mater Today Proc* 2020;43:320–5.
<https://doi.org/10.1016/j.matpr.2020.11.670>.
- [21] Fuchs ERH, Field FR, Roth R, Kirchain RE. Strategic materials selection in the automobile body: Economic opportunities for polymer composite design. *Compos Sci Technol* 2008;68:1989–2002.
<https://doi.org/10.1016/j.compscitech.2008.01.015>.
- [22] Grove S. Fundamentals of composites manufacturing: materials, methods and applications. *Compos Manuf* 1991;2:52.
[https://doi.org/10.1016/0956-7143\(91\)90159-e](https://doi.org/10.1016/0956-7143(91)90159-e).
- [23]<https://www.worldautosteel.org/steel-basics/automotive-advanced-high-strength-steel-ahss-definitions/> n.d.
- [24] Hilditch TB, de Souza T, Hodgson PD. Properties and automotive applications of advanced high-strength steels (AHSS). Elsevier Ltd; 2015.
<https://doi.org/10.1016/B978-0-85709-436-0.00002-3>.
- [25] Khan MS, Soleimani M, Midawi ARH, Aderibigbe I, Zhou YN, Biro E. A review on heat affected zone softening of dual-phase steels during laser welding. *J Manuf Process* 2023;102:663–84. <https://doi.org/10.1016/j.jmapro.2023.07.059>.
- [26] Shome M, Tumuluru M. Introduction to welding and joining of advanced high-strength steels (AHSS). Elsevier Ltd; 2015.
<https://doi.org/10.1016/B978-0-85709-436-0.00001-1>.
- [27]<https://www.media.volvocars.com/global/en-gb/media/photos/148215/volvo-xc90-body-structure> n.d.
- [28]<https://www.ssab.com/en-us/brands-and-products/docol/automotive-steel-grades>

/dual-phase-steel n.d.

- [29] Jaber HL, Pouranvari M, Salim RK, Hashim FA, Marashi SPH. Peak load and energy absorption of DP600 advanced steel resistance spot welds. *Ironmak Steelmak* 2017;44:699–706. <https://doi.org/10.1080/03019233.2016.1229880>.
- [30] Schmal C, Meschut G. Refill friction stir spot and resistance spot welding of aluminium joints with large total sheet thicknesses (III–1965–19). *Weld World* 2020;64:1471–80. <https://doi.org/10.1007/s40194-020-00922-2>.
- [31] <https://www.kjellberg.de/gas-shielded-metal-arc-welding.html> n.d.
- [32] Gao Q, Hengchang B, Ling W, Zhan X, Shen H. Effect of defocusing amount on morphology and microstructure of 8-mm-thick Ti–6Al–4 V laser deep penetration welded joint. *Int J Adv Manuf Technol* 2022;119:1–10. <https://doi.org/10.1007/s00170-021-08450-z>.
- [33] Carver BL. LIGHT , STRONG , AND DEFECT–FREE LASER WELDING : PERFECTING THE PROCESS FOR THE AUTOMOTIVE INDUSTRY n.d.
- [34] <https://global.honda/en/newsroom/news/2012/4120906beng.html> n.d.
- [35] Sambasivam S, Gupta N, jassim A saeed, Pratap Singh D, Kumar S, Giri JM, et al. A review paper of FSW on dissimilar materials using aluminum. *Mater Today Proc* 2023. <https://doi.org/10.1016/j.matpr.2023.03.304>.
- [36] Henron self–pierce riveting. n.d.
- [37] Kobashi T, Iwase T, Maeda K. Comparison of Methods for Joining Dissimilar Metals. *R&D 神戸製鋼技報* 2018;67:98–103.
- [38] Altvater S, Sikora SP, Siefkes T. Transition between flow–drill screwing systems considering joining process and joint characteristics. *Adv Ind Manuf Eng* 2022;5:100091. <https://doi.org/10.1016/j.aime.2022.100091>.

- [39] Meschut G, Merkein M, Brosius A, Bobbert M. Mechanical joining in versatile process chains. *Prod Eng* 2022;16:187–91. <https://doi.org/10.1007/s11740-022-01125-y>.
- [40] Bunaziv I, Akselsen OM, Ren X, Nyhus B, Eriksson M, Gulbrandsen-Dahl S. A review on laser-assisted joining of aluminium alloys to other metals. *Metals (Basel)* 2021;11. <https://doi.org/10.3390/met11111680>.
- [41] Xia H, Li L, Ma N, Tan C, Gong J. Influence of energy ratio on dual-spot laser welded-brazed Al/steel butt joint. *J Mater Process Technol* 2020;281:116624. <https://doi.org/10.1016/j.jmatprotec.2020.116624>.
- [42] Su Y, Hua X, Wu Y. Effect of input current modes on intermetallic layer and mechanical property of aluminum-steel lap joint obtained by gas metal arc welding. *Mater Sci Eng A* 2013;578:340–5. <https://doi.org/10.1016/j.msea.2013.04.097>.
- [43] Picot F, Gueydan A, Martinez M, Moisy F, Hug E. A correlation between the ultimate shear stress and the thickness affected by intermetallic compounds in friction stir welding of dissimilar aluminum alloy-stainless steel joints. *Metals (Basel)* 2018;8. <https://doi.org/10.3390/met8030179>.
- [44] Lu Z, Xu J, Yu L, Zhang H, Jiang Y. Studies on softening behavior and mechanism of heat-affected zone of spray formed 7055 aluminum alloy under TIG welding. *J Mater Res Technol* 2022;18:1180–90. <https://doi.org/10.1016/j.jmrt.2022.03.074>.
- [45] Liu FC, Ma ZY. Influence of tool dimension and welding parameters on microstructure and mechanical properties of friction-stir-welded 6061-T651 aluminum alloy. *Metall Mater Trans A Phys Metall Mater Sci* 2008;39:2378–88. <https://doi.org/10.1007/s11661-008-9586-2>.
- [46] Cai W, Chen Q, Wang Y, Dong S, Luo P. Microstructural and mechanical characterization of steel-DP780/Al-5052 joints formed using resistance element

- welding with concealed rivet cover. *Compos Adv Mater* 2022;31:263498332211010. <https://doi.org/10.1177/26349833221101076>.
- [47] Kumar R, Dilthey U, Dwivedi DK, Sharma SP, Ghosh PK. Welding of thin sheet of Al alloy (6082) by using Vario wire DC P-GMAW. *Int J Adv Manuf Technol* 2009;42:102–17. <https://doi.org/10.1007/s00170-008-1568-4>.
- [48] Kumar R, Dilthey U, Dwivedi DK, Ghosh PK. Thin sheet welding of Al 6082 alloy by AC pulse-GMA and AC wave pulse-GMA welding. *Mater Des* 2009;30:306–13. <https://doi.org/10.1016/j.matdes.2008.04.073>.
- [49] Bansal P, Zheng Z, Pan B, Meng Y, Wen W, Banu M, et al. Corrosion of Al-Fe self-pierce riveting joints with multiphysics-based modeling and experiments. *J Manuf Process* 2023;95:434–45. <https://doi.org/10.1016/j.jmapro.2023.04.014>.
- [50] Li Y, Wei Z, Wang Z, Li Y. Friction self-piercing riveting of aluminum alloy AA6061-T6 to magnesium alloy AZ31B. *J Manuf Sci Eng* 2013;135:1–7. <https://doi.org/10.1115/1.4025421>.
- [51] Brewis DM, Comyn J, Cope BC, Moloney AC. Effect of carriers on the performance of aluminum alloy joints bonded with a structural film adhesive. *Polym Eng Sci* 1981;21:797–803. <https://doi.org/10.1002/pen.760211210>.
- [52] Bascom WD. Water at the Interface. *J Adhes* 1970;2:161–83. <https://doi.org/10.1080/0021846708544591>.
- [53] Papadimitriou I, Efthymiadis P, Kotadia HR, Sohn IR, Sridhar S. Joining TWIP to TWIP and TWIP to aluminium: A comparative study between joining processes, joint properties and mechanical performance. *J Manuf Process* 2017;30:195–207. <https://doi.org/10.1016/j.jmapro.2017.09.012>.
- [54] Wang C, Cui L, Mi G, Jiang P, Shao X, Rong Y. The influence of heat input on

- microstructure and mechanical properties for dissimilar welding of galvanized steel to 6061 aluminum alloy in a zero-gap lap joint configuration. *J Alloys Compd* 2017;726:556–66. <https://doi.org/10.1016/j.jallcom.2017.08.015>.
- [55] Das T, Rawal S, Panda SK, Paul J. Resistance spot-welding of AISI-1008 steel joints with MWCNT coating interlayer. *Mater Manuf Process* 2021;36:448–56. <https://doi.org/10.1080/10426914.2020.1843667>.
- [56] Yamagishi H. High-productivity and high-strength Fe/Al dissimilar metal joining by spot forge welding. *Mater Lett* 2020;278:128412. <https://doi.org/10.1016/j.matlet.2020.128412>.
- [57] Shen Z, Ding Y, Chen J, Amirkhiz BS, Wen JZ, Fu L, et al. Interfacial bonding mechanism in Al/coated steel dissimilar refill friction stir spot welds. *J Mater Sci Technol* 2019;35:1027–38. <https://doi.org/10.1016/j.jmst.2019.01.001>.
- [58] Sun YF, Fujii H, Takaki N, Okitsu Y. Microstructure and mechanical properties of dissimilar Al alloy/steel joints prepared by a flat spot friction stir welding technique. *Mater Des* 2013;47:350–7. <https://doi.org/10.1016/j.matdes.2012.12.007>.
- [59] Enrique PD, Li C, DiGiovanni C, Peterkin S, Zhou NY. Electrospark deposition interlayers for dissimilar resistance welding of steel to aluminum. *Manuf Lett* 2020;24:123–6. <https://doi.org/10.1016/j.mfglet.2020.04.009>.
- [60] Zhou L, Yu M, Liu B, Zhang Z, Liu S, Song X, et al. Microstructure and mechanical properties of Al/steel dissimilar welds fabricated by friction surfacing assisted friction stir lap welding. *J Mater Res Technol* 2020;9:212–21. <https://doi.org/10.1016/j.jmrt.2019.10.046>.
- [61] Yin Y, Rumman R, Sarvghad M, Bell S, Will G, Clegg RE, et al. Dissimilar weld failure: A forensic analysis to determine primary failure mechanisms. *Eng Fail Anal*

2022;139:106453. <https://doi.org/10.1016/j.engfailanal.2022.106453>.

- [62] Dong L, Ma C, Peng Q, Han EH, Ke W. Microstructure and stress corrosion cracking of a SA508–309L/308L–316L dissimilar metal weld joint in primary pressurized water reactor environment. *J Mater Sci Technol* 2020;40:1–14. <https://doi.org/10.1016/j.jmst.2019.08.035>.
- [63] Lu Z, Xu J, Yu L, Zhang H, Jiang Y. Studies on softening behavior and mechanism of heat-affected zone of spray formed 7055 aluminum alloy under TIG welding. *J Mater Res Technol* 2022;18:1180–90. <https://doi.org/10.1016/j.jmrt.2022.03.074>.
- [64] Meschut G, Janzen V, Olfermann T. Innovative and highly productive joining technologies for multi-material lightweight car body structures. *J Mater Eng Perform* 2014;23:1515–23. <https://doi.org/10.1007/s11665-014-0962-3>.
- [65] Baek S, Go GY, Park JW, Song J, Lee H chul, Lee SJ, et al. Microstructural and interface geometrical influence on the mechanical fatigue property of aluminum/high-strength steel lap joints using resistance element welding for lightweight vehicles: experimental and computational investigation. *J Mater Res Technol* 2022;17:658–78. <https://doi.org/10.1016/j.jmrt.2022.01.041>.
- [66] Baek S, Ma N, Song J, Kim DK, Lee SJ, Chen C, et al. Effect of Mg remelting and mechanical hooks of steel on the mechanical and fatigue responses of resistance element welded AZ31/DP780 joints: Experimental, FEM and thermodynamic calculation studies. *J Mater Res Technol* 2023;22:1210–37. <https://doi.org/10.1016/j.jmrt.2022.11.157>.
- [67] Baek S, Song J, Lee H chul, Park S yeon, Song KH, Lee S, et al. Robust bonding and microstructure behavior of aluminum/high-strength steel lap joints using resistance element welding process for lightweight vehicles: Experimental and numerical

investigation. Mater Sci Eng A 2022;833:142378.

<https://doi.org/10.1016/j.msea.2021.142378>.

- [68] Meschut G, Hahn O, Janzen V, Olfermann T. Innovative joining technologies for multi-material structures. Weld World 2014;58:65–75.
<https://doi.org/10.1007/s40194-013-0098-3>.
- [69] Hörhold R, Müller M, Merklein M, Meschut G. Mechanical properties of an innovative shear-clinching technology for ultra-high-strength steel and aluminium in lightweight car body structures. Weld World 2016;60:613–20.
<https://doi.org/10.1007/s40194-016-0313-0>.
- [70] Günter H, Meschut G. Joining of ultra-high-strength steels using resistance element welding on conventional resistance spot welding guns. Weld World 2021;65:1899–914. <https://doi.org/10.1007/s40194-021-01122-2>.

Chapter 2 Bonding mechanism of REW with Al/Ultra-high strength steel (UHSS)

2.1 Introduction

As the reduction in the weight of vehicles becomes a global trend in automotive industry, the market share of steels, commonly used as a structural materials, has been gradually replaced by lightweight materials such as carbon fibers, Al alloys, Mg alloys, or composites[1,2]. Nowadays, multi-material combinations such as Al alloy-steel and Mg alloy-steel are widely used in automobiles to achieve the vehicle lightweight and increase the structural strength[3]. Among these combinations, Al alloys-steel structures are considered one of the best, contributing to the highest percentage of the overall body of a vehicle[4]. However, a major issue that is continuously emerging which is the great difficulty in joining the materials using the conventional welding methods due to the significant discrepancy in the thermo-mechanical properties between Al alloys and steels[5]. In addition, the interface of the substantial intermetallic compounds (IMCs) formed during the melt-cooling process in fusion welding becomes a decisive factor that degrades mechanical performance[6,7].

To overcome the mentioned issues, active studies have been conducted on joining Al alloys and steels using various bonding methods such as solid-state joining applications[9], low heat input laser welding[10], self-pierce riveting (SPR) and its applications[11,12], etc. Despite these tremendous efforts, there have been significant limitations in effectively suppressing large IMC layers or improving their strengths in the joining process.

In the modern vehicle, approximately 2000–5000 spot welds are made[13]. For this reason, it is with great urgency that the next-generation automobile industry to establish a process technology capable of achieving robust bonding of Al alloy and steel lightweight structures while utilizing the existing resistance spot welding (RSW) process. Considerable progress has been made, according to previous studies[14,15] on lap joints of Al-Steel by RSW including mechanical joining, such as designing electrodes and adhesive materials to achieve joints between Al-Steel. However, the maximum tensile-shear load was limited to less than 5 kN with brittle interface fracture, because common weld defects such as voids, IMCs and poorly bonded areas formed at the joint interfaces.

Holtschke and Jüttner pointed that the challenge in joining technology is the intensive use of ultrahigh-strength steels (UHSS) in cars for high-volume markets, which shall be combined with Al panels or closing plates[17]. Due to the high strength and low ductility of UHSS, established mechanical joining technologies like SPR reach their process limits.

In this chapter 2, the author presents the REW mechanism for joining Al and UHSS. The RSW process is utilized for the REW of Al plates and UHSS plates using steel elements. Tensile-shear tests are conducted on the REWed specimens using digital image correlation (DIC). The fracture behavior and mechanical properties of the REWed joints are thoroughly investigated. Furthermore, the microstructural behavior according to welding current is considered, employing both experimental and numerical methods. Optical microscopy (OM), scanning electron microscopy (SEM), and electron back-scatter diffraction (EBSD) are utilized for this purpose. Finally, the results and

considerations regarding the REW mechanism in relation to welding currents are provided.

2.2 Experimental procedures

2.2.1 Materials and REW processes

AA5052 alloy plates (100 mm × 30 mm × 2.5 mm) and SPFC980 steel plates (100 mm × 30 mm × 1.6 mm) were employed as the base materials, respectively, and S20C low-carbon steel was introduced as the resistant element material. S20C is a low-carbon steel, which is advantageous for workability and weldability, and used as a resistance element because of its low cost. The chemical compositions and mechanical properties of the introduced materials are displayed in Table 2-1 and Table 2-2, respectively. Fig. 2-1 presents the schematic descriptions of AA5052 alloy-SPFC980 steel joints with the S20C resistance element welding (REW) process. In order to implement the structurally sound joining between Al5052 alloy and SPFC980 steel joint, the S20C element was riveted on AA5052 alloy sheet (see Fig. 2-1(a1)). Then, instead of the AA5052 alloy, the S20C element is directly spot-welded with the SPFC980 steel and a robust bonding was performed. The S20C riveted AA5052 is assembled in the shape shown in Fig. 2-1(a2). This process is the pre-piercing of weld rivet during part manufacturing, which is shown in SFig. 2-1 in detail. Then, the S20C riveted AA5052 alloy-SPFC980 steel was resistance element welded by an AC power supply spot welding machine (see Fig. 2-1(a3)). The process conditions were fixed at 2.45 kN and 200 ms for the pressing force and the current time, respectively, and the currents were 3.5 kA, 4.5 kA, 6.5 kA, 8.5 kA, 10.5 kA and 12 kA. All processes were conducted at atmospheric pressure air atmosphere with room temperature. The REWed AA5052/SPFC980 joints finally

completed as shown in Fig. 2-1(a4). Fig. 2-1(b) exhibits the 3D modelling and its material assignment, and Fig. 2-1(c and d) provide the information of top view image and dimension and cross-sectional image of joint geometry, respectively.

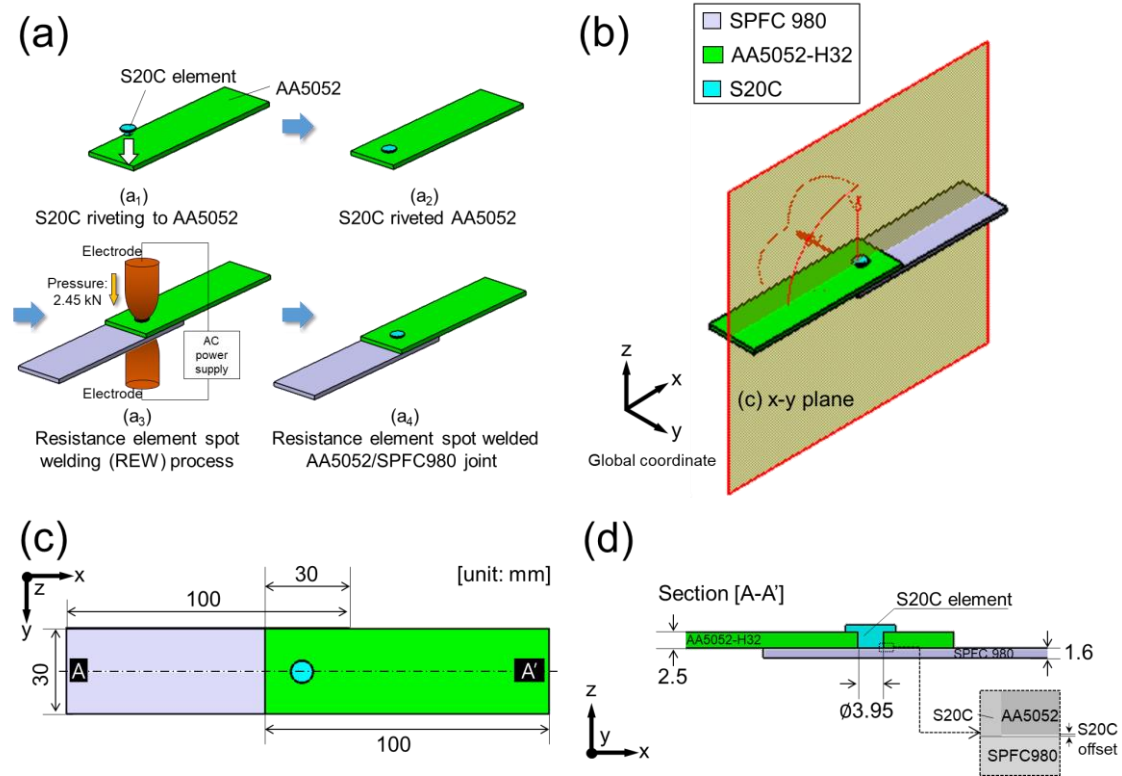


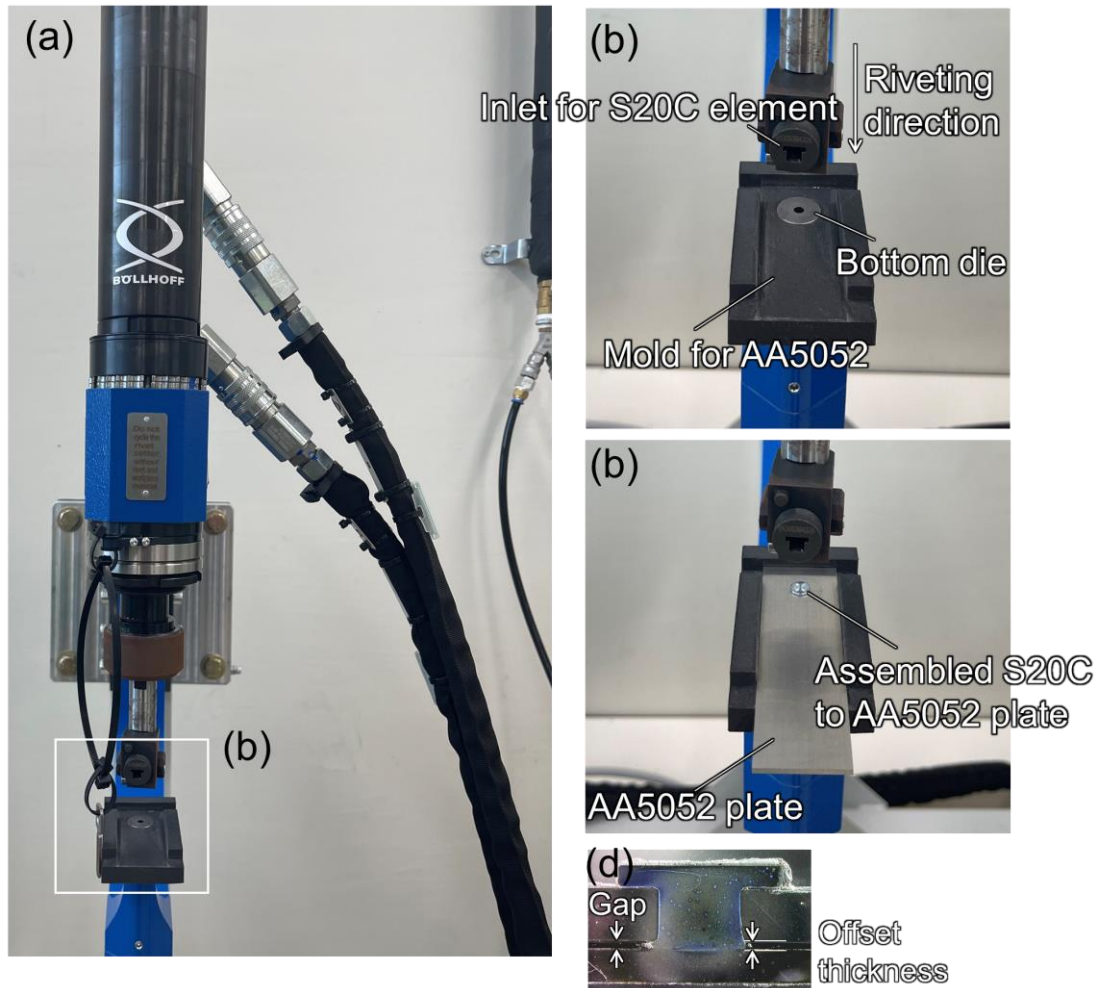
Fig. 2-1 Schematic descriptions of AA5052-SPFC980 steel joints. (a) Joining procedures of AA5052/SPFC980 joint with resistance element welding process, (b) 3D modeling and its material assignment, (c) top view image and dimension and (d) cross-sectional image of joint geometry.

Table. 2-1 Chemical compositions of applied materials.

	Elements (wt%)							
	Al	Cu	Mg	Mn	Fe	C	Si	P
AA5052	Bal.	0.029	2.392	0.027	0.40	-	0.25	-
SPFC980	-	-	-	2.192	Bal.	0.109	0.942	0.014
S20C	-	-	-	0.47	Bal.	0.20	0.20	0.012

Table. 2-2 Mechanical properties of applied materials.

	Density, ρ (kg/m ³)	Young's modulus, E (GPa)	Yield strength, σ_y (MPa)	Poisson's ratio, ν
AA5052	2680	70.3	193	0.33
S20C	7870	186	>245	0.29
SPFC980	7800	190-210	>490	0.3



SFig. 2-1 Machine and process for S20C element riveting into the AA5052 plate. (a) S20C riveting machine, (b) description of S20C element mold die and (c) assembled S20C element with AA5052 plate, (d) description of resistance element welded Al/steel specimen.

2.2.2 Microstructure observations

An optical microscope (OM; GX51, OLYMPUS) was introduced to observe the macro scale of the welded cross-section. The specimens were prepared by using a cutting

machine (Struers/labotom-5) and a hot mounting press (Struers/Citopress-5) as a pre-treatment. All cross sections were prepared using the mechanical polishing method for an optical microscopy analysis, mechanically ground up to grade 4,000 and then polished with 3 μm and 1 μm (Struers/DP-Suspension P). Finally, 0.04 μm aqueous solution containing colloidal silica particles was finally applied to obtain the soundly polished surface (Struers/OP-S). The finished specimen surfaces were etched by 3% Nital solution (97 ml Ethanol and 3 ml Nitric acid) for 10 sec at room temperature.

To evaluate the microstructure characteristic such as grain size, shape, grain boundary and phase, the electron backscattered diffraction (EBSD) method was employed. The specimens were machined by 2 mm \times 20 mm in size, mechanically ground and then polished on the surface. Sample surface were then analyzed by an orientation imaging mapping (OIM) system incorporated with field emission scanning electron microscope (FESEM). In addition, to investigate the fracture surface, energy dispersive x-ray spectrometer (EDX) analysis was introduced.

2.2.3 Evaluation of mechanical properties

To evaluate the mechanical properties, Vickers micro-hardness and tensile-shear test employed. Vickers micro-hardness test was performed on the cross-section of the weld zone with a load of 10 kgf and a dwell time of 10 sec by the hardness testing machine (SIOMM/HV-50AP). For the tensile-shear test, a universal testing machine (UTM, MTDI/UT100F) was introduced. The black-and-white dot pattern was applied to the specimen as a pretreatment of digital image correlation (DIC) observation to deeply observe the in-situ strain behavior occurring during the tensile-shear test. The interval between the DIC measurements of the sample surface is about 510 mm \pm 10 mm. DIC

was quantified with Gom Aramis software by focusing on this interval range. Here, the test was carried out at a speed of 2 mm/min, the comprehensive test system with DIC camera which is shown in Fig. 2-2.

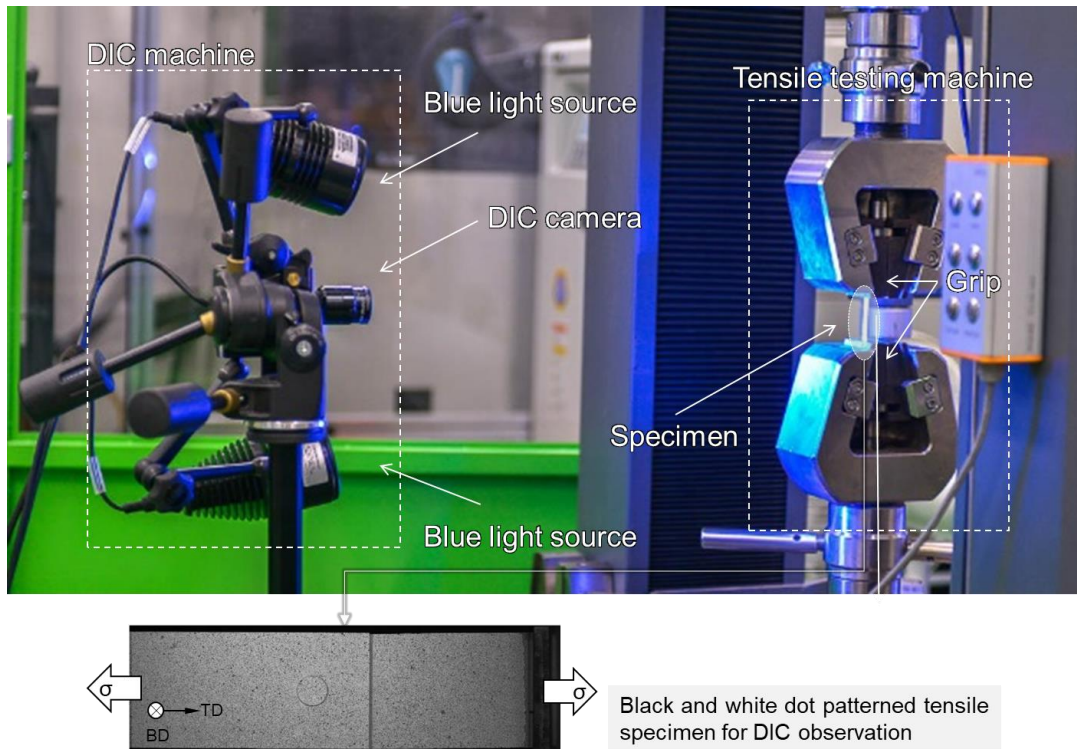


Fig. 2-2 Description of tensile-shear system device components. DIC: digital image correlation.

2.3 Results

2.3.1 Mechanical strength

Fig. 2-3 presents the tensile shear load-displacement curves depend on the resistance element welding current conditions. In the mechanical evaluation, 5 specimens for each condition were subjected to a tensile-shear test. Overall, the tensile-shear peak loads were gradually increased as the input current increases. In the 3.5kA condition, the peak loads were distributed between 5000 N and 7000 N and had a

deviation. In the 4.5kA welding current condition, where the current of 1kA was increased compared to the previous condition, the peak loads were between 7000N and 8000N with increased displacements, the deviation was relatively smaller than 3.5kA of the welding current. When the welding current was increased to 6.5kA, the tensile-shear peak loads had a high strength approaching 9000N. When the welding current applied by 8.5kA, the tensile-shear peak load exceeded the 9200N maximum with a serration behavior. When the welding current reached 10.5kA, the tensile shear load was about 9000N, and the displacements were observed to be more than 6 mm. Finally, when the welding current was increased to 12 kA, the strength no longer increased, and had a tendency to decrease to less than 9000N. The specimens welded under the conditions of relatively low currents of 3.5kA and 4.5kA showed relatively little displacement with low strength. On the other hand, the specimens welded with a relatively high current had a maximum load of more than about 9000N, and serration behavior was observed in the relatively large amount of deformation and the tensile-shear curves. Beukel et al. (1975) reported that the serration behavior called “Portevin–Le Chatelier effect”, PLC describes a serrated stress–strain curve or jerky flow, which some materials exhibit as they undergo plastic deformation, specifically inhomogeneous deformation. This effect has been long associated with dynamic strain aging or the competition between diffusing solutes pinning dislocations and dislocations breaking free of this stoppage [19]. In particular, [19] the precipitates, often found in Al alloys (especially of the Mg variety), complicate the PLC effect. Consequently, this serration behavior can cause different fracture behavior in each welding current condition. The results are further discussed in the fracture surface analysis part and discussion section.

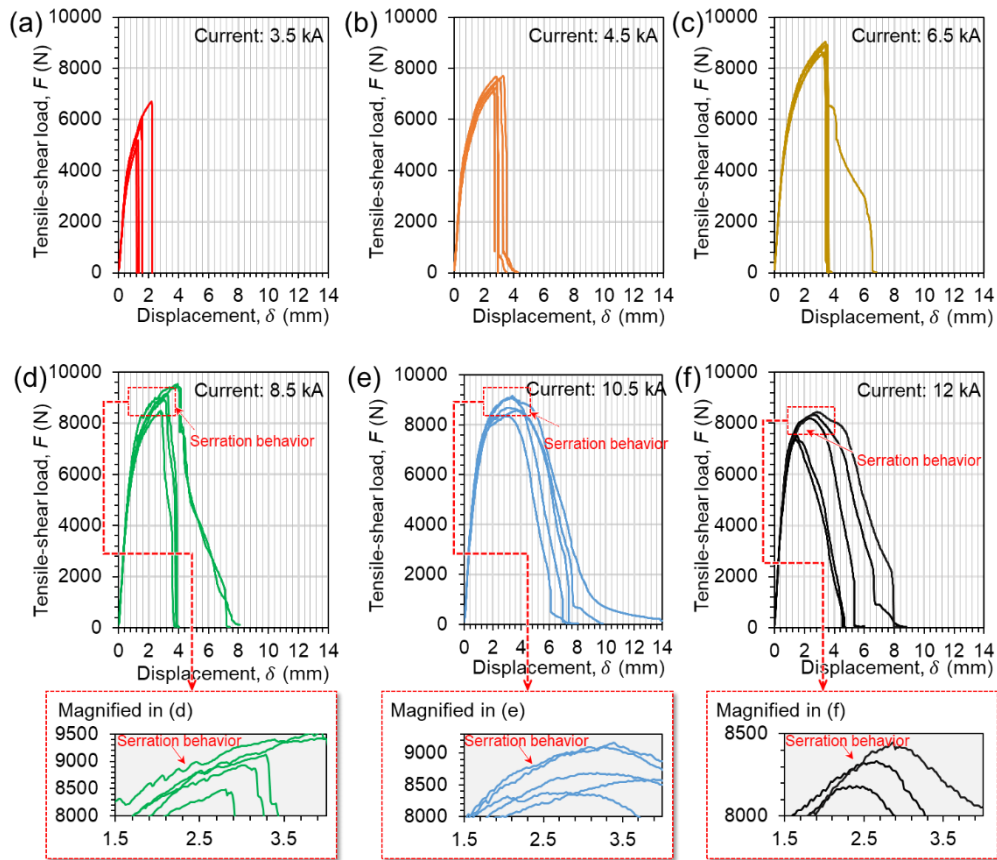


Fig. 2-3 Tensile-shear load-displacement curve after tension-shear tests. (a) welding current: 3.5 kA, (b) welding current: 4.5 kA, (c) welding current: 6.5 kA, (d) welding current: 8.5 kA, (e) welding current: 10.5 kA, and (f) welding current: 12 kA. Serration parts are magnified in red dot box.

2.3.2 Cross-sectional observations

2.3.2.1 Welding current of 3.5kA and 4.5kA

The cross-sections of the joints were investigated by a combination of an optical microscope (OM) macrograph and SEM-EDX analysis. The cross-sectional observation is explained through the welding current conditions by dividing it into 3 groups based on the tensile-shear peak load of 9000 N. Fig. 2-4 shows the cross-sectional image of the REW joint with the S20C pre riveted on AA5052 and the SPFC980 joint with a 3.5 kA welding current. Fig. 2-4(a) exhibits OM image of the joint cross section, the S20C pre

riveting structure shows a bonded structure without deformation. Gaps were observed in all interfaces except the S20C-SPFC980 nugget zone. It was observed with the interfaces of S20C-AA5052 (see Fig. 2-4(b,c)) and the three interfaces that form the nugget region with the SPFC980. As seen in Fig. 2-4(d), the joint interface between S20C and SPFC980 was an unfinished bond zone with a width of about 2.597 mm. The unfinished bond zone of 2.597 mm occupies about 65.7% of the 3.95 mm diameter of the S20C. For this reason, there was low displacement and relatively degraded load-displacement which is shown in the graph of Fig. 2-3 (a). This mechanical behavior is investigated in further detail in the discussion section. Fig. 2-4(e, g) exhibits the joint shank corners respectively. A micro-crack was observed in the right part with an insufficient input of thermal energy (see Fig. 2-4(d)), which was a part formed by compression deformation due to heat and pressure during the bonding process. As a result of the analysis the EDX line around the third material of the shank, the Fe and Al element mixing zone was observed (Fig. 2-4 (f)). As seen in Fig. 2-4 (h, i), the head of S20C remained intact during the REW procedure.

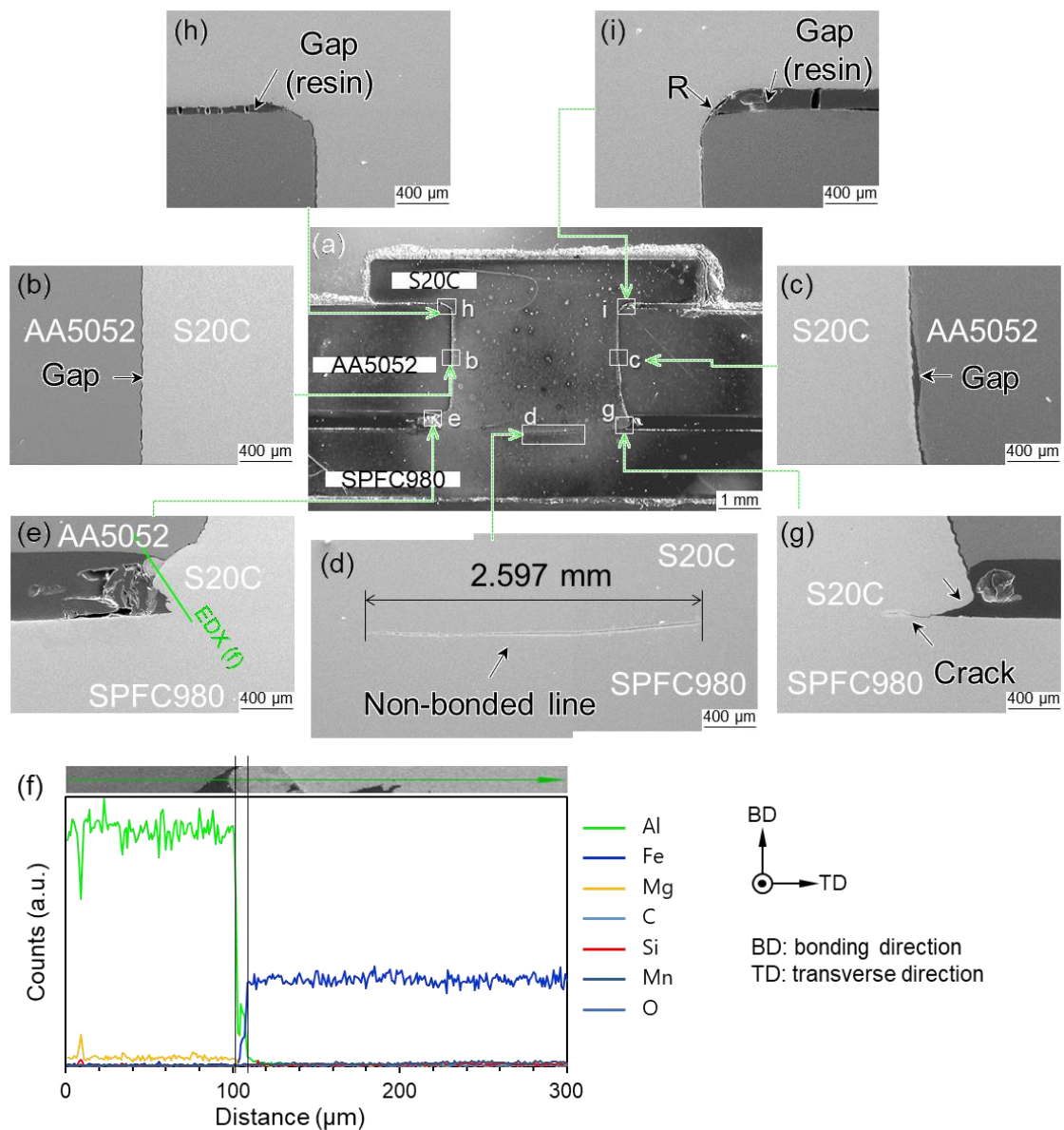
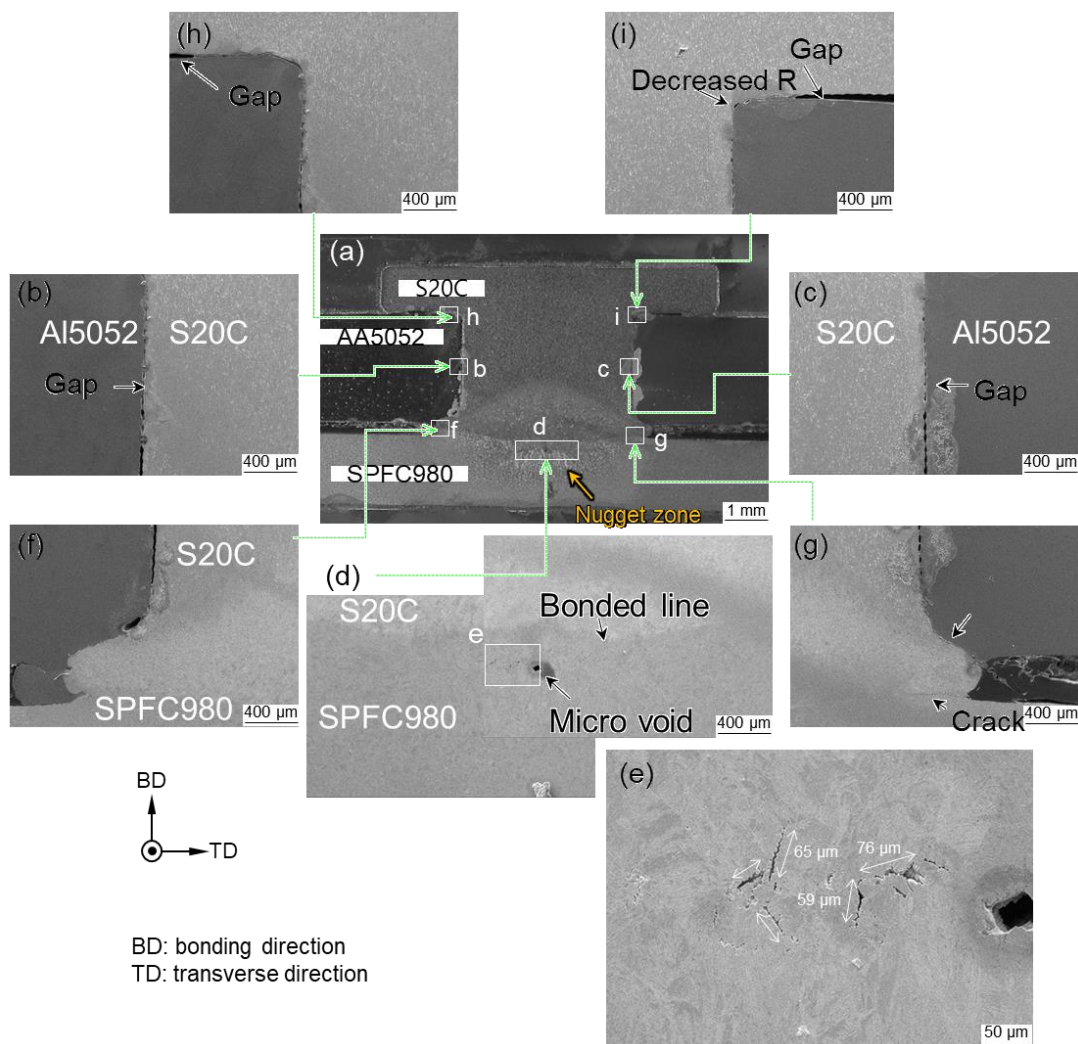


Fig. 2-4 Cross-sectional images of AA5052/SPFC980 joint by 3.5 kA welding current. (a) optical microscope image, (b, c) AA5052-S20C interfaces, (d) fusion line between S20C and SPFC980, (e, g) corner parts of fusion line, (f) result of EDS line scan in (e), (h, i) corner parts of S20C rivet element. BD: bonding direction; TD: transverse direction.

SFig. 2-2 displays cross-sectional images of the REW joint with the S20C pre riveted on the AA5052 and SPFC980 joint by a 4.5 kA welding current. When the input current was increased to 4.5kA, the cross-section images of interfaces between AA5052

and S20C had a similar tendency with the 3.5kA condition. However, the micro-cracks of size $59\ \mu\text{m} \sim 76\ \mu\text{m}$ were distributed at the weld joint interface as shown in SFig. 2-2(e). The micro-cracks are considered a decisive factor influencing the mechanical properties degradation. All the material components maintained their initial state without any plastic deformation under these current welding conditions.



SFig. 2-2 Cross-sectional images of AA5052/SPFC980 joint by 4.5 kA welding current.

2.3.2.2 Welding current of 6.5kA and 8.5kA

As seen in Fig. 2-5 (a-c), the cross-section images of 6.5kA are similar with the morphological characteristics of 4.5kA. In addition, the Fe-Al diffusion area detected at the interface between S20C and AA5052 by EDX line scan analysis as shown in Fig. 2-5(d). This is because as the amount of heat input increases, the gap between AA5052 and S20C was compressed enough to disappear, and Fe and Al can form an interface. As displayed in Fig. 2-5(e), the nugget zone was welded completely without any non-bonding areas, in some areas there were minor micro-cracks. The shank on both sides was further developed with deformation by the thermo-mechanical deformation, the AA5052 and S20C interacted with each other (see Fig. 2-5(f, g)). No damage behavior was observed, such as deformation of the head of the S20C was observed (Fig. 2-5 (h, i)). SFig. 2-3 exhibits the observation of the cross-sectional images of the joints by an 8.5 kA welding current with relatively further deformed interfaces were observed than the joint with a lower heat input. In SFig. 2-3(a), the heat affected zone (HAZ) was clearly observed at the both sides. In addition, deformation from the compressive force at the head of the S20C rivet was similar with the shank deformation as displayed in SFig. 2-3(h, i). From these conditions, the AA5052 plates were plastically deformed with the shank formation.

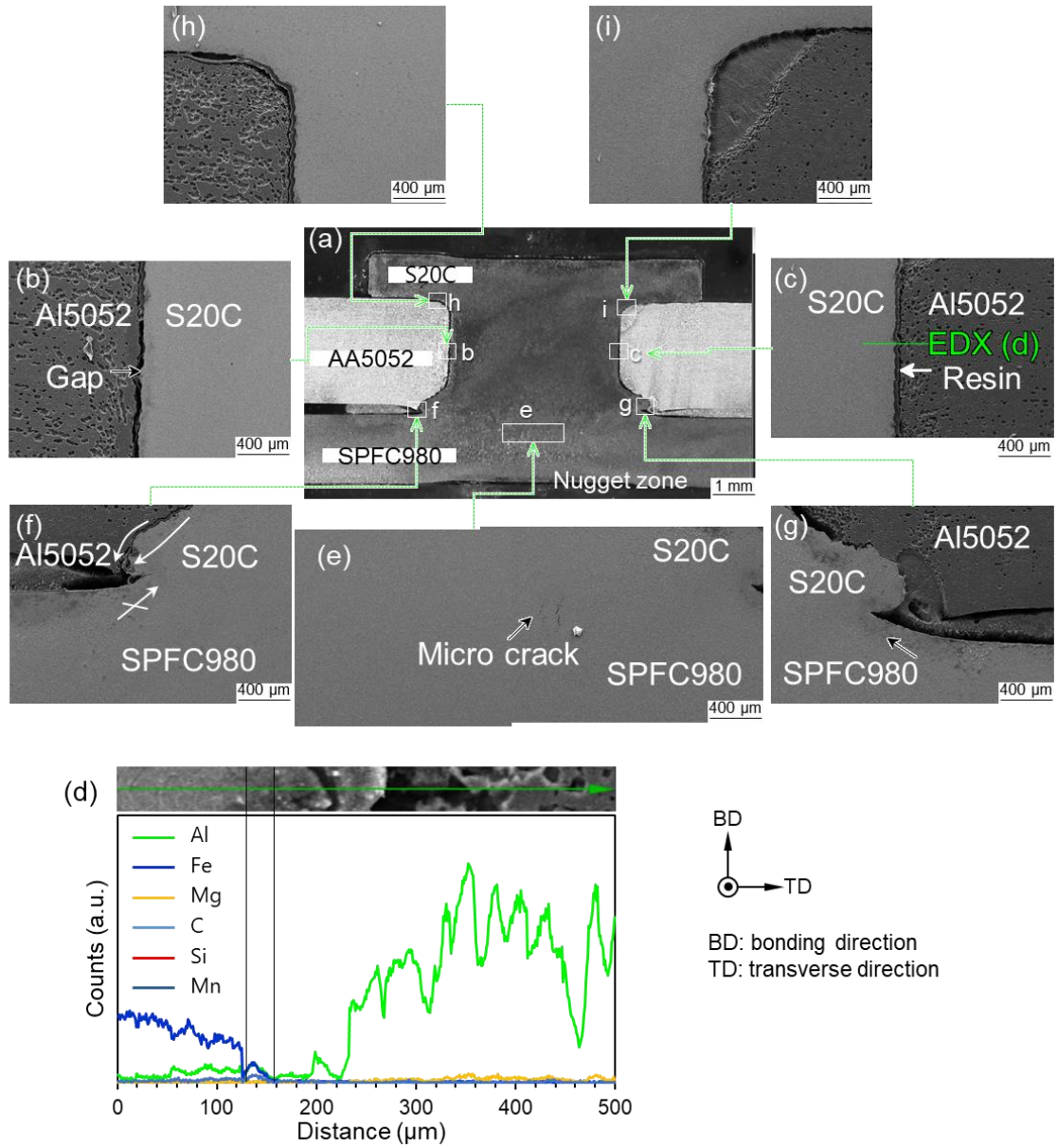
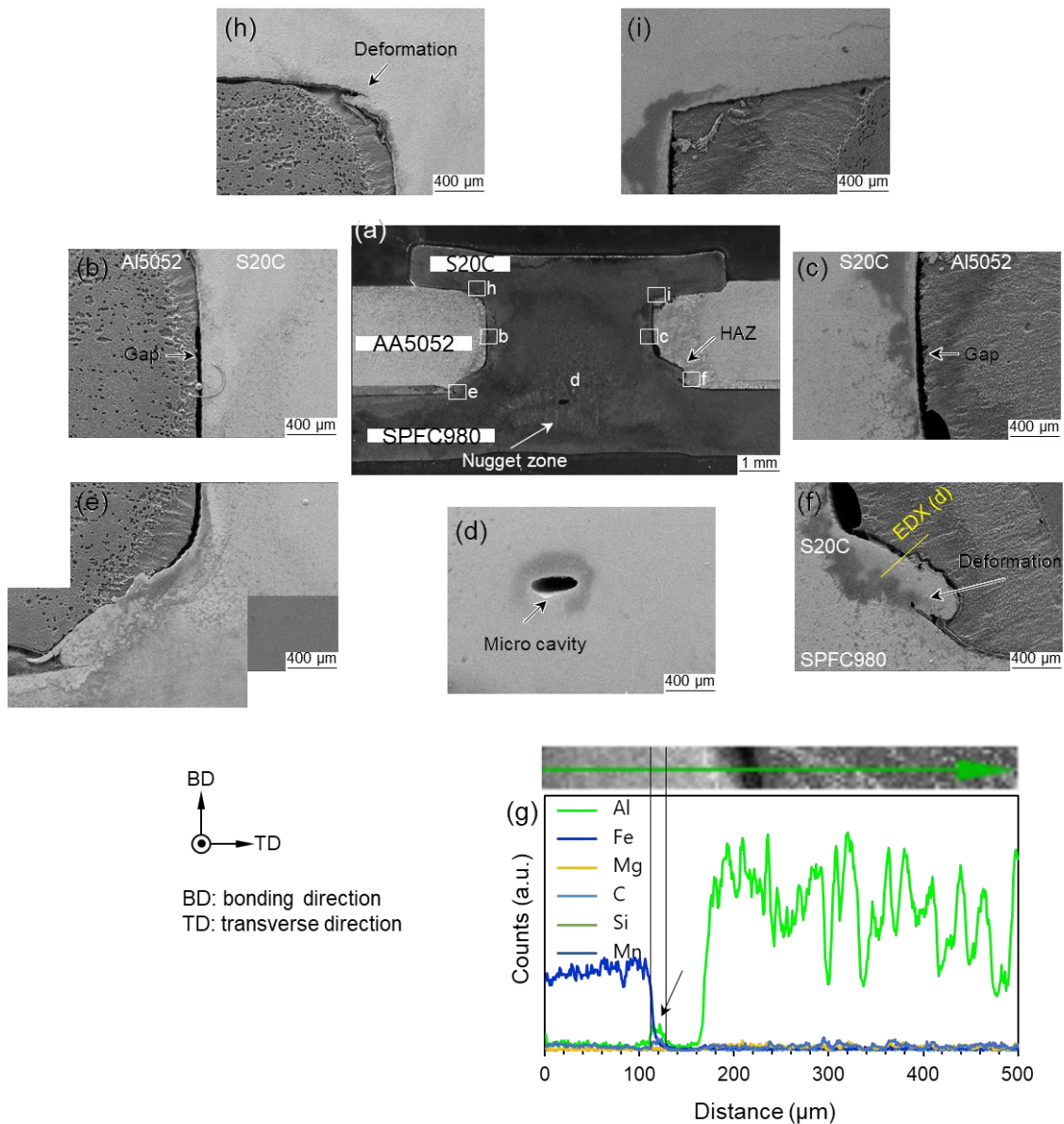


Fig. 2-5 Cross-sectional images of AA5052/SPFC980 joint by 6.5 kA welding current. (a) optical microscope image, (b, c) AA5052-S20C interfaces, (d) result of EDS line scan in (c), (e) nugget zone, (f, g) corner parts of fusion line, (h, i) corner parts of S20C rivet element.



SFig. 2-3 Cross-sectional images of AA5052/SPFC980 joint by 8.5 kA welding current.

2.3.2.3 Welding current of 10.5kA and 12kA

When the input current reached 10.5kA, the compression deformation and HAZ of S20C appeared remarkably, the head of S20C rivet was perfectly dug into the AA5052 (see Fig. 2-6(a)). Due to the increased heat input, there is a possibility that the material become soft or that the low melting point of AA5052 melted. Fig. 2-6(b, d) shows the

shank on the both sides and protruding hooks were observed. Fig. 2-6(c) presents the EDX face mapping result around the hook, it was observed that the Al element diffused into the Fe element. Fig. 2-6(f, g) shows the head part of the S20C. Severe plastic deformed interfaces were observed even at the head of the S20C at the current condition of 10.5kA. SFig. 2-4 presents cross-section image of 12kA, and the interface between AA5052 and S20C a severe plastic deformation occurred (b, c). The head of the S20C was compressed enough to insert a shank, and it was accompanied by many protruding hooks and micro-cracks. In addition, the S20C was excessively compressed by heat and pressure, causing an undercut, which caused a severely damaged AA5052. In SFig. 2-4(d), the SEM image shows a severely geometrical degradation area which was observed around both sides of the shank. The weld microstructure development found in cross-sectional observations is quantitatively discussed in the next section.

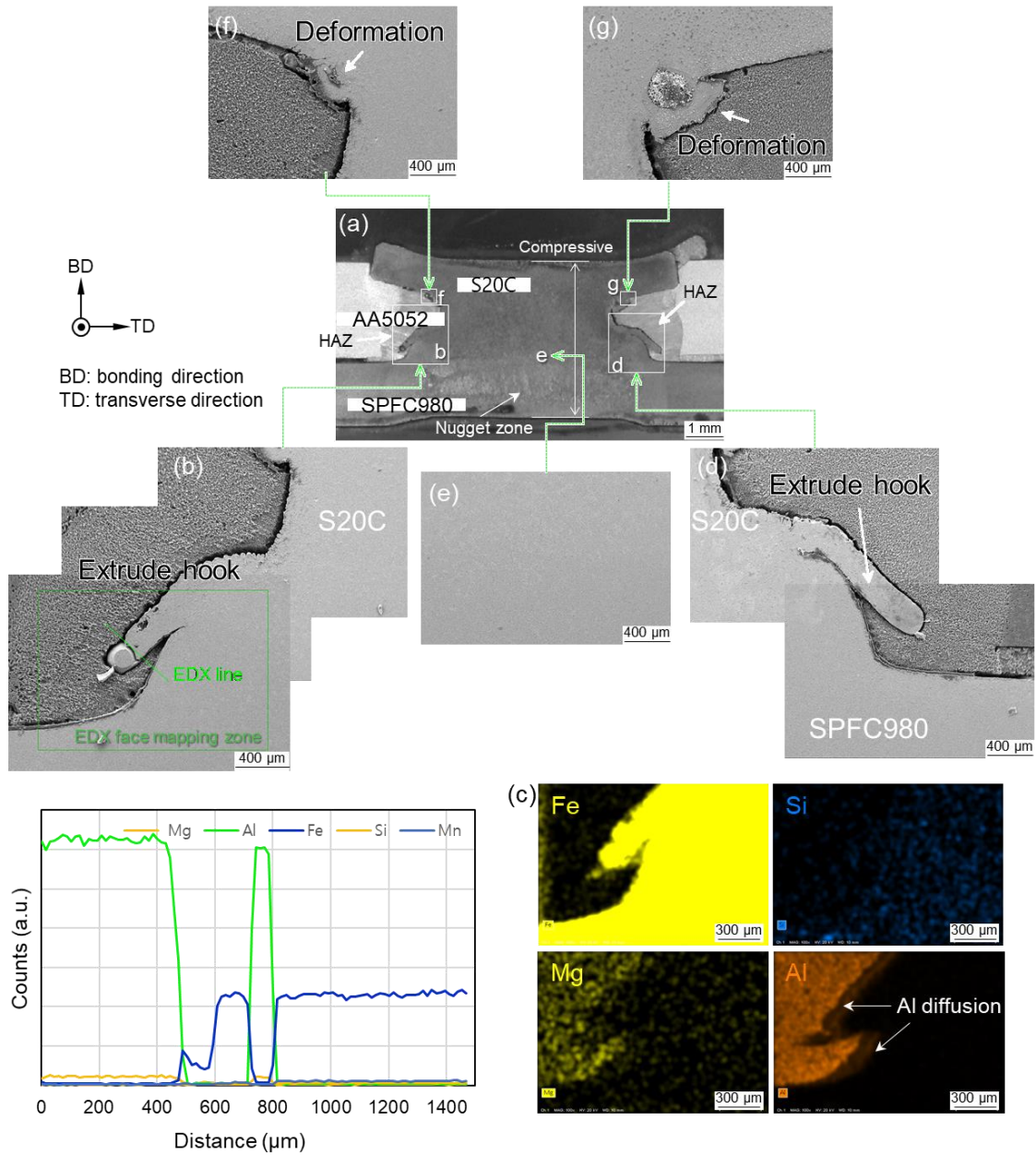
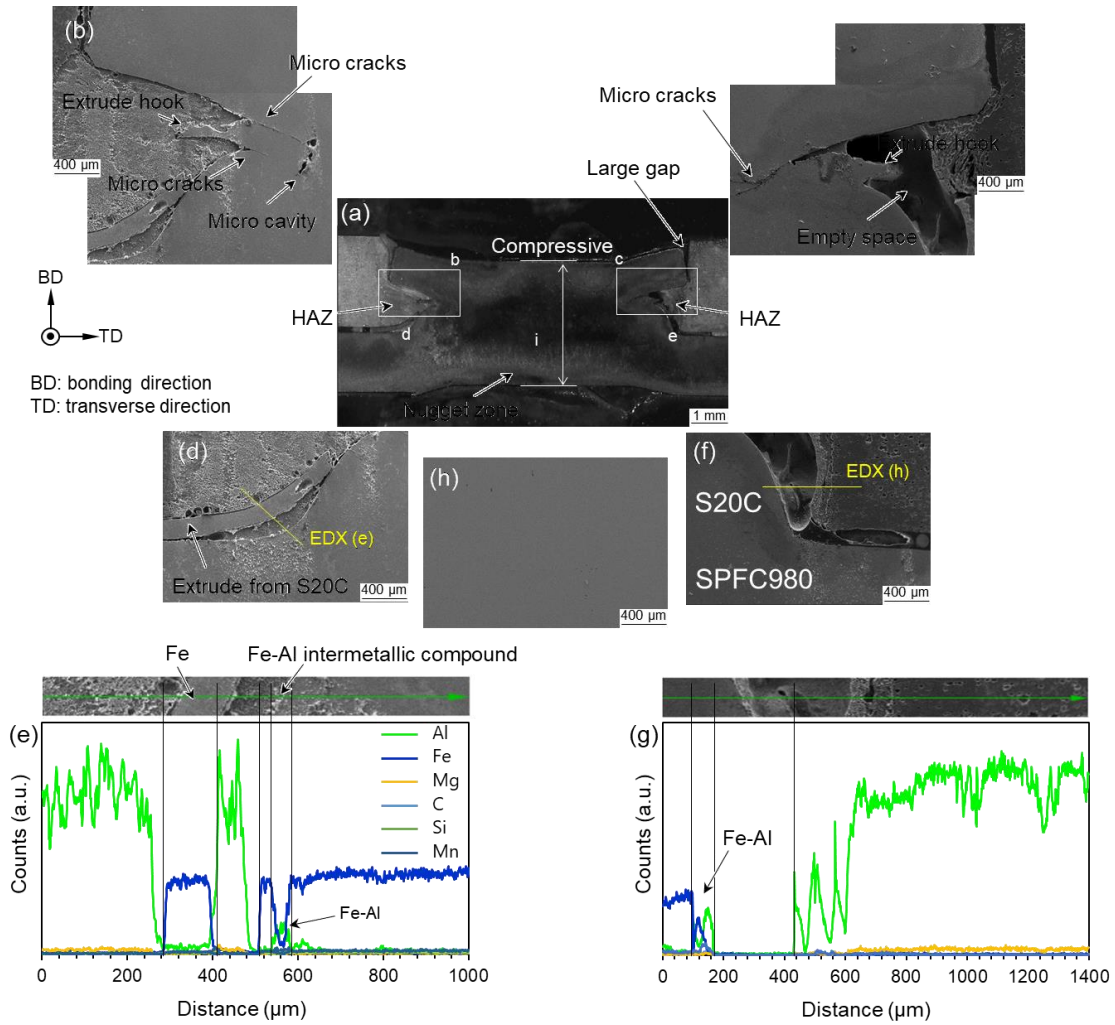


Fig. 2-6 Cross-sectional images of AA5052/SPFC980 joint by 10.5 kA welding current. (a) optical microscope image, (b, d) AA5052-S20C interfaces and its extrude hook in the corner parts, (c) result of EDS face mapping in (b), (e) nugget zone, (f, g) corner parts of fusion line.



SFig. 2-4 Cross-sectional images of AA5052/SPFC980 joint by 12 kA welding current.

2.3.3 Microstructure observation

Fig. 2-7 presents the base materials of the initial state. The grain size measured by using grain plot in TSL-OIM software. The grains of S20C are equiaxed grains, and most of them are $19.1 \mu\text{m} \pm 8.08 \mu\text{m}$ grains mixed with ferrite and pearlite as displayed in Fig. 2-7(a). SPFC980 was a low-carbon steel containing ferrite and pearlite with equiaxed grains of $6.88 \mu\text{m} \pm 4.25 \mu\text{m}$ (see Fig. 2-7(b)). The grain size of AA5052 was $23.9 \mu\text{m} \pm 6.16 \mu\text{m}$ as shown Fig. 2-7(c). To investigate the crystallographic

characteristics of the fusion zone, weld metals were analyzed with the electron back-scatter diffraction (EBSD) method. Fig. 2-8 exhibits the EBSD analysis results for the welded metals by 3.5 kA, 6.5 kA and 10.5 kA welding conditions. The schematic sketch at the top of the figure describes the EBSD observation area (Fig. 2-8(a)). As seen in Fig. 2-8(b), the crystallographic orientations were randomly distributed in all conditions. The microstructures of the fusion zone were distributed as needle-like structure under all conditions, the average grain size was about 8 μm at 3.5kA, about 9.7 μm at 6.5kA, and 13.6 μm at 10.5kA. This result shows a remarkable difference from the initial state of equiaxed grains. The size of the grains increased as the heat input energy increased. Fig. 2-8 (c) presents the phase map of EBSD observation, the red color is alpha Ferrite or α' martensite (B.C.C: body centered cubic lattice) phase, the green color is epsilon Martensite (H.C.P: hexagonal close packed lattice) phase and the yellow color is gamma Austenite (F.C.C: face centered cubic lattice) phase, respectively. Overall, most of the phases were occupied by the alpha phase, no gamma phase was detected. On the other hand, the epsilon phase was detected in the specimen with the welding current reaching 10.5kA. This result can be related to the welding temperature and cooling rate of the melt nugget. The result show that when the amount of heat input increases, the grains may grow somewhat, but phase transformation was accompanied. Fig. 2-8(d) shows the grain boundary maps, overall, there were distributed high and low angle grain boundaries about a lath martensitic hierarchy of α' -phase such as packet and block.

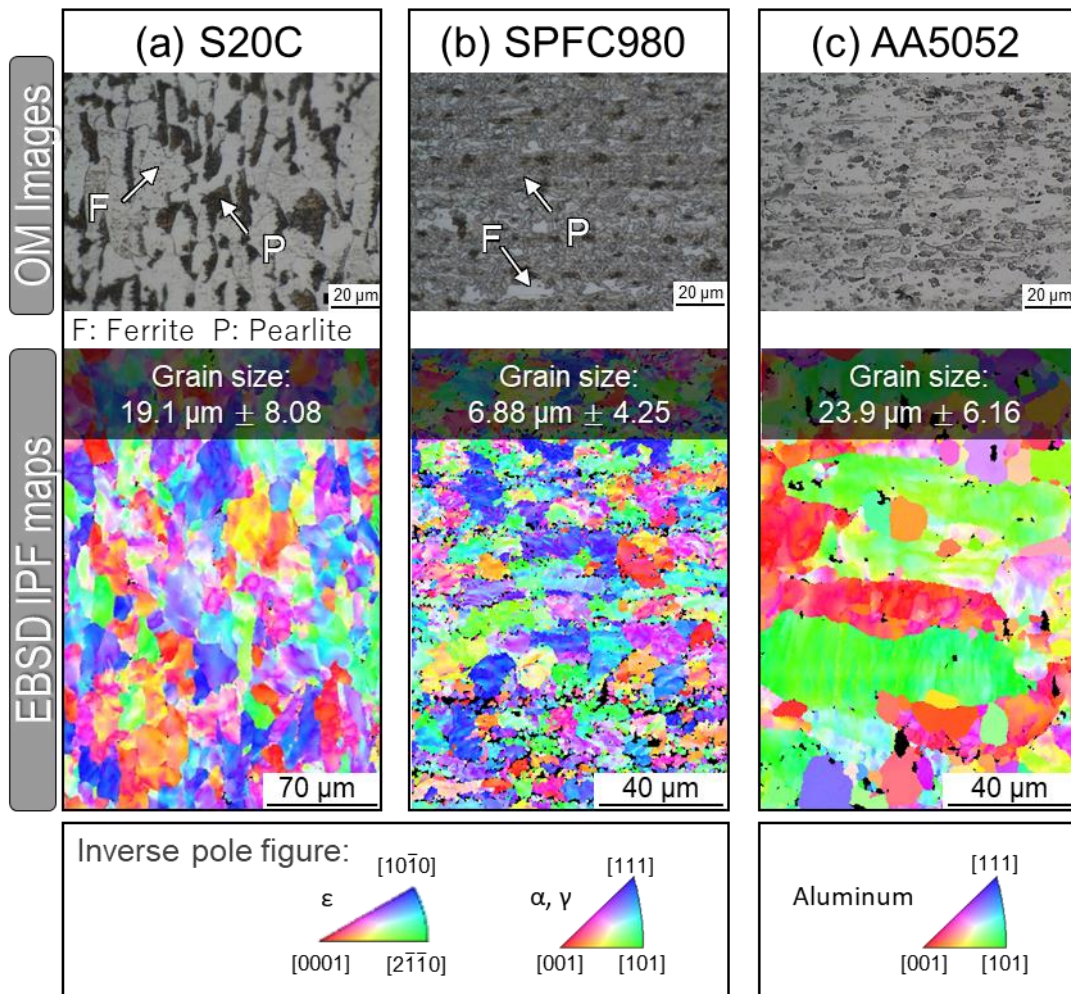


Fig. 2-7 Microstructures of an initial base material state: (a) S20C steel, (b) SPFC980 steel, and (c) AA5052-H32.

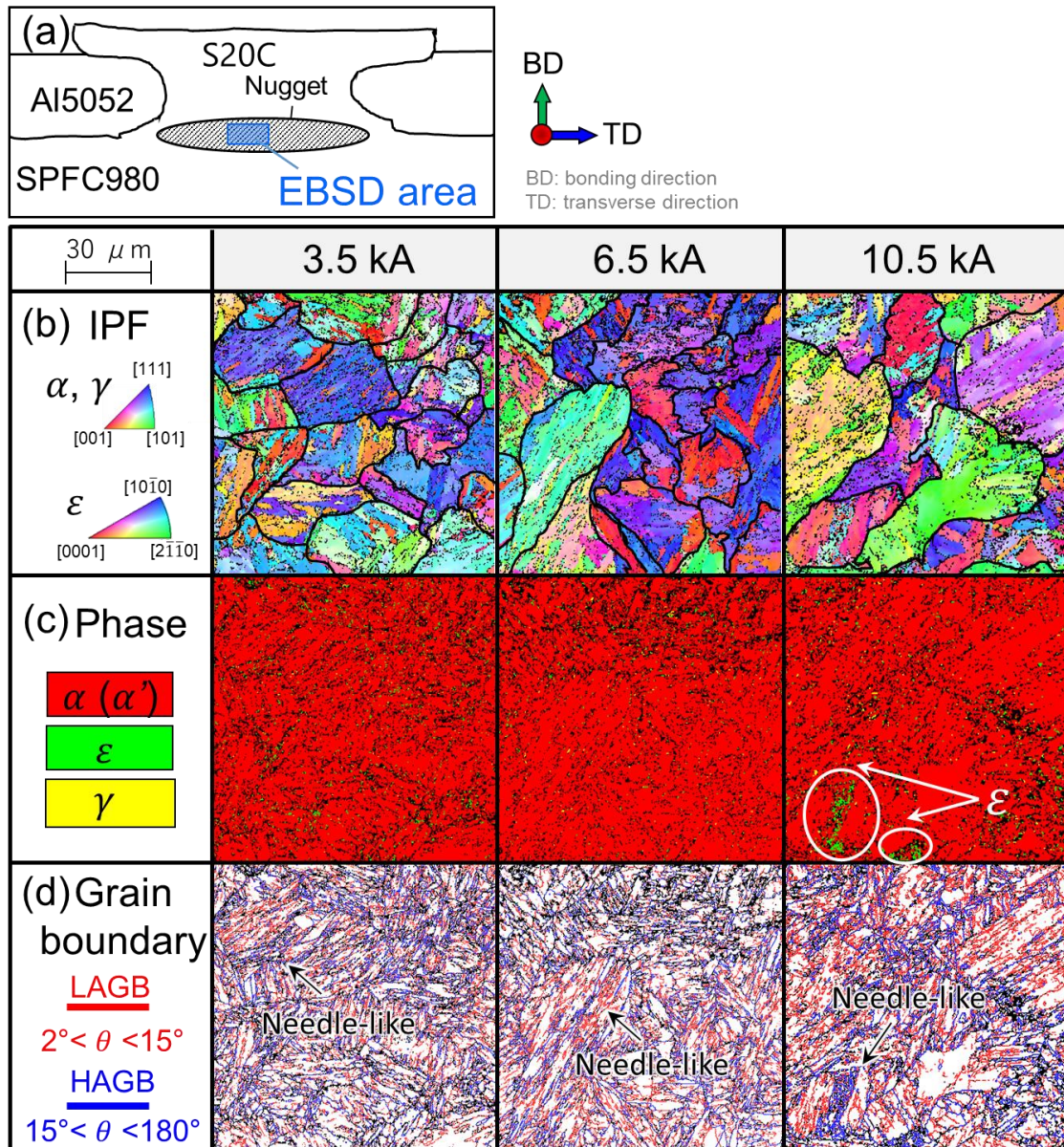


Fig. 2-8 EBSD analysis results for weld metals by 3.5 kA, 6.5 kA and 10.5 kA welding conditions. (a) Investigation area, (b) IPF map, (c) phase map and (d) grain boundary map. EBSD: electron back-scatter diffraction; IPF: inverse pole Fig.; LAGB: low angle grain boundary; HAGB: high angle grain boundary; PAGB: prior austenite grain boundary. Black dots in grain boundary map are below 0.1 CI value.

2.3.4 Microhardness distributions

The microhardness profiles across the interfaces of S20C were pre-riveted

AA5052-to-SPFC980 steel joints at different levels of the welding current, shown in Fig. 2-8. The map of hardness measurements is displayed in Fig. 2-9 (a), the y-direction (transverse line) profile across Al and S20C and the hardness profile in the x-direction (vertical line) from the head of S20C to the bottom of SPFC980 were investigated. Fig. 2-9(b) exhibits the shank diameters on the different welding current conditions. The current condition of 3.5kA was about 4 mm, similar to the diameter of the initial-state S20C. As the input current value increases, the shank diameter tends to increase linearly. As seen in Fig. 2-9(c), there was almost no change in hardness on the Al side, the welding current of 3.5kA was sustained hardness for the initial state of the base materials.

On the other hand, when the welding currents were increased to 4.5 kA and 6.5 kA, the hardness of S20C tended to increase significantly from the initial state of 192 Hv to about 350 Hv. When the welding current exceeds 8.5kA, the hardness of the S20C part increased up to 450 Hv. This dramatically increase in hardness can be attributed to Martensite transformation. From the previous work, [20] reported similar tendency that around weld nugget hardness is about 2 times the value for base metal, due to Martensite formation in this zone. The hardness distributions of the vertical line presented the same tendency with hardness distributions of the transverse line (see Fig. 2-9 (d)). The welding conditions of 3.5kA and 4.5kA had a relatively low hardness distribution, but their tendency of hardness increased significantly near the fusion zone. This hardness distribution can be attributed to the grain refinement or phase transformation effect from compression behavior of S20C which changed according to the amount of heat input.

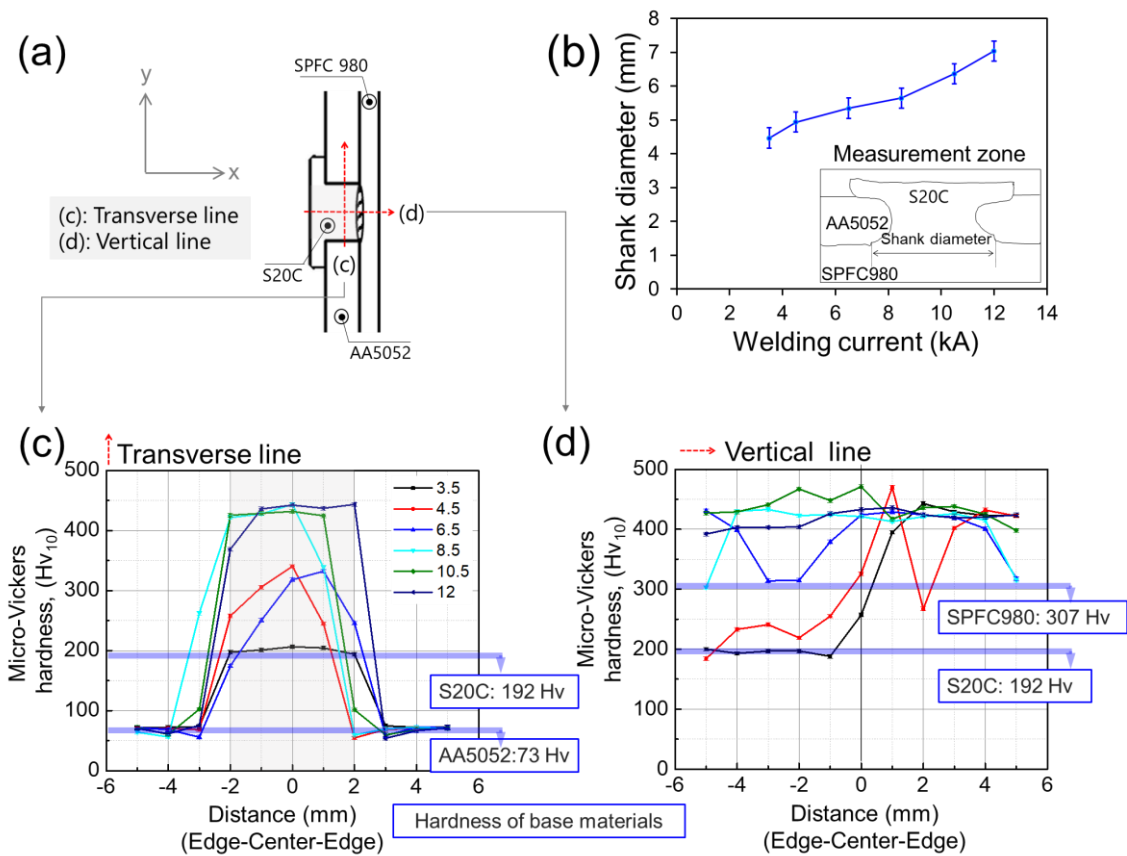


Fig. 2-9 Hardness distributions. (a) Map of hardness measurements, (b) relation between welding current and shank diameter, (c) hardness development of the transverse line and (d) hardness distribution of the vertical line.

2.3.5 Fracture characterizations

To clarify the underlying mechanisms of the fracture behavior during the tensile-shear tests, we conducted fracture surface investigations. Fig. 2-10(a) exhibits OM images for morphology of the fracture surfaces welding current condition from 3.5 kA to 12 kA. The upper part is AA5052 side and the lower part presents SPFC980 side, respectively. Under the conditions of 3.5kA and 4.5kA the fracture of the S20C-SPFC980 joint interfaces were observed. Fig. 2-10 (b) is an enlarged SEM image and EDX point analysis result of 3.5kA of SPFC980 side. No patterns such as dimple, which are traces

of resistance to destruction, were detected on the fracture surface, as can be seen from the results from the EDX, there is no IMC at the interface. It suggests that only the SPFC980 side in which the non-bonded zone detected in Fig. 2-4(d). From the 6.5 kA condition, Al expulsion was observed, the fracture occurred in the Al base material, not the S20C-SPFC980 interfaces. Fig. 2-10(c) presents the high magnification image of the Al side of welding current condition of 10.5 kA, the fracture pattern was significantly different from the fracture surface with the 3.5 kA condition. In addition, this fracture surface can be divide by two parts to Fig. 2-10(d) and (e). In the Fig. 2-10(d), coarse grains with typical shear dimples were observed, when it goes over the shear dimple area, the area where the fine dimples were distributed appeared.

Fig. 2-10(f-g) exhibits a failure energy on various welding conditions in load-displacement curves. Failure energy is the energy consumed when failure occurs. Peak load and failure energy (measured as the area under the load–displacement curve up to the peak load) were extracted from the load–displacement curve. Fig. 2-10(f) exhibits define of failure energy, peak load and failure energy corresponding to maximum displacement were determined from the load-displacement plot using OriginPro® 2015 software. Typical load-displacement plot representation extracted parameters i.e peak load (P_{max}) and failure energy (J) at maximum displacement (L_{max}). As seen in the Fig. 2-10(g), the failure energy was found to be a value of less than 10J under the condition of 3.5kA, the condition of 4.5kA was 20J. These results can be attributed from the non-bonding area or micro-cracking in Fig. 2-4 and 2-5. The welding current conditions from 6.5 kA to 12 kA of the specimens, which fracture occurred on the Al side with dimples were exceeded by 30J of failure energies. The specimens in which the ductile fracture were induced in the Al base material due to the robust bonding of

the joints interface were implemented with high strength/high elongation and high fracture energy characteristics.

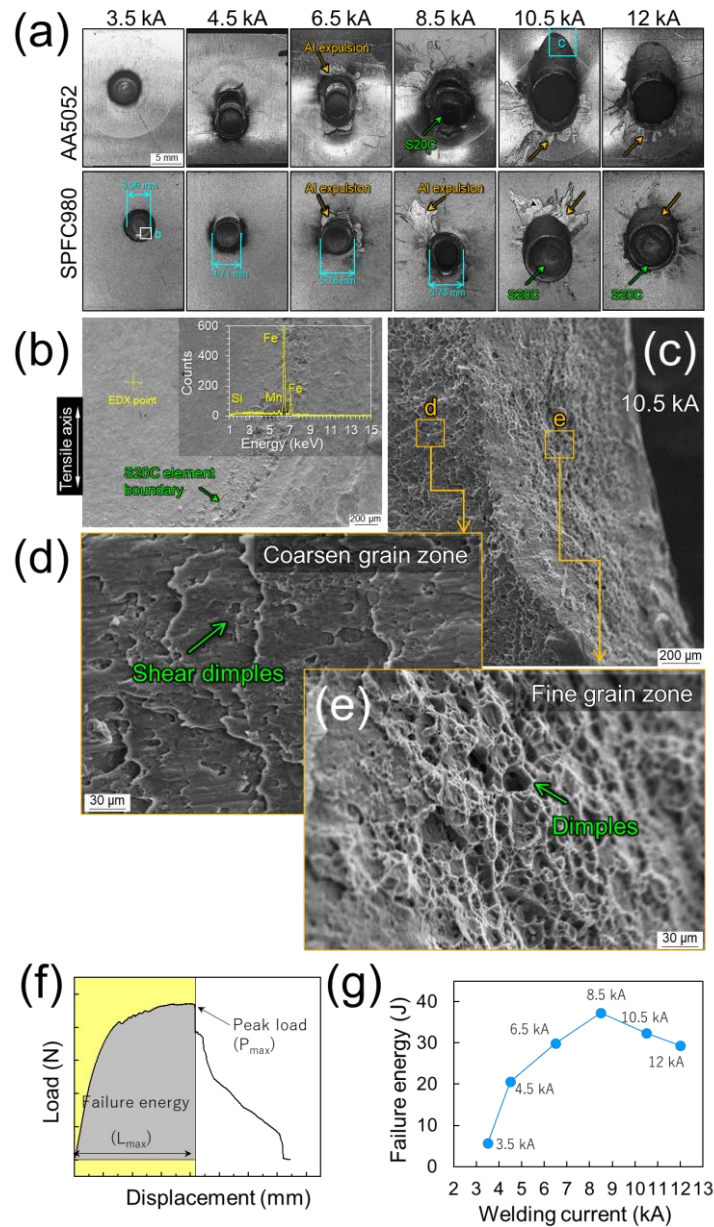


Fig. 2-10 Fractographs. (a) macroscale fracture surfaces with optical microscopic images, (b) high magnification fracture surface image with EDX point graph of 3.5 kA current welded joint in SPFC980 side and (c) high magnification fracture surface SEM image of 10.5 kA current welded joint in AA5052 side, (d) coarse grain zone with shear dimples of the (c), and (e) fine grain zone with dimples in (c), and (f) definition of the failure energy, (g) failure energies on the welding current conditions.

2.4 Discussion

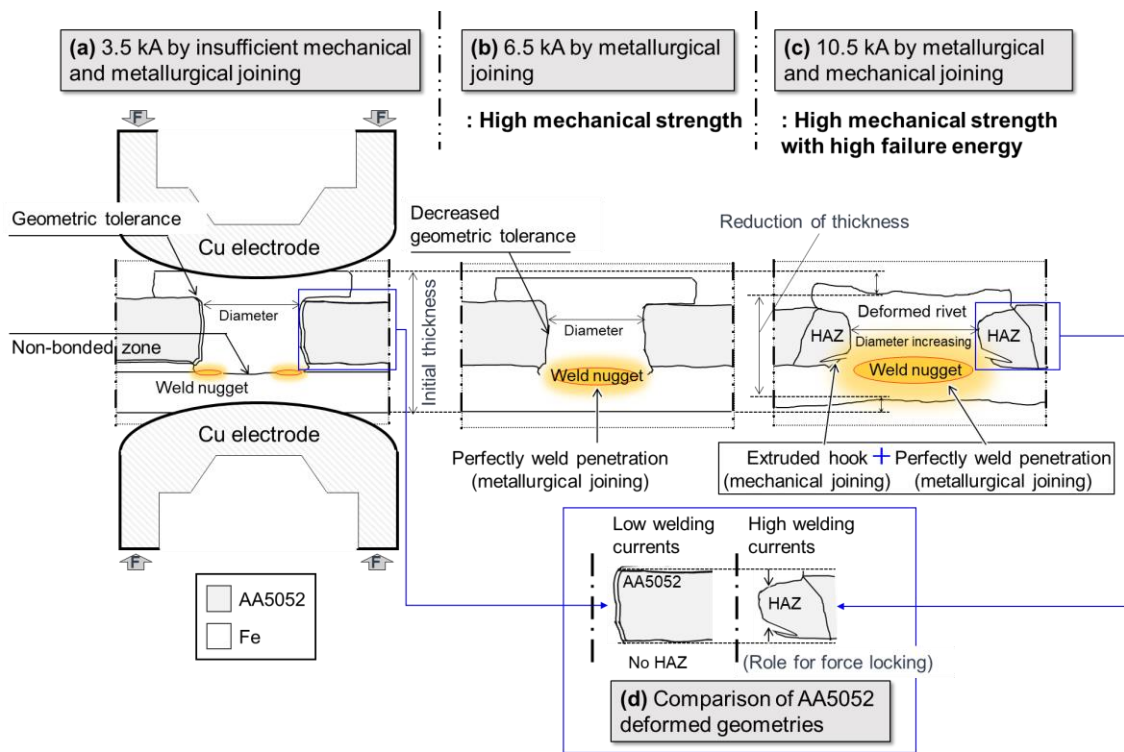
2.4.1 Welding mechanism determining mechanical strength

In this welding process, two connection methods of riveting and resistance spot welding were used. The joining of aluminum and steel combined mechanical joining and metallurgical joining. These two types of bonding are the main determinants of mechanical strength. Fig. 2-11 depicts a comprehensive configuration of a welding mechanism for determining mechanical strength. In this study, three groups of mechanical strength and microstructural relationships can be distinguished by the insufficient metallurgical joining without mechanical joining (Fig. 2-11(a)), the metallurgical joining only (Fig. 2-11(b)) and the metallurgical and mechanical joining with force lock effects by hook formations (see Fig. 2-11(c)). In the case of mechanical joining between AA5052 and the rivet, at the beginning of welding or at the low welding current, the rivet-SPFC980 interface showed an insufficient penetration completely as shown in Fig. 2-11(a). This means that the rivet melted insufficiently because there was not enough penetration. For this reason, the compressive deformation of the rivet due to the squeezing force was not significant enough to occur. Therefore, the geometrical tolerance of the material remained such as an initial state, and both mechanical and metallurgical bonding were not robustly achieved. As seen in Fig. 2-11(b), under the condition of 6.5 kA or higher, it can be confirmed that the only sufficient penetration without significant mechanical bonding were completed in cross-sectional observations with a consistent mechanical strength improvement of over 8000 N.

On the other hand, when the welding current increased about 10 kA, the rivet fully melted which caused a significant compressive deformation with an extruded hook as displayed in Fig. 2-11(c, d). In this case, the extruded hook formed by increasing the

rivet diameter and decreasing the geometrical tolerance during the rivet and SPFC980 welding can be a positive aspect that makes the mechanical bonding further robust. This means that a larger rivet diameter and hook formation can contribute to a mechanical force lock, such as clamping effects between the rivet and the AA5052. The relationship between the riveting compression force, thickness and mechanical strength has been reported in a previous rivet study with similar results[21]. With metallurgical bonding such as a perfect penetration, the displacement was limited to within 4 mm (see welding current of 6.5 KA), whereas the combination of mechanical bonding like extruding hooks entails slightly higher strength and displacement in excess of 6 mm (over welding currents of 8.5 kA). In that context, the structurally sound welding interface and metallurgical joining including the phase transformation obtained with sufficient penetration can be notable factors in improving the mechanical properties in this study. For this reason, the combination of an increased diameter, the force lock with hook bonding, and metallurgical bonding resulted in a remarkable increase in mechanical strength, and failure energy of more than about 90% (see Fig. 2-10g). However, as seen in the failure energy and tensile-shear strength, excessive welding current causes welding defects like undercuts and degradations of mechanical properties. The schematic in Fig. 2-11(e) was further used to illustrate the mechanism for the force locking formation by welding current increasing in detail. The order of the hook formation is ①the fusion line formation and compression of the rivet → ②fully melted the nugget and promotion of rivet compression → ③forced locking with the hook extrusion and anchor formation. When the welding current was low (3.5 kA), a crack was observed in the non-bonded part of the central part and the deformation and the crack of the corner part by a compressive force. As the welding current increased further

by 4.5 kA, the non-bonded crack line fully melted which formed a fusion line. Due to the compressive force and reaction force, the corner undergoes more protruding deformation, and this deformed corner formed the crack at the interface again. When the current increased further, this crack melted and formed the welding interface. When the current reached to 6.5kA, the crack interface between the rivet and SPFC980 becomes ambiguous in accordance to the fully melted interfaces. Then the corner protrudes more and adheres to the AA5052 side. When the welding current increased by 10.5 kA, the metallurgical bonding is completed, and the complete hook formed by the compressive force-reaction force action and is force locked to the AA5052. The diameter of the rivet increased further by this melting-deformation interaction, which promoted the hook extruding. There is further discussion of the phase transformations in detail in section 4.2. Consequently, the determination of robust mechanical strength made by combining the mechanical bonding due to the compression behavior of the rivet and the metallurgical bonding accompanied by sufficient penetration in the welding nugget.



(e) Mechanism for the force locking formation by welding current increasing

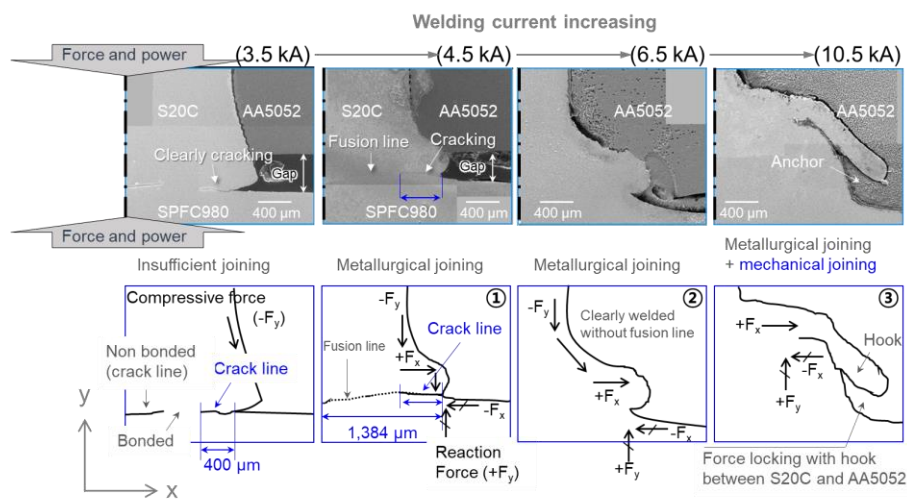


Fig. 2-11 A comprehensive description of the welding mechanism determining mechanical strength. (a) 3.5 kA by insufficient mechanical and metallurgical joining, (b) 6.5 kA by metallurgical joining, (c) 10.5 kA by mechanical and metallurgical joining and (d) comparison of AA5052 deformed geometries, and (e) mechanism for the force locking formation by welding current increasing.

2.4.2 Welding current influence on the microstructure developments

The microstructure of fusion zone of low carbon steel after RSWs mainly depends on the austenite stability and cooling rate[20,22]. Namely, lower austenite stability and higher cooling rate drive more active α' - and/or ε -martensitic transformation during cooling after RSW. Regarding the austenite stability, it can be evaluated quantitatively by means of α' - and ε -martensite start temperatures. The effect of alloying elements on martensite start temperatures for α' - and ε -phases was suggested by Mahieu et al. (2002) and Yang et al. (2012), respectively[23,24]:

$$M_s^0 (\text{ }^\circ\text{C}) = 539 - 423C - 30.4Mn - 7.5Si + 30Al \quad (1)$$

for α' -martensite, and

$$M_s^0 (\text{ }^\circ\text{C}) = 576 \pm 8 - (9.1 \pm 0.4)Mn + (4.1 \pm 1)Si + (21.3 \pm 2)Al - (489 \pm 31)C + 273.15 \quad (2)$$

for ε -martensite[24], where Mn, Si, Al, and C denote the concentration of the Mn, Si, Al, and C in weight percent. The effect of prior austenite grain size on the M_s^0 temperature was derived by Yang and Bhadeshia et al. (2009)[25] and Yen et al. (2015)[26], as follow:

$$M_s^0 - M_s = \frac{1}{b} \ln \left[\frac{1}{\bar{V}_\gamma} \left\{ \exp \left(-\frac{\ln(1-f)}{m} \right) - 1 \right\} + 1 \right] \quad (3)$$

where M_s means α' - or ε -martensite start temperatures reflecting the effects of both alloying elements and prior austenite grain size. b denotes the fitting parameters (0.2689 for α' -martensite and 0.19 for ε -martensite), \bar{V}_γ is the average austenite grain

volume of (unit: mm³), related to the prior austenite grain size, m is the aspect ratio of the martensite plate (0.05 for α' -martensite and 0.03 for ε -martensite), and f is the first detectable fraction of martensite which is assumed to be 0.01. For the present SPFC980 steel, the M_S^0 values of α' - or ε -martensite were calculated as 419.2 and 233.5 °C, respectively. Moreover, in the case of S20C steel, the values of α' - or ε -martensite were calculated as 438.6 and 201.5 °C, respectively. Namely, based on these temperature ranges, martensite can be formed at the temperature of S20C near the top of the nugget and the calculated M_S^0 temperature of SPFC980 near bottom of the nugget. These results indicate that the nugget zone consisting of both steels can possess the martensites at room temperature during cooling above the critical cooling rate for the martensitic transformation after welding. The result means that the lower austenite stability and more active α' -martensitic transformation during cooling relative to ε -martensitic transformation, supported by EBSD results (Fig. 2-8b-d) about a lath martensitic hierarchy of α' -phase such as packet and block. The size of prior austenite grains roughly increased from ~25 to 65 μm as a function of welding current from 3.5 to 10.5 kA; prior austenite grain boundary was highlighted as black lines in inverse pole figure map by misorientation angle ranging from 20 to 50° with reference to results of Lee et al. (2019) [27], and the area with similar crystallographic orientation increased and retouched by an image analyzer (Fig. 2-8b). For M_S^0 of ε phase, it reduced from 176.6 to 191.7 °C, as a function of welding current from 3.5 to 10.5 kA. As a result, it is thought that the reduction of austenite stability with grain coarsening drives relatively active transformation of thermal ε -martensite in weldment at 10.5 kA (Fig. 2-7f).

In addition, the critical cooling rate for martensitic transformation can be estimated

using the equation consisting of chemical composition (wt.%) as follows by Goodarzi et al. (2009) [20].

$$\text{Log}(v) = 7.42 - 3.13C - 0.71Mn - 0.31Ni - 0.34Cr - 0.45Mo \quad (4)$$

where, v is the critical cooling rate in $K \cdot h^{-1}$. For the investigated steel, the critical cooling rate is about $2,757.96 K \cdot s^{-1}$. If the cooling rate exceeds this critical value, it can be also speculated that the fusion zone microstructure consists of mainly martensite phase. To verify the cooling rate of the present materials during RSW, the numerically thermal behavior of RSW was calculated via the finite element method (FEM) simulation. To apply the boundary conditions, the material properties used for the simulation are shown in the Table. 3 and nonlinear material properties as a function of temperature were applied. Here, the electrical resistivity was assumed to no temperature dependence, as shown in Table 2-3. Thermal conductivity, density, coefficient of thermal expansion and specific heat are functions of temperature, and the physical properties of temperature-dependent low-carbon steel and Al alloy provided by the ANSYS Granta material database platform were applied as input for transient thermal analysis. A commercial finite element analysis program, ANSYS R18 workbench was employed. The heat transfer in RSW is transient thermal behavior. The governed equation for the transient temperature field is as follows:

$$\rho C_p \frac{\partial T}{\partial t} = \frac{\partial}{\partial x} \left(k \frac{\partial T}{\partial x} \right) + \frac{\partial}{\partial y} \left(k \frac{\partial T}{\partial y} \right) + \frac{\partial}{\partial z} \left(k \frac{\partial T}{\partial z} \right) + q_v \quad (5)$$

where T is temperature, t is time; q_v is the heat generation rate per volume; k is the

thermal conductivity; ρ is the density; C_p is specific heat capacity; k , ρ , C_p are all function of temperature. C_p is related to the enthalpy H:

$$C_{p,m} = \lim_{\Delta T \rightarrow 0} \left(\frac{\Delta H_m}{\Delta T} \right)_p = \left(\frac{\partial H_m}{\partial T} \right)_p \quad (6)$$

The governing equation for the electrical potential field is as follows:

$$\frac{\partial}{\partial x} \left(\frac{1}{\rho E} \cdot \frac{\partial U}{\partial x} \right) + \frac{\partial}{\partial y} \left(\frac{1}{\rho E} \cdot \frac{\partial U}{\partial y} \right) + \frac{\partial}{\partial z} \left(\frac{1}{\rho E} \cdot \frac{\partial U}{\partial z} \right) = 0 \quad (7)$$

where x, y and z are x-axis, y-axis, and z-axis, respectively; U denotes the voltage; ρE is the electrical resistivity, which consists of the bulk resistance and contact resistance; ρE is a function of temperature.

Fig. 2-12 shows descriptions of transient welding thermal simulation. FE modelling was performed with design modeler in ANSYS workbench, all nodes of components are shared with each interface exists as displayed in Fig. 2-12(a). As seen in Fig. 2-12(b), boundary conditions were implemented with the heat input as an electrical current (6500A) and ground voltage with 0.45 sec of an energization time by using an electro-thermal coupled field ACT (application customization toolkit) module. The cooling was computed using the heat transfer coefficient of natural convection in a transient state. The computed temperature distribution at the peak temperature is shown in Fig. 2-12(c). Each nugget, fusion zone and HAZ were directly compared with an etched actual welding cross-section (see Fig. 2-12d). The result showed the temperature distribution similar to that of the previous study[28]. As with the actual

cross-sectional structure, high temperatures occurred around the fusion joint, and there was a tendency that high temperature was not reached to aluminum side. Finally, Fig. 2-12(e) exhibits temperature history during the process. The temperature was cooled to near 200 °C at the melting point within 10 sec. Consequently, both theoretically and numerically, the results can be supported that the martensite structure can be sufficiently formed during the processes, matching with the evaluation via both EBSD result and calculated M_s temperature.

Table. 2-3 Generalized material properties for the transient thermal simulation (RT).

	Density, ρ (kg/m ³)	Thermal conductivity, k (Wm ⁻¹ K ⁻¹)	Specific heat, C_p (J/kg·K)	CTE, α (K ⁻¹)	Resistivity (10 ⁻⁷ Ω·m)
AA5052	2700	140	900	2.4E-5	0.49
SPFC980	7800	22	213	1.2E-5	1.74
S20C	7800	25	465	1.3E-5	1.43

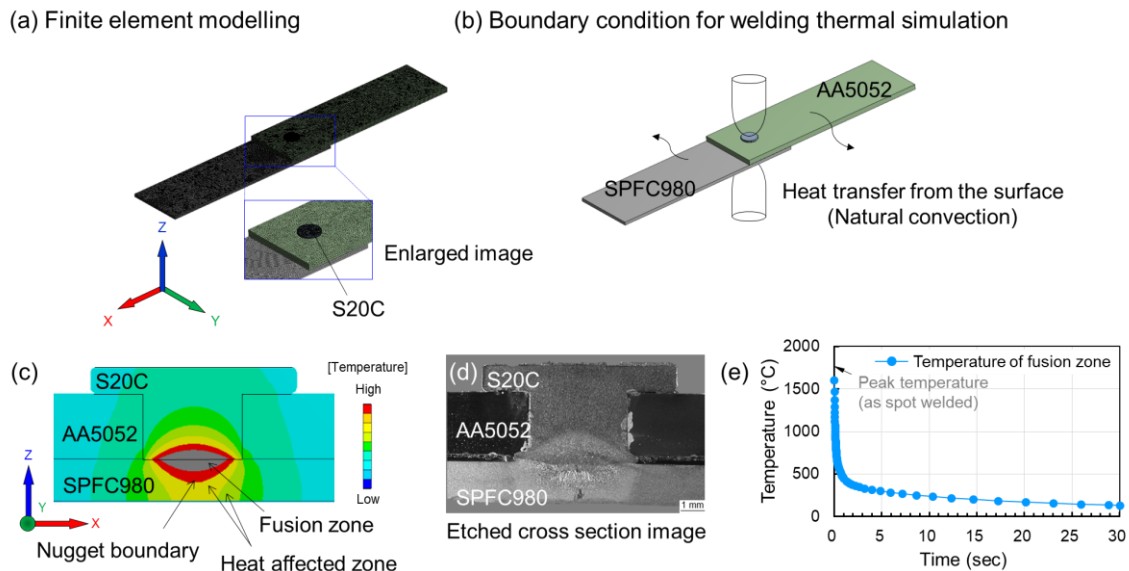


Fig. 2-12 Description of transient welding thermal simulation. (a) 3D FE modelling of specimen, (b) boundary condition, (c) peak temperature distribution during the resistance element welding process, (d) actual cross-sectional image corresponding to the thermal simulation, (e) temperature history during the process.

2.4.3 Microstructure and deformation influence on the tensile-shear behavior

It is well known that the mechanical properties change with microstructure developments. The results can be attributed from needle-like structure with phase transformation from EBSD analysis results in Fig. 2-8. In the hardness distribution section, it was observed that the hardness increased as the amount of heat input increased. This trend is similar to shear strength including failure energy. The hardness distribution provides indirect information about the strength and the deformation behavior of spot-welded joints which normally, increase in hardness results in decreasing formability while simultaneously increasing strength. However, the 3.5kA condition of an interfacial failure (IF) mode was the low hardness distribution with the formation of insufficiently bonding nuggets, which caused a low tensile-shear strength and a low elongation. In contrast, conditions above 6.5kA had high hardness, but it successfully induced the fracture mode of the Al base material; pull out failure (PF) due to the robust interfacial bonding with the compressive deformation. In summary, the mechanical behavior of the fracture due to the microstructure development and its geometrical degradations of the interface can be explained as shown in the Fig. 2-13. The welding condition of 3.5kA of the fracture mechanism where the non-bonded area appeared due to the insufficient melting is presented in Fig. 2-13(a). The arrow indicates the mechanical force flow when the tensile-shear behavior occurs, its free body diagram (FBD) is shown in Fig. 2-13(b). The diagram describes the shear force and bending moment diagram in detail, and it means that fracture was easily reached by the shear-force concentrated near the non-bonded area. Fig. 2-13(c) exhibits the fracture mechanism of welding condition of 8.5 kA, in which deformation structure formed by the sufficient melting and the compression force and the slight hook are considered to be

major factors for fracture resistance. Furthermore, in the free body diagram (see Fig. 2-13(d)), the robust bonded interface does not create the stress concentration. These combinations can be induced by increasing the failure energy with the ductile fracture of the Al base material. Finally, when the amount of heat input is excessive, a further enhanced compressive force caused a geometrical degradation like severe undercut damages as displayed in Fig. 2-13(e). Then, the Al was severely damaged, in which the Al cannot resist shear forces and reaches fracture relatively easily. For this reason, in the case of S20C pre-riveting resistance element welding, it can be clearly seen that geometrical plastic deformation has a greater influence on fracture resistance than phase transformation or crystallographic grain boundary behavior.

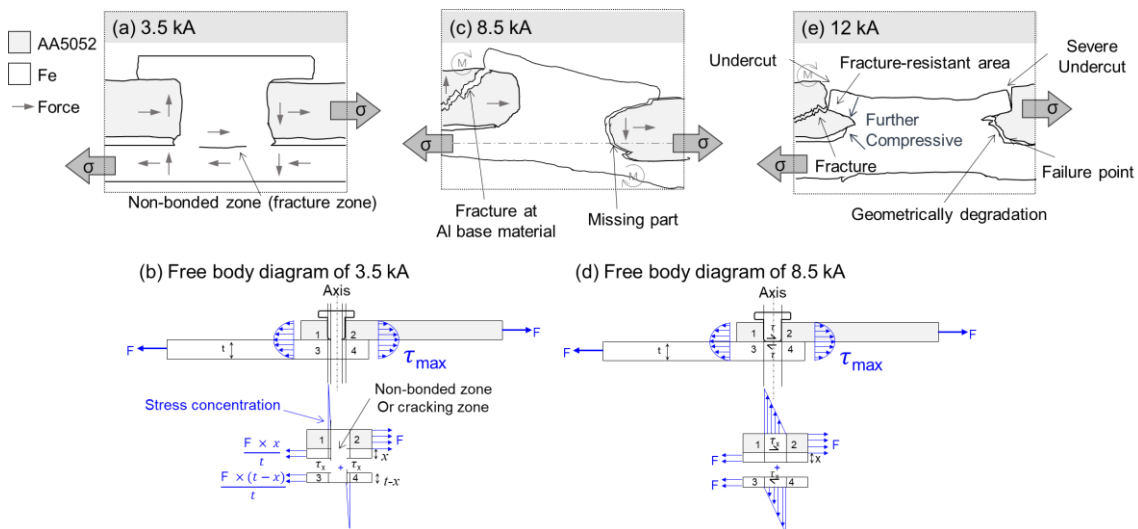


Fig. 2-13 Schematic illustration of fracture mechanics. (a) 3.5 kA, its description of free body diagram (b), (c) 8.5 kA, its description of free body diagram (d) and (e) fracture mechanism of 12 kA.

2.4.4 Relation between fracture mode and Portevin–Le Chatelier effect

In the mechanical strength section, we observed serration behavior of some welding conditions in load-displacement curves. Fig. 2-14(a) displays the

load-displacement curve from this work, the serration behavior during the tensile-shear tests were clear from the current condition of 6.5 kA to the condition of 12 kA. A major feature of these conditions was a ductile fracture at AA5052 base materials. Caillard et al. (2016)[29] investigated that serrations have been considered as a result of interactions between dislocations and solute atoms, which is called dynamic strain aging (DSA) or Portevin–Le Chatelier (PLC) effect. Previous studies [30,31] reported that the serrations reduced or disappeared in the deformed samples. Previous studies have reported that serrations have also been observed in Al-Mg and other 5xxx series aluminum alloys. This phenomenon is said to occur during the tensile testing of some Al-Mg alloys at room temperature at low strain rates (10^{-4} – 10^{-3} s $^{-1}$). Therefore, it can be clearly seen that the condition under which serration behavior is detected is when the fracture of Al base materials occur as observed in this study. To further understand the serration behavior and fracture mode, the DIC method was applied.

Fig. 2-14(b) exhibits the time dependent load-strain and strain rate curve. The strain and strain rate rise rapidly to the maximum value near the peak load. The enlarged graph of the serration behavior section is shown in the Fig. 2-14(c). Each time the load updates the peak value, the strain rate decreases rapidly. Then, when a new strain rate formed, the strain rate rises rapidly reaching up to peak value, which behavior occurs repetitively up to failure. The image maps visualizing this behavior are shown in the Fig. 2-14(d). In the strain distributions, initially, the strain was distributed in AA5052 and SPFC base materials, but the strain was distributed with high strength in the S20C corner. As time passed, strain nucleation proceeded in Al side near the S20C, and the range gradually widened. The 8.5kA specimen with the robust bonding had maximum intensities of the strain distribution significantly spread at the

Al base material before fracture, which finally occurred to failure at the Al base material. The DIC behavior of the REW bonded AA5052/SPFC980 at 3.5kA is shown in Fig. 2-14(e). By contrast, the tensile-shear behavior at the beginning and the strain distribution was similar with the current condition of 8.5 kA, but the maximum strain distribution was concentrated only at the edge of S20C until failure. This proves that the shear force was concentrated in the defects at the interface and the stress was not concentrated in Al base material.

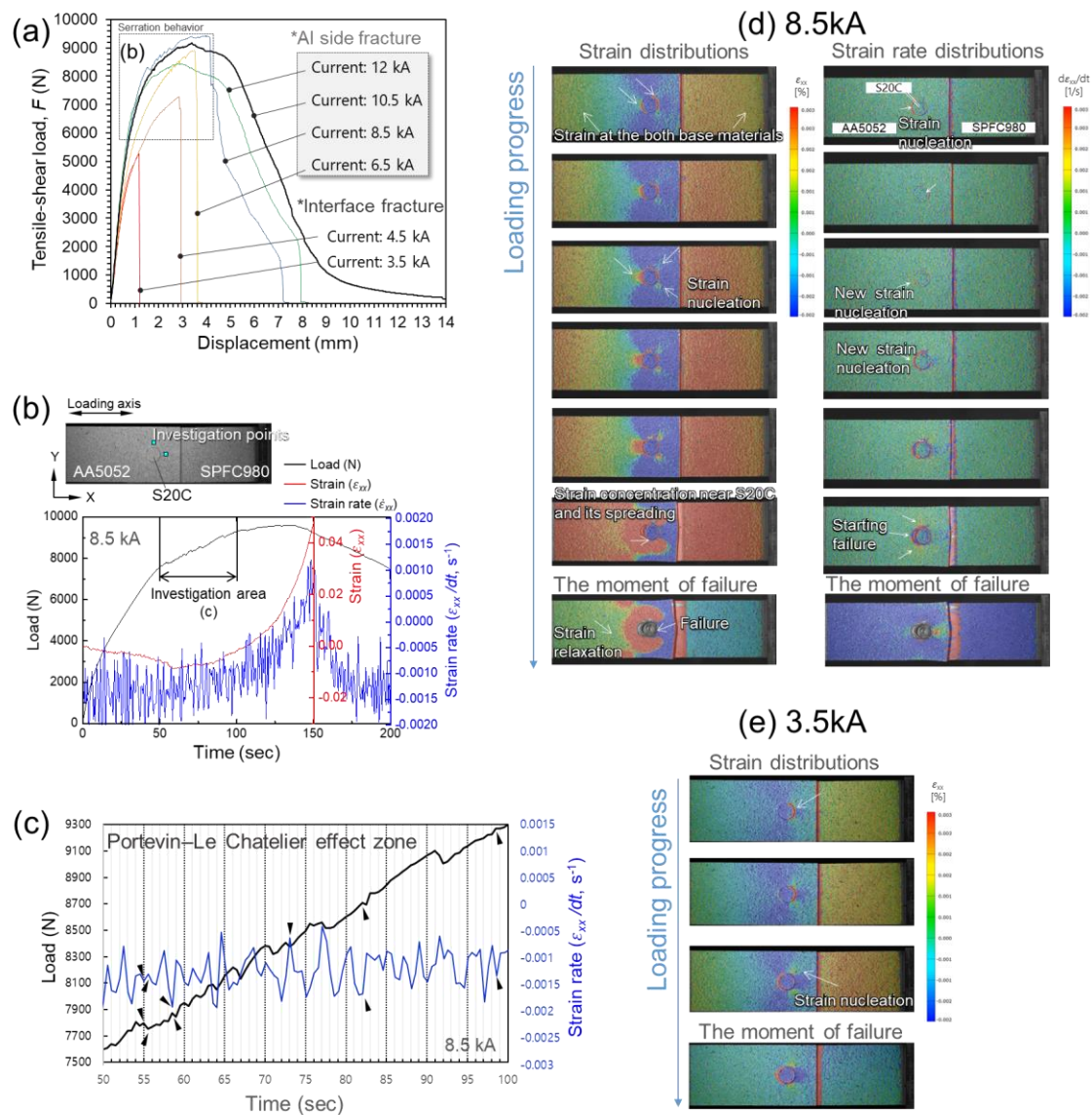


Fig. 2-14 Investigation of serration behaviors by DIC method. (a) load-displacement curves from this study, (b) load-strain-strain rate graphs of 8.5 kA, and (c) investigation of serration behavior zone, (d) visualized images for 8.5 kA of strain and strain rate measured during tensile-shear behavior measured by *in-situ* DIC and (e) strain distributions of 3.5kA during tensile-shear testing. DIC: digital image correlation.

2.4.5 Comparison with Al/Fe joining candidate processes

Fig. 2-15 shows an overview progress of the strength developments of Al-Steel lap joints by various next-generation joining technologies. Among the various candidates of

Al/Fe joint technologies, laser welding, friction-stir-process (FSP), and self-pierce-rivet, have attracted attention over the years for the next-generation joining. Many previous studies have been done on the laser application welding for Al/Fe dissimilar joining, which has been in the spotlight as a low heat input fusion welding technology. However, the strength characteristics degraded due to IMC growth at the bonding interface were limited to 2000 N with low displacement. The traditional resistance spot welding (RSW) presents also lower than 2000 N. In the solid-state bonding technologies, FSP[32], spot forging bonding have limitations of a peak load under 5000 N[33]. In addition, FSP and spot forging bonding have critical disadvantage that trace of the tool remains after the process. Papadimitriou et al. (2017) proposed advanced processes that rivet drilling to sheet technology and kerb konus riveting have reported twinning-induced plasticity (TWIP) steel/Al bonding[34]. Considerable progress has been made for dissimilar material bonding, but the peak loads still have no exceeding mechanical properties of this study. The results obtained with our approach are not limited to the joining of Al and Fe. It is possible to obtain low-cost and mass-production of robust bonding of next-generation lightweight non-ferrous materials. Therefore, the results present a substantial alternative for robust bonding/mass production of automotive lightweight structures.

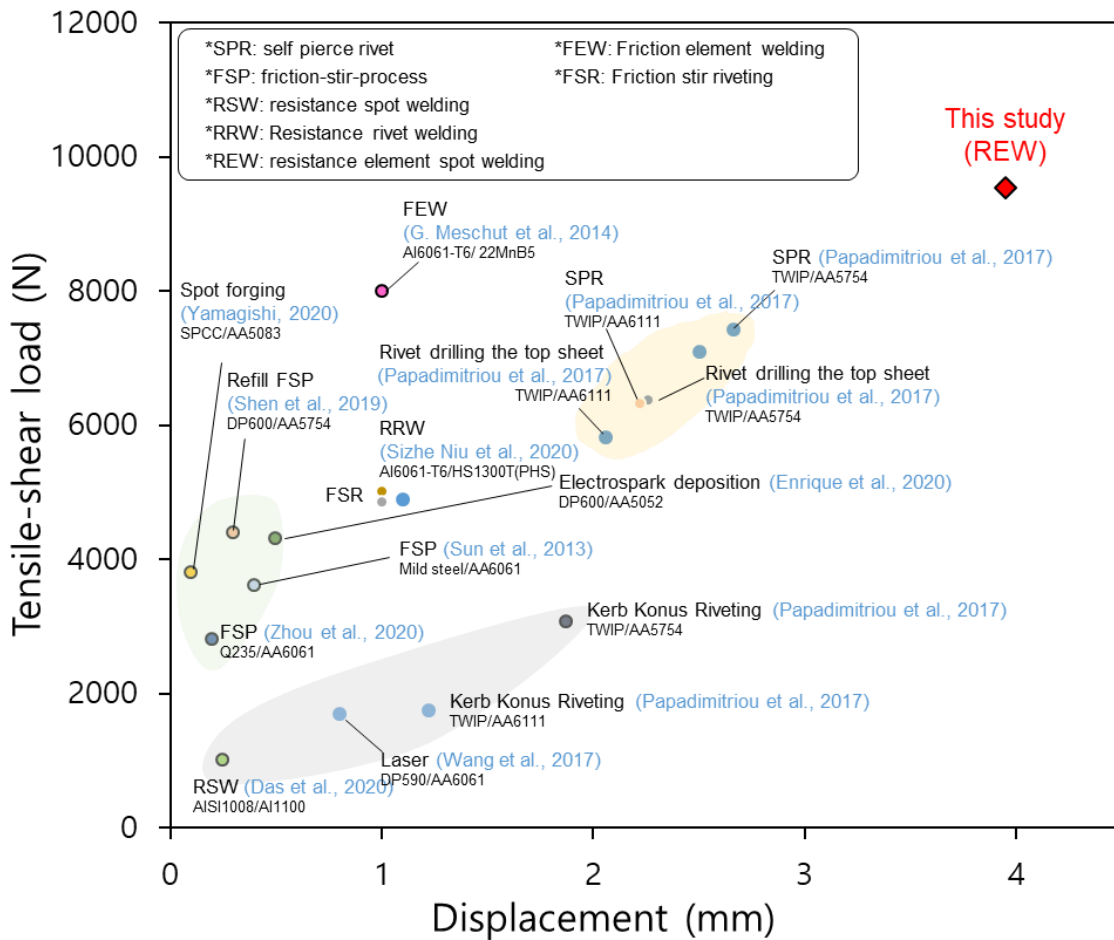


Fig. 2-15 Overview progress of the mechanical strength developments of Al-Steel lap joints by various next-generation joining technologies.

2.5 Conclusions

To achieve the robust bonding Al/Fe joint for automotive lightweight structures, the S20C pre-riveted AA5052 alloy and SPFC980 steel lap joints were successfully welded using resistance element welding (REW). As a result, the REW process demonstrated exceptional mechanical properties based on the integrity of the microstructure as well as the compatibility with existing resistance spot welding (RSW) processes was proven. The main results from this study were obtained as follows:

1. The test specimens bonded with 3.5kA and 4.5kA input currents were not sufficiently melted to achieve robust bonding, and gaps and micro-cracks at the bonding interface were the main causes for inducing the brittle failure of the bonding interfaces.
2. As the input current increases, the tensile-shear strength gradually increases and the peak load exceeding 9000N, but when the input current exceeds 10.5kA, the tensile-shear strength gradually decreases. In addition, the fracture mode of the specimens with a peak load over 9000N was an Al base material failure with ductile fracture and high failure energy.
3. The ϵ phase was detected at the interface of 10.5 kA current condition where the Al base material fracture was successfully induced by robust bonding. In addition, the cooling rate was numerically confirmed to be within the critical region where the ϵ phase could be sufficiently realized through theoretical calculations and transient welding thermal simulation.
4. The mechanical behavior of the conditions in which the joint interface fractures and the Al base material fractures occurred were clearly revealed with the help of the in-situ digital image correlation (DIC) method. As a result, the specimens were not perfectly bonded at the interface which caused the strain distribution to be concentrated in the root of the S20C element, causing radical fracture. On the other hand, the robust bonded specimens were fractured by the high intensity strain distributions with serration behavior to the Al and steel base material before the

fracture occurred.

5. We present that directly compared with the previous reported results of Al/Fe lap joints bonded using various next-generation joining process candidates including self-pierce riveting (SPR), laser welding, friction-stir-process (FSP), etc. Remarkably, our results obtained exceptional mechanical properties of Al/Fe robust bonding while using the resistance spot welding (RSW) facility. Consequently, our demonstration provides an implementation of satisfactory mechanical properties with resistance element welding, and it can be adopted as a substantial alternative for robust bonding and mass production of automotive lightweight structures.

References

- [1] Kim SH, Kim H, Kim NJ. Brittle intermetallic compound makes ultrastrong low-density steel with large ductility. *Nature* 2015;518:77–9. <https://doi.org/10.1038/nature14144>.
- [2] Militzer M. Materials science: A synchrotron look at steel. *Science* (80-) 2002;298:975–6. <https://doi.org/10.1126/science.1078210>.
- [3] Qin G, Ao Z, Chen Y, Zhang C, Geng P. Formability behavior of Al/steel MIG arc brazed-fusion welded joint. *J Mater Process Technol* 2019;273:116255. <https://doi.org/10.1016/j.jmatprotec.2019.116255>.
- [4] Kaushik P, Dwivedi DK. Effect of tool geometry in dissimilar Al-Steel Friction Stir Welding. *J Manuf Process* 2020. <https://doi.org/10.1016/j.jmapro.2020.08.007>.
- [5] Cui L, Wei Z, Ma B, He D, Huang H, Cao Q. Microstructure inhomogeneity of dissimilar steel/Al butt joints produced by laser offset welding. *J Manuf Process* 2020;50:561–72. <https://doi.org/10.1016/j.jmapro.2020.01.011>.
- [6] Wang H, Qin G, Geng P, Ma X. Interfacial microstructures and mechanical properties of friction welded Al/steel dissimilar joints. *J Manuf Process* 2020;49:18–25. <https://doi.org/10.1016/j.jmapro.2019.11.009>.
- [7] Chen J, Feng Z, Wang HP, Carlson BE, Brown T, Sigler D. Multi-scale mechanical modeling of Al-steel resistance spot welds. *Mater Sci Eng A* 2018;735:145–53. <https://doi.org/10.1016/j.msea.2018.08.039>.
- [8] Hu S, Haselhuhn AS, Ma Y, Li Y, Carlson BE, Lin Z. Influencing mechanism of inherent aluminum oxide film on coach peel performance of baked Al-Steel RSW. *Mater Des* 2021;197:109250. <https://doi.org/10.1016/j.matdes.2020.109250>.
- [9] Zhou L, Yu M, Liu B, Zhang Z, Liu S, Song X, et al. Microstructure and mechanical

- properties of Al/steel dissimilar welds fabricated by friction surfacing assisted friction stir lap welding. *J Mater Res Technol* 2020;9:212–21.
<https://doi.org/10.1016/j.jmrt.2019.10.046>.
- [10] Yu G, Chen S, Zou T, Li S, Huang J, Yang J, et al. Laser beam joining of Al/steel dissimilar metals with Sn-Zn filler wire in overlap configuration. *J Manuf Process* 2020;60:481–93. <https://doi.org/10.1016/j.jmapro.2020.10.079>.
- [11] Huang Y, Huang T, Wan L, Meng X, Zhou L. Material flow and mechanical properties of aluminum-to-steel self-riveting friction stir lap joints. *J Mater Process Technol* 2019;263:129–37. <https://doi.org/10.1016/j.jmatprotec.2018.08.011>.
- [12] Mori K, Abe Y, Kato T. Self-pierce riveting of multiple steel and aluminium alloy sheets. *J Mater Process Technol* 2014;214:2002–8.
<https://doi.org/10.1016/j.jmatprotec.2013.09.007>.
- [13] Jaber HL, Pouranvari M, Salim RK, Hashim FA, Marashi SPH. Peak load and energy absorption of DP600 advanced steel resistance spot welds. *Ironmak Steelmak* 2017;44:699–706. <https://doi.org/10.1080/03019233.2016.1229880>.
- [14] Cao X, Li Z, Zhou X, Luo Z, Duan J. Modeling and optimization of resistance spot welded aluminum to Al-Si coated boron steel using response surface methodology and genetic algorithm. *Meas J Int Meas Confed* 2021;171:108766.
<https://doi.org/10.1016/j.measurement.2020.108766>.
- [15] Chen C, Kong L, Wang M, Haselhuhn AS, Sigler DR, Wang HP, et al. The robustness of Al-steel resistance spot welding process. *J Manuf Process* 2019;43:300–10.
<https://doi.org/10.1016/j.jmapro.2019.02.030>.
- [16] Niu S, Ma Y, Lou M, Zhang C, Li Y. Joint formation mechanism and performance of resistance rivet welding (RRW) for aluminum alloy and press hardened steel. *J Mater*

- Process Technol 2020;286:116830. <https://doi.org/10.1016/j.jmatprotec.2020.116830>.
- [17] Holtschke N, Jüttner S. Joining lightweight components by short-time resistance spot welding. *Weld World* 2017;61:413–21. <https://doi.org/10.1007/s40194-016-0398-5>.
- [18] Beukel A. Theory of the effect of dynamic strain aging on mechanical properties. *Phys Status Solidi* 1975;30:197–206.
- [19] Hu Z, Qi Y, Nie X, Zhang H, Zhu H. The Portevin-Le Chatelier (PLC) effect in an Al-Cu aluminum alloy fabricated by selective laser melting. *Mater Charact* 2021;178:111198. <https://doi.org/10.1016/j.matchar.2021.111198>.
- [20] Goodarzi M, Marashi SPH, Pouranvari M. Dependence of overload performance on weld attributes for resistance spot welded galvanized low carbon steel. *J Mater Process Technol* 2009;209:4379–84. <https://doi.org/10.1016/j.jmatprotec.2008.11.017>.
- [21] Li M, Tian W, Hu J, Wang C, Liao W. Study on shear behavior of riveted lap joints of aircraft fuselage with different hole diameters and squeeze forces. *Eng Fail Anal* 2021;127:105499. <https://doi.org/10.1016/j.engfailanal.2021.105499>.
- [22] Gould JE, Khurana SP, Li T. Predictions of microstructures when welding automotive advanced high-strength steels. *Weld J (Miami, Fla)* 2006;85.
- [23] Mahieu J, Maki J, De Cooman BC, Claessens S. Phase transformation and mechanical properties of Si-free CMnAl transformation-induced plasticity-aided steel. *Metall Mater Trans A Phys Metall Mater Sci* 2002;33:2573–80. <https://doi.org/10.1007/s11661-002-0378-9>.
- [24] Yang HS, Jang JH, Bhadeshia HKDH, Suh DW. Critical assessment: Martensite-start temperature for the $\gamma \rightarrow \epsilon$ transformation. *Calphad Comput Coupling Phase Diagrams Thermochem* 2012;36:16–22.

- <https://doi.org/10.1016/j.calphad.2011.10.008>.
- [25] Yang HS, Bhadeshia HKDH. Austenite grain size and the martensite-start temperature. *Scr Mater* 2009;60:493–5.
<https://doi.org/10.1016/j.scriptamat.2008.11.043>.
- [26] Yen HW, Ooi SW, Eizadjou M, Breen A, Huang CY, Bhadeshia HKDH, et al. Role of stress-assisted martensite in the design of strong ultrafine-grained duplex steels. *Acta Mater* 2015;82:100–14. <https://doi.org/10.1016/j.actamat.2014.09.017>.
- [27] Lee SJ, Shin SE, Ushioda K, Fujii H. Microstructure, mechanical properties, and damping capacity in stir zone after friction stir welding of Fe–17Mn damping alloy. *J Alloys Compd* 2019;803:1155–67. <https://doi.org/10.1016/j.jallcom.2019.06.367>.
- [28] Eshraghi M, Tschopp MA, Asle Zaeem M, Felicelli SD. Effect of resistance spot welding parameters on weld pool properties in a DP600 dual-phase steel: A parametric study using thermomechanically-coupled finite element analysis. *Mater Des* 2014;56:387–97. <https://doi.org/10.1016/j.matdes.2013.11.026>.
- [29] Caillard D. Dynamic strain ageing in iron alloys: The shielding effect of carbon. *Acta Mater* 2016;112:273–84. <https://doi.org/10.1016/j.actamat.2016.04.018>.
- [30] Zha M, Li Y, Mathiesen RH, Bjørge R, Roven HJ. Microstructure evolution and mechanical behavior of a binary Al-7Mg alloy processed by equal-channel angular pressing. *Acta Mater* 2015;84:42–54. <https://doi.org/10.1016/j.actamat.2014.10.025>.
- [31] Zha M, Li Y, Mathiesen RH, Bjørge R, Roven HJ. High ductility bulk nanostructured Al-Mg binary alloy processed by equal channel angular pressing and inter-pass annealing. *Scr Mater* 2015;105:22–5.
<https://doi.org/10.1016/j.scriptamat.2015.04.018>.
- [32] Sun YF, Fujii H, Takaki N, Okitsu Y. Microstructure and mechanical properties of

dissimilar Al alloy/steel joints prepared by a flat spot friction stir welding technique.

Mater Des 2013;47:350–7. <https://doi.org/10.1016/j.matdes.2012.12.007>.

- [33] Yamagishi H. High-productivity and high-strength Fe/Al dissimilar metal joining by spot forge welding. *Mater Lett* 2020;278:128412.

<https://doi.org/10.1016/j.matlet.2020.128412>.

- [34] Papadimitriou I, Efthymiadis P, Kotadia HR, Sohn IR, Sridhar S. Joining TWIP to TWIP and TWIP to aluminium: A comparative study between joining processes, joint properties and mechanical performance. *J Manuf Process* 2017;30:195–207.

<https://doi.org/10.1016/j.jmapro.2017.09.012>.

Chapter 3 Microstructural and interface geometrical influence on the mechanical fatigue property of Al/UHSS lap joints using REW

3.1 Introduction

One of the challenges for welding processes, a significant challenge arises when the Al and Fe are directly welded, the difficulty of suppressing interfacial behaviors including intermetallic compounds (IMCs) layer generated at the joining interface still exists because of an inconsistency of inherent material properties[1–4]. In particular, these IMCs have a potential causing the additional defects like voids, diffusions, etc., which are a dominant factor determining the fracture mode and mechanical property[5]. Nevertheless, very few studies have been reported, not only focusing on lap shear strength but also emphasizing the improvement of fatigue life in Al/Fe joining. The fatigue research has been one of the main topics of metallic materials, and in fact, fatigue failure constitutes a significant portion of structural failures. Among them, there have been reports of fatigue tests on some Al/Fe lap joints, the previous study[6] examined on the fatigue life assessment of Al/Fe resistance spot welds, which mainly focused on that the fatigue life of RSWed Al/Fe was evaluating the fatigue life by applying tensile-shear fatigue and coach peel-type fatigue test methods. Although many advanced Al/Fe bonding studies have been actively conducted[7], fatigue endurance for Al/Fe lap joints through ultrasonic spot welding still remains limited to 104 cycles at 3,000 N and 106 cycles at 1,000 N. The fatigue performance of Al-Fe lap joints is well known to rely on the microstructure integrity of the joint interface. While there has been significant progress in Al/Fe joining worldwide, the reports of fatigue tests conducted on Al/Fe lap assemblies are remarkably insufficient in overall research works.

In the previous study[8], resistance element welding (REW) was introduced as a new alternative, however, the relationship between microstructure integrity and fatigue life has not yet been studied in detail.

In chapter 3, the present work aims to implement high strength and improved fatigue properties in the Al/Fe (about 1 GPa class) assembly joint with suppressing the welding defects while maintaining the RSW process. In here, the optimal welding current is determined through an assessment of static tensile-shear strength and the calculation of the minimum spot diameter recommended by the American Welding Society (AWS, D8.9M). Furthermore, Al/Fe joints, welded through the resistance element welding (REW) process, undergo fatigue testing up to 80% of the tensile-shear loads with a load ratio of 0.1. The fatigue fracture mode for each welding condition was analyzed using a field-emission scanning electron microscope (FESEM). Additionally, a three-dimensional finite element (FE) computational model was established to conduct a numerical investigation into the mechanism of the fatigue fracture mode.

3.2 Experimental procedures

The aluminum alloy, AA5052 and automotive steel plate, SPFC980 were introduced as a base material, and S20C was employed as a spot element. Chemical compositions of selected materials are shown in Table 1. A schematic sketch of AA5052 and SPFC980 lap joint assembly with REW was given in Fig. 3-1. In order to implement the lap joining between the AA5052 and SPFC980, the S20C spot element was riveted on the AA5052 (see Fig. 3-1(a1)). Then, the S20C element can directly resistance spot weld with the SPFC980. The S20C riveted AA5052 is assembled in the shape as shown in Fig. 3-1(a2). Then, the S20C riveted AA5052-SPFC980 plate were resistance element

welded by an AC power supply spot welding machine as displayed in Fig. 3-1(a3). The process conditions were fixed at 2.45 kN and 200 ms for a pressing force and current time, respectively, and the currents were 3.5 kA, 4.5 kA, 10.5 kA and 12 kA. Namely, a resistance element welding (REW) can be thought of as the RSW process in which spot elements are necessarily involved. The REWed AA5052/SPFC980 joint finally completed, the geometrical information was given in Fig. 3-1(a4). Fig. 3-1(b) exhibits cross-sectional images of the REWed AA5052/SPFC980 joint geometry.

In order to evaluate a mechanical property, a universal testing machine (UTM, MTDI/UT100F) was introduced. The fatigue tests were performed by a fatigue test machine (MTS Landmark™ Servohydraulic Test System, MTS Model 370.10 Load Frame) according to the procedure in Figs. 3-1(c-d). To avoid potential bending of the test specimens, the fatigue tests were conducted at $R = 0.1$ and a 40 Hz sinusoidal wave frequency, as specified in ASTM E466. The stress ratio (R) is defined as follows:

$$R = \sigma_{\max}/\sigma_{\min} \quad (1)$$

where σ_{\max} is the desired maximum stress and σ_{\min} is the desired minimum stress. Here, a S_y is defined tensile-shear strength. The stresses were applied in the range of $0.2S_y$ to $0.8S_y$, a value less than the tensile-shear strength (S_y), and high-cycle fatigue tests were performed. It is defined as an intensity of 20% of S_y and 80% of S_y . This study tested three specimens under one condition to obtain an approximate range and fatigue life trend.

Microstructures of the joint was investigated on cross-sections perpendicular to the welding direction using optical microscopy (OM; GX51, OLYMPUS) and electron

backscattered diffraction (EBSD). For EBSD analysis, the analysis points with a confidence index (CI) ≤ 0.1 were indicated as black regions. Specimens for optical microscopy were polished and then etched with 3% Nital solution. In order to investigate the EBSD of Al/Fe joint interfaces, cross-sections were machined by electro-chemical polishing with Nitric acid 30% and Methanol 70% by 9V for 30s at -20 °C.

Table. 3-1 Chemical compositions of materials.

	Elements (wt%)							
	Al	Cu	Mg	Mn	Fe	C	Si	P
AA5052	Bal	0.029	2.392	0.027	0.40	-	0.25	-
SPFC980	-	-	-	2.192	Bal.	0.109	0.942	0.014
S20C	-	-	-	0.47	Bal.	0.20	0.20	0.012

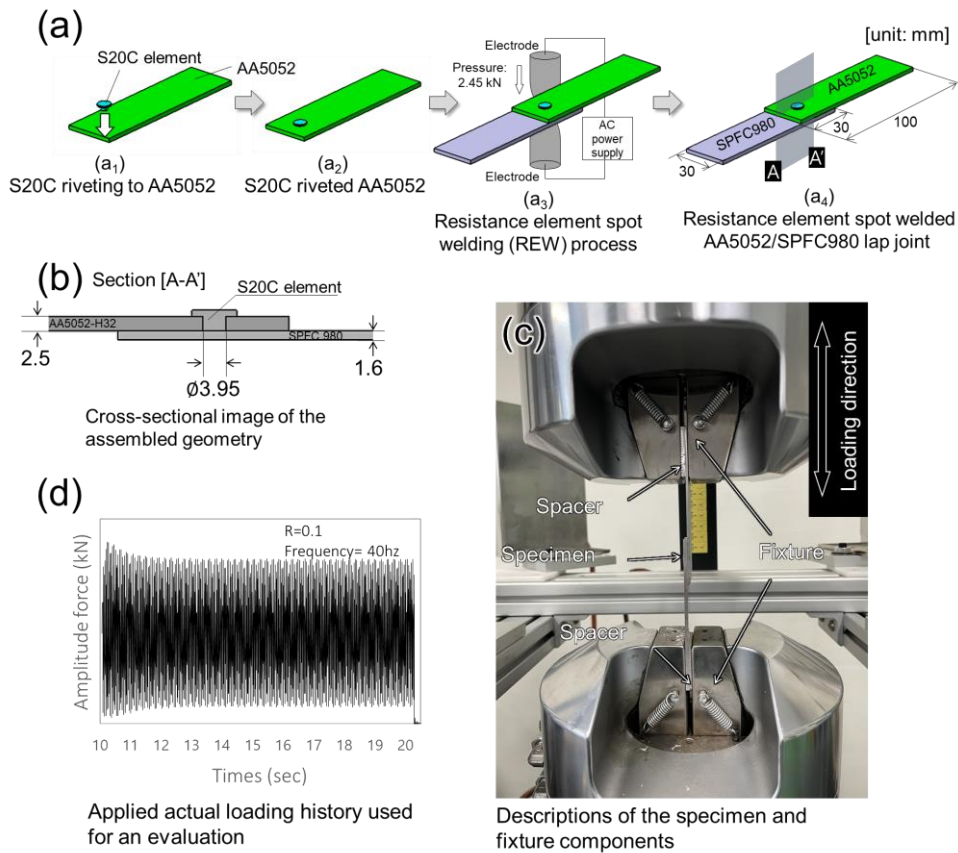


Fig. 3-1 Descriptions for resistance element welding (REW) process of S20C pre-ripping AA5052/SPFC980 steel lap joints and fatigue tests.

3.3 Results

3.3.1 Welding morphologies

Fig. 3-2(a) represents a schematic illustration of an investigation area and welding formation mechanism by REW process in detail. Inside the copper electrode, it is cooled by the water cooling circulation system, the heat and electrical current flow like the grey dot arrows and yellow arrows in the figure, and a welding nugget is formed by the resistance heat generated at this time. Actual cross-sectional images formed according to the various welding conditions are shown in Figs. 3-2(b-e). Fig. 3-2(b) exhibits OM images of the joint cross section by 3.5 kA condition, the S20C pre riveting structure

shows a bonded structure without deformations. The non-bonded gap was observed in the nugget zone with an insufficient resistance heat input. In Fig. 3-2(c), the joint structure was not severely deformed, and the bonding interface line was clearly observed with a quenching structure. In the REW conditions of 3.5kA and 4.5kA, no significant deformations were observed in the cross section images, but it is characterized by insufficient penetrations. When the input welding current reached 10.5kA, the S20C was remarkably plastically deformed, and an extruded shape was observed into AA5052 (see Fig. 3-2(d)). In the process of deformations, the materials were in perfectly contact between the Al and Fe, and the heat affected zone (HAZ) was clearly formed on Al by thermal conduction. In Fig. 3-2(e), significant defects such as a separation between the undercut and S20C-AA5052 were observed in the welded structure with a current of 12kA. The microstructure developments and HAZ formation mechanisms are further discussed in the next section in detail.

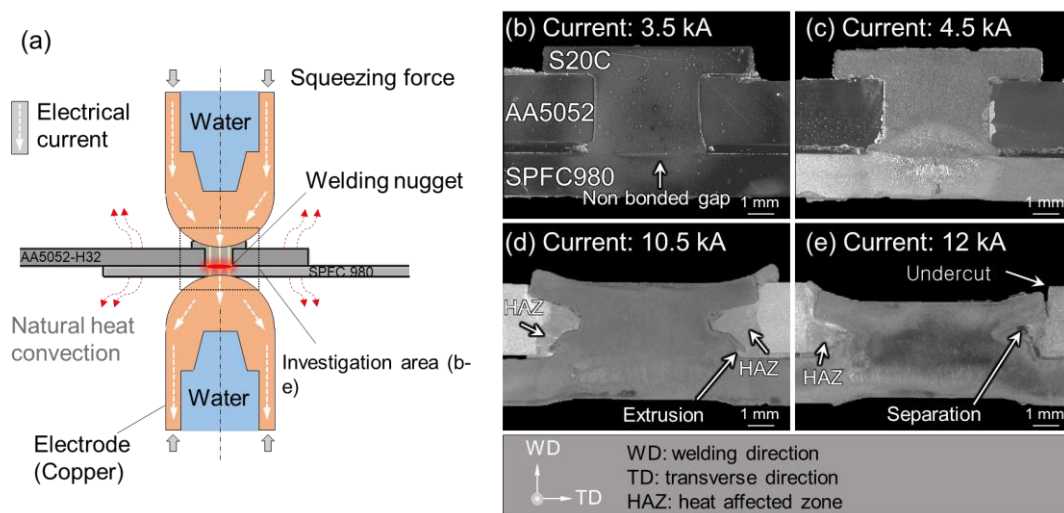


Fig. 3-2 (a) A schematic illustration of an investigation area and welding formation mechanism by REW process, and (b-e) cross-sectional morphologies of the resistance element welded AA5052/SPFC980 steel lap joints.

3.3.2 Microstructure investigations

3.3.2.1 Initial state of base materials

Fig. 3-3 depicts an initial state of base materials, SPFC980 was a low-carbon steel containing α -phase (alpha, B.C.C: body centered cubic structure) with equiaxed grains of $6.88 \mu\text{m} \pm 4.25 \mu\text{m}$. In the inverse pole figure (IPF) map, orientations were randomly distributed (see Fig. 3-3(a)). The grains of S20C are equiaxed grains, and the most of them are $19.1 \mu\text{m} \pm 8.08 \mu\text{m}$ grains mixed with ferrite and pearlite as displayed in Fig. 3-3(b). The phase of S20C also was B.C.C structure without any ϵ (epsilon, H.C.P: hexagonal closed packed structure) and γ (gamma, F.C.C: face centered cubic structure) phase. The grain size of AA5052 was $23.9 \mu\text{m} \pm 6.16 \mu\text{m}$, and orientations were randomly distributed as shown in Fig. 3-3(c). Consequently, most of the initial materials consisted of single phase, and the orientations were randomly distributed.

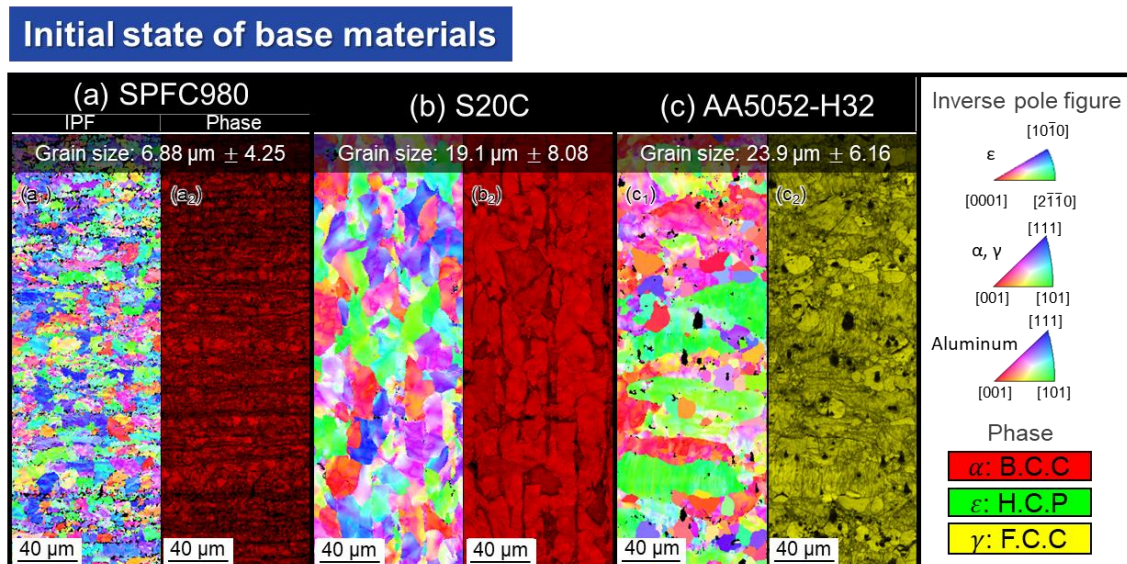


Fig. 3-3 EBSD analysis results for initial state of base materials. (a) SPFC980 steel, (b) S20C steel and (c) AA5052-H32. EBSD: electron backscattered diffraction; IPF: inverse pole figure.

3.3.2.2 Welding interfaces

A welding current of REW alters the microstructure of the AA5052/SPFC980 lap joint. Welding morphologies can be divided into two groups: the conditions of 3.5 kA and 4.5 kA, and the conditions of 10.5 kA and 12 kA from the OM images of Fig. 3-2. Since the 3.5 kA condition barely melted, the microstructure can be considered to be similar to that of the initial base metal. Therefore, here we take a closer look at the condition of 4.5 kA, and the microstructure of 10.5 kA, which had the highest tensile-shear strength. Fig. 3-4 presents the EBSD analysis results of welding interface microstructures after REW process by 4.5 kA current condition, the microstructure of the welding interface was developed into random grain orientations in the IPF map (see Fig. 3-4(a)). The thick white line means prior austenite grain boundary (PAGB, $20^\circ \leq \theta \leq 50^\circ$), PAGBs is an austenite grain boundary at high temperature, and a ferrite phase transformation occurs from this grain boundary during cooling processes. PAGBs were highlighted in inverse pole figure map by misorientation angle ranging from 20 to 50° with reference to results of Lee et al. (2019)[9]. In Fig. 3-4(b), most of the phase of the welding interface welded under the 4.5 kA condition were occupied by α' -phase (B.C.C: body centered cubic structure). The KAM value was overall $2.48^\circ \pm 0.84^\circ$ as shown in Fig. 3-4(c).

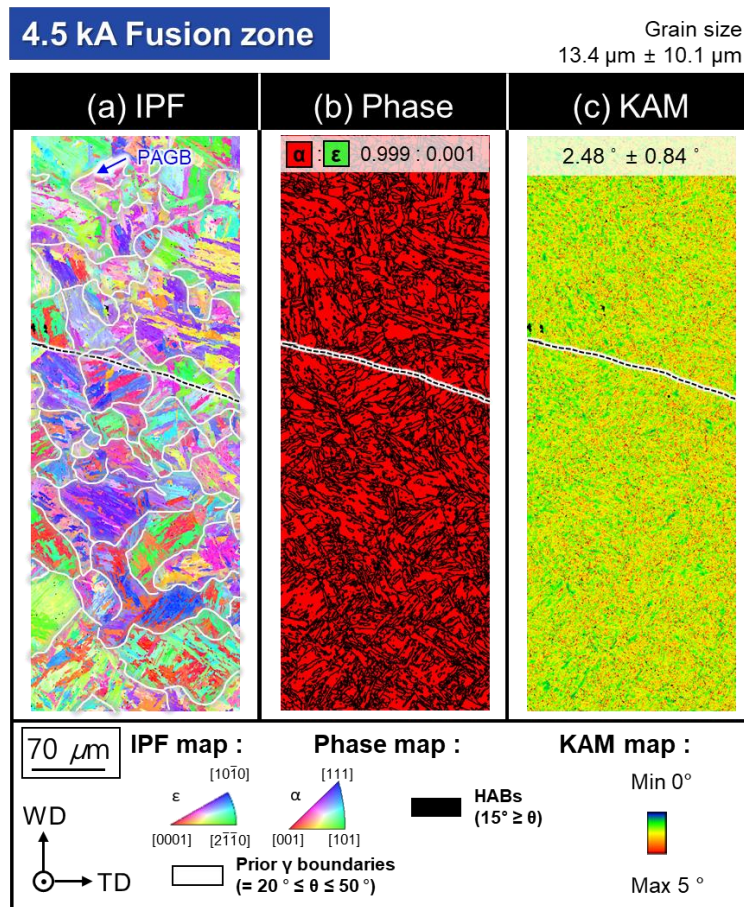


Fig. 3-4 EBSD analysis results for welding interface between S20C and SPFC980 steel welded by 4.5 kA. (a) IPF map, (b) phase map and (c) KAM map. IPF: inverse pole figure; KAM: kernel average misorientation; PAGB: prior austenite grain boundary; HAB: high angle boundary.

Fig. 3-5 exhibits EBSD analysis results of the welding interface between S20C and SPFC980 steel welded by 10.5 kA. In Fig. 3-5(a), the grain orientation was randomly distributed in IPF map, most of the phase is occupied by α' -phase. The size of PAGBs was larger than the condition of 4.5 kA. The ϵ (epsilon, H.C.P: hexagonal closed packed structure) was also formed (Fig. 3-5(b)). In the welded interface with the current of 10.5 kA, $\alpha \rightarrow \epsilon$ phase transformation was partially observed with the development of an acicular structure. Therefore, the microstructure was developed as a composite phase in which the ϵ phase (3%) was mixed with the base of α' phase. The KAM value was overall

1.99° ± 1.09° as shown in Fig. 3-5(c). As the welding current increased, the KAM value was decreased overall, but very high KAM distribution characteristics appeared near the portion where the ε phase was formed. This is due to the mechanical strain caused by the essentially different microstructures of α' phase and ε phase.

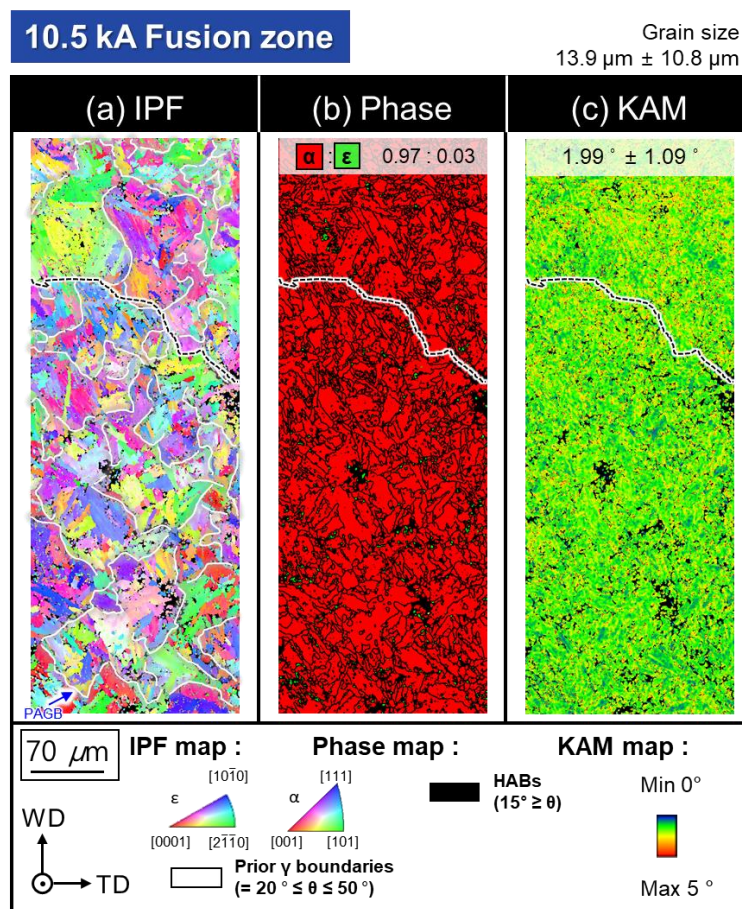


Fig. 3-5 EBSD analysis results for welding interface between S20C and SPFC980 steel welded by 10.5 kA. (a) IPF map, (b) phase map and (c) KAM map.

3.3.2.3 Heat affected zone of AA5052

Microstructures of AA5052 were significantly changed compared to the initial state because the heat affected zone (HAZ) was formed in different by welding heat inputs. Fig. 3-6 (a-c) exhibits EBSD-GOS (grain orientation spread) maps of the heat

affected zone of AA5052. Here, a grain with a grain boundary of less than 2° was defined as a grain with complete recrystallization (grey color), and the grain with the grain boundary exceeding 2° was defined as the grain without complete recrystallization (white color). In the initial state, the recrystallized grain fraction was about 24.3%. The grains of HAZ of AA5052 joined with the welding current of 4.5 kA were dominated by pressing forces rather than heat, and most of them were grains that were not recrystallized due to the formation of low angle boundaries (LABs) as displayed in Fig. 3-6(b). On the other hand, when the welding current is increased to 10.5 kA, the grain size was significantly increased, and the fraction of the recrystallized grain was also increased to 67% as shown in Fig. 3-6(c). The fraction of the recrystallized grain and change of the grain size were plotted in Fig. 3-6(d, e), respectively.

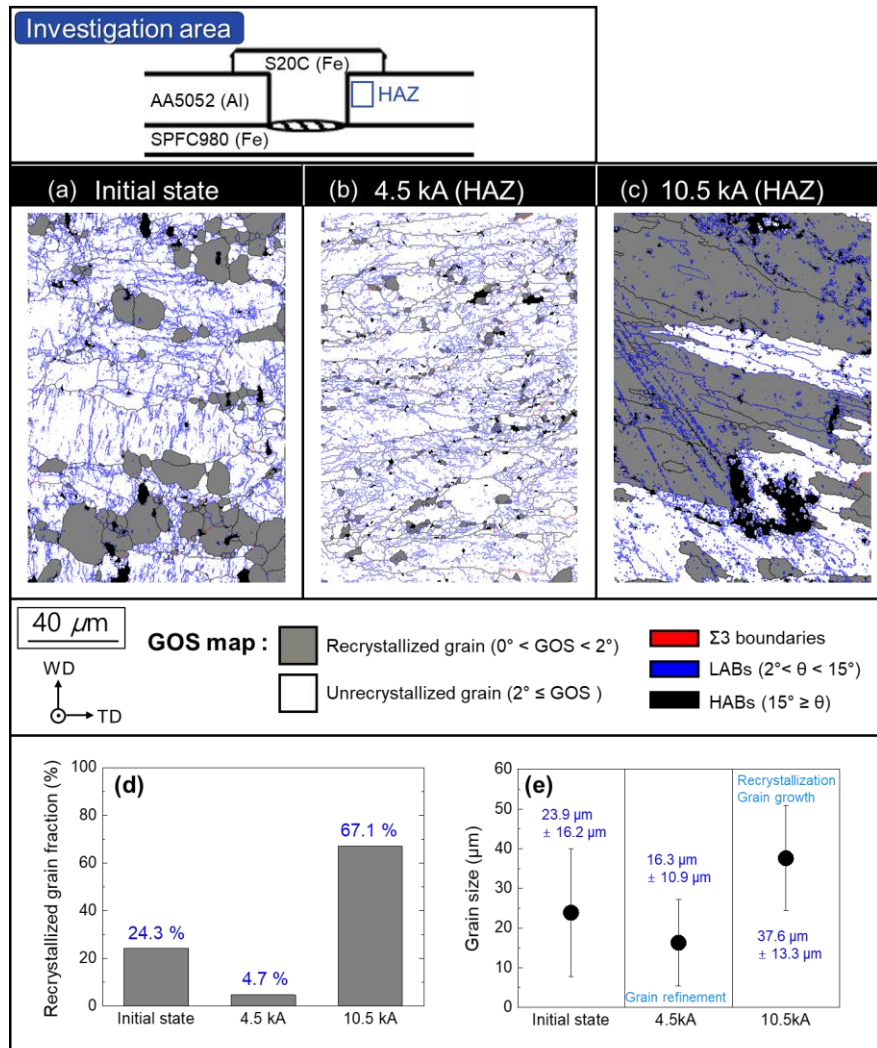


Fig. 3-6 EBSD-GOS maps of heat affected zone of AA5052. (a) Initial state of base material, (b) 4.5 kA and (c) 10.5 kA and (d) fraction of recrystallized grain, (e) change of grain size. GOS: grain orientation spread; LAB: low angle boundary; HAB: high angle boundary.

3.3.3 Mechanical behaviors

3.3.3.1 Tensile-shear tests

In order to determine the fatigue load, we performed a tensile-shear test. Fig. 3-7(a) depicts the tensile shear load-displacement curves depend on the resistance element welding current conditions of the AA5052/SPFC980 lap joint. The tensile-shear

peak loads were gradually increased as the input current increases. In the 3.5kA condition, the peak load was about 6000 N. In the 4.5kA welding current condition, the peak load was about 7500 N with further increased the displacement. When the welding current reached 10.5kA, the tensile shear load exceeding 9000 N, and the displacements were observed to be more than 5 mm. These results significantly surpass the previous reported strength of the Al/Fe assembly joints. Finally, when the welding current was increased to 12 kA, the strength no longer increased, and had a tendency to decrease to less than 8500 N. The strength obtained in the tensile-shear tests is applied as an applied load in the fatigue test. Fig. 3-7(b) presents the failure energies, which are the energy consumed until fractures. The tendency of the failure energy appeared in proportion to the tensile-shear test results. Welding currents of 3.5kA and 4.5kA, both cases caused interfacial fractures with relatively low failure energies. However, relative high welding currents (10.5 kA and 12 kA) occurred AA5052 base material fractures with dimples. This result was also confirmed by the results of the previous study[10]. Fig. 3-7(c) displays the correlation minimum spot diameters based on American Welding Society (AWS, D8.9M; Test Methods for Evaluating the Resistance Spot Welding Behavior of Automotive Sheet Steel Materials) and actual measurements for the fracture mode investigation. To ensure the fracture modes are base material fracture or interfacial fracture, AWS recommended a minimum size of the spot weld for a given sheet thickness as follow:

$$d_{\text{spot}} = 4\sqrt{t} \quad (2)$$

where d is the weld nugget diameter and t is the sheet thickness. However, this is valid

for the steel RSWs where higher tensile strength is usually seen for the weld nugget. This equation might not be suitable for the aluminum/steel REWs especially for the hybrid assembled structures as the weld nugget usually has the weakest strength. Therefore, the d_{spot} was derived by applying both the AA5052 standard (red line) and the SPFC980 standard (blue line) for thickness, and welding conditions that could the base material fracture were selected in Fig. 3-7(c). When the SPFC980 base material thickness was applied, interfacial fracture may occur below the welding current condition of 4.5 kA. In the case of AA5052 based calculated d_{spot} , which was a more conservative condition, interfacial fracture may occur in samples welded below the welding current condition of 10.5 kA. Whether the calculated AWS recommended spot diameter is also related to the failure mode of fatigue life is further discussed in the next section.

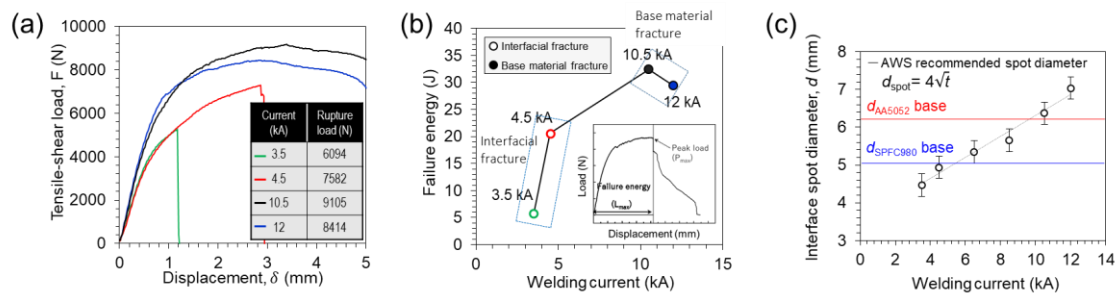


Fig. 3-7 Results of tensile-shear tests (a) and its failure energies (b) and (c) correlation minimum spot diameters based on AWS and actual measurements for the fracture mode investigation. AWS: American Welding Society.

3.3.3.2 Fatigue endurance

Fatigue loads were applied up to 80% of the tensile-shear strength (S_y), which is shown in Table 2. Fig. 3-8 exhibits fatigue endurance diagrams and its failure modes.

The vertical axis of the graph is load amplitude, and the horizontal axis is cycle to fatigue failure. Three specimens per condition were used for the fatigue test, and the amplitude load was applied from 80% to 20% of the tensile-shear peak load. Whereas number of cycles to failure for all cases was almost the same at the lowest load level, the 10.5 kA and 12 kA joints had higher fatigue life up to an order of magnitude higher than that of the 3.5 kA and 4.5 kA joints at increased load levels. In the case of 3.5 kA, when 80% of the peak load (about 4,600 N) were applied, the fracture occurred at bonding interfaces in only 418 cycles as shown in Fig. 3-8(a). It is obviously low cycle fatigue below 10^3 cycles. The specimen bonded with 3.5kA was fractured at the bonding interface when it reached 410,414 cycles with the amplitude load of about 1,000N was applied (see Fig. 3-8(b)). Therefore, insufficient penetration was the dominant factor causing the joint interfacial failure. In Fig. 3-8(c), the specimens joined at 4.5 kA withstand more cyclic loads at higher loads than the 3.5 kA condition, but showed similar failure patterns when the 80% of peak load amplitude was applied. However, when a load amplitude of less than 2,000N was applied, the base metal fracture occurred in 738,946 cycles in the SPFC980 steel side (Fig. 3-8(d)).

Table. 3-2 Applied fatigue loads. (S_y : tensile-shear strength)

	12 kA	10 kA	4.5 kA	3.5 kA
80% S_y (N)	6410	7032	6012	4602
70% S_y (N)	5609	6153	5261	4027
50% S_y (N)	4006	4395	3758	2876
40% S_y (N)	3205	3516	3006	2301
30% S_y (N)	2404	2637	2255	1726
20% S_y (N)	1602	1758	1503	1150

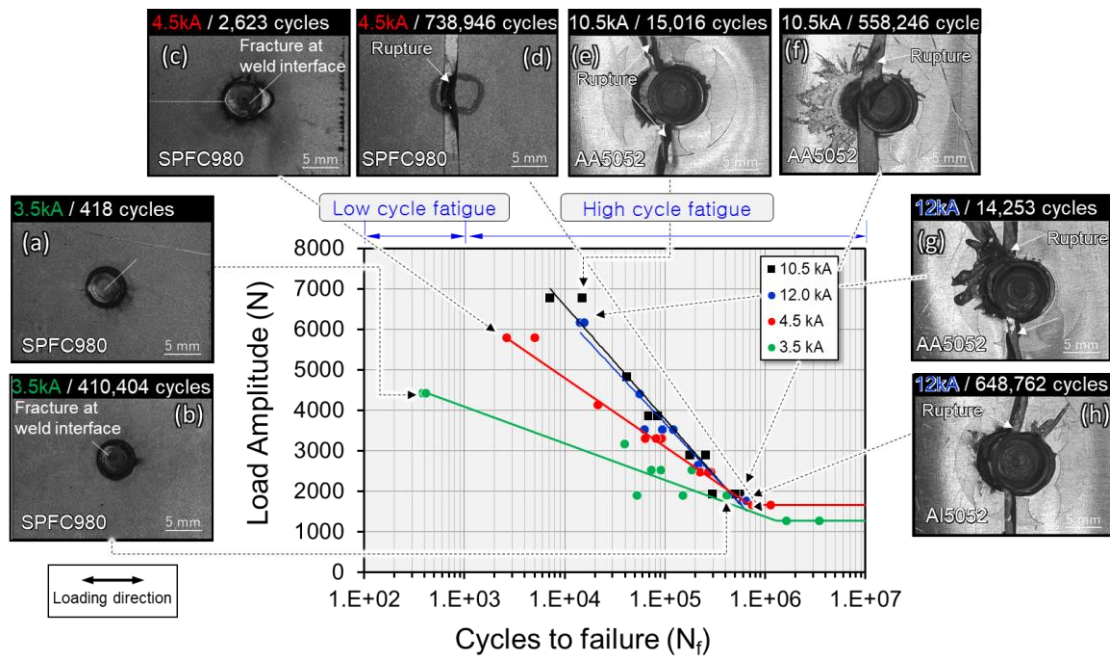


Fig. 3-8 Fatigue endurance diagrams and its failure modes in the macroscale.

The specimens bonded at 10 kA and 12 kA show almost similar gradients of the fatigue curve. However, the condition of 10.5 kA withstand about 7,032N up to 15,016 cycles, the fracture caused at Al base material as displayed in Fig. 3-8(e). Even with an applied load of 2,000N, the Al base material fracture occurred at 558,246 cycles (see Fig. 3-8(f)). In the case of 12 kA condition, when the amplitude load of about 6,000N was applied, the base metal fracture occurred in 14,253 cycles. Compared to the condition of 10.5 kA, about 1,000N shows a fatigue life as low as 1,000 cycles at low applied load (see Fig. 3-8(g)). Fig. 3-8(h) presents the fracture image assembled under the condition of 12kA. When applied at 2,000N, it fractured at 648,762 cycles. Consequently, in the case of 3.5kA and 4.5kA were interfacial fractures at the low amplitude load and high amplitude load. The welding condition of 10.5 kA and 12 kA, regardless of the amplitude loading and fatigue cycle, successfully induced an Al base material fracture due to the

exceptional bonding implementation. To seek the origin of the fracture mode mechanism, 3D finite element analysis will be investigated further in the discussion section.

3.3.4 Fractography

Fatigue characteristics also can be divided into two groups, one group for 3.5kA and 4.5kA and the other group for 10.5kA and 12kA, based on fracture characteristics and fatigue performances. Fig. 3-9 represents FESEM images for fracture surfaces of Al/Fe welded with 3.5kA which fractured at 418 cycles by 4,500 N of amplitude loading. In Fig. 3-9(a), it is clearly seen that the fatigue fracture was apparently occurred at the welding interface between SPFC980 and S20C based on an energy dispersive X-ray spectroscopy (EDS) point analysis. In addition, the central non-bonded area and the HAZ area near the bonding area were observed. Fig. 3-9(b) depicts the high magnification view of (a), bonding area with dimples and non-bonding areas were significantly distinguished. Fig. 3-9(c) displays further high magnification image for Fig. 3-9(b), the dimple of about 3 μm was clearly observed on the fracture surface, which is morphologically similar to the ductile fracture caused by typical static strength testing. On the other hand, about 2,000 N of amplitude loading applied specimens were fractured at the welding interface and some part of S20C at 410,404 cycles as displayed in Fig. 3-10(a). As the result of EDS analysis, Fe element was dominant on the failure area. When the fracture surface is further enlarged, the dimple shape was not found as shown in Fig. 3-10(b). Fatigue striations were observed on the fracture surface where the S20C was fractured. This form is typical of fatigue failure (see Fig. 3-10(c)). The test specimen bonded at 4.5kA had a low-cycle fatigue fracture surface similar to that of the test specimen bonded under the 3.5kA condition (see SFig. 3-1). On the other hand, the

fractured surface of the specimen bonded under the 4.5kA condition after high cycle fatigue induced fracture of the joint interface and the SPFC980 base material (see SFig. 3-2).

3-2.

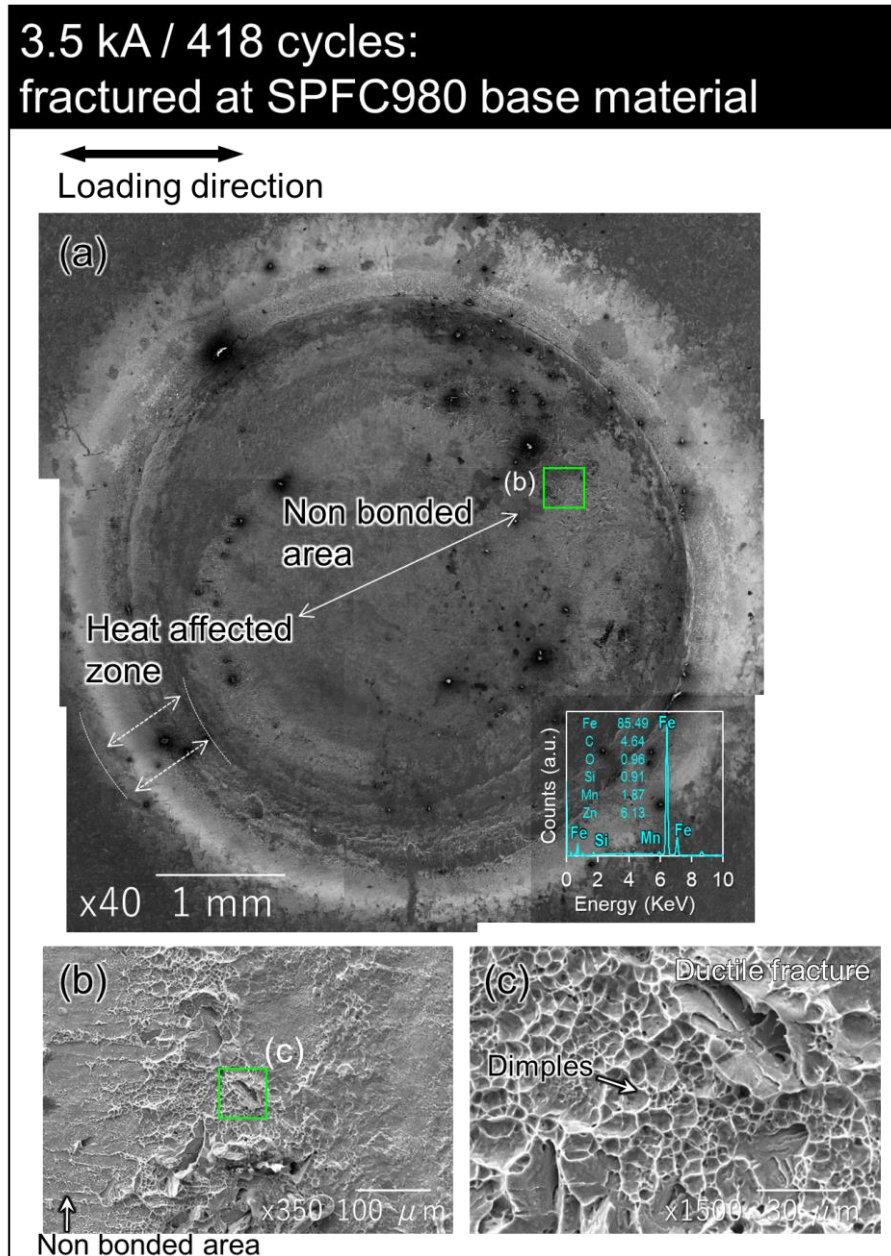


Fig. 3-9 Fracture surfaces of Al/Fe bonded with 3.5kA which fractured at 418 cycles by 4,500N. (a) SEM image of overall fractured surface on SPFC980 side, (b) high magnification view of (a), and (c) further high magnification image of (b).

3.5 kA / 410,404 cycles:
fractured at SPFC980 base material

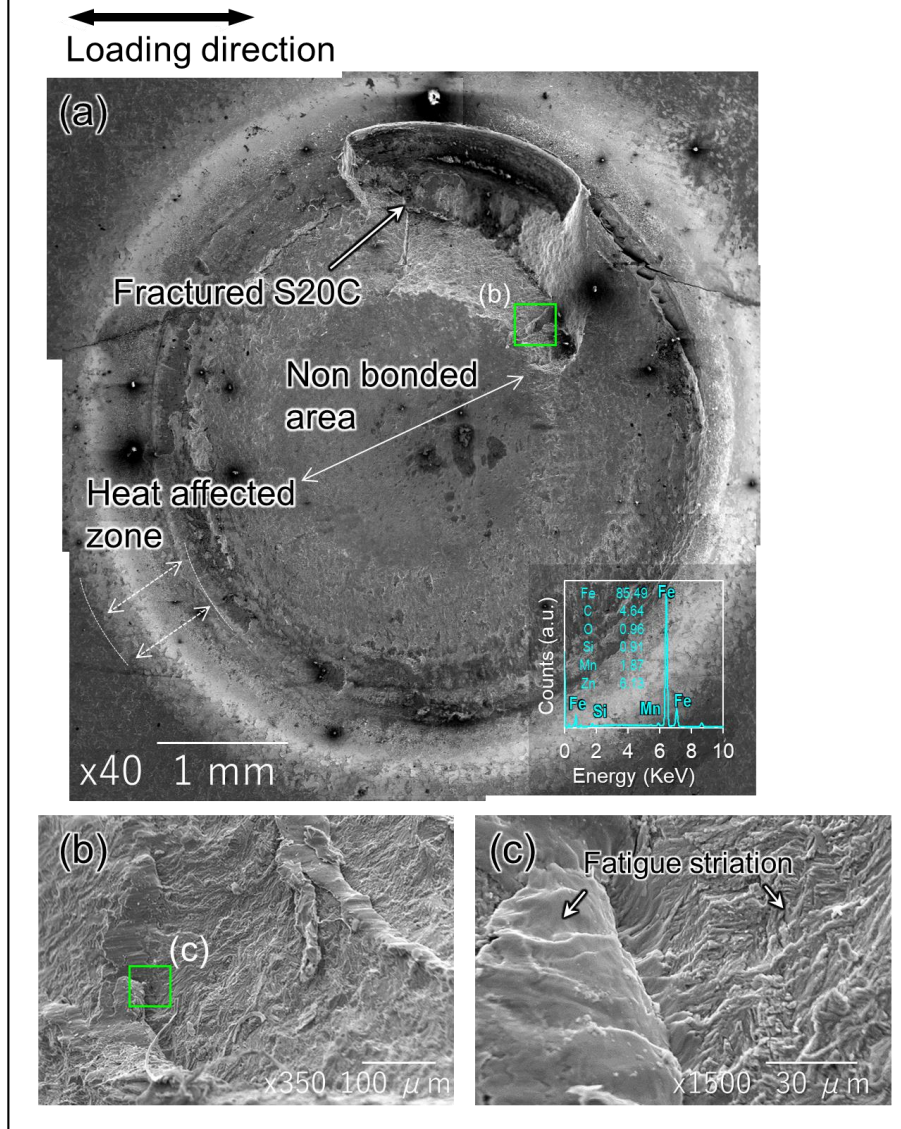
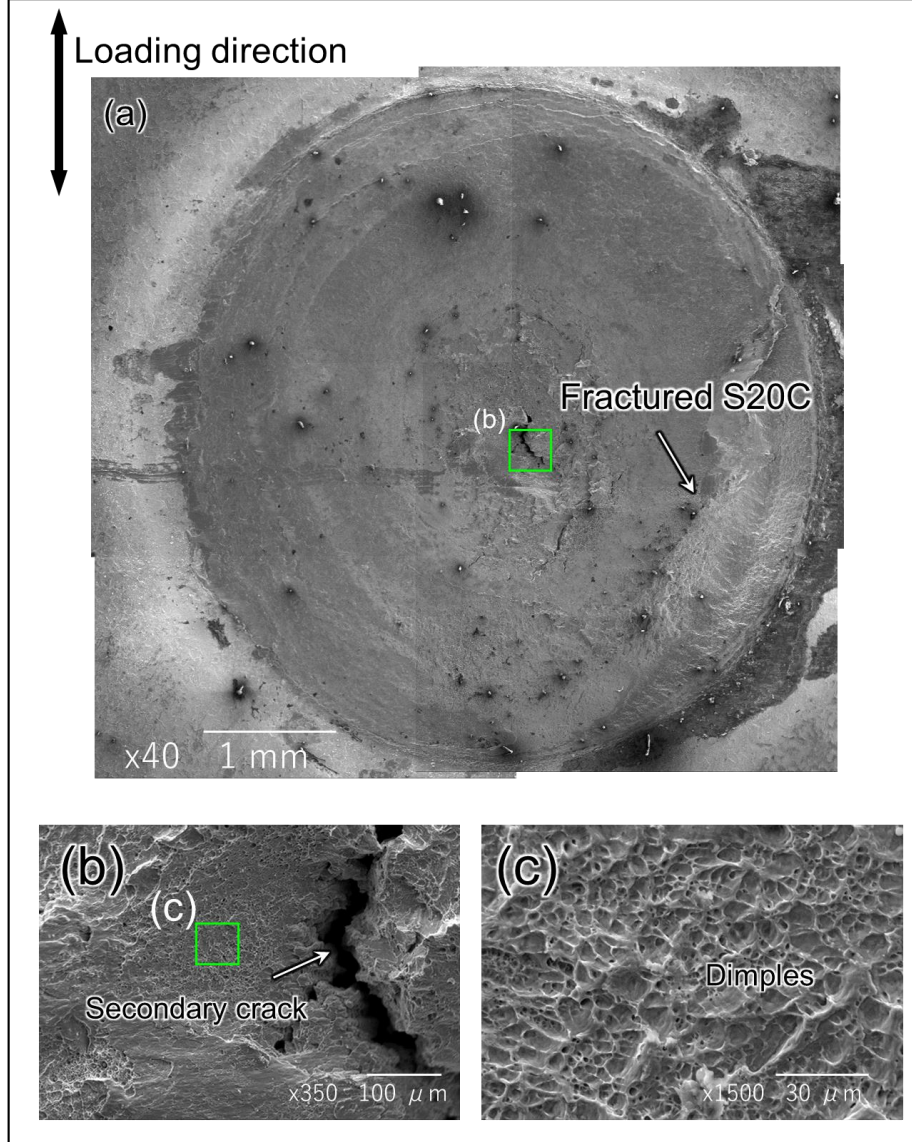
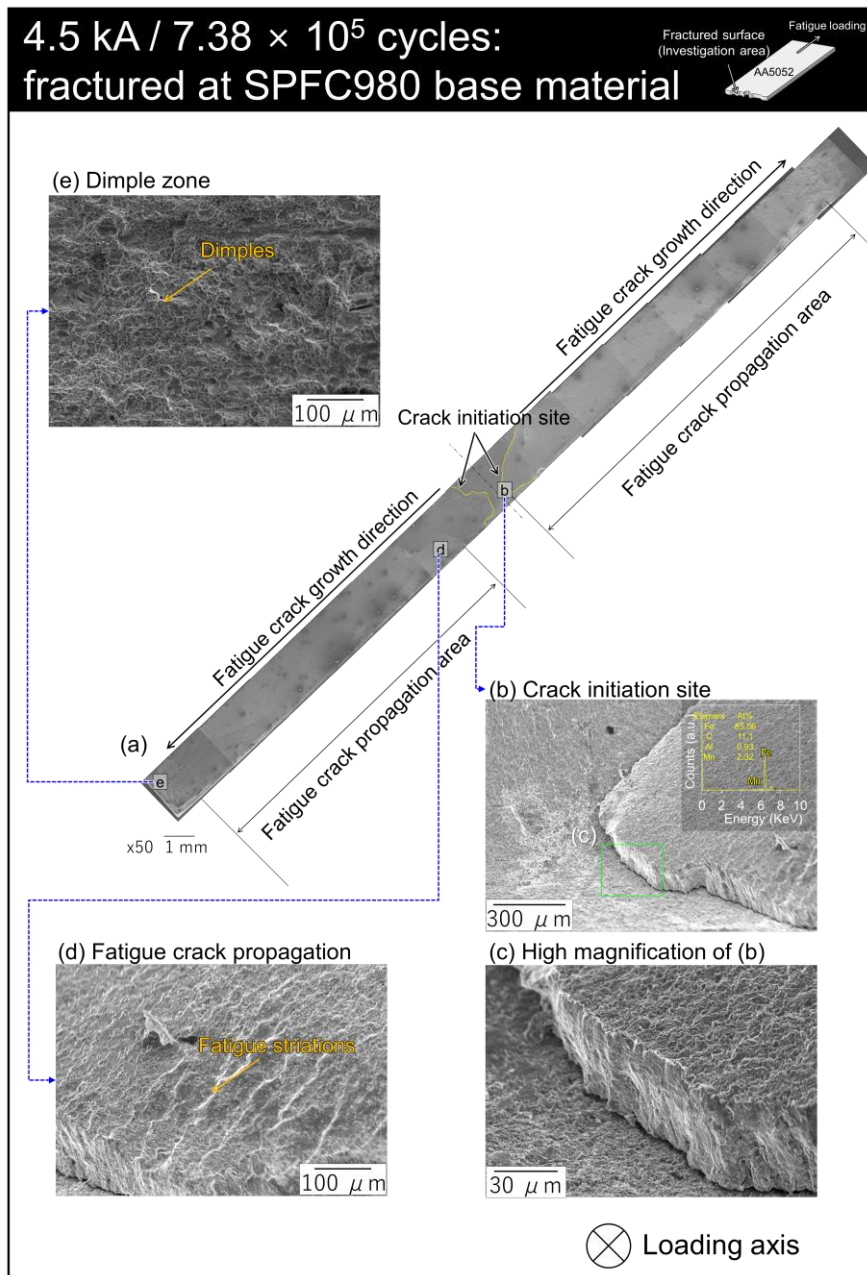


Fig. 3-10 Fracture surfaces of Al/Fe bonded with 3.5kA which fractured at 410,418 cycles by about 2,000N. (a) SEM image of overall fractured surface on SPFC980 side, (b) high magnification view of (a), and (c) further high magnification image of (b).

4.5 kA / 2,623 cycles:
fractured at SPFC980 base material



SFig. 3-1 Fracture surfaces of Al/Fe bonded with 4.5kA which fractured at 2,623 cycles by 6,012N. (a) SEM image of overall fractured surface on SPFC980 side, (b) high magnification view of (a), and (c) further high magnification image of (b).



SFig. 3-2 Fatigue fractured surfaces of Al/Fe bonded with 10.5kA which fractured at 7.38×10^5 cycles by about 1,503N. (a) SPFC base material fractured by fatigue loading, (b) high magnification image of the crack initiation area, (c) crack propagation zone and (d) dimple zone by overloading.

Fig. 3-11 depicts the fatigue fractured surfaces of Al/Fe bonded with 10.5kA which fractured at 1.5×10^4 cycles by about 70% of tensile-shear strength. In Fig. 3-11(a), the

fracture surface is clearly divided into area 1 (crack propagation area) and area 2 (dimple area). Fatigue striations were clearly observed in the enlarged image of the crack propagation area that looked like a wave pattern as displayed in Fig. 3-11(b). This clearly means that the crack propagated due to the fatigue loading. In addition, the interval of striation is equal to the crack propagation distance per cycle. Near the point where crack propagation ends, the area where the fatigue striations area transitioned to the dimple area was observed as shown in Fig. 3-11(c). In the enlarged image, streaks were observed within the particles, a typical feature obtained in specimens where non-ferrous metals were fatigue subjected in the air atmosphere, as the previous report[11]. From the area divided into the transition area to the edge of the specimen, a dimple shape, which is characteristic of ductile failure due to overload, was observed (see Fig. 3-11(d)). The load amplitude reduced to 2000N was, the crack propagation area was further expanded, as displayed in Fig. 3-12, and the expanded crack propagation area improved fatigue cycles. As the crack propagation area was remarkably expanded, the dimple area was observed to be very narrow. In the crack initiation area, the Fe element was detected by EDS line scan analysis. The result clearly shows the hook of S20C penetrated into the AA5052 HAZ area (see Fig. 3-12b), this mean that the fatigue cracking initiated from the AA5052 HAZ. The morphological characteristics of the fracture surface showed a tendency similar to that of the specimen subjected to fatigue with 70% tensile shear strength. The specimen bonded with 12kA was generally fatigued with a tendency similar to that of 10.5kA (see SFig. 3-3 and SFig. 3-4. However, according to the bonding conditions, the difference in the area of the crack propagation area was observed. This trend is in good agreement with previous fatigue studies of the riveting structure of Al alloys of the previous work[12].

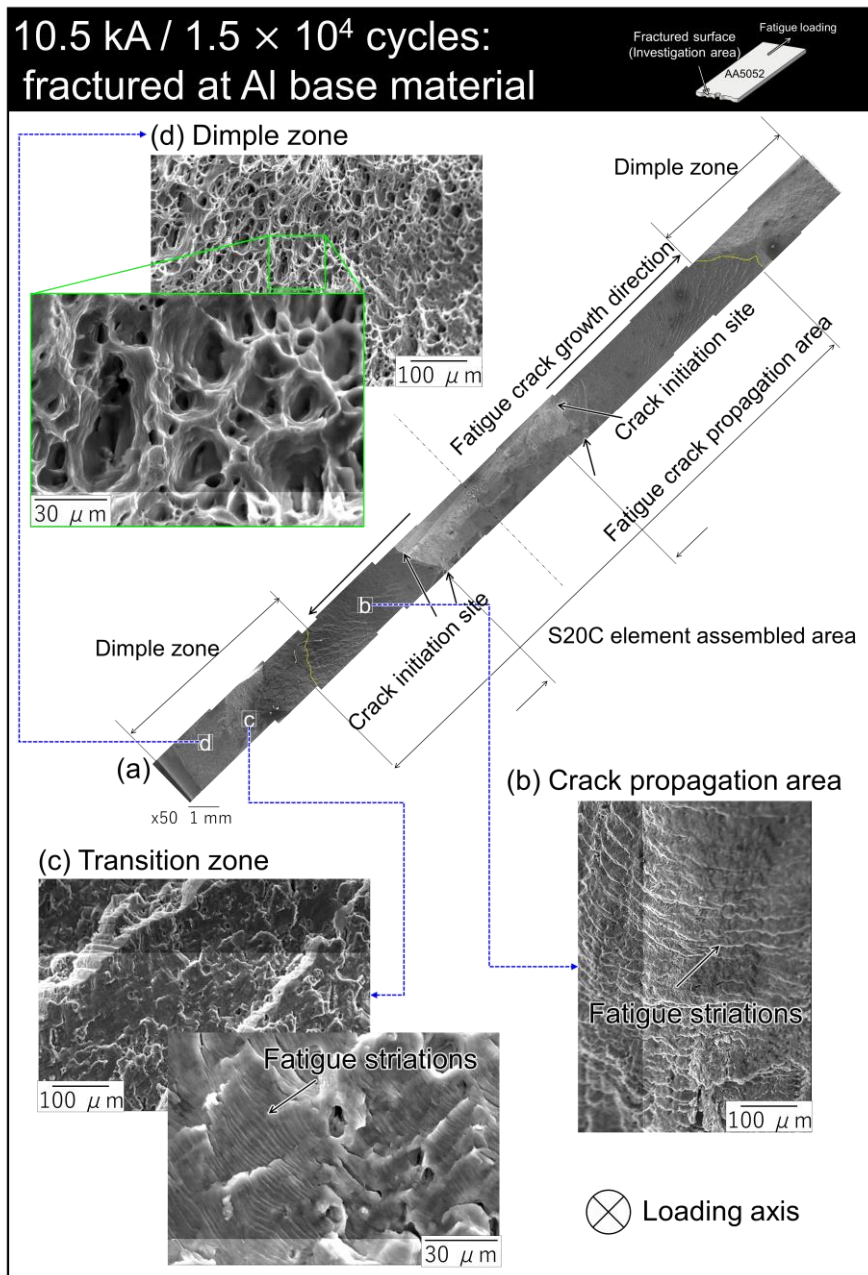


Fig. 3-11 Fatigue fractured surfaces of Al/Fe bonded with 10.5kA which fractured at 1.5×10^4 cycles by about 6,700N. (a) Al base material fractured by fatigue loading, (b) high magnification image of the crack propagation area, (c) transition zone and crack propagation zone, (d) the dimple zone.

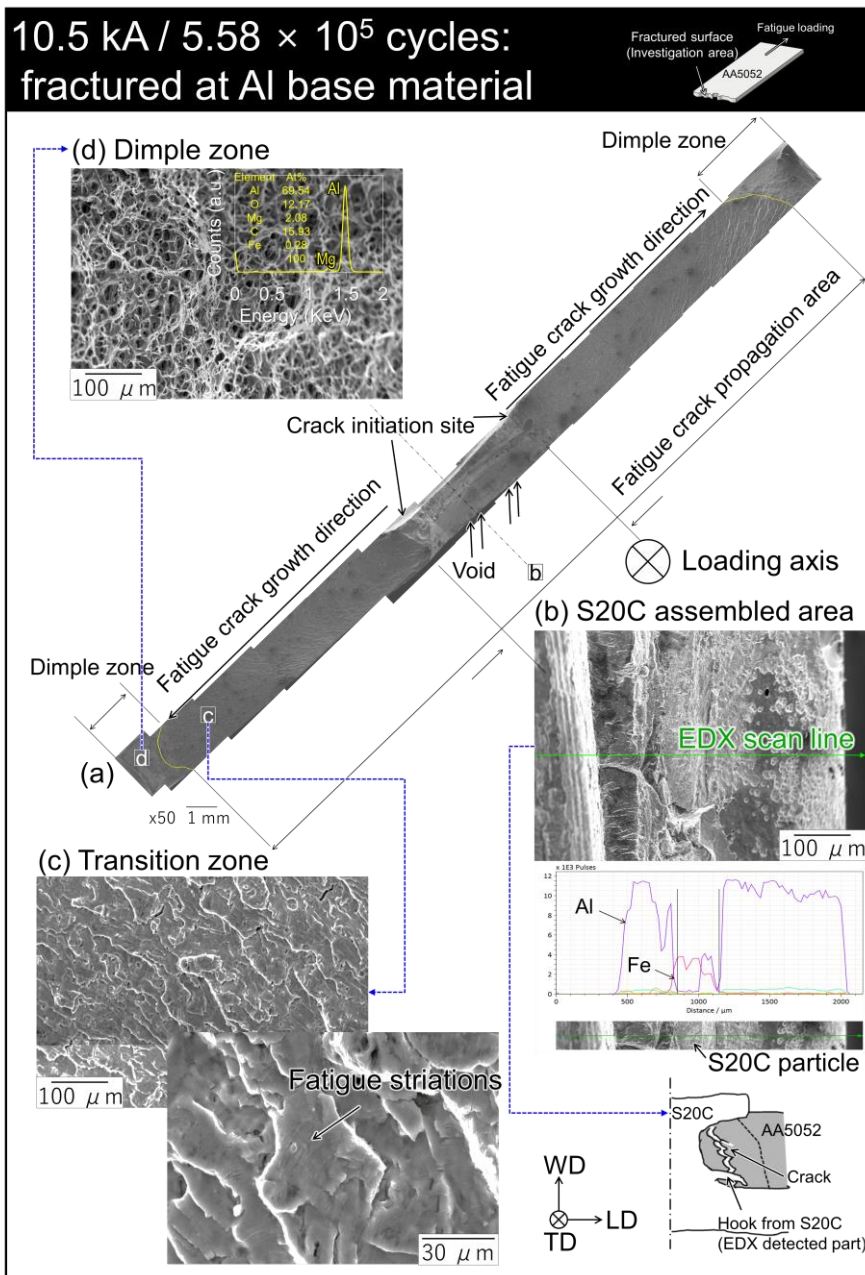
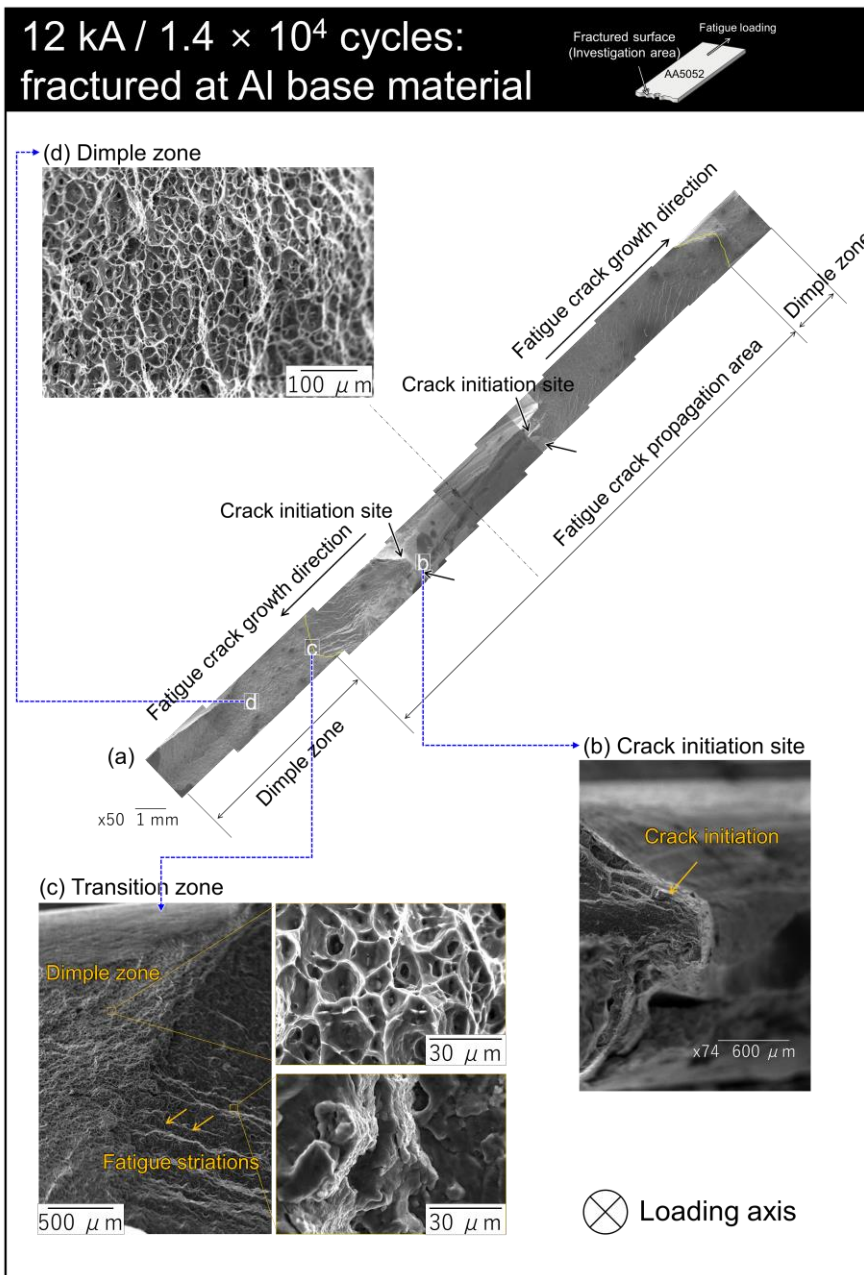
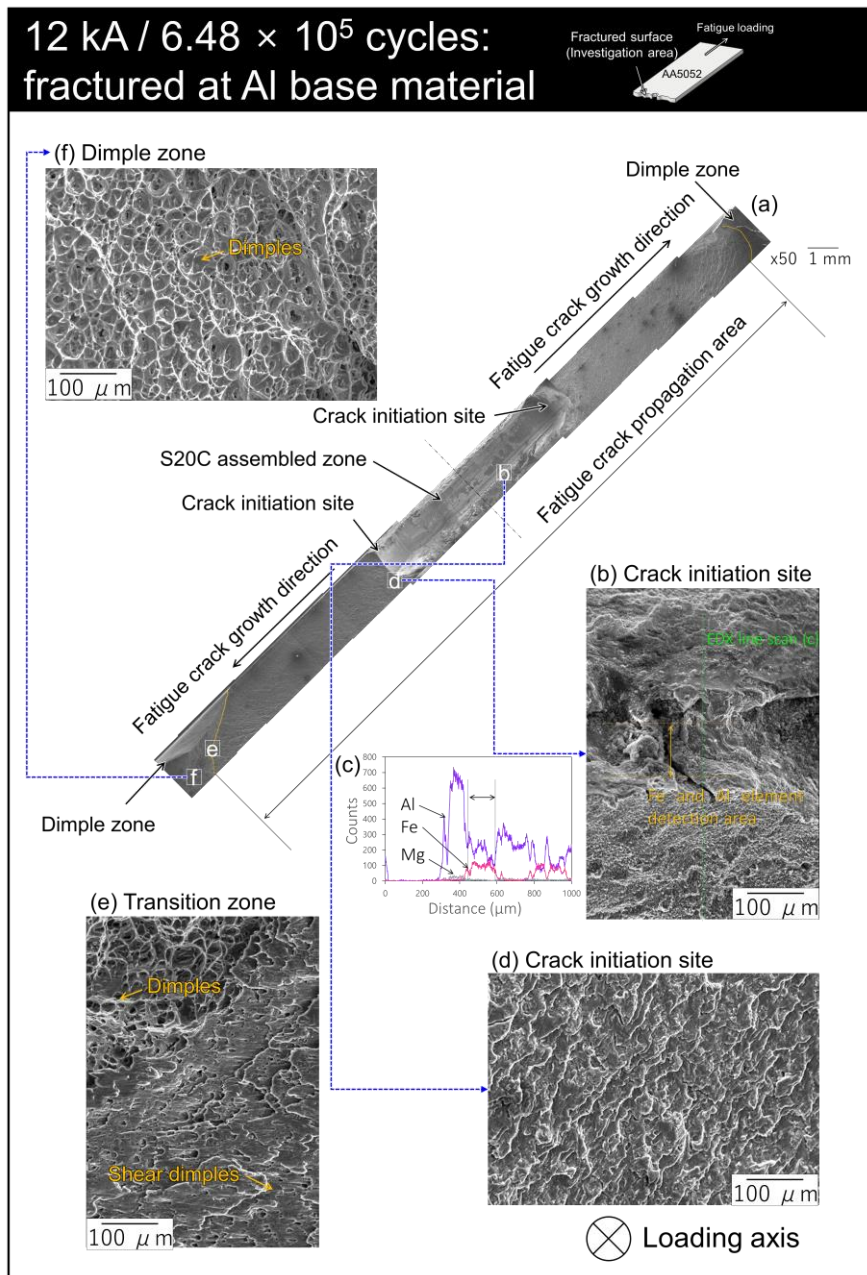


Fig. 3-12 Fatigue fractured surfaces of Al/Fe bonded with 10.5kA which fractured at 5.58×10^5 cycles by about 2,000N. (a) Al base material fractured by fatigue loading, (b) high magnification image of the crack initiation, (c) transition zone and crack propagation, and (d) the dimple zone image by overloading.



SFig. 3-3 Fatigue fractured surfaces of Al/Fe bonded with 12kA which fractured at 1.4×10^4 cycles. (a) SPFC base material fractured by fatigue loading, (b) high magnification image of the crack initiation area, (c) crack propagation zone and (d) dimple zone by overloading.



SFig. 3-4 Fatigue fractured surfaces of Al/Fe bonded with 12kA which fractured at 6.48×10^5 cycles. (a) SPFC base material fractured by fatigue loading, (b) high magnification image of the crack initiation area, (c) crack propagation zone and (d) dimple zone by overloading.

3.3.5 Fatigue crack propagations

Fatigue crack propagations and striations are important parameters for the fatigue life. In general, it is well known that the more the crack propagation area, the greater the fatigue life. Fig. 3-13 shows the measurement result of the fatigue crack propagation length observed in the low-cycle fatigue and high-cycle fatigue tests of the specimens joined at 10.5kA and 12kA. The specimen fatigued with 70% of the tensile-shear strength exhibited the crack propagation length of about 11 mm ~ 12 mm regardless of the bonding conditions. However, there was a significant difference in the crack propagation length of the specimens subjected to high-cycle fatigue. The specimen joined at 12kA reached about 15mm crack propagation length, and the ductile dimple fracture mode occurred. The specimen assembled at 10.5 kA was crack propagated up to about 22 mm and fracture occurred. The result accounts for about 73% of the crack propagation length, given that the total specimen width is 30 mm. It has been reported[12][13] that when the bonding has high squeezing forces, the crack propagation length and fatigue strength increases. In that context, this result showed a similar trend to the previously reported findings. Moreover, previous works[14][15] have been reported that the mechanical properties and fatigue properties of Al alloy are significantly reduced as the grains are coarsened. It has been reported that the occurrence of HAZ after welding is remarkable for the degradation of mechanical properties including fracture toughness[16]. Thus, the grain coarsening and recrystallization of AA5052, discussed in the microstructure section, which can significantly influence fatigue crack propagations.

The fatigue crack propagation area is characterized by fatigue striations and corresponds to stage II in fatigue progress (see SFig. 3-5).

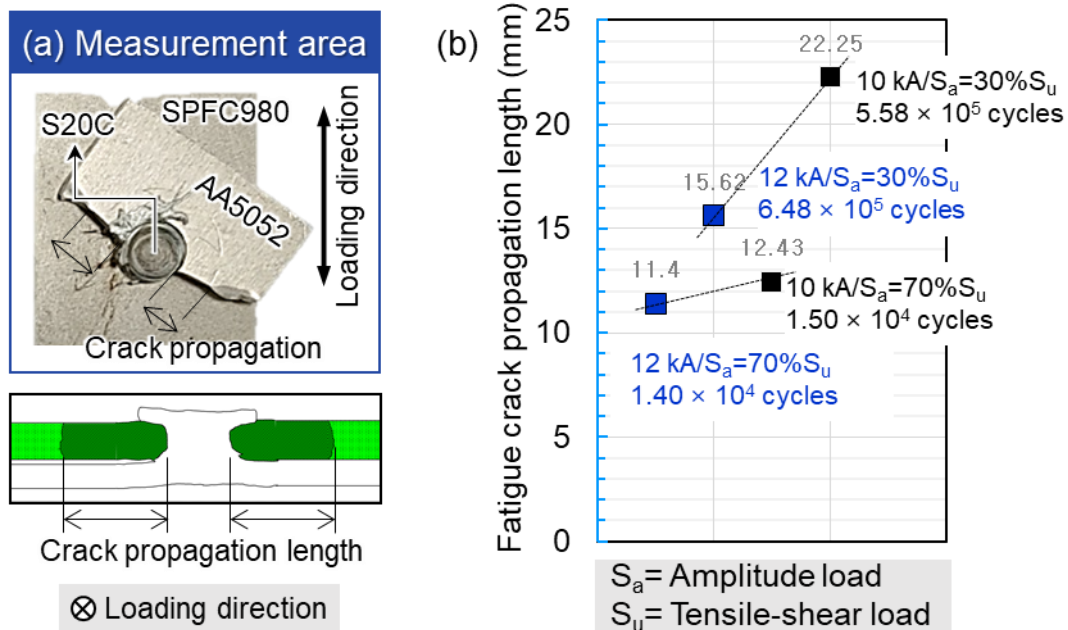
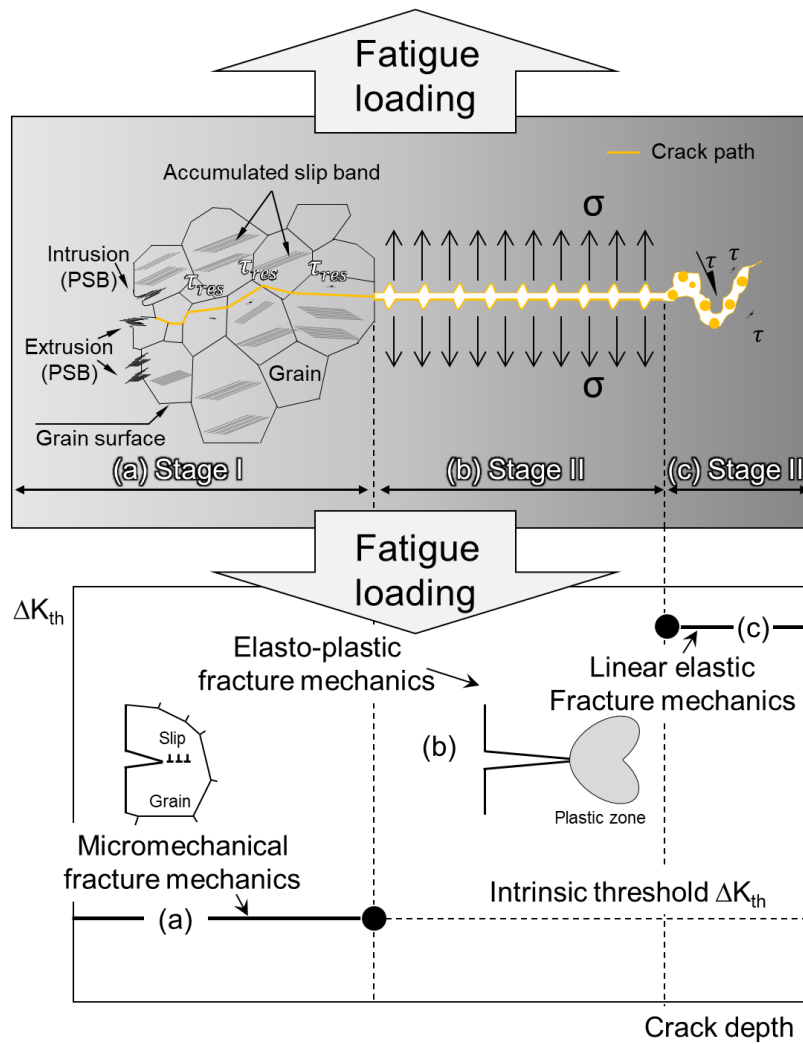


Fig. 3-13 A comparison of the fatigue crack propagation length depending on the welding currents. (a) the measurement area definition and (b) results of fatigue crack propagation lengths.

In the generalized crack propagation process, stage I is the stage that causes microstructurally short cracks (see SFig. 3-5). This state include initiation of cracks occurring on the surface, crystallographic crack propagation, i.e. permanent slip bands (PSBs), extrusion, intrusion, etc. In SFig. 3-5(b), when the crack front length exceeds a certain value and encloses, depending on the material, a larger number of grains, the crack will become a mechanically short one. The influence of the local microstructural features is declining and the crack propagation becomes more continuous. Eventually, the crack growth reaches the stage II, where it is no longer affected by any interfaces, and continues until the final fracture. As the result, in order to improve the substantial fatigue characteristics of REWed Al/Fe joints, it is key to find the ideal condition that minimizes the total penetration of the steel part and the HAZ area of the aluminum.



SFig. 3-5 Generalized fatigue crack propagation process.

3.4. Discussion

3.4.1 Microstructure developments

The welding interface made of steel and microstructure developments of the AA5052 material were observed in section 3.2. Lath martensite has substructure that consists of various kinds of grain boundaries, such as prior austenite grain boundaries (PAGBs), packet boundaries, block boundaries and lath boundaries as represented in Fig. 3-14(a)[17]. These lath martensite and PAGB were observed in all welding conditions (see Fig. 3-14(b)). The lath is the fundamental crystallographic unit of

martensite. The Kurdjumov–Sachs (K–S) orientation relation between parent austenite and lath martensite predicts that 24 unique crystallographic lath variants may develop from a single parent austenite grain. Laths align parallel to each other to form blocks which consist of a pair of different variants. Parallel blocks that have a common habit plane with a prior austenite grain (PAG) arrange in packets. In fact, we can verify that martensite structures can be created based on the empirical formulas and evidence of previous studies.

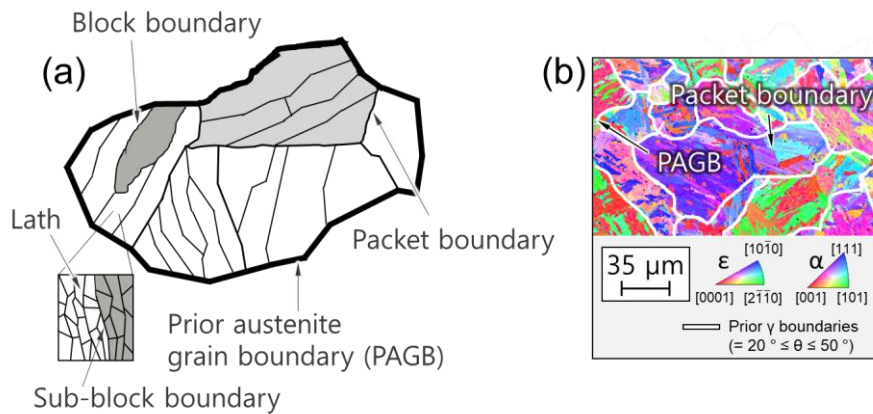


Fig. 3-14 (a) A schematic description of the prior austenite grain boundary and (b) the example structure including PAGB in the result of this study.

Here we can consider the phase transformation by the results of studies on the effect of alloying elements on the martensite start temperatures for α' - and ϵ -phases from the previous studies[18,19]. In addition, previous works have been studied the effect of a prior austenite grain size (PAGS) on the morphology and mechanical properties of lath martensite[20–22]. Previous results have mentioned that packets and block sizes are commonly observed to be reduced with a reduction of PAGS. This implies an increase in the number of high-angle boundaries in the as-quenched martensite microstructure, which act as effective barriers to dislocation movement during lath

martensite deformation and have a significant effect on the strengthening of the material. The effect of PAGS on the M_s^0 temperature was derived[23][24], as follow:

$$M_s^0 - M_s = \frac{1}{b} \ln \left[\frac{1}{\overline{V}_\gamma} \left\{ \exp \left(-\frac{\ln(1-f)}{m} \right) - 1 \right\} + 1 \right] \quad (3)$$

where M_s means α' - or ε -martensite start temperatures reflecting the effects of both alloying elements and PAGS. b denotes the fitting parameters (0.2689 for α' -martensite and 0.19 for ε -martensite), \overline{V}_γ is the average austenite grain volume of (unit: mm³), related to the PAGS, m is the aspect ratio of the martensite plate (0.05 for α' -martensite and 0.03 for ε -martensite), and f is the first detectable fraction of martensite which is assumed to be 0.01. For the present SPFC980 steel, the M_s^0 values of α' - or ε -martensite were calculated as 419.2 and 233.5 °C, respectively. Moreover, in the case of S20C steel, the values of α' - or ε -martensite were calculated as 438.6 and 201.5 °C, respectively. Namely, based on these temperature ranges, martensite can be formed at the temperature of S20C near the top of the nugget and the calculated M_s^0 temperature of SPFC980 near bottom of the welding nugget[10].

Whereas microstructural characteristics of S20C-SPFC980 welding interfaces were not significantly different in different welding currents, the HAZ development of AA5052 had a significant change according to the welding currents. The possible mechanism of AA5052 HAZ microstructure formations is displayed in Fig. 3-15. In here, thermal resistances can efficiently be associated with the transfer of heat and represented in circuits similarly to electrical resistances. Circuit representations

provide a useful tool for both conceptualizing and quantifying heat transfer problems. AA5052 HAZ welded with a relatively low welding current of 3.5kA and 4.5kA was sustained geometric tolerances due to the relatively low thermal behavior as shown in Fig. 3-15(a). This gap causes insufficient heat transfer to the AA5052 due to its high thermal resistance (R_{th}). With terms for the thermal resistance for conduction, as follows:

$$R_{th} = L/kA \text{ [K/W]} \quad (4)$$

where k is the materials conductivity ($Wm^{-1}K^{-1}$), L is the plane thickness (m), and A is the plane area (m^2). Therefore, thermal resistance is inversely proportional to thermal conductivity and area. The formula for calculating thermal resistance with tolerance is as follows:

$$R_{th} = R_{Al} + R_{Air (tolerance)} + R_{Fe} \quad (5)$$

where R_{Al} is the thermal resistance of AA5052, $R_{Air (tolerance)}$ is the thermal resistance of tolerance, and R_{Fe} is the thermal resistance term of Fe materials.

Therefore, the grains of Al were refined to 16 μm , and the low angle boundary (LAB) fraction was increased compared to the initial grains by the effect of only 2.45 kN of pressing force. When the welding current exceeds 10 kA, the geometrical tolerance disappears and the interface was perfectly joined, effectively heat conduction from the nugget to Al. Then, the thermal resistance can be calculated as follows:

$$R_{th} = R_{Al} + R_{Fe} \quad (6)$$

For this reason, the recrystallized grain fraction was significantly increased from the initial to about 67% at 10.5 kA of the welding current, and the grain were greatly grown to about 37.6 μm (see Fig. 3-6 results). The development of the HAZ microstructure of AA5052 can be a decisive factor that affects the mechanical and fatigue performances including fracture modes.

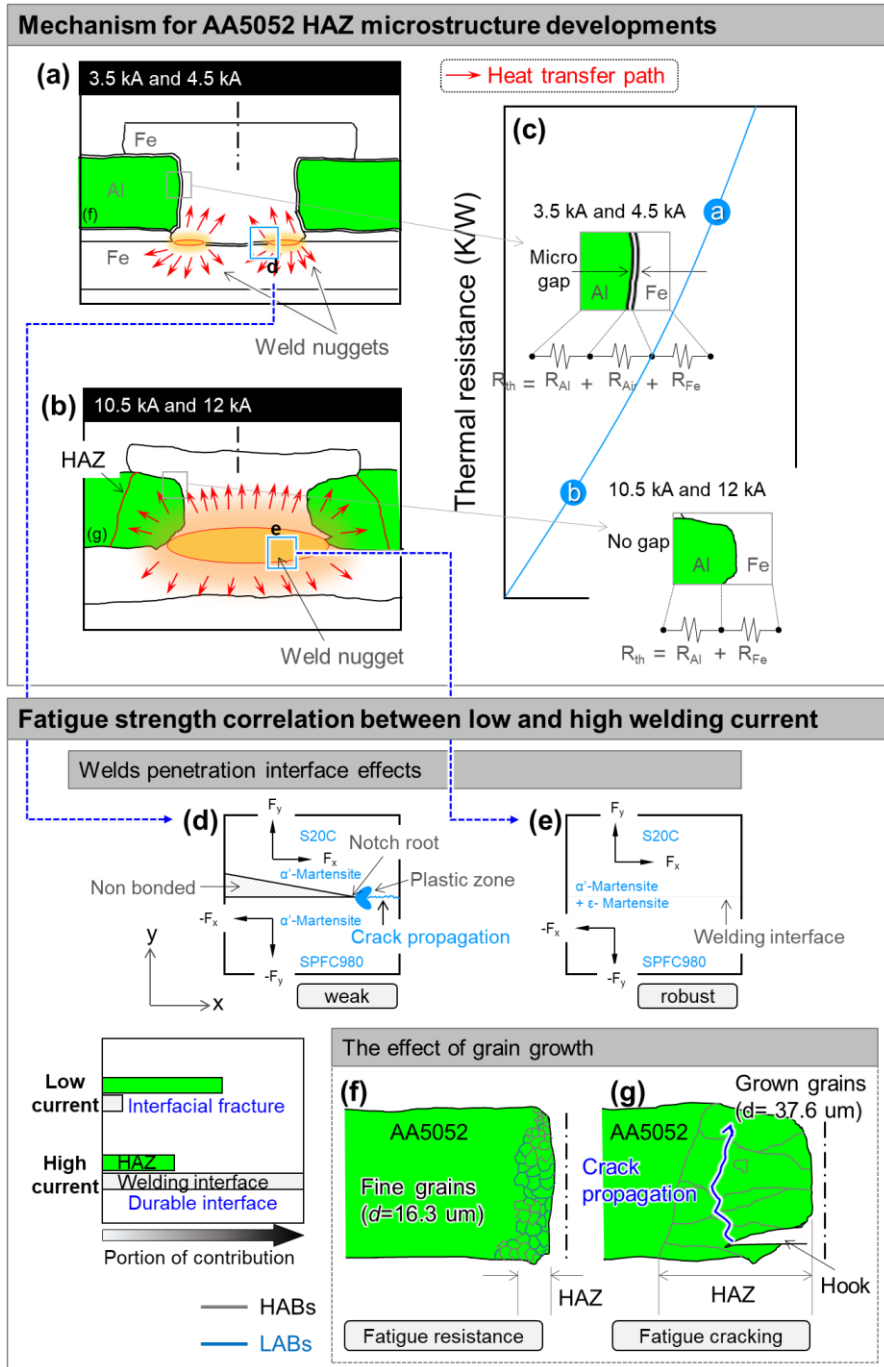


Fig. 3-15 The mechanism for AA5052 HAZ microstructure developments. (a) Heat transfer mechanism of 3.5 kA and 4.5 kA with small nugget, (b) heat transfer mechanism of 10.5 kA and 12 kA with big nugget, and (c) description for thermal resistance change with thermal resistance circuit maps, (d,e) fatigue strength correlation between low and high welding currents; welds penetration interface effects, (f,g) grain growth effects.

3.4.2 Microstructures influence on the fatigue strength

It is well known that the microstructural and morphological characteristic are key parameters determining mechanical and fatigue properties. In terms of the welding interfaces, the phase fractions were distributed similarly in all conditions. Most of the phases were formed α' phases from the PAGBs, and the KAM value and fraction of phase also had similar tendency. The main factors that determine interface failure of the spot joint are related to complete penetration, geometrical shape effect of the welded joint and the diameter of the spot (d_{spot}) form AWS recommendation. In addition, HAZ degradations of AA5052 also can be key issue for fatigue fracture characteristics in this case. Welding conditions of 3.5 and 4.5 kA were insufficient welding penetration between S20C and SPFC980, and non-degraded HAZ of AA5052. Welding conditions of 10.5 and 12 kA have sufficient welding interface penetrations which caused active heat transfer between Al and Fe by reducing R_{air} . This heat transfer promoted degradation of HAZ in AA5052. Therefore, a high welding current leads to grain growth and a larger heat affected zone, which can reduce the quality of the weld, while a high welding current will have a more perfect weld area. The correlation between these two effects on the fatigue strength of the joint can be summarized by Fig. 3-15(d-g). In the case of welds penetration and interface effects, low welding currents generated the notch root formation at the welding interface with insufficient penetrations, and fatigue fracture occurred near this site by fatigue loading as shown in Fig. 3-15(d). This notch stress effect on the fatigue strength relationship is a well-known issue that has been reported in previous studies[25–27]. However, the high welding currents have formed sufficient welding interface, which has suppressed fatigue fractures at this zone (see Fig. 3-15(e)). The influence of grain growth on fatigue strength is depicted in Fig. 3-15(f,g). The fine

grains of AA5052 are relatively robust in terms of fatigue resistance. It appears that coarse grains can be fracture relative easily by stress when combined with a hook-like stress singularity site. Even previous study has also described an instance where grain refining enhanced fatigue strength in 5XXX series aluminum alloys[28]. Consequently, the factor had a dominant influence on the fatigue life was not only the microstructure in this study. The next section will discuss the geometrical effect of the joint on the fatigue properties.

3.4.3 Geometrical effect for fatigue fracture modes

To seek the origins of such joint geometrical effect on the fatigue behavior of resistance element welded Al/Fe lap joints between 3.5 kA~4.5kA (Model A) and 10.5 kA~12 kA (Model B) of the welding condition, we conducted detailed the stress distribution and strain behavior at joint interfaces for different specimen geometry were investigated by a three-dimensional (3D) FEM computational modeling. Fig. 3-16(a) represents the 3D finite element modeling of the REWed Al/Fe lap joint. In Fig. 3-16(b), the model A presents the specimen welded by 3.5 kA ~ 4.5 kA of welding conditions, the model B exhibits the specimen welded by 10.5 kA ~ 12 kA of welding conditions. The design was reverse-engineered by reconstructing in the 3D CAD program based on the actual cross-sectional images (see Fig. 3-2), and the mechanical simulation was performed using the commercial finite element code ANSYS R18 workbench. As in the actual fatigue test conditions, one side was completely constrained ($U_x=U_y=U_z=0$), and the other side applied to tensile loading with 5,000 N in y-direction for both model A and B. To investigate the mechanical behavior, equivalent total strain (ϵ_{eq}) was applied, and the components were calculated as follow:

$$\varepsilon_{eq} = \frac{1}{\sqrt{2(1+\nu)}} [(\varepsilon_x + \varepsilon_y)^2 + (\varepsilon_y + \varepsilon_z)^2 + (\varepsilon_z + \varepsilon_x)^2 + \frac{3}{2}(\gamma_{xy}^2 + \gamma_{yz}^2 + \gamma_{zx}^2)]^{1/2} \quad (7)$$

where ν is poisson's ratio, γ is shear strain. The mechanical properties were applied as shown in **Table. 3-3**

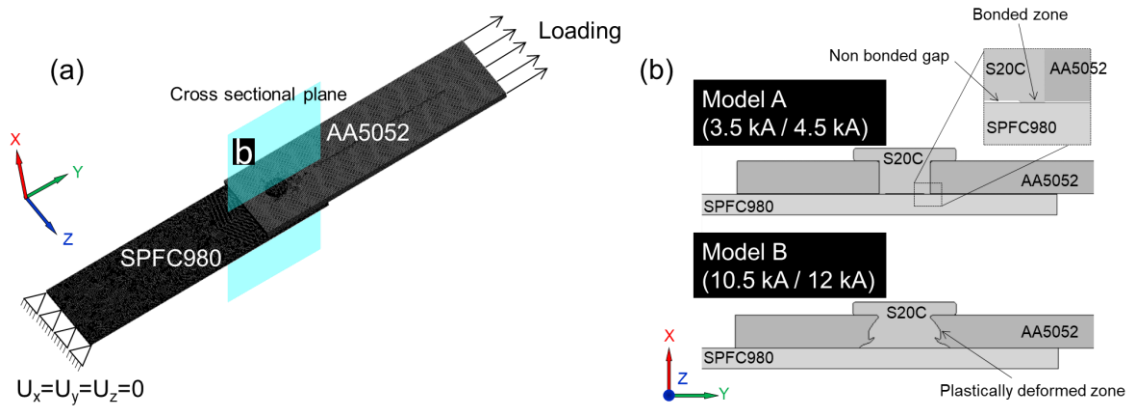


Fig. 3-16 Boundary conditions of finite element model and analysis. (a) Finite element modeling of the resistance element welded Al/Fe lap joint and (b) cross-sectional images with geometric shape parameters according to welding conditions.

Table. 3-3 Mechanical properties for finite element method simulation.

	Density, ρ (kg/m ³)	Young's modulus, E (GPa)	Yield strength, σ_y (MPa)	Poisson's ratio, ν
AA5052	2680	70.3	193	0.33
S20C	7870	186	245	0.29
SPFC980	7800	190-210	490	0.3

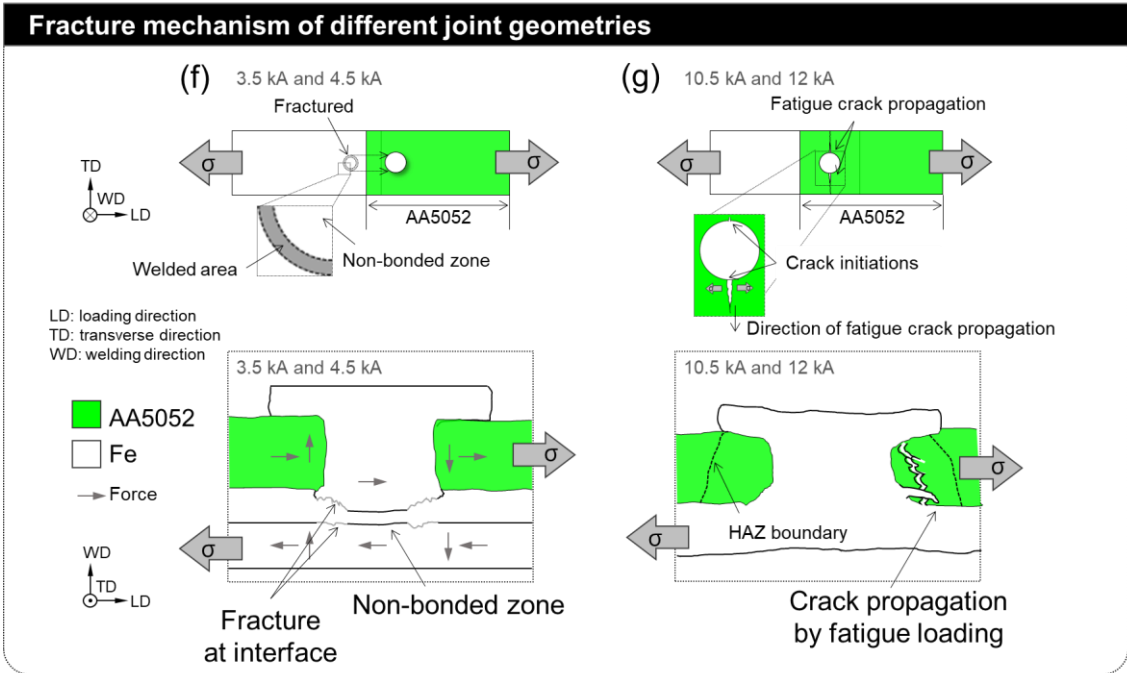
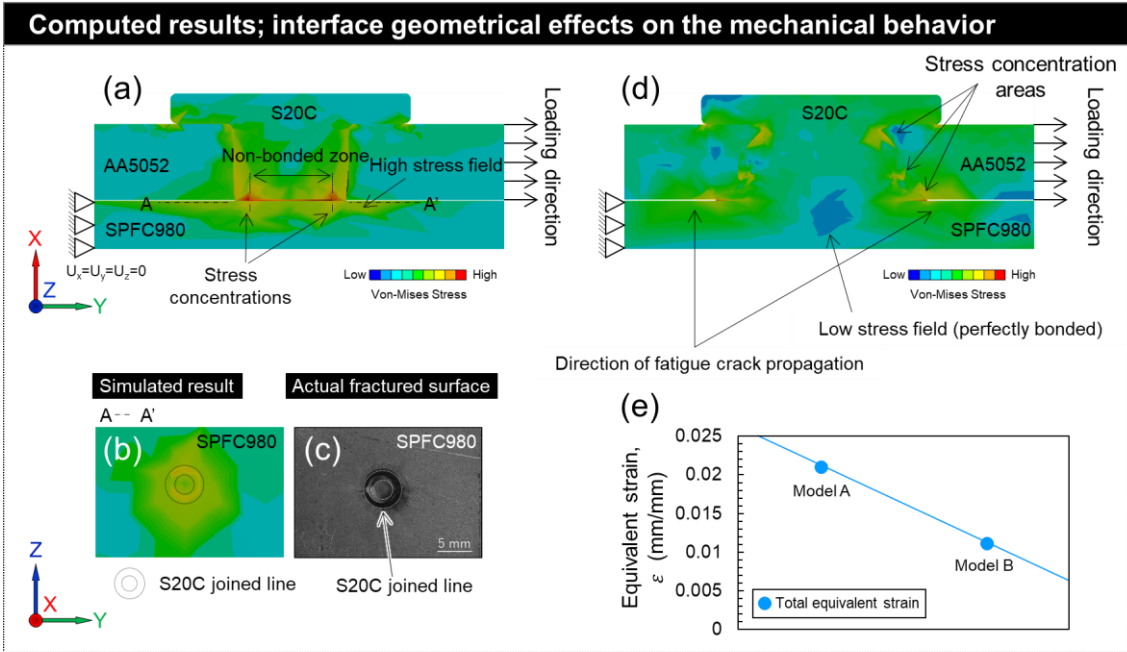


Fig. 3-17 Computed results of finite element simulation. (a) Stress distribution of x-y plane for model A, its tilted image of y-z plane (b), and actual fractured mesoscopic image (c), (d) stress distribution of x-y plane for model B, and (e) strain intensity of model A and model B, (f) fracture mechanism of model A, (g) failure mechanism of model B.

Fig. 3-17 represents the computed results of the finite element simulation for resistance element welded Al/Fe lap joints depending on geometrical shape parameters. Fig. 3-17(a) depicts the stress intensity distribution of cross-sectional x-y plane view for specimen bonded by 3.5 kA ~ 4.5 kA of current conditions, which occurred stress concentration at the joint interface between S20C and SPFC980 significantly. No significant stress concentration was observed on the aluminum side. Fig. 3-17(b) exhibits tilted y-z plane view of Fig. 3-17(a), it shows the stress concentration state of SPFC980. The stress strength was remarkably high in the tube shape to which S20C was clearly bonded, which is correlated with an actual mesoscopic image of the fracture surface (see Fig. 3-17(c)). For this reason, it was found through numerical simulation that the interfacial fracture was caused by the concentration of the interfacial stress. In Fig. 3-17(d), the stress intensity of specimen bonded by 10.5kA ~12kA was distributed at a lower value than that of the bonded specimen with a relatively 3.5 kA ~ 4.5kA. This means that more energy needs to be consumed for destruction, with a condition of 10.5 kA. In particular, no stress concentration occurred at the interface between the fully bonded S20C and SPFC980, and relatively high stress was generated at the interface between AA5052 and S20C. The interface between S20C and AA5052 can be suggested a fatigue crack initiation site. In addition, the geometrical shape parameter showed a remarkable difference in the mechanical strain (see Fig. 3-17(e)). Namely, model A means that deformation easily occurs at the bonding interface, and model B means that deformation can easily occur between S20C and AA5052. When the same load was applied according to the geometric shape, the strain presented a remarkable difference of more than two times. The mechanical response can be noticeable when the specimen

geometry or evaluation method is different[6]. Therefore, geometrical parameters can be a major influence on fatigue properties.

Fig. 3-17(f, g) exhibits the graphical description of fatigue failure mechanism depending on the different joint geometries. The Al/Fe assembly in which the bonding of the S20C element and SPFC980 is insufficient due to the low current is fracture at the interface as shown in Fig. 3-17(f), which causes relatively low static strength and fatigue strength. On the other hand, the relatively high welding current of the robust bonding, as shown in Fig. 3-17(g), caused the failure in the Al base material, and excellent mechanical performance was realized.

3.5 Conclusions

A method of assembling lap joints through a simple approach to AA5052 and SPFC980 steel using resistance element welding (REW) has been studied. Fatigue tests were run for various fatigue load conditions in order to determine how the microstructure and interfacial geometry evolved by welding conditions and what effect this had on the mechanical fatigue performance. The findings can be summarized as follows:

1. When the REW was processed with 10.5 kA, exceeded maximum of 9 kN of the tensile-shear property, and the integrity of the microstructure was demonstrated.
2. The AA5052/SPFC980 lap joint welded with a welding current of 3.5~4.5 kA, the joint interface fracture occurred in both low cycle and high cycle fatigue,

and joints welded under the condition of 10.5~12 kA, AA5052 base material fracture was induced under all conditions.

3. Fatigue properties also had the highest fatigue strength at 10.5 kA. However, in the case of the AA5052/SPFC980 joints welded under the condition of 10.5~12 kA, the fatigue cracks initiated and propagated at the heat affected zone (HAZ) of AA5052 and the fatigue strength rapidly limited in high fatigue cycles. The results were attributed from the development of HAZ of AA5052 like a grain size, growth and grain recrystallization.
4. In addition, the constructed 3D finite element method (FEM) modeling revealed that the stress and strain distribution showed a significant difference to the same fatigue load according to the geometrical effect of the welding interface. This trend was in good agreement with the experimental results of the fracture mode and fatigue S-N curve.
5. This result provides an implementation of satisfactory mechanical properties with REW, and it can be adopted as a substantial alternative for robust bonding and the mass production of next-generation automotive lightweight structures.

References

- [1] Chen N, Wang HP, Carlson BE, Sigler DR, Wang M. Fracture mechanisms of Al/steel resistance spot welds in lap shear test. *J Mater Process Technol* 2017;243:347–54. <https://doi.org/10.1016/j.jmatprotec.2016.12.015>.
- [2] Chen N, Wang HP, Wang M, Carlson BE, Sigler DR. Schedule and electrode design for resistance spot weld bonding Al to steels. *J Mater Process Technol* 2019;265:158–72. <https://doi.org/10.1016/j.jmatprotec.2018.10.011>.
- [3] Zhou L, Yu M, Liu B, Zhang Z, Liu S, Song X, et al. Microstructure and mechanical properties of Al/steel dissimilar welds fabricated by friction surfacing assisted friction stir lap welding. *J Mater Res Technol* 2020;9:212–21. <https://doi.org/10.1016/j.jmrt.2019.10.046>.
- [4] Sandnes L, Bergh T, Grong Ø, Holmestad R, Vullum PE, Berto F. Interface microstructure and tensile properties of a third generation aluminium-steel butt weld produced using the Hybrid Metal Extrusion & Bonding (HYB) process. *Mater Sci Eng A* 2021;809. <https://doi.org/10.1016/j.msea.2021.140975>.
- [5] Li R, Yuan X, Zhang H, Yang J, Wu K, Li T, et al. Effect of axial magnetic field on TIG welding-brazing of AA6061 aluminum alloy to HSLA350 steel. *J Mater Res Technol* 2021;12:882–93. <https://doi.org/10.1016/j.jmrt.2021.03.039>.
- [6] Shi L, Kang J, Gesing M, Chen X, Haselhuhn AS, Carlson BE. Fatigue life assessment of Al-steel resistance spot welds using the maximum principal strain approach considering material inhomogeneity. *Int J Fatigue* 2020;140:105851. <https://doi.org/10.1016/j.ijfatigue.2020.105851>.
- [7] Mirza FA, Macwan A, Bhole SD, Chen DL, Chen XG. Microstructure, tensile and fatigue properties of ultrasonic spot welded aluminum to galvanized

- high-strength-low-alloy and low-carbon steel sheets. *Mater Sci Eng A* 2017;690:323–36. <https://doi.org/10.1016/j.msea.2017.03.023>.
- [8] Meschut G, Janzen V, Olfermann T. Innovative and highly productive joining technologies for multi-material lightweight car body structures. *J Mater Eng Perform* 2014;23:1515–23. <https://doi.org/10.1007/s11665-014-0962-3>.
- [9] Lee SJ, Shin SE, Ushioda K, Fujii H. Microstructure, mechanical properties, and damping capacity in stir zone after friction stir welding of Fe–17Mn damping alloy. *J Alloys Compd* 2019;803:1155–67. <https://doi.org/10.1016/j.jallcom.2019.06.367>.
- [10] Baek S, Song J, Lee H chul, Park S yeon, Song KH, Lee S, et al. Robust bonding and microstructure behavior of aluminum/high-strength steel lap joints using resistance element welding process for lightweight vehicles: Experimental and numerical investigation. *Mater Sci Eng A* 2022;833:142378. <https://doi.org/10.1016/j.msea.2021.142378>.
- [11] Yoshinaka F, Xue G, Fujimura N, Nakamura T. Effect of vacuum pressure on small crack propagation in Ti-6Al-4V. *Int J Fatigue* 2021;142:105961. <https://doi.org/10.1016/j.ijfatigue.2020.105961>.
- [12] Zeng C, Xue JT, Liu XY, Tian W. Design variables influencing the fatigue of Al 2024-T3 in riveted aircraft lap joints: Squeeze force and initial fit tolerance. *Int J Fatigue* 2020;140:105751. <https://doi.org/10.1016/j.ijfatigue.2020.105751>.
- [13] Skorupa M, Machniewicz T, Skorupa A, Korbel A. Fatigue strength reduction factors at rivet holes for aircraft fuselage lap joints. *Int J Fatigue* 2015;80:417–25. <https://doi.org/10.1016/j.ijfatigue.2015.06.025>.
- [14] Lin S, Deng YL, Tang JG, Deng SH, Lin HQ, Ye LY, et al. Microstructures and fatigue behavior of metal-inert-gas-welded joints for extruded Al-Mg-Si alloy. *Mater*

- Sci Eng A 2019;745:63–73. <https://doi.org/10.1016/j.msea.2018.12.080>.
- [15] Kalinenko A, Vysotskii I, Malopheyev S, Mironov S, Kaibyshev R. Relationship between welding conditions, abnormal grain growth and mechanical performance in friction-stir welded 6061-T6 aluminum alloy. Mater Sci Eng A 2021;817:141409. <https://doi.org/10.1016/j.msea.2021.141409>.
- [16] Milella PP. Fatigue and corrosion in metals. vol. 42. 2005. <https://doi.org/10.1017/CBO9781107415324.004>.
- [17] Furuhashi T, Kobayashi K, Maki T. Control of cementite precipitation in lath martensite by rapid heating and tempering. ISIJ Int 2004;44:1937–44. <https://doi.org/10.2355/isijinternational.44.1937>.
- [18] Mahieu J, Maki J, De Cooman BC, Claessens S. Phase transformation and mechanical properties of Si-free CMnAl transformation-induced plasticity-aided steel. Metall Mater Trans A Phys Metall Mater Sci 2002;33:2573–80. <https://doi.org/10.1007/s11661-002-0378-9>.
- [19] Yang HS, Jang JH, Bhadeshia HKDH, Suh DW. Critical assessment: Martensite-start temperature for the $\gamma \rightarrow \epsilon$ transformation. Calphad Comput Coupling Phase Diagrams Thermochem 2012;36:16–22. <https://doi.org/10.1016/j.calphad.2011.10.008>.
- [20] Furuhashi T, Kikumoto K, Saito H, Sekine T, Ogawa T, Morito S, et al. Phase transformation from fine-grained austenite. ISIJ Int 2008;48:1038–45. <https://doi.org/10.2355/isijinternational.48.1038>.
- [21] Hanamura T, Torizuka S, Tamura S, Enokida S, Takechi H. Effect of austenite grain size on the mechanical properties in air-cooled 0.1c-5Mn martensitic steel. Mater Sci Forum 2014;783–786:1027–32.

<https://doi.org/10.4028/www.scientific.net/msf.783-786.1027>.

- [22] Morris Jr. JW. Comments on the microstructure and properties of ultrafine grained steel. *Isij Int* 2008;48:1063–70.
- [23] Yang HS, Bhadeshia HKDH. Austenite grain size and the martensite-start temperature. *Scr Mater* 2009;60:493–5.
<https://doi.org/10.1016/j.scriptamat.2008.11.043>.
- [24] Yen HW, Ooi SW, Eizadjou M, Breen A, Huang CY, Bhadeshia HKDH, et al. Role of stress-assisted martensite in the design of strong ultrafine-grained duplex steels. *Acta Mater* 2015;82:100–14. <https://doi.org/10.1016/j.actamat.2014.09.017>.
- [25] Baumgartner J, Hobbacher AF, Rennert R. Fatigue assessment of welded thin sheets with the notch stress approach – Proposal for recommendations. *Int J Fatigue* 2020;140:105844. <https://doi.org/10.1016/j.ijfatigue.2020.105844>.
- [26] N'Diaye A, Hariri S, Pluvinage G, Azari Z. Stress concentration factor analysis for notched welded tubular T-joints. *Int J Fatigue* 2007;29:1554–70.
<https://doi.org/10.1016/j.ijfatigue.2006.10.030>.
- [27] Rohani Raftar H, Dabiri M, Ahola A, Björk T. Re-evaluation of weld root fatigue strength for load-carrying fillet welded joints using the notch stress concept. *Int J Fatigue* 2021;144. <https://doi.org/10.1016/j.ijfatigue.2020.106076>.
- [28] Shukla S, Komarasamy M, Mishra RS. Grain size dependence of fatigue properties of friction stir processed ultrafine-grained Al-5024 alloy. *Int J Fatigue* 2018;109:1–9.
<https://doi.org/10.1016/j.ijfatigue.2017.12.007>.

Chapter 4 Investigation of microstructural transition and fracture due to heat transfer in Al REW lap joints of Al/UHSS without heat affected zones

4.1 Introduction

Resistance element welding (REW), a process that entails welding light metals and steel materials using the existing equipment of Resistance Spot Welding (RSW) [1–4], is considered a viable alternative to the aforementioned conventional welding processes. In REW, the steel element pre-riveted to the lightweight material of the upper plate is welded to the lower steel plate, i.e., welding is conducted between similar materials; thus, this alternative method effectively circumvents the shortcomings arising from differences in the physical and chemical properties between dissimilar materials[3,5,6].

However, HAZ inevitably forms during the welding of dissimilar materials. Notably, the structural integrity of a joint may change owing to microstructural deterioration, i.e., its initial microstructure changes due to the formation of coarse or segregated grains, fundamentally affecting the fracture mode and mechanical performance of the welded system[4]. Nevertheless, extensive efforts have been divested to minimize defects resulting from dissimilar welding in automobile structures and enhance their safety characteristics. Consequently, suitable methods, i.e., HAZ-less technologies, are required to minimize the risk associated with the formation of HAZs, which can be considered as a welding defect.

Therefore, in this chapter 4, the author developed a process that can inhibit the formation of Al HAZs during the REW of a lap joint of hard 1GPa class SPFC980 steel and Al5052-H32 alloy. Two specimens were prepared: one in which the element and

aluminum (Al) on the top plate were in direct contact (i.e., hot wall), and another composed of a heat transfer shield between the element and top-plate Al (i.e., cold wall). The microstructures of the Al and Fe alloys, which developed differently due to these differences, were characterized, and their mechanical properties were analyzed through thermodynamic calculations, experimental temperature measurements, and electron backscattered diffraction (EBSD) analyses. To the best of our knowledge, this is the first report on the formation of an HAZ-less Al alloy via REW of an Al alloy–ultra-high-strength steel. Herein, the author systematically discuss the contribution of this HAZ-less microstructure to the structural integrity of the welded system, as well as possible side effects.

4.2 Experimental procedures

4.2.1 Al HAZ-less REW

Fig. 4-1 illustrates the Al HAZ-less REW process along with its conceptual definition. For REW, a conventional RSW system (Chowel/ASP-75, Republic of Korea) commonly used in the mass production of automobile structures was adopted, as depicted in Fig. 4-1(a). Fig. 4-1(b) provides an overview of the REW process, including detailed dimensions of each base material (BM) and the corresponding REW parameters. In the REW procedure, first, the author pre-riveted the element (S20C) onto the AA5052-H32 alloy. The upper BM (AA5052-H32: 100 mm × 30 mm × 2.5 mm), with the S20C element component, and lower BM (SPFC980: 100 mm × 30 mm × 1.6 mm) were then aligned and securely fixed to the fixture jig, and subsequently, the welding process was initiated. In other words, welding is performed using a conventional resistance welding machine, joining a steel element pre-riveted to the

upper aluminum plate with a steel plate on the lower side. During the REW process, the author applied an insulating barrier coating (polyvinyl chloride-based coating) and introduced gap between the S20C rivet element and AA5052 to suppress the Al HAZ generation. As illustrated in Fig. 4-1(e), the coating layer is applied to the area where the steel element contacts the upper aluminum plate, as well as to the column portion of the element, and indicated by the red line. As shown in Fig. 4-1(c), a hot wall and a cold wall are formed due to the difference caused by the gap and the coating layer. During the REW, the following specific parameters were set: a fixed pressing force of 2.45 kN and an energization time of 200 ms. The current was set to 8.5, 10.5, and 12 kA. The chemical compositions and mechanical properties of the applied materials are indicated in Tables 1 and 2, respectively.

Table. 4-1 Chemical compositions of applied materials

	Elements (wt %)									
	Al	C	Mg	Si	Fe	Cu	Mn	Cr	Zn	P
AA5052	Bal.	-	2.392	0.133	0.282	0.029	0.027	0.183	0.002	-
SPFC980	-	0.109	-	0.942	Bal.	-	2.192	-	-	0.014
S20C	-	0.19	-	0.2	Bal.	-	0.47	-	-	0.012

Table. 4-2 Mechanical properties of applied materials

	Density, ρ (kg/m ³)	Young`s Modulus, E (GPa)	Yield strength, σ_y (MPa)	Poisson`s ratio, ν
AA5052	2680	70.3	193	0.33
SPFC980	7800	190-210	>490	0.3
S20C	7870	186	>245	0.29

4.2.2 Measurement of Al HAZ and fusion zone (FZ) temperature

In this study, our main objectives were to implement Al HAZ-less welding and to establish a correlation between the evolving microstructure and strength. The Al HAZ-less REW lap joint is defined here as a cold wall, and the conventional REW lap joint with Al HAZ is called a hot wall in this paper. The author directly measured the temperature of each material at specific positions using thermocouples (k-type, Temperature range: 0- 1372 °C), to validate the Al HAZ-less phenomenon empirically, as shown in Fig. 4-1(d). The detailed geometry used to measure the temperatures of the hot and cold walls is depicted in Fig. 4-1(e).

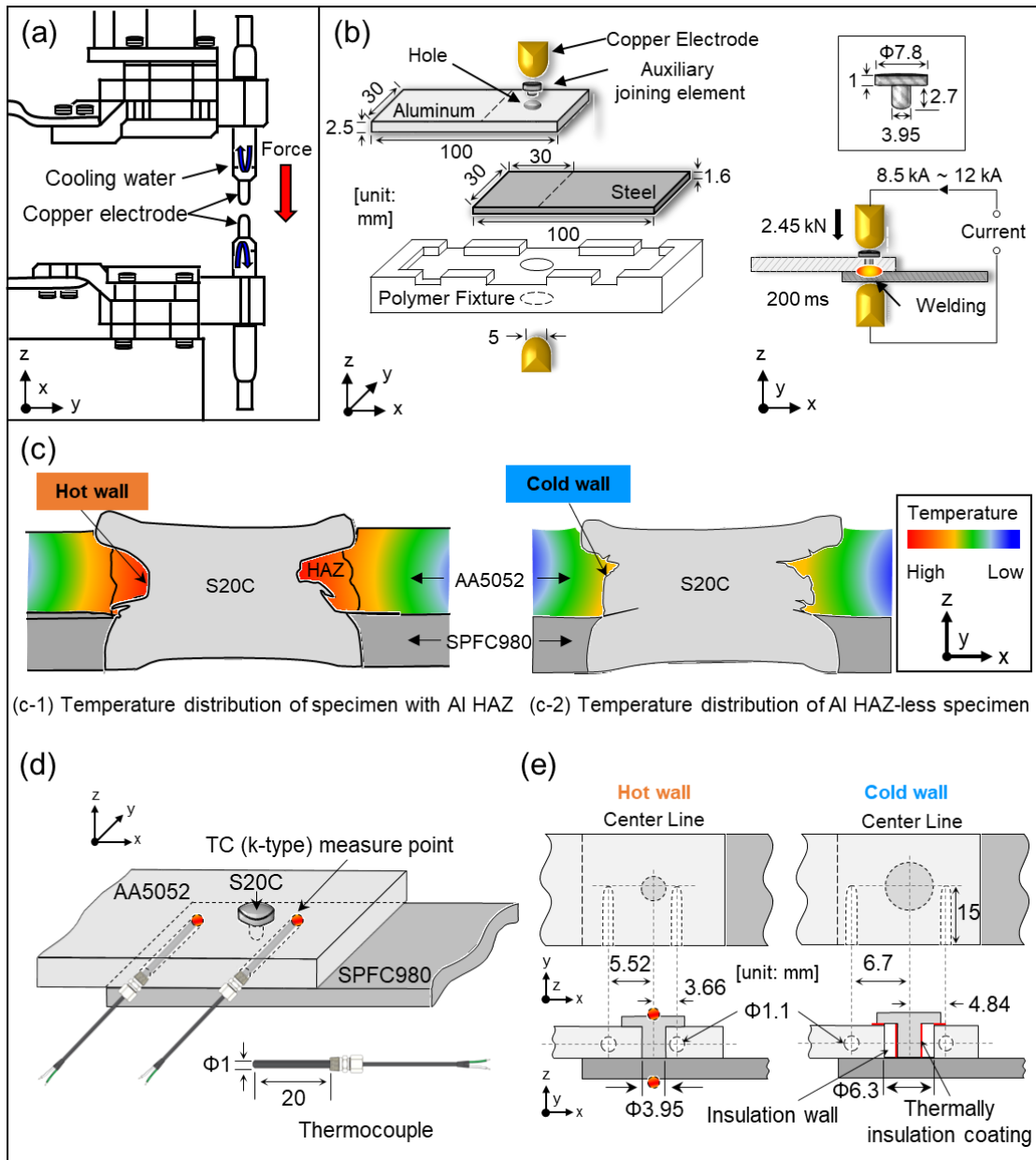


Fig. 4-1 REW process. (a) RSW machine, (b) specimen dimensions, (c) temperature distribution on specimens, (d) TC position of specimens and (e) configuration of the TC position. TC: thermo couple.

4.2.3 Microstructural and mechanical characterizations

To analyze the microstructure evolution and fracture surface under various welding conditions and in the presence/absence of the Al HAZ, the author used a three-dimensional (3D) display microscope (Leica/DVM6) and observed the

cross-sections of the specimens. Prior to the observation, the cut surface of the weld was mechanically polishing up to #4000. The author used a 4% Nital solution (96 mL ethanol, 4 mL nitric acid) to observe SPFC980 and S20C and a Keller solution (95 mL distilled water, 2.5 mL nitric acid, 1.5 mL hydrochloric acid, 1 mL hydrofluoric acid) to observe AA5052-H32. Next, the author performed EBSD analyses to investigate the microstructural properties, such as grain size, shape, grain boundaries, and phases. The cross-sectional samples were prepared and processed by EBSD, and the sample surface was examined using an orientation imaging microscopy (OIM) software.

Micro-Vickers hardness measurements and tensile tests were conducted to evaluate the mechanical properties of the specimens. The micro-Vickers hardness measurements were performed using a hardness tester (Mitutoyo/HM-200) with a load and dwell time of 0.1 gf and 10 s, respectively, at 0.4 mm intervals. Based on the hardness measurement results, cross-sectional hardness mapping of the specimens was performed, and the hardness distributions were visualized and compared for all the welding conditions. Tensile-shear tests were performed using a universal testing machine (UTM, MTDI/UT100F) at room temperature with a crosshead speed of 2 mm/min. The tensile-shear tests were continued until fracture occurred to determine the fracture modes under each welding condition.

4.3 Results

4.3.1 Morphological characteristics of the welded joints

A rigorous quantitative investigation was conducted to analyze the morphological characteristics of the weld. The author performed precise geometric measurements of the welded joints and analyzed the macroscale attributes of the cross-sections of the welded parts. For this analysis, the author compared the results observed after the two

welding processes, i.e., the Al HAZ-less process and conventional REW process. Fig. 4-2(a) illustrates the 3D geometry used to measure the characteristics of S20C riveted on the AA5052-H32 alloy (i.e., before the REW process) and its surface profile. The profile clearly indicates that, in the case in which only the S20C rivet is inserted into the AA5052 alloy before the REW process, the head of the S20C rivet remains flat without severe deformation. The geometrical features of hot and cold walls (i.e., Al HAZ-less joint) are illustrated in Figs. 4-2(b) and (c), respectively. In the case of the hot wall joint, an indentation depth of 0.1 mm is observed under an input energy of 10.5 kA. This phenomenon can be attributed to steel softening due to melting (i.e., S20C-SPFC980) and the indentation resistance of the Al alloy. The absence of insulation walls between Al and S20C results in a direct contact, leading to the formation of an HAZ. This contact can cause melting and solidification of Al because of the inability of the Al wall to accommodate the thickness change of S20C. However, for the cold wall joint, despite utilizing the same input energy of 10.5 kA, the Al HAZ-less joint exhibits a larger penetration depth of 0.34 mm, and the diameter of the S20C head is also noticeably larger than that observed in the case of the hot wall joint. Because of the polyvinyl chloride (PVC)-based insulation wall and air barrier of the Al HAZ-less joint (i.e., cold wall), S20C becomes thick and deformed upon press-fitting of the S20C rivet during the REW process. These findings highlight the unique characteristics of the Al HAZ-less joint design and its impact on the welding process. Fig. 4-2(d) summarizes the indentation depth trends for all the parameters used in this study. Notably, at 12 kA, the indentation depths for the hot and cold wall joints remain approximately the same, i.e., around 0.6 mm. These effects are quantitatively addressed in the microstructure section.

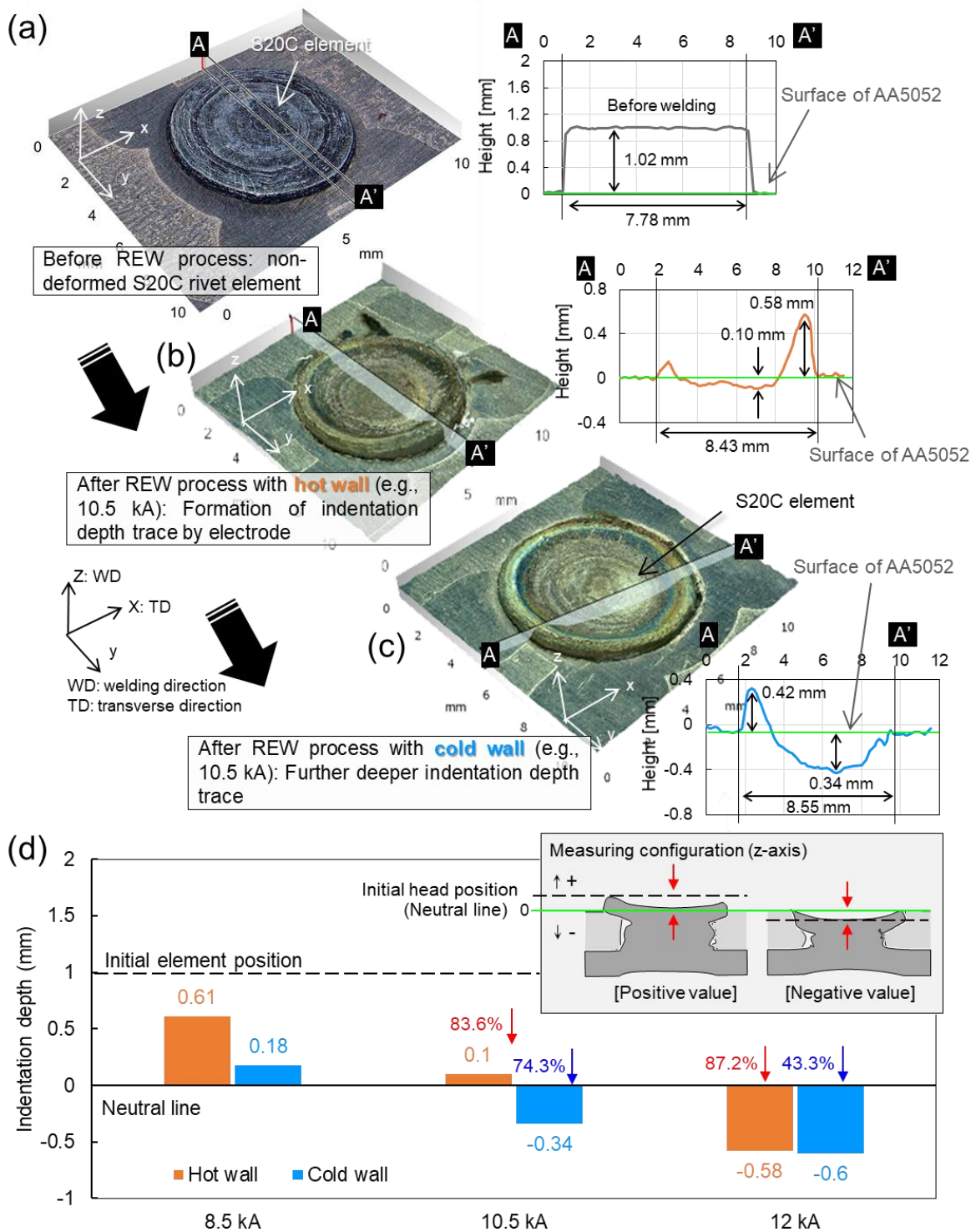


Fig. 4-2 Indentation depth of the REW specimens at different currents. Three-dimensional geometry and surface profile (a) before the REW process and after the REW process with (b) a hot wall and (c) a cold wall, and (d) indentation depths of S20C rivet after REW.

4.3.2 Microstructures of the welded joints

Fig. 4-3(a-f) present the etched macroscale cross-sectional images of the welded joints. These images depict the measured shank diameters corresponding to different welding currents under both the hot and cold wall conditions. These results indicate the effects of the welding current on the joint characteristics in the respective wall configurations and the direct influence of the Al HAZ presence or absence on the geometries of the FZ and joint in the cross section. The changes in the shank diameter under different parameters are shown in Fig. 4-3(g). For the hot wall joints, the shank diameter linearly increases from 5.74 mm at 8.5 kA to a maximum of 7.19 mm at 12 kA. In the case of the cold wall joints, the shank diameter increases significantly at 12 kA. Thus, with the same current, the shank diameter of the cold wall joint is ~6.7% larger than that of the hot wall joint, and this diameter difference highlights the differing effects of the welding current on the shank formation under hot and cold wall conditions. Fig. 4-3(h) displays the minimum nugget diameter based on recommendations of the American Welding Society (AWS; D8.9M: Test methods for evaluating the RSW behavior of automotive sheet metal steel materials). The minimum diameter of the nugget that induces parent metal fracture can be calculated as follows:

$$d_{spot} = 4\sqrt{t} \quad (1)$$

where d_{spot} is the weld nugget diameter, and t is the sheet thickness. These recommendations are valid for steel-based weld nuggets and may not be suitable for dissimilar weld nuggets and different sheet thicknesses (such as Al–steel systems). The thicknesses of the AA5052 and SPFC980 sheets were calculated to be 6.32 and 5.05 mm,

respectively. The minimum nugget diameter in the cold wall case at 8.5 kA is 6.57 mm, higher than the conservative recommended diameter for AA5052 (6.32 mm); this finding implies that parent metal fracture can occur under all parameter settings.

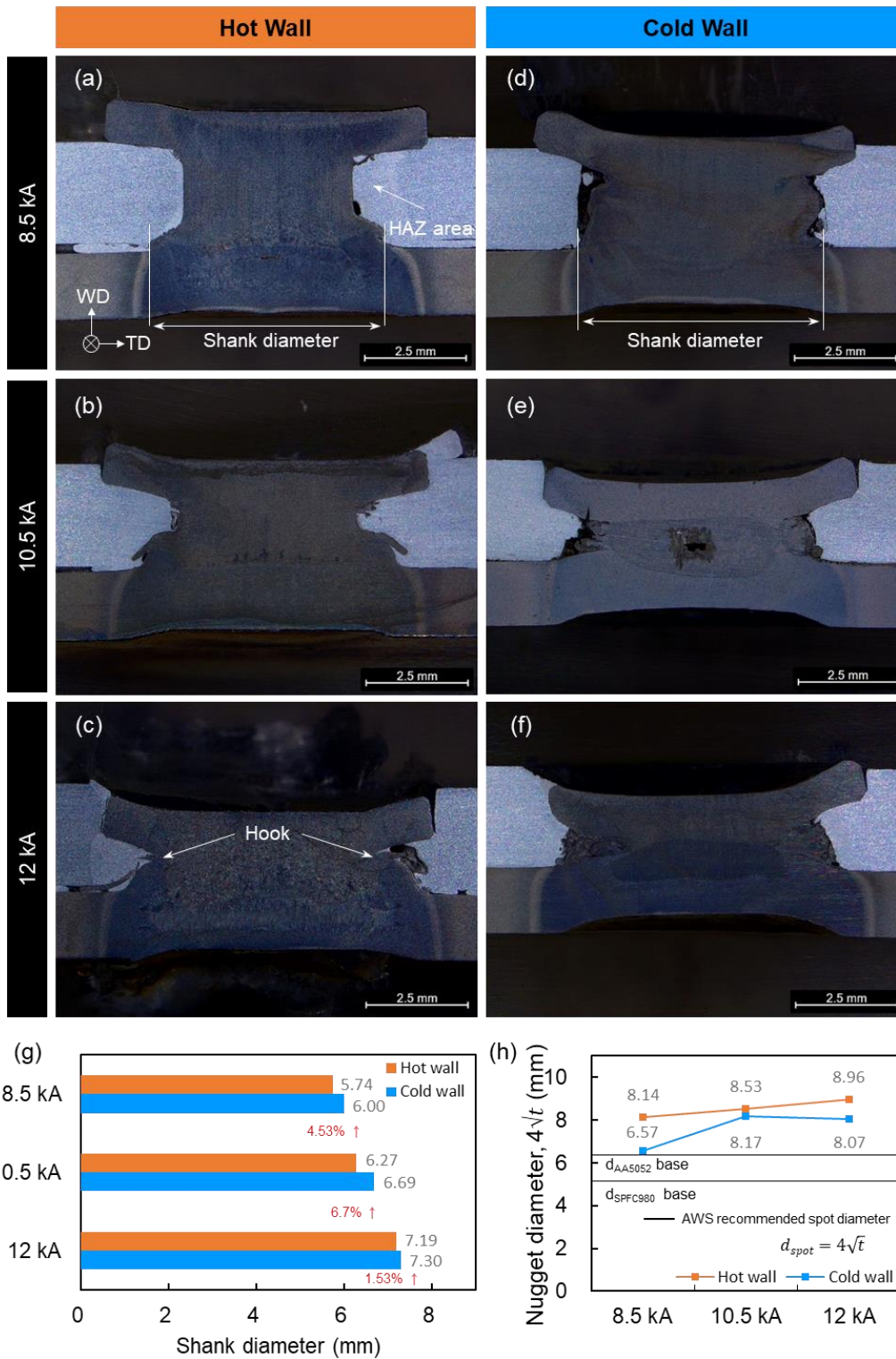


Fig. 4-3 Cross-sectional images of the REW joints. Joints with (a-c) hot wall parameters and (d-f) cold wall parameters depending on welding currents, (g) shank diameter and (h) correlation minimum spot diameters based on AWS. AWS: American Welding Society.

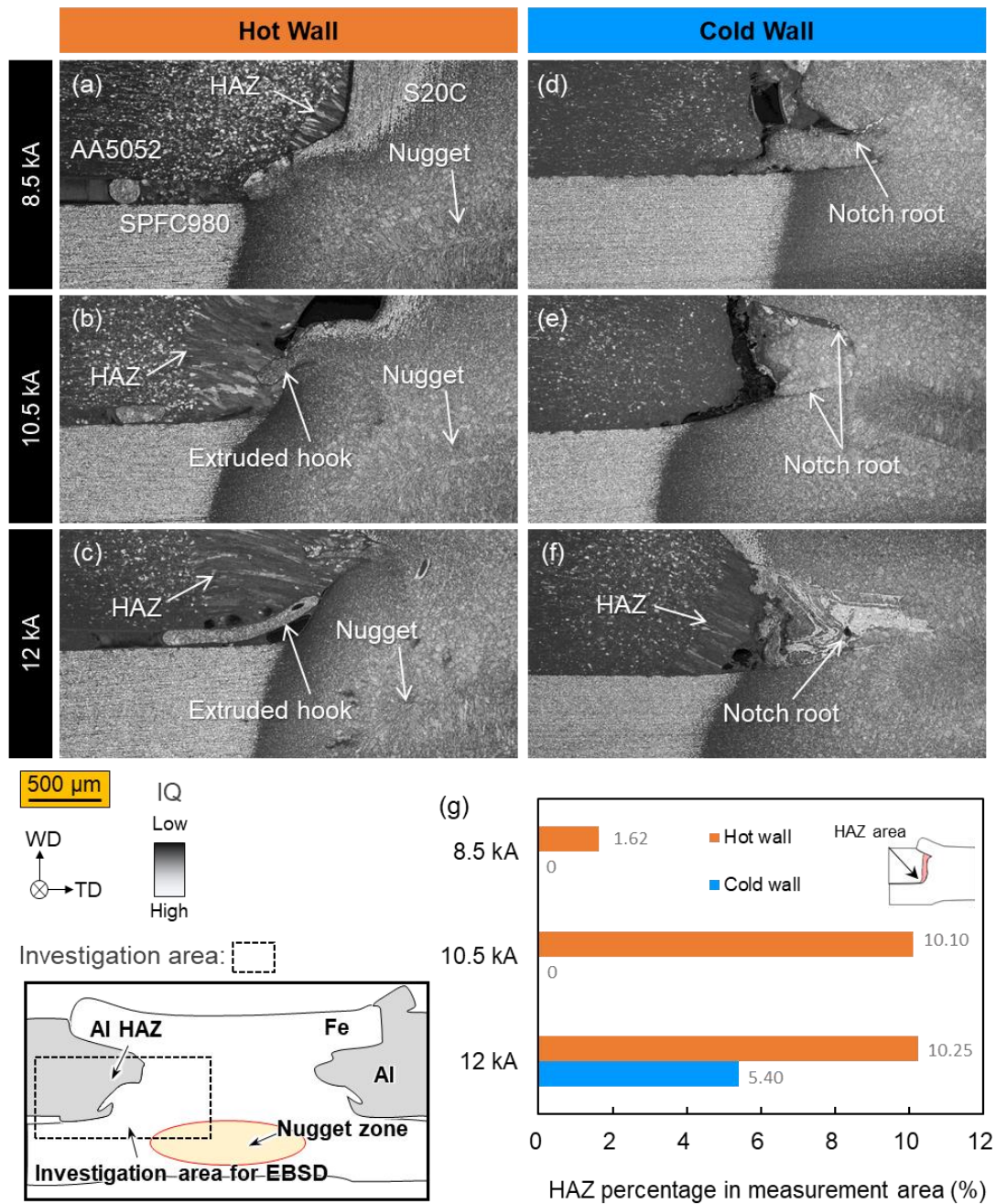


Fig. 4-4 IQ map of the interfaces between the Al HAZ and FZs. IQ maps obtained with (a-c) wall parameters and (d-f) cold wall parameters depending on the welding currents, and (g) Al HAZ percentage in the measurement area. IQ: Image quality.

To distinguish the presence of the Al HAZ in terms of crystallography, EBSD analyses were conducted. Fig. 4-4 presents large-area EBSD maps, i.e., image quality (IQ) maps of the REW joints, including the AA5052, S20C, and SPFC980 alloys. Fig. 4-4(a-c) illustrate the hot wall cases, where the presence of the HAZ with extruded hooks in the Al alloys is clearly evident irrespective of the applied welding current. These visual representations provide clear evidence of HAZ formation and its consistent occurrence in the Al alloys with the hot wall configuration. Conversely, in the cold wall case, despite the application of high welding currents of 8.5 and 10.5 kA, dendrites presumed to be HAZ or obvious coarse grains are not visible in the Al alloys as evident in Figs. 4-4(d) and (f). This result is in stark contrast to that obtained for the hot wall condition, and evidently, the insulating coating formed a cold wall. Nevertheless, a welding current of 12 kA partially neutralized the insulating coating and created an Al HAZ. Further, contrary to effectively suppressing the Al HAZ, a notch root formed owing to the deformation of S20C. This phenomenon occurred in all the cold wall cases, irrespective of the increase in the welding current. The correlation between the process parameters and Al HAZ is shown in Fig. 4-4(g); it was calculated as the percentage occupied by the Al HAZ over the EBSD scan area (i.e., total EBSD measuring area). Compared to all the applied currents, the HAZ percentage, hot wall, and cold wall detected at 8.5 kA are relatively small, 1.62%, and 0% (i.e., not formed), respectively. As the welding current is increased to 10.5 kA, the HAZ percentage in the hot wall case increases remarkably to 10.1%, whereas it is 8.48% at 8.5 kA. By contrast, no HAZ forms in the cold wall case (0% HAZ presence) at any of the applied welding currents. At 12 kA, the HAZ percentage at the hot wall increased to 10.25%, which is slightly higher (by 0.15%) than that observed at 10.5 kA. Furthermore, a HAZ percentage of 5.4%

occurs in the cold wall case. In summary, at 8.5 and 10.5 kA, no HAZ formation is observed in the cold wall case because of the presence of the insulating coating. Conversely, at 12 kA with a large shank diameter, Al HAZ formation is observed owing to thermal conduction through the contact between the Al alloy and S20C.

The highly-magnified Al HAZ was further analyzed to determine its recrystallization ability, grain orientation distribution, and grain size, and the results are displayed in Fig. 4-5. The inverse pole figure (IPF) map (see Figs. 4-5(a₁-f₁)) shows that the grain orientation, a major feature of the hot and cold walls, is random after welding. At all currents, dendrites are formed in the solidified part of Al HAZ in the hot wall after melting. As the welding current increases, the dendrites of the Al HAZ become longer or wider. In contrast, no solidification phenomena, such as dendritic formation, are observed within the Al alloy in the cold wall case at welding currents of 8.5 and 10.5 kA; furthermore, a more refined grain structure is evident relative to the AA5052 BM, as presented in Fig. 4-5(d₁-e₂). This grain clearly suppresses heat transfer to the Al alloy because of thermal insulation and proves that Al is only affected by the compressive force of the indentation load applied during welding. Nevertheless, even in the cold wall case, dendrites of Al are observed, because the increase in the shank diameter of S20C caused by the increased heat and press-fitting results in direct contact with the Al alloy as displayed in Figs. 4-5(f₁) and (f₂). In this study, the grain orientation spread (GOS) was assumed to be a recrystallized grain with an orientation difference of less than 2° and was used to indicate the recrystallized fraction. As seen in Fig. 4-5(g), the recrystallized fraction of the AA5052-H32 BM is 33.9%, and the recrystallized fraction is significantly higher than that of the BM under all welding conditions. Notably, the recrystallization fraction is high in the cold wall case, in which dendrites

are not found, and a value of 99.5% (i.e., close to 100%) is obtained even under the condition of 12 kA. This finding suggests that the cold wall temperature does not cause melting, which would increase the grain size; instead, the temperature range is suitable for recrystallization. The measured grain sizes, presented in Fig. 4-5(h), are representative of the initial state of the AA5052-H32 BM. At all currents applied in the hot wall case, the observed grain exhibits coarser dimensions in contrast to the 14.8 μm baseline of the initial Al BM. Notably, this coarsening trend persisted even at 12 kA in the cold wall case; however, at 8.5 and 10.5 kA, both the walls are devoid of Al HAZ and exhibit finer grains.

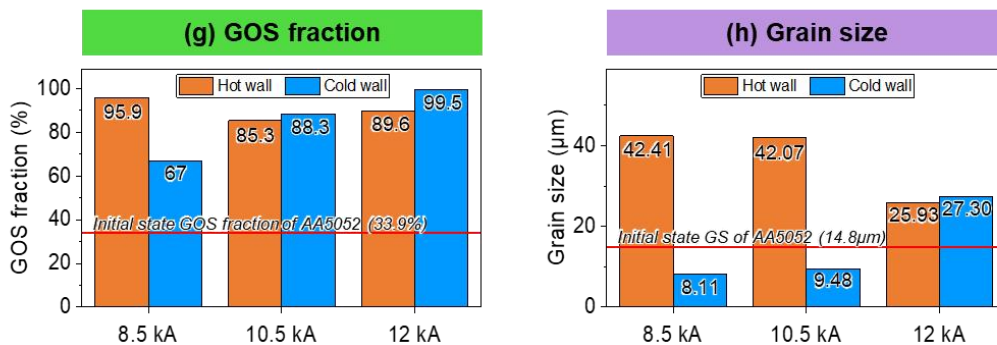
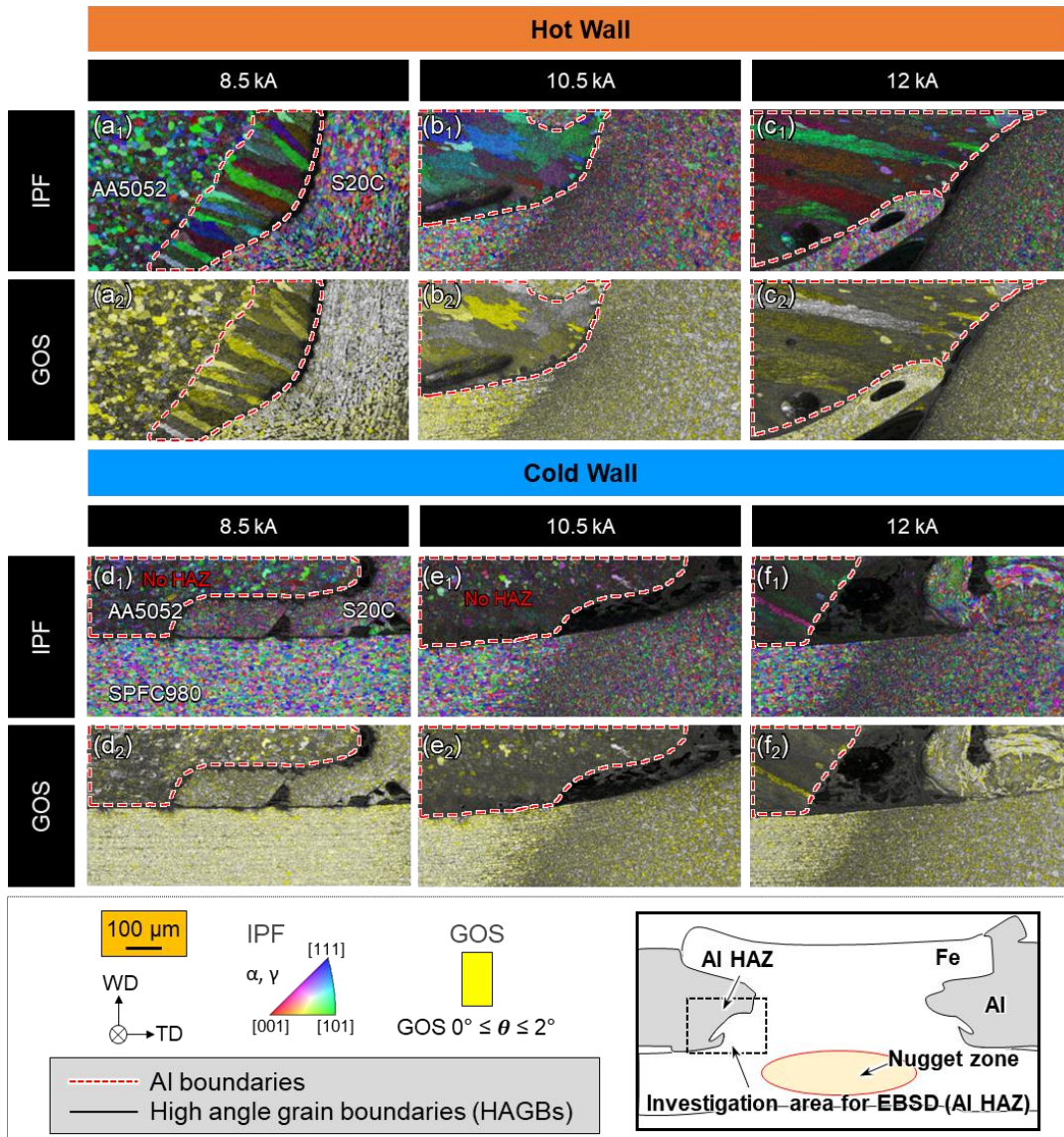


Fig. 4-5 EBSD results of the Al HAZ depending on welding parameter. (a₁-c₁) IPF map and (a₂-c₂) GOS map of hot wall parameter, (d₁-f₁) IPF map and (d₂-f₂) GOS map in the cold wall case, (g) fraction of GOS, and (h) value of GS. IPF: inverse pole figure; GOS: grain orientation spread, GS: grain size.

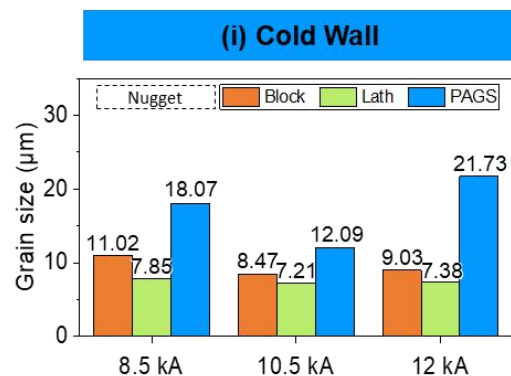
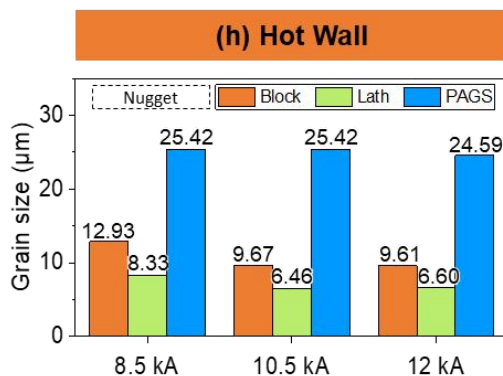
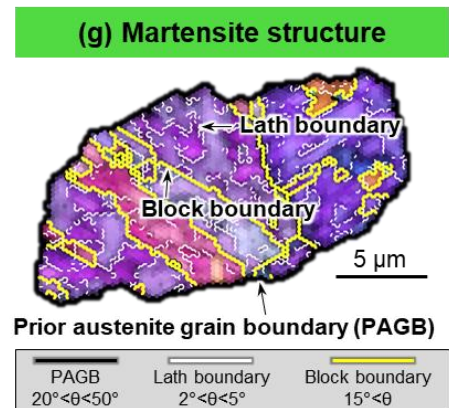
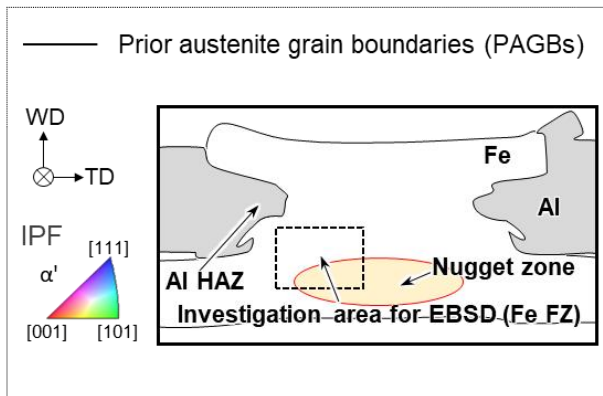
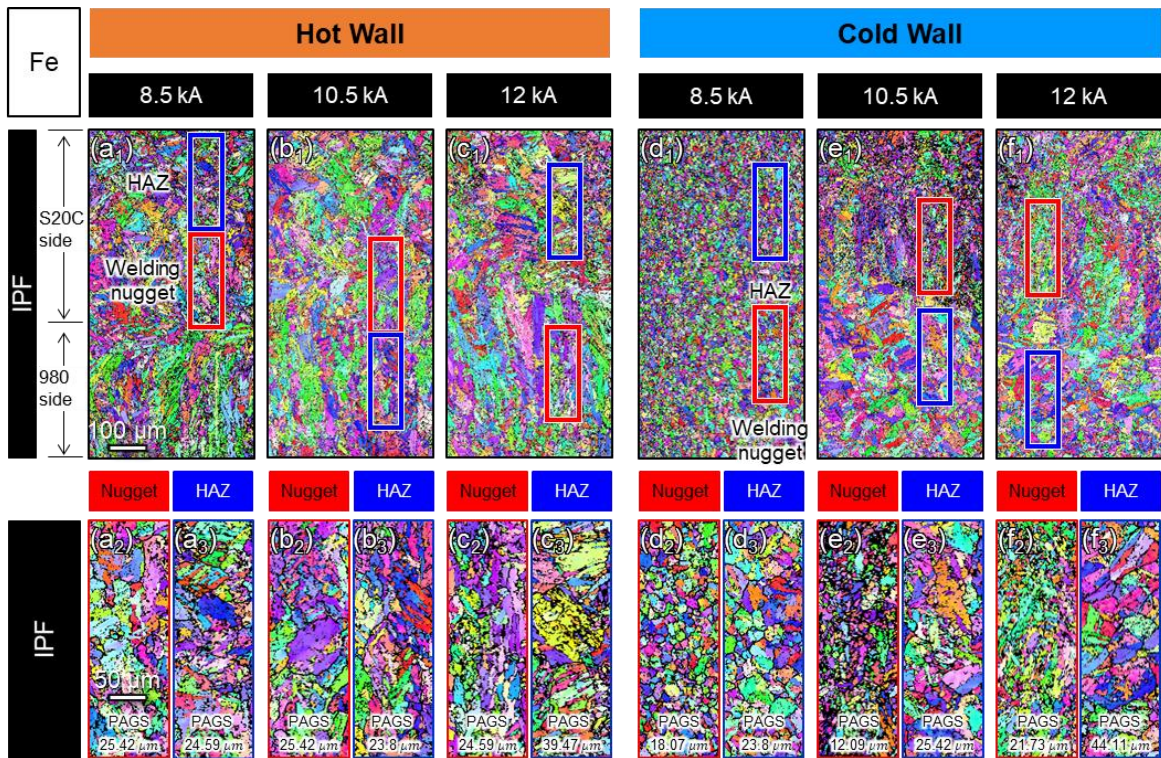


Fig. 4-6 IPF maps with PAGBs around FZ. (a₁-f₃) IPF map and PAGS in FZ, (g) martensite structure, and nugget grain size changes in the (h) hot wall and (i) cold wall cases. PAGB: prior austenite grain boundary; PAGS: prior austenite grain size.

Fig. 4-6 presents the IPF maps and prior austenite grain boundaries (PAGBs, $20^\circ < \theta < 50^\circ$) around the FZ. Fig. 4-6 (a₁-f₃) show the changes in the welding nugget and HAZ dimensions (i.e., grain distributions) according to the welding currents in the hot and cold wall cases, together with the high-magnification image, and the grain orientations are all randomly distributed. Figs. 4-6 (a₂), (b₂), and (c₂) depict enlarged images of the nugget parts shown in Figs. 4-6 (a₁), (b₁), and (c₁) under the hot wall condition. At 8.5 kA, the prior austenite grain size (PAGS) is 25.42 μm , and at 10.5 and 12 kA, the PAGSs are 25.42 and 24.59 μm , respectively. As shown in Figs. 4-6(a₃), (b₃), and (c₃), the PAGSs of the HAZ are 24.59 and 23.8 μm for the notch region under current conditions of 8.5 and 10.5 kA, respectively. However, at 12 kA, the PAGS increases to 39.47 μm . The PAGSs in the cold wall condition are generally lower than those in the hot wall condition. Figs. 4-6 (d₁), (e₁), and (f₁) show enlarged images of the nuggets, and their measured values are shown in Figs. 4-6 (d₂), (e₂), and (f₂). At 8.5 kA, the PAGS is 18.07 μm , whereas at 10.5 kA, it decreases to 12.09 μm , and at 12 kA, the PAGS significantly increases to 21.73 μm . Overall, the grains of the nugget under the cold wall current condition are finer than those in the hot wall condition. In particular, finer grains were observed at 10.5 kA than at 8.5 kA. The PAGSs of the HAZ in the cold wall case are similar to those observed in the hot wall case at each applied current, and the corresponding enlarged images and measured values are shown in Figs. 4-6 (d₃), (e₃), and (f₃). The PAGSs are 23.8 and 25.42 μm at 8.5 kA and 10.5 kA, respectively, and when the current increases to 12 kA, the PAGS increases to 44.11 μm ; this increasing trend is similar to that observed in the hot wall case. The crystal grains in the HAZ at 12 kA HAZ coarser than those observed at low currents.

The thick black line denotes the PAGB highlighted in the IPF. Fig. 4-6(g) shows

the structure of the PAGB schematically. When low-carbon steel is welded, the molten zone transforms into austenite at a temperature above AC3 and then transforms into martensite, bainite, and ferrite depending on the cooling rate; the higher the cooling rate, the higher the martensite fraction[7]. That is, the grain boundaries that become austenite at high temperatures (i.e., over AC3 point) are called PAGBs. A previous study reported that the FZs of the SPFC980 and S20C elements can contain martensite at room temperature during cooling[3]. In general, it can be divided into several martensite packets with HAGB's misorientation angle $\theta > 15^\circ$ inside one PAG (i.e., $20^\circ < \theta < 50^\circ$). This packet is subdivided into blocks consisting of $\theta > 15^\circ$, and each block consists of several laths with LAGBs $2^\circ < \theta < 5^\circ$ in a parallel arrangement[8–10]. Blocks are the fundamental unit that governs the toughness and strength of martensitic steel. Scholars have reported that the hardness increases as the average size of a block decreases[9,11–13]. The measurement results of the blocks, lath, and PAGS at the FZs of the hot wall and cold wall joints based on the welding current are presented in Figs. 4-6(h) and (i). Under the hot wall condition, the block size is 12.93 μm at 8.5 kA, which decreased to 9.67 μm at 10.5 kA and further to 9.61 μm at 12 kA, exhibiting a linear decreasing trend. The lath size also displayed a diminishing trend, measuring 8.33 μm at 8.5 kA and 6.60 μm at 12 kA, with a slight increase of 0.14 μm compared to the 10.5 kA case. Overall, both the block and PAGS sizes at each current are smaller in the cold and hot wall cases.

4.3.3. Mechanical behaviors

A micro-Vickers hardness test was conducted to assess how the hot and cold walls contributed to the mechanical properties of the weld joint. Fig. 4-7(a) illustrates the

micro-Vickers hardness measurement position on the REW weldment and the hardness value of each BM. The average hardness values of the nugget part within the FZ for each welding current under different wall conditions are presented in Fig. 4-7(b). Under the hot wall condition with 8.5 kA, the average hardness of the nugget reaches 426 HV, surpassing the 307 HV of the as-received SPFC980. When the welding current increases to 10.5 kA, the hardness value slightly increased to 454 HV compared to that in the 8.5 kA case, but it exhibits a slight decrease to 439 HV at 12 kA. The cold wall case at 8.5 kA yields a hardness value of 422 HV, similar to that of the hot wall case. As the welding current increases to 10.5 kA, the hardness increases by 85 HV, reaching 539 HV. This value marks a significant increase compared to the same current conditions with the hot wall configuration. At a welding current of 12 kA, the HV hardness value measures 477 HV, displaying a slightly reduced hardness in a manner similar to that of the hot wall. The hardness values obtained in the nugget section surpass those of the SPFC980 BM under all conditions, a phenomenon attributable to martensitic transformation. It is well known that the RSW process tends to increase hardness due to the formation of martensite resulting from rapid cooling rates[14]. Furthermore, the large difference in hardness values observed with the 10.5 kA welding current distinctly demonstrated that the distinction between hot and cold walls, determined by the presence or absence of an Al HAZ, governs the FZ hardness of steel. The hardness distribution across the cross sections of the hot wall and cold wall junctions are displayed in Figs. 4-7(c) and (d). Overall, the hardness mapping image clearly reveal consistently lower hardness values on the hot wall compared to the cold wall. Notably, higher maximum hardness—is obtained in the cold wall case across all current conditions, surpassing the corresponding values in the hot wall case. The hardness differential between the cold

and hot walls can be as high as 198 HV.

The hardness of the nugget part is affected by the size of the blocks or laths that constitute martensite. Fig. 4-6(g) shows that lath martensite is composed of different boundaries, including the PAGB, block boundary, and lath boundary. This lath martensite and PAGB are observed in all FZs in both the hot and cold wall cases (see Figs. 4-6 (a₁-f₃)). Previous studies have highlighted that the block size generally decreases with the PAGS. This reduction hinders dislocation movement during the deformation of lath martensite and has a significant impact on material strengthening [15,16]. This can be correlated with the average hardness of the nugget, as shown in Fig. 4-7(b). As confirmed in Figs. 4-6(h) and (i), the block size of the nugget part in the hot wall case is 12.93 μm and 9.67 μm under the current conditions of 8.5 kA and 10.5 kA, respectively. The average hardness of the nugget part is 426 HV and 454 HV, respectively, displaying an increasing trend as the block size decreases. For the 12 kA current condition, a hardness of 439 HV was measured with a block size of 9.61 μm , which showed a value similar to that obtained at 10.5 kA. Trends similar to those of the block size and hardness are also observed in the lath size. In the cold wall cases, the relationship between the block and lath size and hardness is more evident. At 8.5 kA, which exhibits the lowest average hardness value of the nugget part at 422 HV, the block and lath sizes are 11.07 μm and 7.85 μm , respectively. Conversely, at 10.5 kA, which displayed the highest average hardness value of 539 HV, the block and lath sizes are 8.47 μm and 7.21 μm , respectively, representing the smallest values among the welding current conditions. At 12 kA, the block and lath sizes increased to 9.03 μm and 7.38 μm , respectively, accompanied by a reduced hardness of 477 HV compared to 10.5 kA. These results confirm that both block and lath sizes affect the hardness of the

material.

In all Al HAZs generated by thermal conduction upon contact with steel, hardness values ranging from 70 to 79 were measured, and no significant difference from the hardness of the Al BM, which was 74 HV, was observed. However, in the absence of an Al HAZ, e.g., cold wall conditions with 8.5 kA and 10.5 kA, the hardness values of the Al side adjacent to the steel were measured to be 62 HV and 67 HV, respectively. These values were lower than those of the base metal. The decrease in hardness on the Al side at 8.5 kA and 10.5 kA in the cold wall case could be attributed to the softening of the strain-hardened Al material. The AA5052- H32 alloy exhibits work-hardening characteristics, and upon experiencing recrystallization due to heating, a softening effect occurs, leading to a reduction in hardness compared with that of the initial BM [17,18]. As shown in Fig. 4-5(g), recrystallization is confirmed under all current conditions, indicating that softening resulting from strain hardening was the cause of the decrease in hardness. Fig. 4-7(e) shows the relationship between Al grain size and hardness obtained by applying the Hall–Petch relation equation. The mechanism through which grain refinement influences the physical properties can be explained by the Hall–Petch relationship and can be expressed as follows:

$$HV = HV_0 + kd^{-1/2} \quad (2)$$

where HV is the hardness, d is the average grain diameter, and HV₀ and K are constants. Although the grain refinement was remarkable for Al, the effect of increased hardness due to grain refinement was not observed because work hardening was released by recrystallization. Despite softening occurring under all conditions,

relatively no decrease in hardness compared to the BM was observed in the hot and cold wall cases with a welding current of 12 kA, where the Al HAZ was present. Thus, a particular factor (e.g., chunks of IMCs) can increase the hardness even when the work hardening effect is lost along with the softening of Al HAZ. In this regard, the temperature measurements and phases are further described in the discussion section.

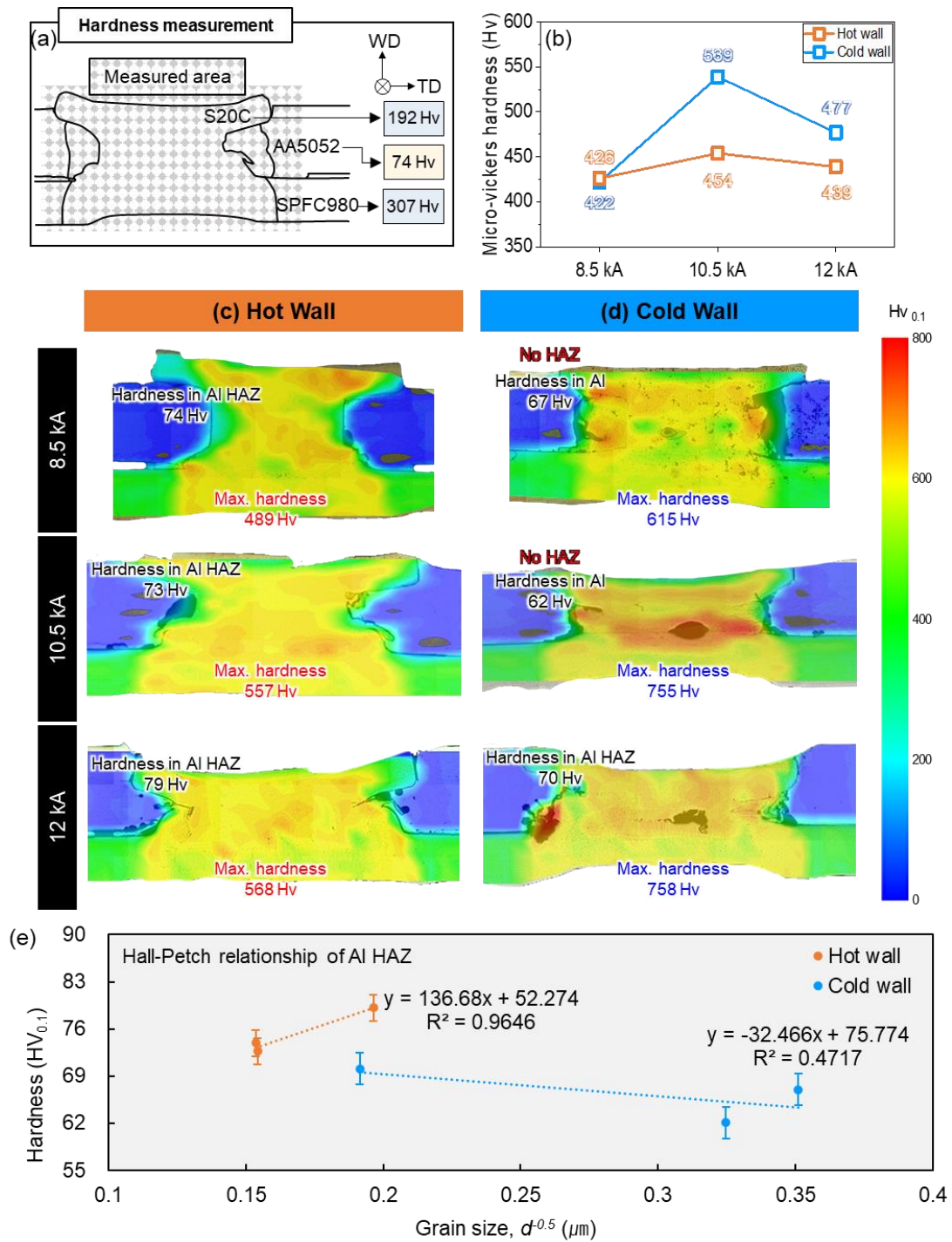


Fig. 4-7 Micro-Vickers hardness distributions of specimens based on the wall and current parameters. (a) Hardness measurement positions, (b) average hardness of nugget zone, hardness distributions of (c) hot wall parameter specimens and (d) cold wall parameter specimens, and (e) Hall Petch plot of Al alloys.

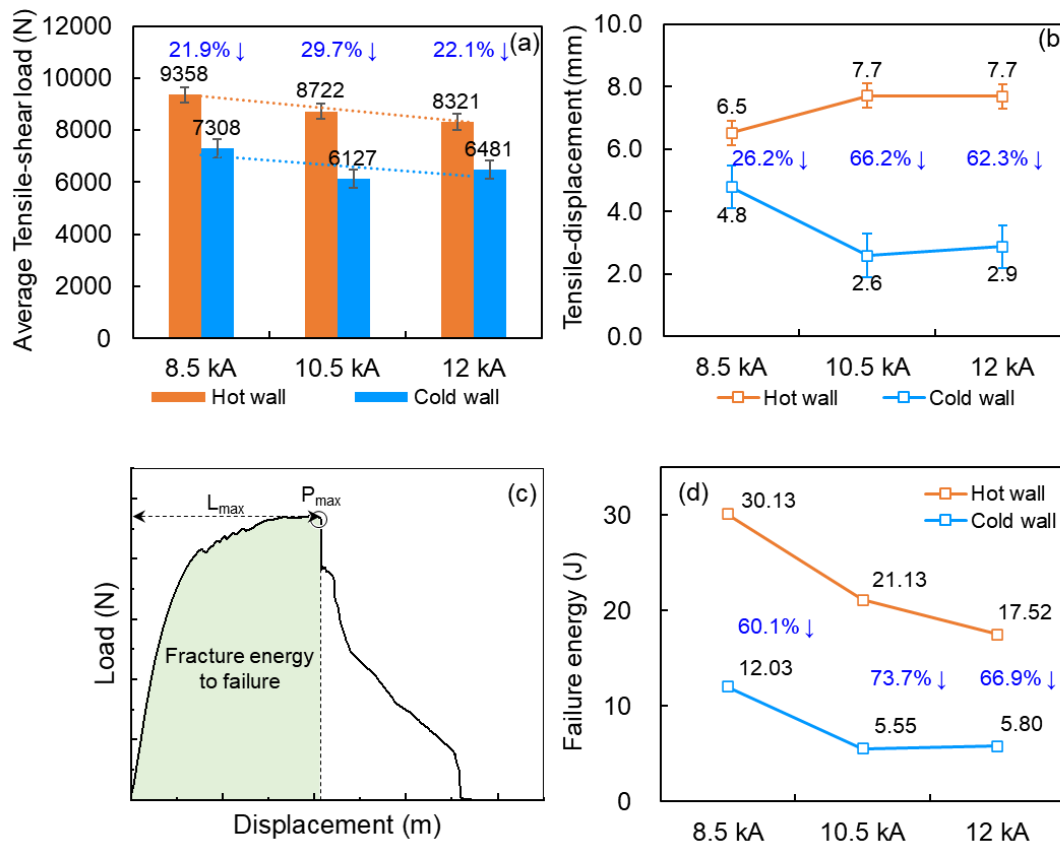


Fig. 4-8 Results of tensile-shear test for the REW specimens based on wall parameters. (a) tensile-shear load, (b) Tensile-shear displacement, (c) definition of failure energy, and (d) failure energies for different welding currents.

Fig. 4-8 illustrates the results of the tensile-shear load tests, along with the failure energy, providing quantifiable insights into the energy expended up to the point of fracture for both the hot and cold wall weld joints. The variations in tensile-shear load and displacements of the hot and cold wall weld joints due to welding current are presented in Figs. 4-8(a) and (b). For the hot wall joints, a peak load of 9358 N is obtained at a welding current of 8.5 kA. As the welding current increased to 10.5 kA, the load decreases to 8722 N. Upon reaching a welding current of 12 kA, the tensile-shear load exhibits a value of 8321 N, displaying a progressive linear decrease. In contrast to the hot wall joints, the cold wall joints exhibit a consistently lower tensile-shear load,

ranging from approximately 22% to 30% across all current conditions. However, unlike the gradual decrease observed in the hot wall joints, the load reduction in the cold wall joints exhibited a notable deviation. Specifically, when the current exceeds 10.5 kA, the diminishing load increases to 6481 N, indicating an increment of approximately 300 N compared to the 6127 N observed at 8.5 kA. Regarding displacement, the hot wall exhibits a displacement of 6.5 mm at a welding current of 8.5 kA. Increasing the welding current to 10.5 kA results in a displacement of 7.7 mm, marking a 1.2 mm augmentation compared to the 8.5 kA condition. Conversely, the displacement of the cold wall joints remained consistently lower than that of the hot wall joints across all current conditions. At a welding current of 8.5 kA, the measured displacement is 4.8 mm, signifying a reduction of approximately 26% in comparison to the corresponding hot wall current condition. Notably, a substantial reduction of approximately 66% is observed in the cold wall displacement as the current condition surpassed 10.5 kA, resulting in a displacement of 2.6 mm. At a current of 12 kA, a slightly increased displacement of 2.9 mm was measured compared to that at 10.5 kA. However, this finding still reflects a considerable decrease relative to the hot wall displacement. These characteristics are intrinsically connected to the failure energy expended prior to fracture. Fig. 4-8(c) shows the definition of the failure energy corresponding to the maximum displacement (L_{\max}) of the peak load (P_{\max}) determined from the load-displacement plot using OriginPro® 2021 software. The failure energy, which reflects the contribution of peak load and displacement to physical properties, can be expressed as follows:

$$W = \int_0^x f(x)dx \quad (3)$$

where W is the failure energy and x is the displacement at the peak load. As depicted in Fig. 4-8(d), the failure energy is 30.13 J for the 8.5 kA condition and 17.52 J for the 12 kA condition of the hot wall. These values exhibit a noticeable trend of proportional decrease, aligning with the results obtained from the tensile-shear tests. The outcomes pertaining to the cold wall joints demonstrated reduced failure energy in comparison to the hot wall joints. Notably, at 10.5 kA, only 5.55 J of failure energy is observed, signifying a substantial reduction of approximately 74% when compared with the failure energy of the hot wall joints. This lower failure energy propensity can be attributed to the occurrence of interfacial failure (IF), a phenomenon corroborated by preceding research findings[5].

3.4. Fracture modes

Fracture mode analysis is an effective method of identifying the weakest point in a joint. After conducting the tensile-shear test under various welding conditions for the hot wall joint, a comprehensive 3D scanning procedure was performed to capture the fractured morphology. The outcomes of this scanning process are visually presented in Fig. 4-9. Under the welding condition of 8.5 kA, the S20C element tears off along with the 980 steel on the lower plate, resulting in a bottom pullout failure (PF) mode of fracture, as depicted in Fig. 4-9(a). An approximately 0.4-0.5 mm residue is observed at the edge of the torn part, as shown in Fig. 4-9(b). In contrast, under the welding condition of 10.5 kA, partial degradation of the element occurs, leading to the formation of a partial plug (PP) mode, as seen in Figs. 4-9(c) and (d). It is essential to note that the AA5052 alloy experiences fracture, and the residual element height measures 3.13 mm above the lower steel plate. Under the significantly elevated current condition of 12 kA,

the structural integrity of the element remains after the tensile-shear test. However, a distinctive transformation is observed near the element, where the AA5052 material of the upper plate undergoes elongation. This phenomenon leads to the establishment of an upper PF mode, characterized by a morphology that indicated deformation. In this instance, the element experiences a press-fit displacement of 0.71 mm from the conditions observed at 10.5 kA, resulting in a measured height of 2.42 mm. The fracture configuration and its corresponding profile are visually documented in Figs. 4-9(e) and (f).

The tensile-shear fracture shape of cold wall conditions was also analyzed through 3D scanning, and the results are shown in Fig. 4-10. A distinctive feature is that, unlike the occurrence of various fracture modes in the specimens for each hot wall current condition, IF occurs in the cold wall specimen under all current conditions, and a clear difference in the fracture mode is observed. Thus, the maximum load and displacement obtained in the tensile-shear test may be lower than that of the hot wall. IF mode is generated in the cold wall specimens under all current conditions, but a difference in the shape of the fracture interface is noted. Under the 8.5 kA condition, an irregular fracture interface is discernible, attributed to the fracture pattern that seemingly originated from the S20C element itself (refer to Fig. 4-10(a)). In addition, the profile measurement result of the fracture surface showed that the fracture occurs at the S20C side, as displayed in Fig. 4-10(b). In the case of 10.5 kA (see Figs. 4-10(c) and (d)), the fracture mode can be characterized as an interfacial fracture, extending into the FZ. Nonetheless, the fracture morphology exhibits a concave contour compared to the configuration observed under the 8.5 kA condition. Additionally, a remnant S20C element is observed. Based on the discerned profile, it can be postulated that a fracture

occurs within the welding nugget on the S20C side. When the welding current reached 12 kA, SPFC980 exhibits a torn shape with a depth of 0.41 mm at the time of fracture, indicating that the fracture occurred in the nugget or HAZ area of the SPFC980 side as shown in Figs. 4-10(e) and (f). Fracture mode analysis revealed IF, demonstrating markedly lower energy consumption to fracture compared to the PP mode. This disparity in fracture energies can be interpreted as an additional repercussion of the steel melting effect induced by the Al HAZ.

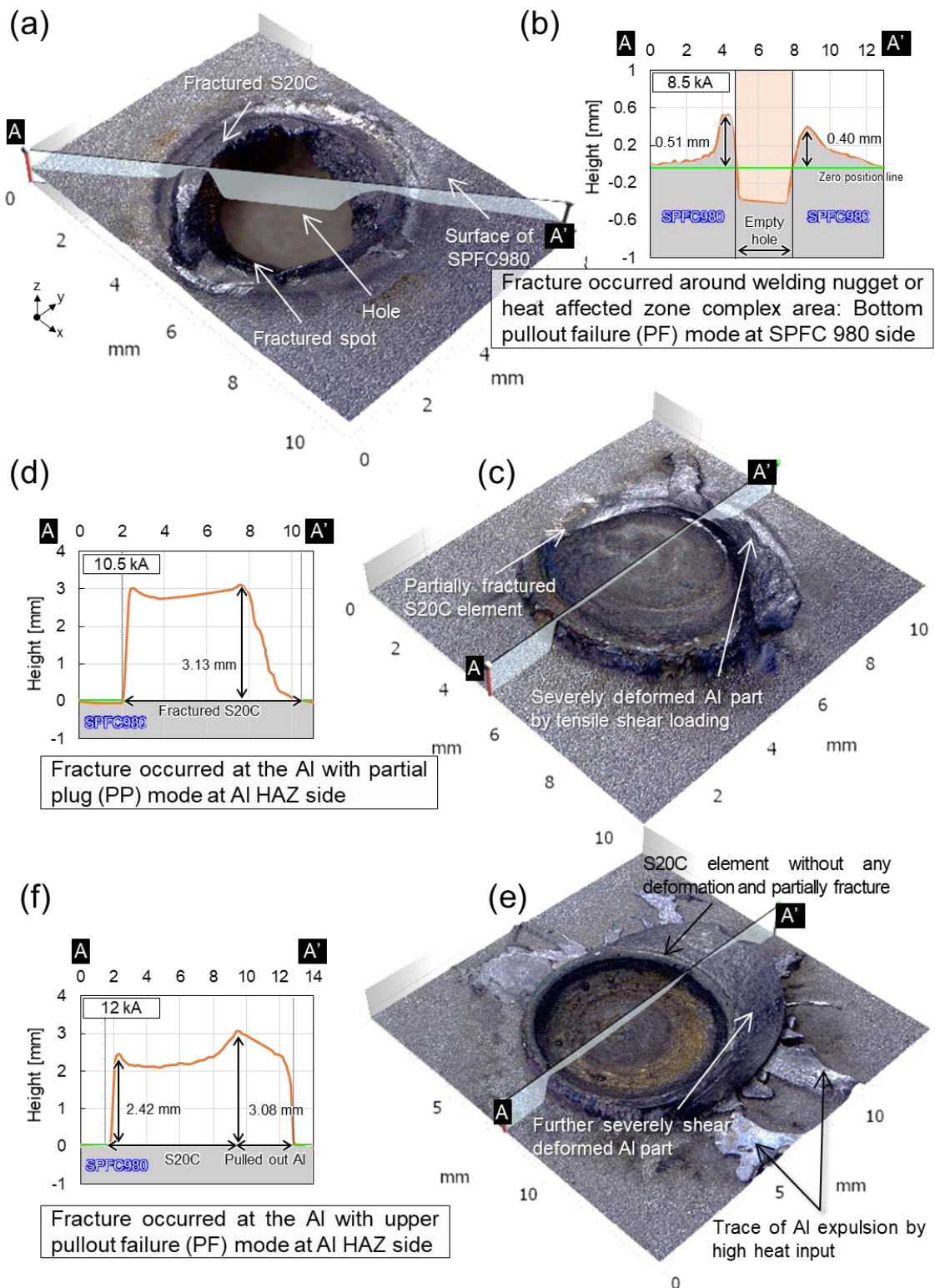


Fig. 4-9 Three-dimensional scanning results of the fractured surface in the hot wall case. Fractured surface with failure mode and profiles corresponding to (a) and (b) 8.5 kA, (c) and (d) 10.5 kA and (e) and (f) 12 kA.

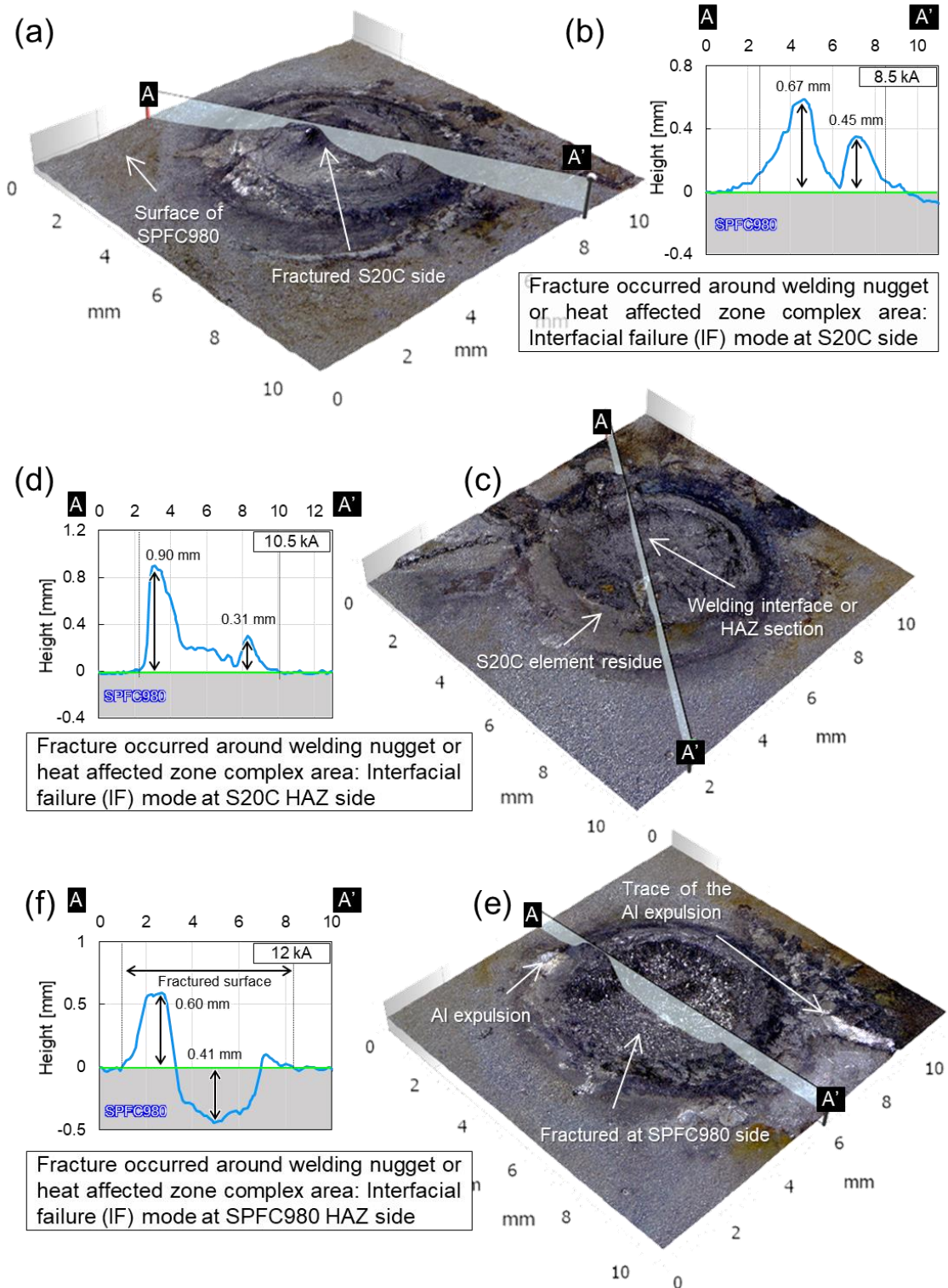


Fig. 4-10 Three-dimensional scanning results of the fractured surface in the cold wall case. Fractured surface with failure mode and profiles corresponding to (a) and (b) 8.5 kA, (c) and (d) 10.5 kA, and (e) and (f) 12 kA.

4.4 Discussion

4.4.1 Temperature behaviors inside weld joints

In the case of RSW, due to the rapid cooling rate, it has been reported that most of the phase transformation to martensite occurs during solidification in low-carbon steel nuggets[7]. Additionally, as AA5052 is a work-hardening material, the work-hardening effect can be lost due to heat[17]. Consequently, understanding the thermal behavior is crucial, as the temperature at each location of the weld can significantly impact the mechanical behavior of the joint. The temperature conducted by the heat generated by the nugget during welding was measured for each location and is presented in Fig. 4-11. This temperature measurement was performed under the condition of 10.5 kA welding current for both the hot and cold wall conditions. In the case of steel, the temperature was measured at the top of the S20C element (Figs. 4-11(a) and (e)) and the bottom of SPFC980 (Figs. 4-11(b) and (f)). For the Al alloys, temperature measurements were taken in the Al HAZ (Figs. 4-11(c) and (g), corresponding to the Al HAZ of the hot wall in the cold wall) and also in the Al base material located relatively distant from the heat source (Figs. 4-11(d, h). In both hot wall and cold wall cases, the measured temperature of the upper part of the S20C element during welding is 1372 °C. The temperature at the bottom of the SPFC980 is 1372 °C for the hot wall and 1033.3 °C for the cold wall, resulting in a peak temperature difference of approximately 340 °C. This discrepancy in temperature could be due to the contact area with the electrode being wider in the cold wall due to it being pushed in more than in the hot wall by 0.44 mm. This difference in shape is also confirmed by the shank diameter being 6.7% longer than that of the hot wall. The lower temperature in the cold wall could be due to the relatively large amount of heat being taken away from the electrode because of the water-cooling system flowing through the copper electrode. At the cold wall location shown in Fig. 4-11(g), the

measured temperature is 292.2 °C. This temperature is significant because it is in the range in which the hardening effect of AA5052, a work-hardening material, can be lost due to softening through recrystallization. Previous reports have indicated that Al 5xxx series alloys exhibit structural recovery in the temperature range of 100 - 280 °C and recrystallization temperature range of 300 - 340 °C[19,20]. The hardness measurements obtained at positions proximate to the steel within the cold wall and encompassing the Al HAZ indicate values of 67 HV, 62 HV, and 70 HV, respectively. These values are consistently lower than the baseline hardness measurement of 74 HV associated with the Al BM across all examined current conditions. This decrease in hardness suggests that Al softening occurred under all current conditions in the cold wall. In contrast, in Fig. 4-11(c), which corresponds to the Al HAZ location of the hot wall, the measured temperature is 408.8 °C. Despite the conditions conducive to softening, the hardness remains unaltered, which is likely due to the direct contact between steel and Al in the hot wall resulting in higher temperatures and hardness values. The hardness of the Al HAZ under all current conditions is consistently higher than that of the cold wall, potentially due to the presence of Fe_xAl_x series IMCs formed during steel-Al fusion welding. These IMCs are known to have brittle characteristics, and the hardness reduction resulting from the disappearance of the work-hardening effect of the material can be reversed[18,21,22]. Dendrites formed during solidification after melting may also contribute to the hardness increase by forming IMC lumps between the grains, as observed in Figs. 4-4(a), (b), (c), and(f). Additionally, contact between the Al and steel occurs on only one side under in cold wall current case at 12 kA, resulting in the formation of an Al HAZ due to thermal conduction. This finding could explain why the Al HAZ hardness in the cold wall case at 12 kA is higher than those at 8.5 kA and 10.5

kA due to the presence of IMCs. Further discussion of intermetallics in this regard is provided in the Texture and Phase section.

The measured welding temperatures in Figs. 4-11(d) and (h) are 126.6 °C and 170.6 °C, respectively. The difference in temperature at the two locations is related to the cooling rate measured at SPFC980. The measured cooling rates in Figs. 4-11(b) and (f) are 3,409 °C/s and 313.8 °C/s, respectively. Under the 10.5 kA current condition, the cold wall cooling rate is only 9.2% compared to that of the hot wall. This difference in cooling rate is due to the faster escape of heat from the electrode in contact with the material, facilitated by the water cooling system, in the hot wall. The austenite stability can be quantitatively evaluated through the AC3 temperature (fully austenitic temperature) and M_s temperature (martensite start temperature), as recommended by Trzaska et al. (2007) [23] and Wang et al. (2000) [24].

$$Ac3(^{\circ}C) = 973 - 224.5C^{\frac{1}{2}} - 17Mn + 34Si - 14Ni + 21.6Mo + 41.8V - 20Cu \quad (6)$$

$$M_s^0(^{\circ}C) = 545 - 470.4C - 3.96Si - 37.7Mn - 21.5Cr + 38.9Mo \quad (7)$$

where C, Mn, Si, Ni, Mo, Cr, V and Cu represent their respective concentrations as weight percentages. Figs. 4-11(i) and (j) present both the empirical and thermodynamic calculation results. According to the thermodynamic calculations, the AC3 temperatures are 888.3 °C and 883.5 °C for S20C and SPFC980, respectively. In contrast, the empirical formula-based calculations yield values of 874.0 °C and 893.6 °C for S20C and SPFC980, respectively. Similarly, the thermodynamic calculations for the M_s temperature in S20C and SPFC980 result in values of 444.4 °C and 393.8 °C,

respectively, whereas the empirical formula-based calculations give values of 437.1 °C and 407.4 °C for S20C and SPFC980, respectively. The differences between the empirical and thermodynamic values are minimal, with only ±1.6% and ±3.3% variations for AC3 and M_s, respectively. This level of consistency suggests that the results are reliable. Consequently, when the cooling rate measured in Fig. 4-11 is input into the thermodynamic calculation software to calculate the phase fraction, it can be predicted that most of the microstructure in the weld nugget region will exist in the martensite phase.

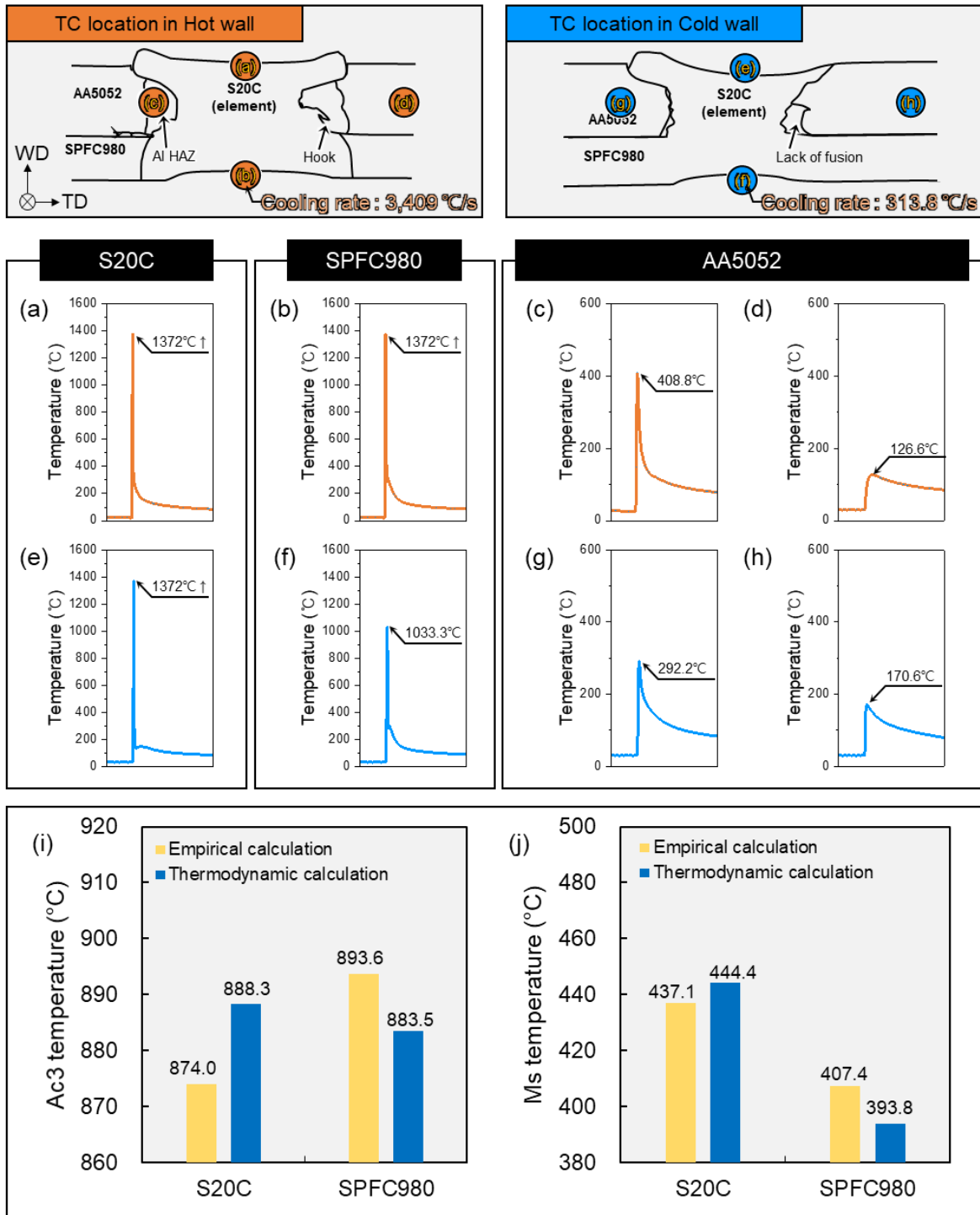


Fig. 4-11 (a-h) Temperature measurements of the REW joints under 10.5 kA current. Numerical prediction results for the (i) AC3 temperature and (j) Ms temperature of S20C and SPFC980.

4.4.2 Phase and texture formation

As a result of welding under the currents of 8.5 kA and 10.5 kA, HAZ was formed on the Al side in the hot wall, but no HAZ was observed in the cold wall. During this process, the average hardness of the Al HAZ on the hot wall was measured to be 74 HV and 73 HV at 8.5 kA and 10.5 kA, respectively. Conversely, the average hardness of the Al side in the cold wall case was measured to be 67 HV and 62 HV under the same current conditions. Previous studies have established that Al_xFe_x IMCs can form at the welding interface during the joining of dissimilar metals, such as steel and Al. These compounds can play a decisive role in altering the mechanical performance of the welded region[4,25–30]. To gain a deeper understanding of the relationship between changes in hardness and the presence of IMCs under various welding conditions, a quantitative analysis of these compounds was conducted using X-ray diffraction (XRD) analysis. Fig. 4-12(a) illustrates the XRD component analysis results for specimens manufactured under the 10.5 kA current condition, and Figs. 4-12(b-e) provide detailed analysis results for each diffraction peak. In Fig. 4-12(b), the diffraction peaks corresponding to Al (111) are clearly observed in the Al BM, hot wall, and cold wall. Fig. 4-12(c) reveals that the diffraction peak of Al (002) coincides with the diffraction peak of the Al BM and cold wall. In contrast, the diffraction peaks of the Fe_1Al_6 , Mg_5Si_6 , and Fe_7Al_{11} phases are evident in the hot wall. Figs. 4-12(d) and (e) display diffraction peaks matching the Al (022) and (113) phases in the cold wall and Al BMs. In the hot wall, the diffraction peaks align with Fe_1Al_6 , Fe_2Al_9 , Fe_5Al_8 , and Fe_7Al_{11} . These findings indicate that a HAZ is formed in the hot wall, unlike the cold wall under the 10.5 kA current condition, and IMCs capable of increasing hardness are generated. If the formation of these IMC aggregates is more prominent in the hot wall, this

characteristic could be the primary factor contributing to the increase in hardness, despite the larger grain size.

For the AA5052 material applied in this study, the weight percentage (%wt) of Fe was adjusted within the range of 0.282 to 5% for thermodynamic simulations. Then thermodynamic simulations were conducted using JmatPro software to investigate the phases that can be formed under these varying Fe concentrations. As shown in Fig. 4-13, it has been confirmed that phases such as Al_3Fe , Mg_2Si , and Al_3Mg_2 could be formed when the iron (Fe) content is 0.282%, which corresponds to the composition of the raw material in the AA5052 material. In the process of increasing the Fe content of Al alloy material to 5%, no newly created phase was found, but the Wt% of Al_3Fe gradually increased. Based on thermodynamic simulation results, it was confirmed that Fe_2Al_5 was not formed in the AA5052 material applied in this study.

As a result of XRD measurement in this study, the IMC of Al_6Fe , Al_9Fe_2 , Al_3Fe_5 and $\text{Al}_{11}\text{Fe}_7$ were measured. Al_6Fe is a metastable intermetallic phase first discovered by Hollingsworth and is reported to form through rapid cooling[31]. It was also found that at cooling rates between 10^{-1} K/s and 10 K/s, a mixture of Al_xFe IMC phases is generally formed, at cooling rates between 2 and 5 K/s a mixture of Al_xFe and Al_6Fe intermetallic phases can form, and at rates above 20 K/s, a metastable Al_xFe phase or a metastable Al_9Fe_2 phase can be obtained[32]. However, the limit above which Al_xFe or Al_9Fe_2 are formed is unknown. These phases occur at very high cooling rates. It is currently assumed that the formation of so many different metastable phases at higher cooling rates is due to increased super cooling and changes in the nucleation conditions and growth of intermetallic phases. It has also been considered that all the different metastable phases may form due to the influence of other alloying elements[33,34]. As a

result of the cooling rate measurement in this study, a very fast cooling rate of approximately 3,680 K/s (3,409 °C/s) was measured (Fig. 4-11(b)). It has also been reported that the Al₁₁Fe₇ phase was also detected by the rapid solidification[35]. Based on the literature mentioned above, such a rapid cooling rate can lead to the formation of IMC of Al₆Fe, Al₉Fe₂ and Al₁₁Fe₇.

Fig. 4-14 shows the IMC formation mechanism during fusion welding using RSW as an example. The formation and growth of FeAl₃ and Fe₂Al₅ intermetallic compounds (IMCs) in Al-Fe joints during fusion welding can be divided into four stages, as depicted in Fig. 4-14. In the first stage (Fig. 4-14(a)), the Al undergoes melting due to the main resistance heat, resulting in the molten Al spreading across the surface of the steel. This stage mainly involves heat and mass transfer processes. The second stage is characterized by the dissolution of Fe in the molten Al alloy. This dissolution occurs as a result of the heat transfer from the molten Al and the main resistance heat to the steel, coupled with the migration and diffusion of Al atoms toward the Fe. Metallurgical reactions occur during this stage, leading to the formation of Fe₂Al₅ IMC at the interface between the Al alloy and the steel. In the second stage, the Fe₂Al₅ IMC formed at the interface between the Al alloy and the steel appears in a plate-like shape, as illustrated in Fig. 4-14(b). The Fe₂Al₅ IMC takes the form of a layer sandwiched between the aluminum alloy and the steel in this stage. This results in the formation of two new interfaces: one between the Fe₂Al₅ IMC layer and the steel, and another between the Fe₂Al₅ IMC layer and the aluminum alloy. In order to form new Al-Fe IMCs during this stage, Fe and Al atoms need to migrate through the existing Fe₂Al₅ IMC layer. This migration process is associated with solid-state diffusion rather than a solid-liquid reaction. In general, Al atoms have a higher diffusivity in Fe₂Al₅ IMC than iron atoms. This trend lead to the third stage, characterized by the formation of a substantial number of Fe₂Al₅ IMCs within the steel and an increase in the

thickness of the IMC layer, as depicted in Fig. 4-14(c). As the Fe_2Al_5 IMC layer forms, only a restricted number of Fe atoms migrate towards the Al alloy. This leads to the formation of FeAl_3 in the Al alloy around the interface between the Fe_2Al_5 IMC layer and the Al alloy, rather than the continued formation of Fe_2Al_5 IMC. The anisotropic characteristics of FeAl_3 contribute to the formation of needle-like structures, as illustrated in Fig. 4-14(d)[36,37].

Fig. 4-15(a) illustrates the REW process and an enlarged view of weld interface applied in this study. Unlike the above mentioned RSW, where steel and aluminum alloy are joined through direct contact, in REW, the welding between similar materials is accomplished by the contact between the steel element and the underlying steel plate. Because steel and Al alloy do not come into direct contact and do not melt, it is difficult for IMC layer to form. As depicted in Fig. 4-15(b), the pressing force eliminates the existing gap between steel and aluminum, and the resistance heat generated from the weld nugget is transferred to the aluminum side. During this process, a PMZ (Partially melted zone) is formed at the interface between steel and aluminum. Fig. 4-15(c) shows that, as a consequence of this process, IMC can be formed locally when a PMZ is generated, depending on the heat input.

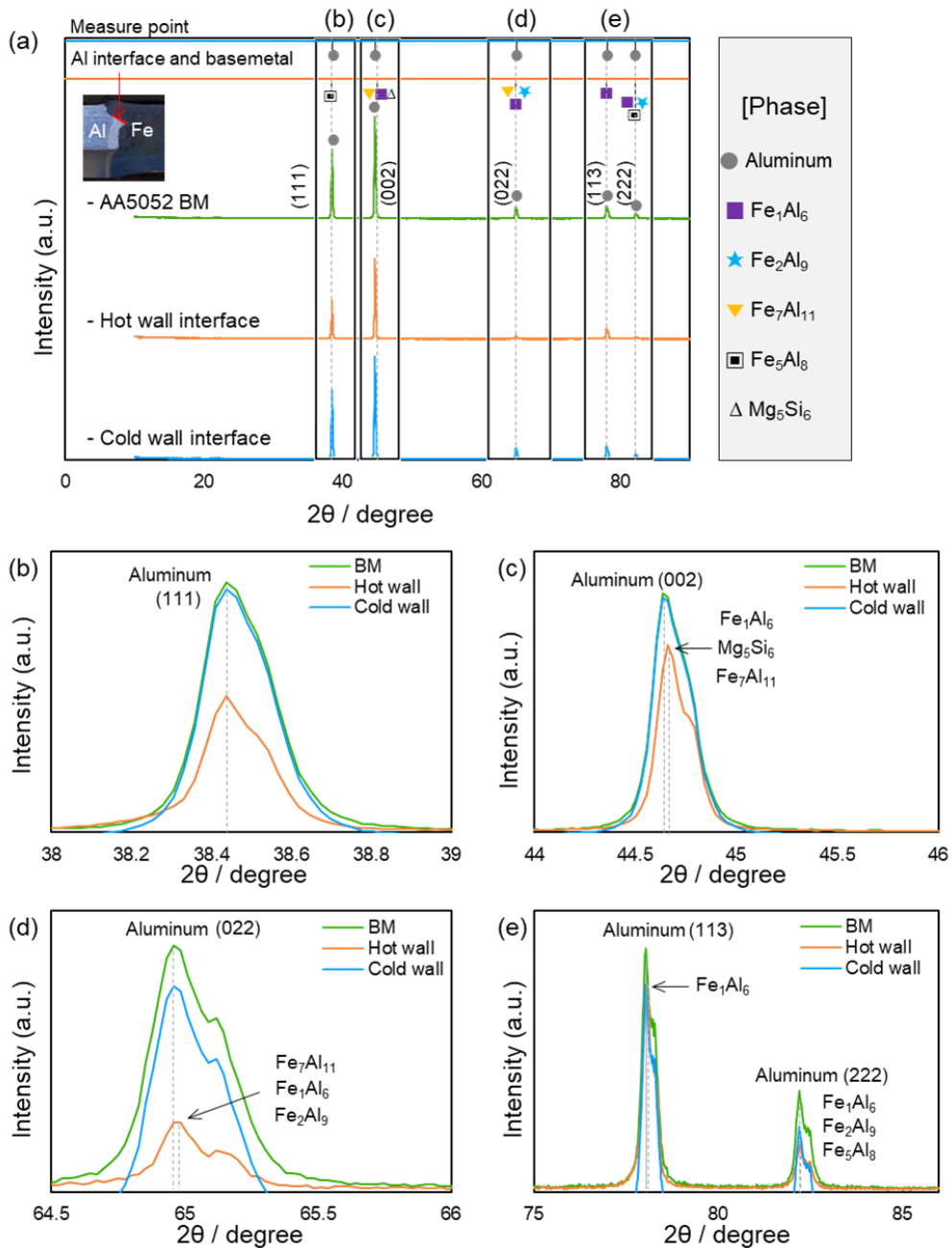


Fig. 4-12 XRD patterns at the interface at 10.5 kA in both wall cases. (a) Results with a definition of the measurement point and components and, (b-e) detected phases in the magnified graph of the peak position. XRD: X-ray diffraction.

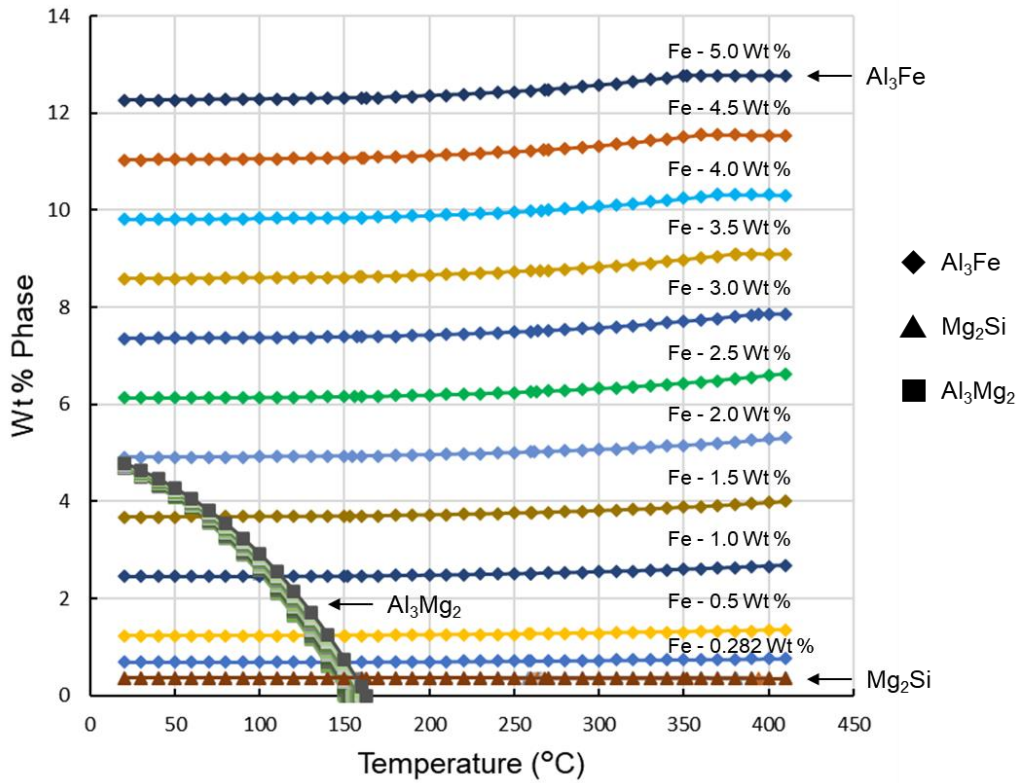


Fig. 4-13 The results of thermodynamic simulations predicting the phases formed based on the weight of Fe in an AA5052.

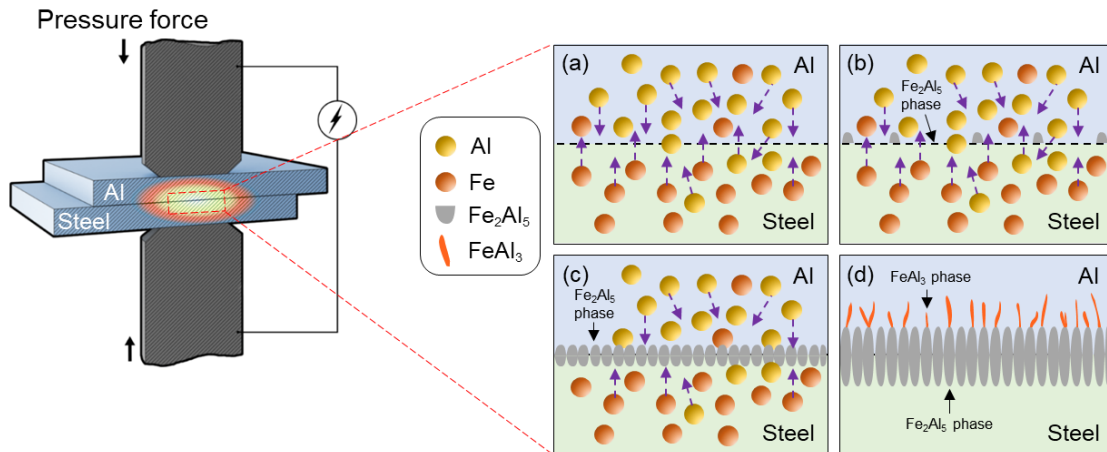


Fig. 4-14 schematic diagrams of the four stages for formation and growth of the Fe-Al IMC layer. (a) the first stage, (b) the second stage, (c) the third stage and (d) the fourth stage.

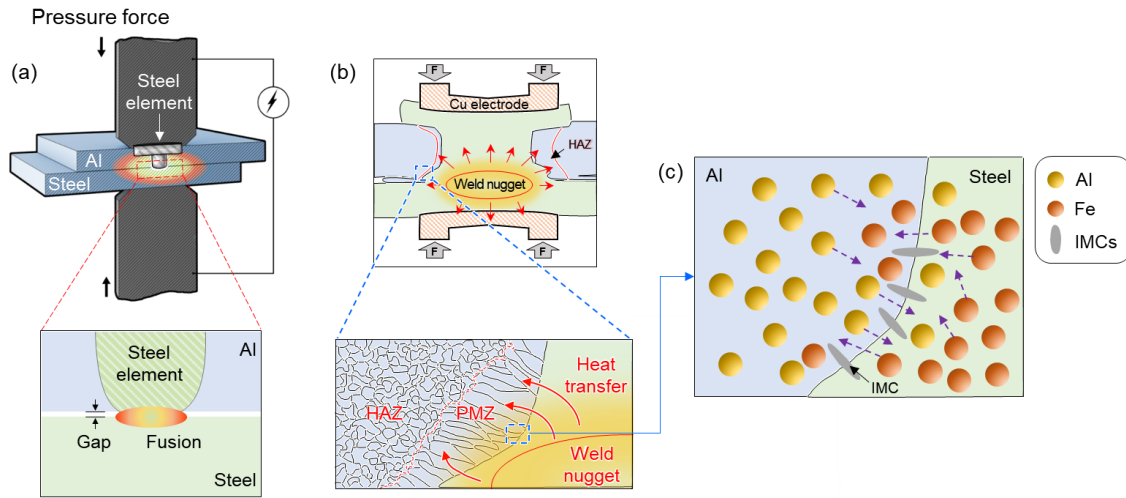
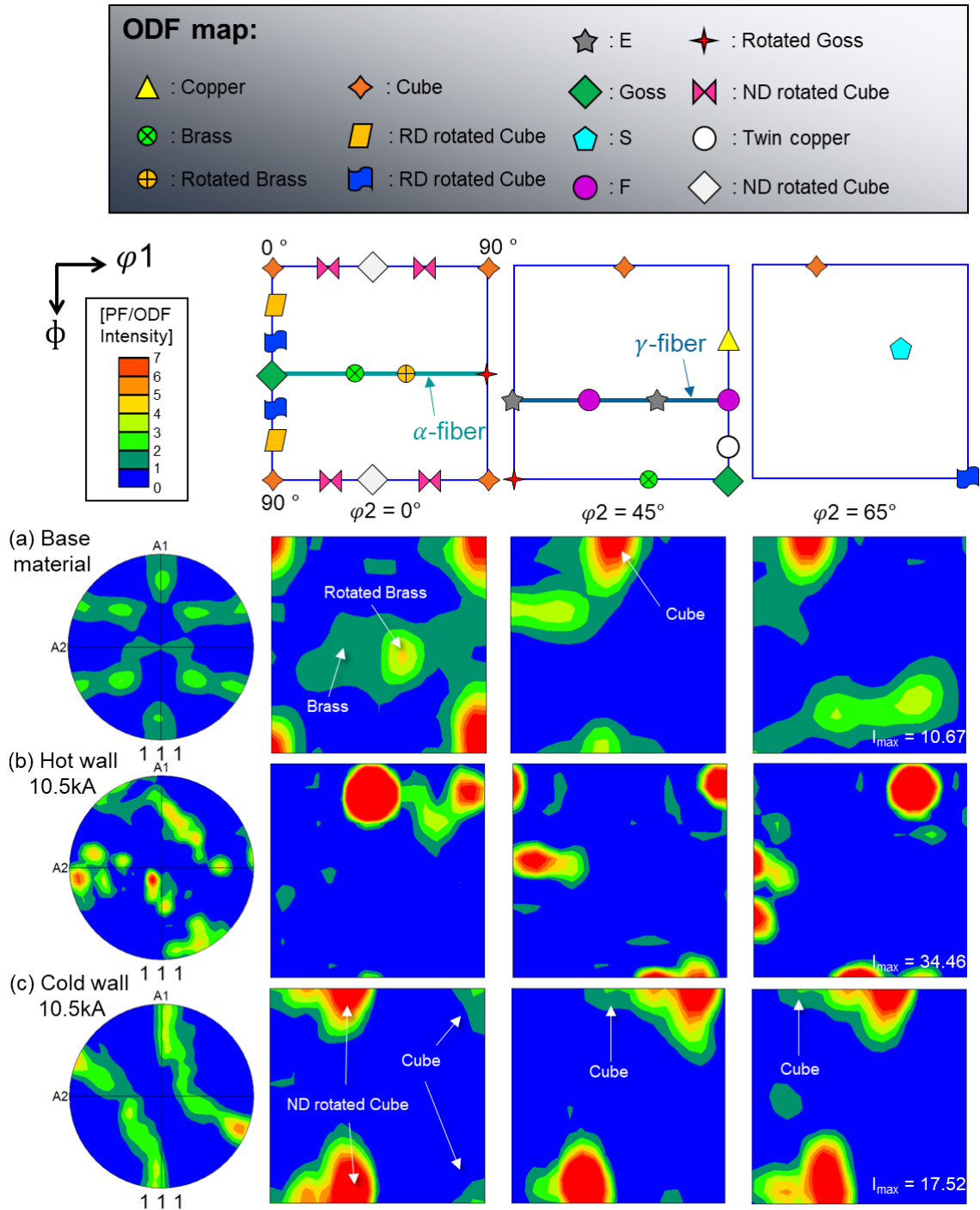


Fig. 4-15 Schematic diagram of during REW. (a) view of enlarged weld interface, (b) formation of PMZ due to heat transfer weld nugget to Al alloy and (c) locally formed IMCs.

The objective of texture development is to compare it directly with the state of the BM. This comparison aids in understanding whether the Al HAZ of the hot wall undergoes solidification subsequent to melting. Furthermore, it helps in determining if the Al within the cold wall remains comparatively less influenced by heat in contrast to the hot wall. The findings depicted in Fig. 4-16 illustrate the texture evolution in both the Al HAZ section and the Al BM using pole figure and orientation distribution function (ODF) maps. The color-coded legend, encompassing a spectrum from 0 to 7, corresponds to varying levels of intensity.

In its as-received state, Al BM possesses a strong cube, rotated brass, and weak brass texture, as displayed in Fig. 4-16(a). The cube texture is characterized by a strong alignment of crystallographic planes parallel to the faces of a cube. The presence of a face-centered cubic (FCC) crystal structure, as seen in Al alloys, often gives rise to cube texture formation during processes like rolling or other deformation methods. Typically, the orientations in the brass texture align with $\{011\}\langle 112 \rangle$ or $\{022\}\langle 110 \rangle$ directions and

can develop during various processing methods such as rolling, extrusion, or annealing. In some cases, a rotated brass texture emerges as a variation, characterized by crystallographic orientations slightly deviating from the standard brass orientations. This variation can occur due to complex deformation processes or other specific conditions during processing. Therefore, AA5052-H32, an Al BM in this study, clearly exhibited a typical rolled and machined texture. However, in the examination of the Al HAZ of the hot wall welded at 10.5 kA, dendrites are evident but without any discernible specific texture. In contrast, in the case of cold wall welding at the same current intensity, a strongly developed ND rotated cube texture is prominent, albeit weaker than that observed in the BM. ND rotated cube textures are commonly observed in Al alloys after processes involving significant rolling, such as hot or cold rolling. Hence, it becomes apparent that the dominant factor influencing texture in the Al during the REW process is the compressive force resulting from the press-fitting of the Cu electrode, rather than the heat in the cold wall.



4.4.3 The mechanism of Al HAZ effects for enhancing the REW lap joints

Fig. 4-17 summarizes the Al HAZ formation mechanism for all welding conditions examined in this study. A notable distinction emerges when comparing the scenarios in which the interface between Al and Fe is in contact during welding (i.e., hot wall) with situations in which a gap (i.e., air barrier) is present (i.e., cold wall). In our previous studies, the author reported that the presence of a gap significantly increases thermal resistance, thereby impeding the efficient transfer from the heat source within the Fe to the Al side[5,6]. Thermal resistance is a thermal property that quantifies the degree to which an object or material resists heat flow. It is essentially the reciprocal of thermal conductivity. The thermal resistance for the hot wall and the modified cold wall can be expressed as follows:

$$R_{th} = R_{Al} + R_{Fe} \quad (4)$$

$$R_{th} = R_{Al} + R_{Air(tolerance)} + R_{Fe} \quad (5)$$

where R_{th} is the thermal resistance, R_{Al} is the thermal resistance of AA5052, R_{Fe} is the thermal resistance term of Fe, and $R_{Air(tolerance)}$ is the thermal resistance of air. The hot wall configuration refers to a structure where the element and the Al of the upper plate are in direct contact without gaps. During welding, efficient heat transfer occurs from the heat source inside Fe to the Al side, which can be represented using the heat resistance equation expressed in Equation (4). As shown in Fig. 4-17(a), in the hot wall case at 8.5 kA, HAZ is formed on the Al side due to thermal conduction, and a partially melted zone (PMZ) emerges in the region in which the temperature surpasses the

melting point of Al alloys. The formation of the PMZ is confirmed by the observation of dendritic structures formed during the solidification process after melting. The grain shape in this zone develops into a long and slender form under the 8.5 kA current condition. Fig. 4-17(b), which represents the condition with a current of 10.5 kA, plastic deformation occurs along with increased heat input. This results in the formation of a hook extruded onto the Al side, along with the press-fit element. This accelerated the heat transfer to the Al side leads to the grains in the PMZ to develop in a wider shape compared to the 8.5 kA condition. Fig. 4-17(c) illustrates the results for the case with a current of 12 kA. The highest current condition results in a more significant press-in of the Cu electrode of the element compared to that under the 10.5 kA condition, forming an extruded hook on the Al side. In proportion to the indentation amount, the shank diameter is also the largest in the hot wall condition. Due to the more accelerated heat transfer compared to 10.5 kA, the grains in the PMZ grow thinner and longer.

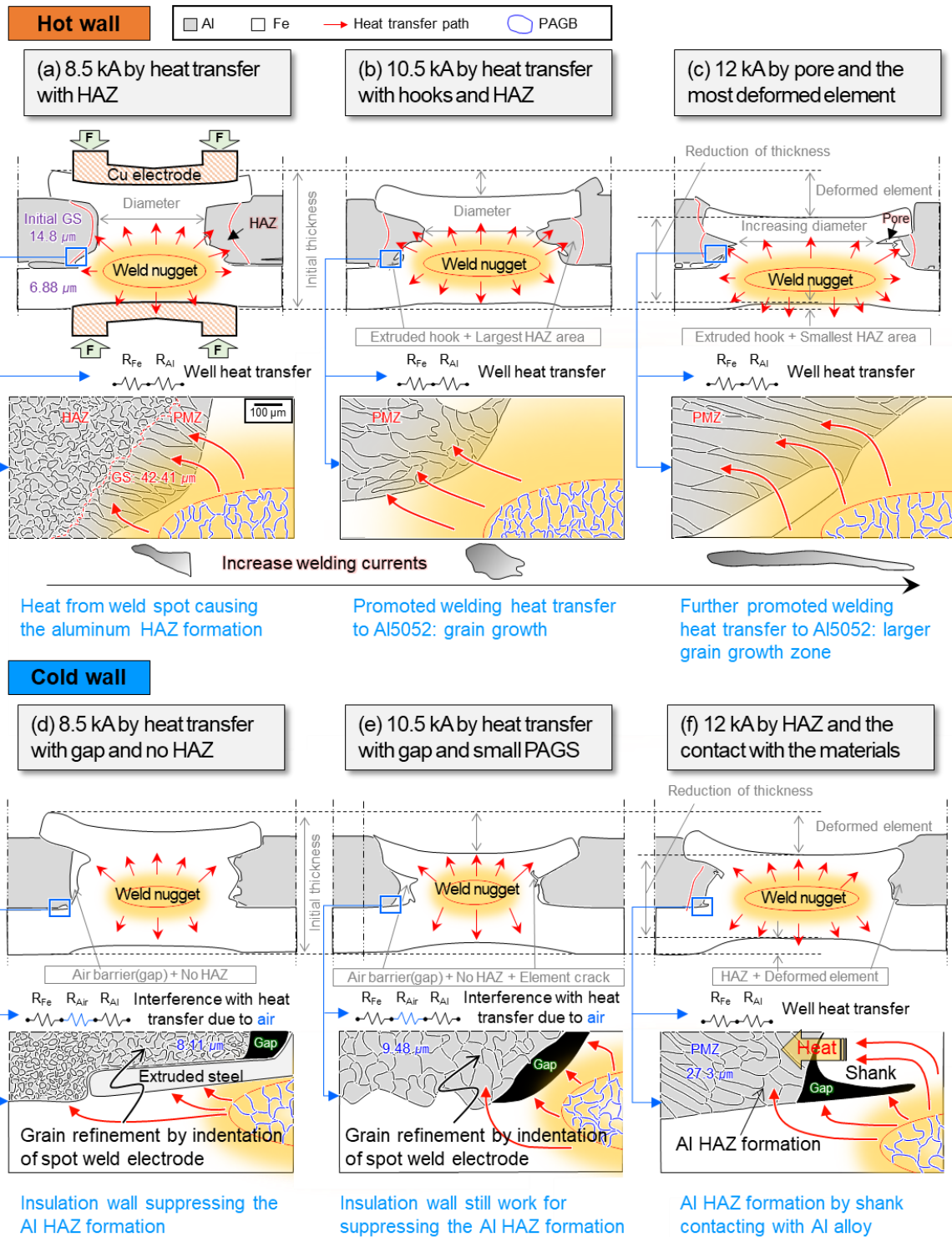


Fig. 4-17 Mechanism of AA5052 HAZ formation at various welding currents. Heat transfer in at (a) 8.5 kA, (b) 10.5 kA, (c) and 12 kA in the hot wall case, and at (d) 8.5 kA, (e) 10.5 kA, and (f) 12 kA under the cold wall case.

In the cold wall configuration, an air barrier (i.e., gap) exists between Fe and Al to prevent the formation of an Al HAZ. In the cold wall condition with an 8.5 kA current, no large plastic deformation occurs in either the S20C element or Al alloy due to the relatively low heat input. The heat transfer mechanism during welding in this scenario is summarized in Fig. 4-17(d). The initial air barrier inhibits heat transfer from the heat source to the Al side, which can be described by the thermal resistance equation in Equation (5). Consequently, an Al HAZ does not form, and the Al grain decreases from the initial state of 14.8 μm to 8.11 μm due to electrodes pressing. Fig. 4-17(e) shows the results for the 10.5 kA current condition. The increased heat input pushes the element further, allowing more heat to be transferred to the Al alloys due to the pressure applied by the head of the element. The original insulation system is maintained, serving as thermal resistance to prevent Al HAZ generation. Thus, the grain size of Al under the 10.5 kA current condition is 9.48 μm , which is 1.37 μm larger than that under the 8.5 kA condition. As shown in Fig. 4-17(f), at the highest current of 12 kA, the element experiences significant plastic deformation and presses into the air barrier. In this process, part of the air barrier is breached, and the element comes into contact with one side of Al. This contact area between the shank and Al becomes a heat transfer path from the heat source, leading to the formation of an Al HAZ. Similar to the hot wall case, dendrites, which are solidification structures formed after melting, are observed in some areas of Al HAZ close to the heat source, indicating temperatures exceeding the melting point of Al. Al HAZs are formed under all current conditions of the hot wall, and the PMZ develops as a solidification structure after melting in all HAZs. Severe plastic deformation due to high welding current of the cold wall can result in the penetration of the air barrier due to the extruded steel during welding. This contact with the Al side

leads to the formation of an Al HAZ. Therefore, selecting an appropriate current condition is crucial for realizing an Al HAZ-less joint.

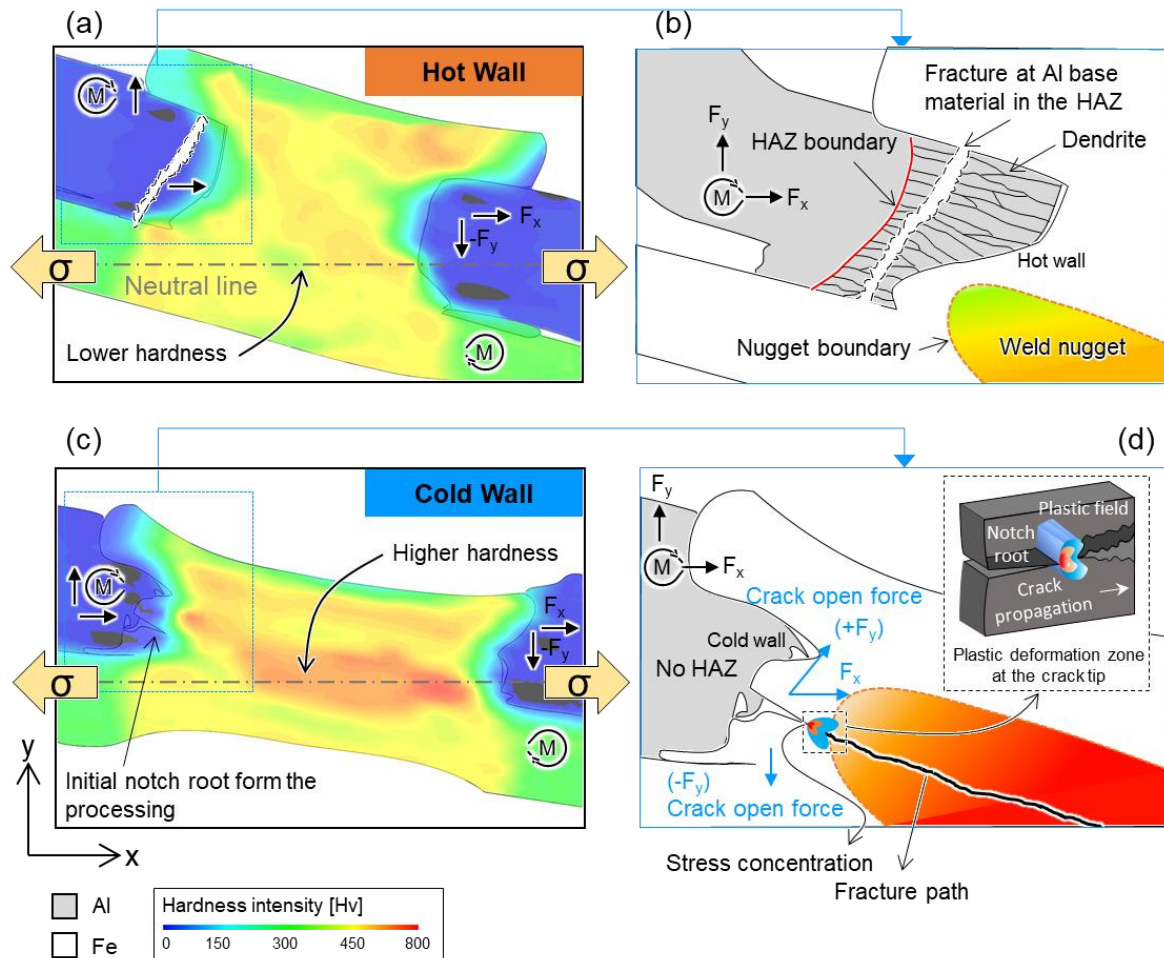


Fig. 4-18 Fracture mode and mechanism according to the wall parameter. (a) Illustration of the hot wall parameter specimen during tensile loading, (b) fracture mechanism in the wall case with Al HAZ fracture, (c) cold wall parameter specimen during tensile loading, and (d) fracture mechanism in the cold wall case in greater detail.

Fig. 4-18 illustrates the failure modes and mechanisms observed during tensile-shear loading of both hot wall and cold wall joints. The primary factors influencing the failure mode of the REW joint are complete fusion, geometrical

characteristics of the weld bead, and adherence to the recommended AWS spot(d_{spot}) guidelines. Most of the hot wall joints exhibit failure modes, as shown in Fig. 4-18(a). When subjected to tensile-shear force, tension is generated along the gray dotted line, and a moment is induced as Al bears the load of F_y . However, the welding nugget, where F_x is mainly applied, exhibits relatively low hardness. Consequently, the Al HAZ region becomes the weakest point in this joint, leading to a rupture occurring in the Al HAZ fracture mode (see Fig. 4-18(b)). In contrast, the cold wall lacks an Al HAZ fracture mode, but a unique notch root is inevitably formed during the welding process in S20C. When subjected to tensile-shear forces, tension is applied along the gray dotted line as shown in Fig. 4-18(c). The gray dotted line is located in the FZ region, where relatively a high hardness is distributed. The moment acting on Al can trigger stress concentration at the notch root. Therefore, this notch root and the embrittled FZ are likely to contribute to brittle fracture around the nugget, particularly after cracks open and propagate to the notch root, as displayed in Fig. 4-18(d). Therefore, IF occurs in the cold wall case, despite meeting the minimum spot diameter recommended by AWS.

4.5 Conclusions

By implementing the REW process, Al HAZ-free lap joints involving AA5052 and SPFC980 were successfully achieved. The inhibition of an Al HAZ prompted a thorough investigation into changes affecting heat transfer, microstructure, and interface morphology in comparison to conventional methods. Additionally, the author examined the resultant impact on the mechanical properties of the joint. The key findings from this research can be summarized as follows:

1. In the context of hot wall joints, the presence of a dendrite-like Al HAZ was consistently observed across all welding current parameters. In contrast, in the cold wall setup, a finer microstructure, devoid of dendritic Al HAZ formations, was identified at welding currents of 8.5 kA and 10.5 kA.
2. A notable disparity in the hardness existed between the Al HAZ in the hot wall case and the Al present in the cold wall case without a HAZ. This discrepancy was rooted in the contrasting pathways of microstructure evolution and texture development. In addition, the hardness of cold wall Al was slightly lower than that of the BM and hot wall Al HAZ, owing to the dissipation of work hardening in AA5052-H32 resulting from process the elevated process temperatures.
3. The presence of Al HAZ exerted a notable impact on the hardness characteristics of the molten steel portion. Particularly, in the case of the cold wall configuration without an Al HAZ, hardness values exceeding those in the hot wall case by approximately 100 HV or more were observed, and these originated from variations in the PAGS.
4. The underlying cause for the incidence of IF in the cold wall case was not attributed to microstructural disparities. Instead, it was linked to the formation of an inherent notch root when S20C melted due to the absence of an Al HAZ. As a result, at a welding current of 10.5 kA, the hot wall configuration exhibited approximately a 30% increase in tensile shear load and a 66% increase in displacement, compared to the cold wall configuration without HAZ.
5. Our findings underscore that although an Al HAZ-less AA5052/1GPa class steel lap joint can be effectively developed, the thermal behavior during the process

must be considered and its effects are due to the geometric joint characteristics. These drawbacks can be mitigated via post-treatment strategies. The results obtained in this study are expected to contribute to the evolving discussion on lightweight components for next-generation automobiles.

References

- [1] Meschut G, Janzen V, Olfermann T. Innovative and highly productive joining technologies for multi-material lightweight car body structures. *J Mater Eng Perform* 2014;23:1515–23. <https://doi.org/10.1007/s11665-014-0962-3>.
- [2] Meschut G, Hahn O, Janzen V, Olfermann T. Innovative joining technologies for multi-material structures. *Weld World* 2014;58:65–75. <https://doi.org/10.1007/s40194-013-0098-3>.
- [3] Baek S, Song J, Lee H chul, Park S yeon, Song KH, Lee S, et al. Robust bonding and microstructure behavior of aluminum/high-strength steel lap joints using resistance element welding process for lightweight vehicles: Experimental and numerical investigation. *Mater Sci Eng A* 2022;833:142378. <https://doi.org/10.1016/j.msea.2021.142378>.
- [4] Sun Y, Huang R, Zhao H, Chen X, Jiang M, Wu L, et al. Enhancement of resistance element welding of AA6061 to DP600 steel by using external magnetic field. *J Manuf Process* 2022;80:347–58. <https://doi.org/10.1016/j.jmapro.2022.06.001>.
- [5] Baek S, Go GY, Park JW, Song J, Lee H chul, Lee SJ, et al. Microstructural and interface geometrical influence on the mechanical fatigue property of aluminum/high-strength steel lap joints using resistance element welding for lightweight vehicles: experimental and computational investigation. *J Mater Res Technol* 2022;17:658–78. <https://doi.org/10.1016/j.jmrt.2022.01.041>.
- [6] Baek S, Ma N, Song J, Kim DK, Lee SJ, Chen C, et al. Effect of Mg remelting and mechanical hooks of steel on the mechanical and fatigue responses of resistance element welded AZ31/DP780 joints: Experimental, FEM and thermodynamic calculation studies. *J Mater Res Technol* 2023;22:1210–37. <https://doi.org/10.1016/j.jmrt.2022.11.157>.
- [7] Pawar S, Singh AK, Kaushik L, Park KS, Shim JH, Choi SH. Characterizing local distribution of microstructural features and its correlation with microhardness in resistance spot welded ultra-low-carbon steel: Experimental and finite element characterization. *Mater Charact* 2022;194. <https://doi.org/10.1016/j.matchar.2022.112382>.
- [8] Zheng Y, Wang F, Garrison WM, Lin Y, Li C. Influence of Martensitic Structure and Carbide Precipitation Behavior on Mechanical Properties of 25CrMoNbB Alloy Steels with Mo Contents of 0.25 and 0.5 Pct. *Metall Mater Trans A Phys Metall Mater Sci*

- 2018;49:4565–80. <https://doi.org/10.1007/s11661-018-4766-1>.
- [9] Celada-Casero C, Sietsma J, Santofimia MJ. The role of the austenite grain size in the martensitic transformation in low carbon steels. *Mater Des* 2019;167. <https://doi.org/10.1016/j.matdes.2019.107625>.
- [10] Gyhlestén Back J, Surreddi KB. Microstructure analysis of martensitic low alloy carbon steel samples subjected to deformation dilatometry. *Mater Charact* 2019;157:109926. <https://doi.org/10.1016/j.matchar.2019.109926>.
- [11] Morris JW. On the ductile-brittle transition in lath martensitic steel. *ISIJ Int* 2011;51:1569–75. <https://doi.org/10.2355/isijinternational.51.1569>.
- [12] Morito S, Yoshida H, Maki T, Huang X. Effect of block size on the strength of lath martensite in low carbon steels. *Mater Sci Eng A* 2006;438–440:237–40. <https://doi.org/10.1016/j.msea.2005.12.048>.
- [13] Wang J, Hong H, Huang A, Yang X, Qian R, Shang C. New insight into the relationship between grain boundaries and hardness in bainitic/martensitic steels from the crystallographic perspective. *Mater Lett* 2022;308:131105. <https://doi.org/10.1016/j.matlet.2021.131105>.
- [14] Wu X, Lin H, Luo W, Jiang H. Microstructure and microhardness evolution of thermal simulated HAZ of Q&P980 steel. *J Mater Res Technol* 2021;15:6067–78. <https://doi.org/10.1016/j.jmrt.2021.11.059>.
- [15] Yen HW, Ooi SW, Eizadjou M, Breen A, Huang CY, Bhadeshia HKDH, et al. Role of stress-assisted martensite in the design of strong ultrafine-grained duplex steels. *Acta Mater* 2015;82:100–14. <https://doi.org/10.1016/j.actamat.2014.09.017>.
- [16] Yang HS, Bhadeshia HKDH. Austenite grain size and the martensite-start temperature. *Scr Mater* 2009;60:493–5. <https://doi.org/10.1016/j.scriptamat.2008.11.043>.
- [17] Chen N, Wang HP, Carlson BE, Sigler DR, Wang M. Fracture mechanisms of Al/steel resistance spot welds in lap shear test. *J Mater Process Technol* 2017;243:347–54. <https://doi.org/10.1016/j.jmatprotec.2016.12.015>.
- [18] Chen J, Yuan X, Hu Z, Sun C, Zhang Y, Zhang Y. Microstructure and mechanical properties of resistance-spot-welded joints for A5052 aluminum alloy and DP 600 steel. *Mater Charact* 2016;120:45–52. <https://doi.org/10.1016/j.matchar.2016.08.015>.

- [19] Czerwinski F. Thermal stability of aluminum alloys. *Materials (Basel)* 2020;13:1–49. <https://doi.org/10.3390/ma13153441>.
- [20] Free JC, Summers PT, Lattimer BY, Case SW. Mechanical properties of 5000 series aluminum alloys following fire exposure. *TMS Annu Meet* 2016;0:657–64. <https://doi.org/10.1002/9781119274896.ch79>.
- [21] Safeen MW, Spena PR. Main issues in quality of friction stir welding joints of aluminum alloy and steel sheets. *Metals (Basel)* 2019;9. <https://doi.org/10.3390/met9050610>.
- [22] Liyakat NA, Veeman D. Improvement of mechanical and microstructural properties of AA 5052-H32 TIG weldment using friction stir processing approach. *J Mater Res Technol* 2022;19:332–44. <https://doi.org/10.1016/j.jmrt.2022.05.015>.
- [23] Trzaska J, Dobrzański LA. Modelling of CCT diagrams for engineering and constructional steels. *J Mater Process Technol* 2007;192–193:504–10. <https://doi.org/10.1016/j.jmatprotec.2007.04.099>.
- [24] Jiajun W, Pieter J, Zwaag S. Determination of martensite start temperature in engineering steels Part 1: empirical relations describing the effect of steel chemistry. *Mater Trans JIM* 2000;41:761–8.
- [25] Nandan G, Kumar G, Arora KS, Kumar A. MIG and CMT brazing of aluminum alloys and steel: A review. *Mater Today Proc* 2022;56:481–8. <https://doi.org/10.1016/j.matpr.2022.02.166>.
- [26] Singh J, Arora KS, Shukla DK. Dissimilar MIG-CMT weld-brazing of aluminium to steel: A review. *J Alloys Compd* 2019;783:753–64. <https://doi.org/10.1016/j.jallcom.2018.12.336>.
- [27] Kotadia HR, Franciosa P, Jabar S, Ceglarek D. Remote laser welding of Zn coated IF steel and 1050 aluminium alloy: processing, microstructure and mechanical properties. *J Mater Res Technol* 2022;19:449–65. <https://doi.org/10.1016/j.jmrt.2022.05.041>.
- [28] Lu Y, Mayton E, Song H, Kimchi M, Zhang W. Dissimilar metal joining of aluminum to steel by ultrasonic plus resistance spot welding - Microstructure and mechanical properties. *Mater Des* 2019;165:107585. <https://doi.org/10.1016/j.matdes.2019.107585>.
- [29] Liu S, Chew Y, Weng F, Sui S, Du Z, Man Y, et al. Effects of laser pulse modulation

on intermetallic compounds formation for welding of Ti-6Al-4V and AA7075 using AA4047 filler. *Mater Des* 2022;213:110325.

<https://doi.org/10.1016/j.matdes.2021.110325>.

- [30] Yao Y, Jing L, Wang S, Li G, Cui J, Tang X, et al. Mechanical properties and joining mechanisms of Al-Fe magnetic pulse welding by spot form for automotive application. *J Manuf Process* 2022;76:504–17. <https://doi.org/10.1016/j.jmapro.2022.02.017>.
- [31] Hollingsworth EH, Willett RE, Frank GR. Identification of a new Al-Fe constituent, FeAl₆. *Trans Metall Soc AIME* 1962;224:188.
- [32] Young RMK, Clyne TW. An Al-Fe intermetallic phase formed during controlled solidification. *Scr Metall* 1981;15:1211–6.
- [33] Allen CM, O'reilly KAQ, Cantor B, Evans P V. Intermetallic phase selection in 1XXX Al alloys. *Prog Mater Sci* 1998;43:89–170.
- [34] Allen CM, O'reilly KAQ, Evans P V, Cantor B. A calorimetric evaluation of the role of impurities in the nucleation of secondary phases in 1xxx Al alloys. *MRS Online Proc Libr* 1997;481:3.
- [35] Michalcová A, Orliček M, Novák P. Aluminum alloys with the addition of reduced deep-sea nodules. *Metals (Basel)* 2021;11:1–11. <https://doi.org/10.3390/met11030421>.
- [36] Zhang G, Chen M, Shi Y, Huang J, Yang F. Analysis and modeling of the growth of intermetallic compounds in aluminum-steel joints. *RSC Adv* 2017;7:37797–805. <https://doi.org/10.1039/c7ra06354g>.
- [37] Yang Y, Luo Z, Bi Y, Zhang Y. Nano-scale characterization of intermetallic compounds in dissimilar aluminum-steel resistance element welded joints. *Mater Charact* 2023;204:113227. <https://doi.org/10.1016/j.matchar.2023.113227>.

Chapter 5 Effect of Mg remelting and mechanical hooks of steel on the mechanical and fatigue responses of REWed Mg/DP780 joints

5.1 Introduction

Magnesium (Mg) alloys are considered attractive structural materials for a range of automotive and aerospace applications due to their lightweight and high strength to weight ratio[1–3]. The density of Mg is approximately 1700 kg/m³, which is only about 60% of the density of aluminum (Al)(approximately 2700 kg/m³) and only 21% of steel (7800 kg/m³), making it an attractive for the weight reduction. Furthermore, Mg alloys close to the density of carbon fiber reinforced plastic (CFRP) yet more affordable than CFRP[4]. According to previous study[5], safety-related automotive parts are mainly made of dual phase (DP) steels, which accounts for 74% of the total advanced high strength steel (AHSS). DP steels have long been used in the automotive industry due to their exceptional characteristics, specifically their strength-ductility balance associated to satisfactory cost as well[6,7]. Therefore, the combination of DP steels of the ductile ferrite (α) and hard martensite (α'), with Mg alloys, can be considered one of the best combinations for the next generation automotive industry that can satisfy both structural integrity and light weight[8]. However, the melting point of Fe (1811 K) is significantly higher than the boiling point of Mg (1363 K). This implies that Mg would evaporate before steel even reaches its melting point[9]. Moreover, N. Farabi and J. Wang et al.[10,11] have pointed out that when DP steel composed of ferrite and martensite is welded, it tends to soften due to a reduction in the fraction of martensite, becoming the weakest part of the weld joint.

Although there have been many advances in dissimilar material welding technologies, reports on the robust bonding between Mg alloys and steels for use in automotive industries are still lacking. Moreover, the reported results mainly pertain to studies on static strength. For application in the automobile industry, a comprehensive understanding of all details concerning the development of mechanical properties, including changes in microstructures such as phase transformations in joints, degradations, and ultimately fatigue behavior, is essential. In dual-phase (DP) steels composed of ferrite and martensite, the softening phenomenon of martensite after welding acts as an Achilles heel, weakening the mechanical properties of welding joints[12–14]. Therefore, it is imperative to explore alternatives to overcome this challenge.

In chapter 5, the microstructure properties associated with the weld joint and the heat-affected zone (HAZ) of Mg are quantitatively analyzed through thermodynamic calculation, finite element method (FEM) simulation and electron back-scattered diffraction (EBSD) detector. In addition, the author thoroughly investigates the relationship between the characteristics of the microstructure, welding interface geometry and fracture behavior based on welding current condition. The digital image correlation (DIC) method has been employed to visualize the mechanical behavior during the tensile-shear test. A fatigue load diagram is obtained through a fatigue test, and the characteristic of fatigue fracture are quantitatively analyzed, including the shape of crack propagation for each welding process condition.

5.2 Experimental procedures

5.2.1 Materials and REW processing

AZ31B sheet (100 mm × 30 mm × 2 mm) and DP780 (100 mm × 30 mm × 1.2 mm) were employed as a base material respectively. The element to be riveted to the AZ31B sheet was selected as S20C (Low carbon steel). Chemical compositions of the base materials are shown in Table 5-1. Fig. 5-1(a) summarizes the procedure of element inserting with its machine systems (WELTAC®, BÖLLHOFF). The processing procedure of element riveting shows in Fig. 5-1(b) in detail. In here, the process of S20C riveting on AZ31B sheet can be distinguished by four sections. ①mounting the S20C rivet on the AZ31B sheet, ②starting the rivet assembly process, ③riveting with forcing tool down and ④completed the S20C riveting and tool up. An assembled AZ31B sheet with S20C is resistance-element-welded with DP780 sheet by an AC power supply spot welding machine (see Fig. 5-1(c)). Through this process, the inconsistency of inherent properties between Mg alloys and DP780 steels can be resolved and competitiveness in mass production can be secured by using the low-carbon steel (S20C) element. The welding conditions were fixed at 2.45 kN and 200 ms for the pressing force and the current time, respectively, and the currents were 2.5 kA, 3.5 kA, 8.5 kA and 10.5 kA. The detail configuration and dimension of the REWed AZ31B/DP780 specimen is displayed in Fig. 5-1(d, e).

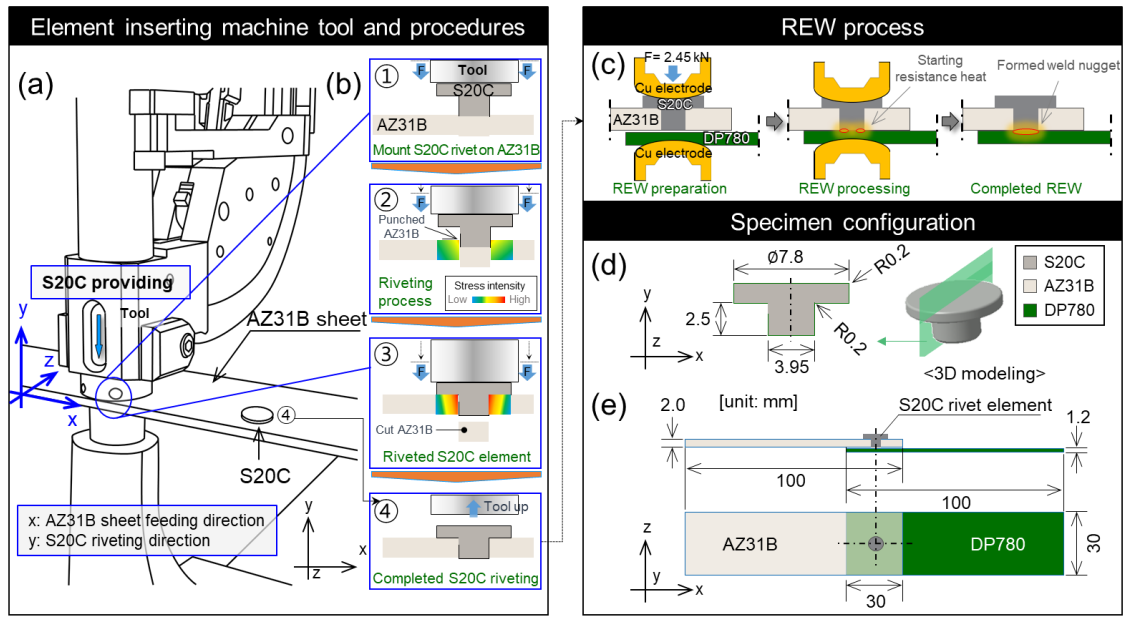


Fig. 5-1 A schematic description of resistance element welding processing for AZ31B and DP780. (a) a machine of S20C element inserting, (b) element inserting procedure with tool, and (c) resistance element welding process, (c) a dimension of S20C element, (e) a configuration of REWed AZ31B/DP780 specimen.

Table. 5-1 Chemical compositions of applied materials.

	Elements (wt%)										
	C	Si	Mn	P	S	Sol-Al	Al	Zn	Cu	Fe	Mg
DP780	0.09	0.18	2.27	0.026	0.002	0.026	-	-	-	Bal.	-
S20C	0.20	0.20	0.47	0.012	-	-	-	-	-	Bal.	-
AZ31B	-	0.1	0.2	-	-	-	3.0	1.0	0.05	0.005	Bal.

5.2.2 Mechanical testing

Mechanical testing conducts on the micro-Vickers hardness tests, tensile-shear tests and fatigue tests, respectively. Fig. 5-2 presents the comprehensive configuration of a mechanical testing. Fig. 5-2 (a, b) exhibits the welded specimen fixing for fatigue test and its schematic description. A fatigue test was performed using the fatigue test machine (MTS Landmark™ Servohydraulic Test System, MTS Model 370.10 Load

Frame). In order to avoid potential bending of the REWed joint, the fatigue tests were performed at $R = 0.1$ and a 40 Hz sinusoidal wave frequency, as specified in ASTM E466. The stress ratio (R) was described as follows:

$$R = \frac{\sigma_{max}}{\sigma_{min}} \quad (1)$$

$$\sigma = \frac{F}{A} \quad (2)$$

where σ_{max} is the desired maximum stress and σ_{min} is the desired minimum stress. F [N] is an applied load, and A is described unit area [mm²]. A F_y is defined a tensile-shear force. The stresses were applied in the range of $0.2F_y$ to $0.8F_y$, a value less than the tensile-shear force (F_y), and high-cycle fatigue tests were performed. It is defined as an intensity of 20% of F_y and 80% of F_y . This study tests three specimens under one condition to obtain an approximate range and fatigue life trend. An example of a fatigue history is displayed in Fig. 5-2(d). To evaluate the mechanical property, a universal testing machine (UTM, MTDI/UT100F) was introduced. The tensile-shear test was conducted at a speed of 2 mm/min. It was *in-situ* monitored with a digital image correlation (DIC) system to observe the distribution of mechanical behaviors during tensile-shear testing as displayed in Fig. 5-2(c). Vickers micro-hardness test was performed on the cross-section of the welding interface area with a load of 10 kgf and a dwell time of 10s by a hardness testing machine (SIOMM/HV-50AP).

5.2.3 Microstructure characterizations

To seek the origin of microstructure behaviors depending on the change of the welding current, a cross section of the joint specimen was prepared for optical microscope investigation by mechanical polishing, mechanically grown up to grade 4000, and then polished up to 1 μm (Struers/DP-Suspension P). Finally, to obtain the mirror polished surface, 0.04 μm aqueous solution containing colloidal silica particles was ultimately applied (Struers/OP-S). The finished specimen surfaces were etched for 15~20sec at room temperature using a 4% Nital solution (96 ml Ethanol and 4 ml Nitric acid) for the optical micrographs. Optical microscope (OM; GX51, OLYMPUS), field-emission scanning electron microscope (FESEM), and electron back-scatter diffraction (EBSD) were introduced to systematically investigate the microstructure including grain size, morphology, grain boundary, phase, etc. For the EBSD observation, cross sections were polished by ion-milling (ArBlade 5000, Hitachi, Japan), which was processed for 30 minutes with an acceleration voltage of 6kV and an Ar^+ gas flow rate of 0.15 cm^3/min . A crystallographic raw data from EBSD was analyzed in detail by using TSL-OIM software, the analysis points with a confidence index (CI) ≤ 0.1 were indicated as black regions.

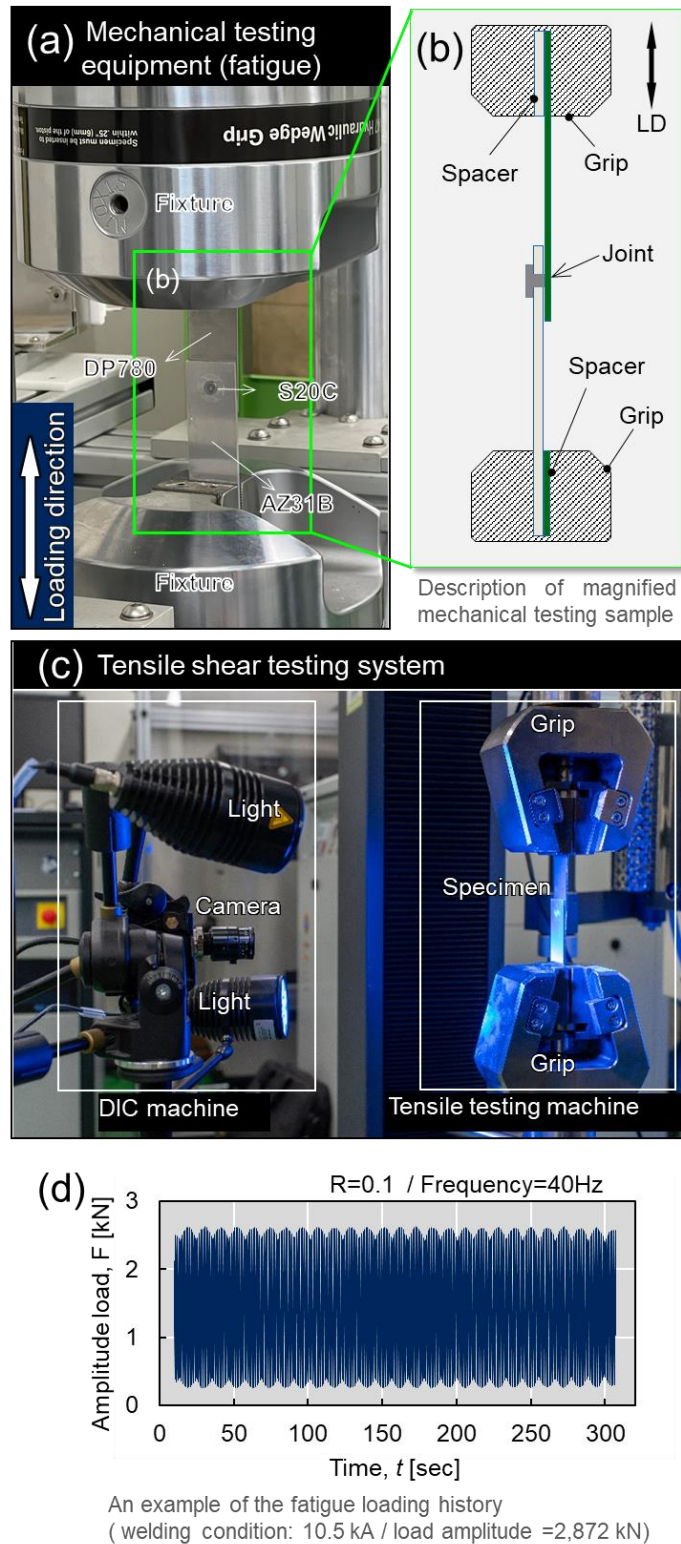


Fig. 5-2 A configuration of mechanical testing. (a) an equipment for fatigue tests, its specimen description (b), (c) tensile-shear tester with digital image correlation equipment and (d) an example of fatigue loading history.

5.3 Results

5.3.1 Welding morphologies and its geometries

Here we investigated how morphologies of welding interfaces change depending on welding current conditions. Fig. 5-3(a-d) depicts a result of an optical microscope (OM) observation. Although the formation of the nugget was observed under the welding current condition of 2.5 kA, it can be confirmed that the fusion line between S20C and DP780 steel was clearly existed (see Fig. 5-3(a)). A distinct fusion line can be considered as insufficient melting at the welding interface. In addition, a defect was detected presumed to be caused by the process of inserting the S20C element into the AZ31B sheet. When the welding current is increased to 3.5 kA, the fusion line at the welding interface between S20C and DP780 was not observed as displayed in Fig. 5-3(b). The diameter of the nugget was slightly larger than 25 kA and the deformed part of AZ31B sheet was observed, but the defect caused by the inserting the S20C element was still observed. In Fig. 5-3(c), the welding current condition of 8.5 kA was found to form a larger spot diameter and hook. However, a heat affected zone (HAZ) and porosity was developed due to the interaction between Fe and Mg elements. When the welding current reached 10.5 kA, the extruded hooks and voids, undercut defects occurred as displayed in the Fig. 5-3(d). The quantitative values of welding morphologies are shown in Fig. 5-3(e-g). Fig. 5-3(e) exhibits the welding current dependence spot diameter changes, which can be important factor determining the fracture mode, i.e. interfacial fractures or base metal fractures. When the welding current was increased from 2.5 kA to 10.5 kA, the spot diameter increased by 55.93%. The spot diameter based on American Welding Society (AWS, D8.9M; Test Methods for Evaluating the Resistance

Spot Welding Behavior of Automotive Sheet Steel Materials) recommendation can be as follow:

$$d_{spot} = 4\sqrt{t} \quad (3)$$

where d_{spot} is the minimum spot diameter that can cause the base metal fracture. When the spot diameter is less than this value, an interfacial failure (IF) may be expected, and when the spot size is greater than this value, a base material fracture can be predicted. t is the thickness of base materials. The calculated minimum spot diameter was found to be 5.65 mm, which means that based on the calculations, the diameter of 2.5 kA was 4.72 mm, which is expected to interfacial fractures. From the welding condition of above 3.5 kA, since all the minimum spot diameter criteria were satisfied, base metal fracture is expected to occur, which is further discussed further in the mechanical properties section. In addition, an increase in welding current was shown to reduce a height of the S20C element with higher heat input as displayed in Fig. 5-3(f). In this process, the formation of hooks was accompanied, and tolerance was also observed to decrease (see Fig. 5-3(g)).

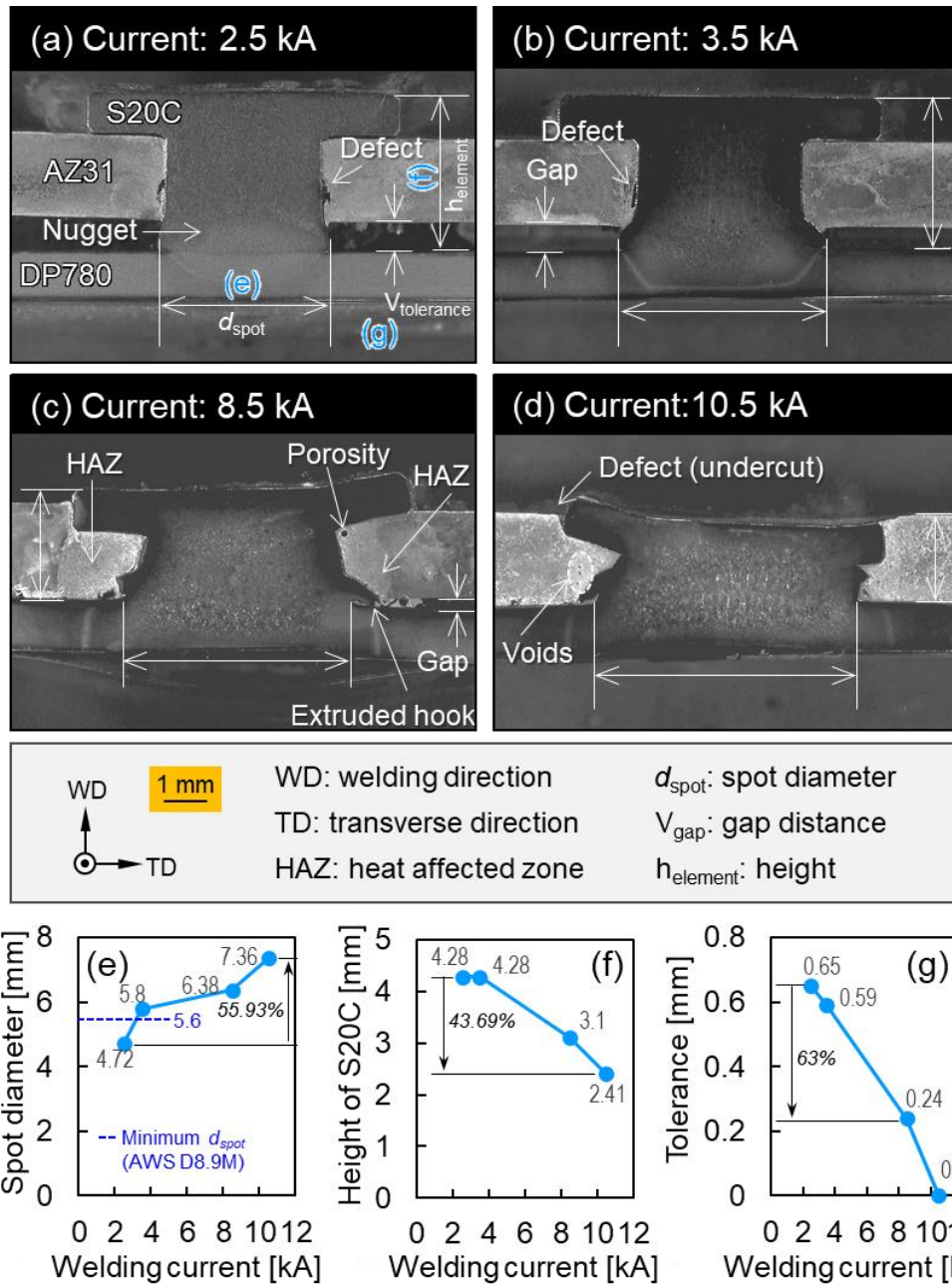


Fig. 5-3 Welding morphologies and geometries. (a) cross sectional OM image of 2.5 kA, (b) 3.5 kA, (c) 8.5 kA and (d) 10.5 kA, (e) spot diameters of welds, (f) height developments of S20C element, (g) tolerance changes after welding processes.

5.3.2 Microstructure behaviors

5.3.2.1 As-received base materials

To quantitatively investigate the development of welding microstructures, the electron back-scattered diffraction (EBSD) method was employed. Fig. 5-4 exhibits as-received state microstructures. In Fig. 5-4(a, b), the S20C material consist of the ferrite and pearlite structure with 17.4 μm of grain size, which is both body-center-cubic (BCC) structure. This is clearly a single phase as a typical low carbon steel. In Fig. 5-4(c), DP780 steel was structure combination with alpha prime (α') martensite and alpha (α) ferrite. A dark part is α' -phase and bright part can be defined alpha phase in OM image. In Fig. 5-4(d), their crystal orientations are randomly distributed, and they have a grain size of about 6.5 μm . In addition, In order to quantify phase fractions for DP780 materials, the grain average image quality (GAIQ) observation was used. GAIQ is the average of image quality values of all points belonging to a grain. L. Ryde et al. mentioned that using a grain tolerance angle value between 0.5° - 1.5° to demarcate grains for GAIQ calculation enables excellent identification of martensite particles in ferrite-martensite DP microstructures[15]. The area with higher GAIQ value indicated the ferrite, whereas one with lower GAIQ value means the martensite. This means that the martensitic transformation during cooling after welding drives the lattice distortion. As a result, black area of the image quality (IQ) map and the high kernel average misorientation angle (KAM) value of the KAM map match the low area of the GAIQ map as shown in Fig. 5-4(e). In the GAIQ map (see Fig. 5-4(f)), we have confirmed two peaks, which was distinguished as $\text{GAIQ} > 87595.7$ (α -ferrite) and $\text{GAIQ} < 87595.7$ (α' -martensite). These results have also been mentioned in previous studies[16–18]. Therefore, the initial phase fractions of DP780 base material were found to be

α' -martensite and ferrite fractions of 0.166 and 0.834, respectively. AZ31B was formed of equiaxed grains with random crystal orientations with a grain size of 14.7 μm (see Fig. 5-4(g, h)).

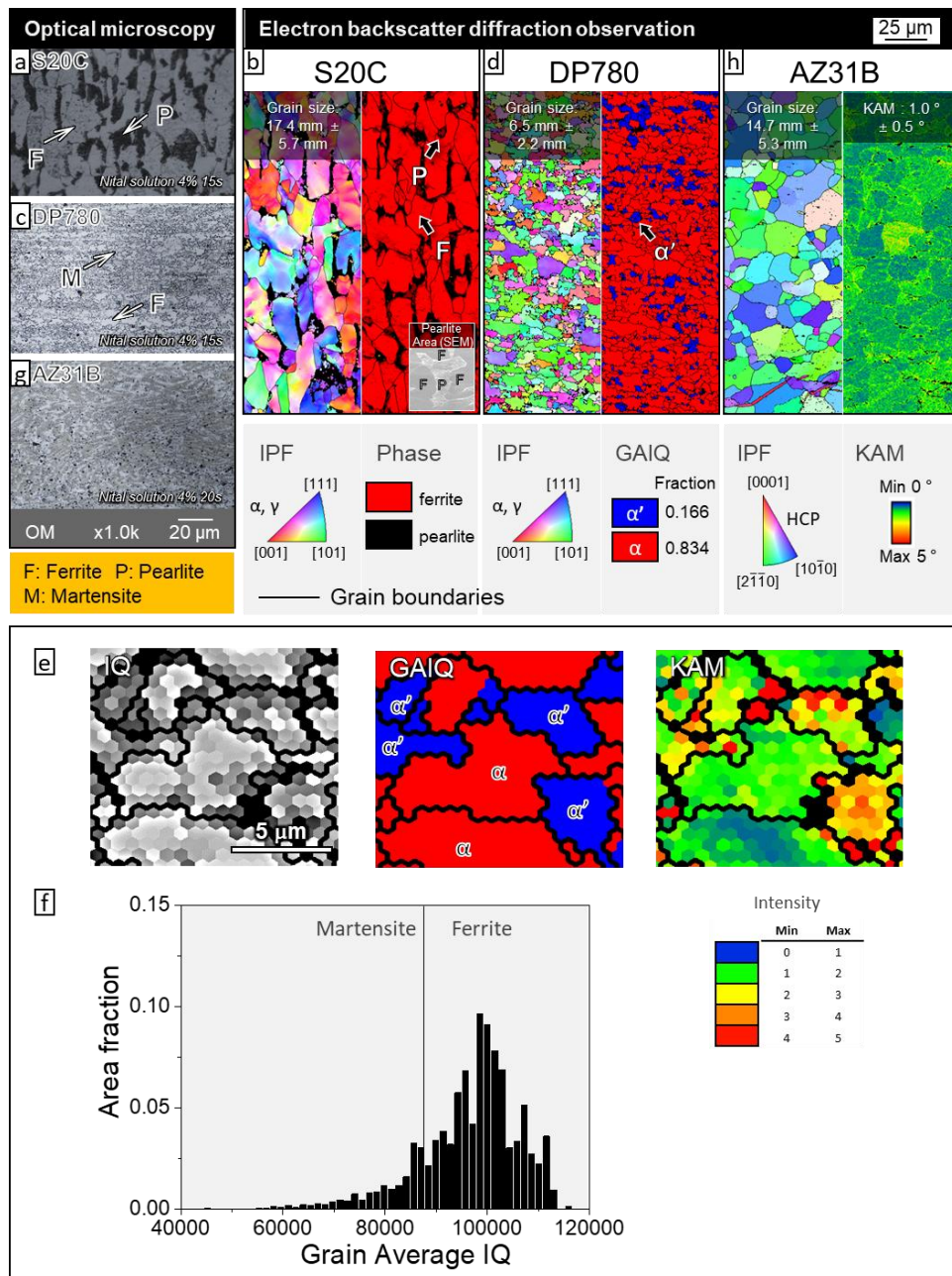


Fig. 5-4 Initial state of base materials. (a) OM micrograph of S20C (Fe-0.47Mn-0.2Si-0.2C-0.012P), its EBSD IPF and phase map (b), and (c) OM image of dual phase 780 steel, and its IPF and GAIQ map (d), (e) distinguished α and α' -martensite phase using IQ, GAIQ and KAM map, its phase peak distinction plot (f). OM: optical microscope; IPF: inverse pole figure; GAIQ: grain average image quality; KAM: kernel average grain misorientation.

5.3.2.2 Welding interfaces

Fig. 5-5 presents EBSD analysis results of interfaces between S20C and DP780 steel. In common features, it can be seen that the crystal orientation after welding is randomly distributed through the inverse pole figure (IPF) map. When the welding current was 3.5 kA, the grain morphology was developed with acicular structures from the equiaxed grain shape of the initial state as shown in Fig. 5-5(a). The average grain size was about 17.4 μm , and the α' -martensite fraction was 0.061, which was confirmed that the dual phase was sustained even after the welding condition of 3.5 kA in GAIQ map. α' -phase was developed around the welding interface. The welding current of 8.5 kA induced sharper acicular structures as displayed in Fig. 5-5(b). The grain size was slightly reduced to 12.8 μm , and α' -martensite fraction was 0.058, similar to the 3.5 kA condition. Fig. 5-5(c, d) exhibits grain size distributions and KAM plots, respectively. The quantitative change in the phase fraction is shown in Fig. 5-5(e). α -phase increased by about 10% compared to the initial phase, and α' -phase showed a trade-off relationship that decreased by about 10%. However, it is noteworthy that the dual phase is still partially maintained after the REW process.

5.3.2.3 Heat affected zone of AZ31B

The development of a heat-affected zone of magnesium alloys has a very important effect on the mechanical properties. Fig. 5-6 displays the HAZ developments of AZ31B materials with different welding currents. The welding current lead to significant differences on the HAZ development of the AZ31B. The relatively low current of 3.5 kA caused no thermal effect on the AZ31B and resulted in grain refinement by the pressing force as shown in Fig. 5-6(a). The grain size significantly changed from initial state 14.7

μm to $5 \mu\text{m}$. The HAZ of the AZ31B of the specimen which welded at 8.5 kA was about $19.2 \mu\text{m}$ with a slightly larger grain size than as-received condition. Namely, this grain refining means many grain boundaries and may be significantly related to mechanical properties. However, it was interesting that no significant changes in Schmid factors or KAM values were observed under both conditions. Fig. 5-6(c, d) illustrates the grain size distributions and Schmid factor distributions, respectively. The pole figures (PFs) results according to the change of welding current from the AZ31B state of the as-received state are also shown in Fig. 5-6(e). Textures in the context of materials science means crystallographic preferred orientation. If a polycrystalline material has texture then that means that the crystal axes are not randomly distributed. Our results exhibit that the as-received condition had texture, whereas the welded specimen showed a change in texture that originated from heat transfer of welding. The HAZ development of the AZ31B is further discussed with the help of a numerical approach in the discussion section.

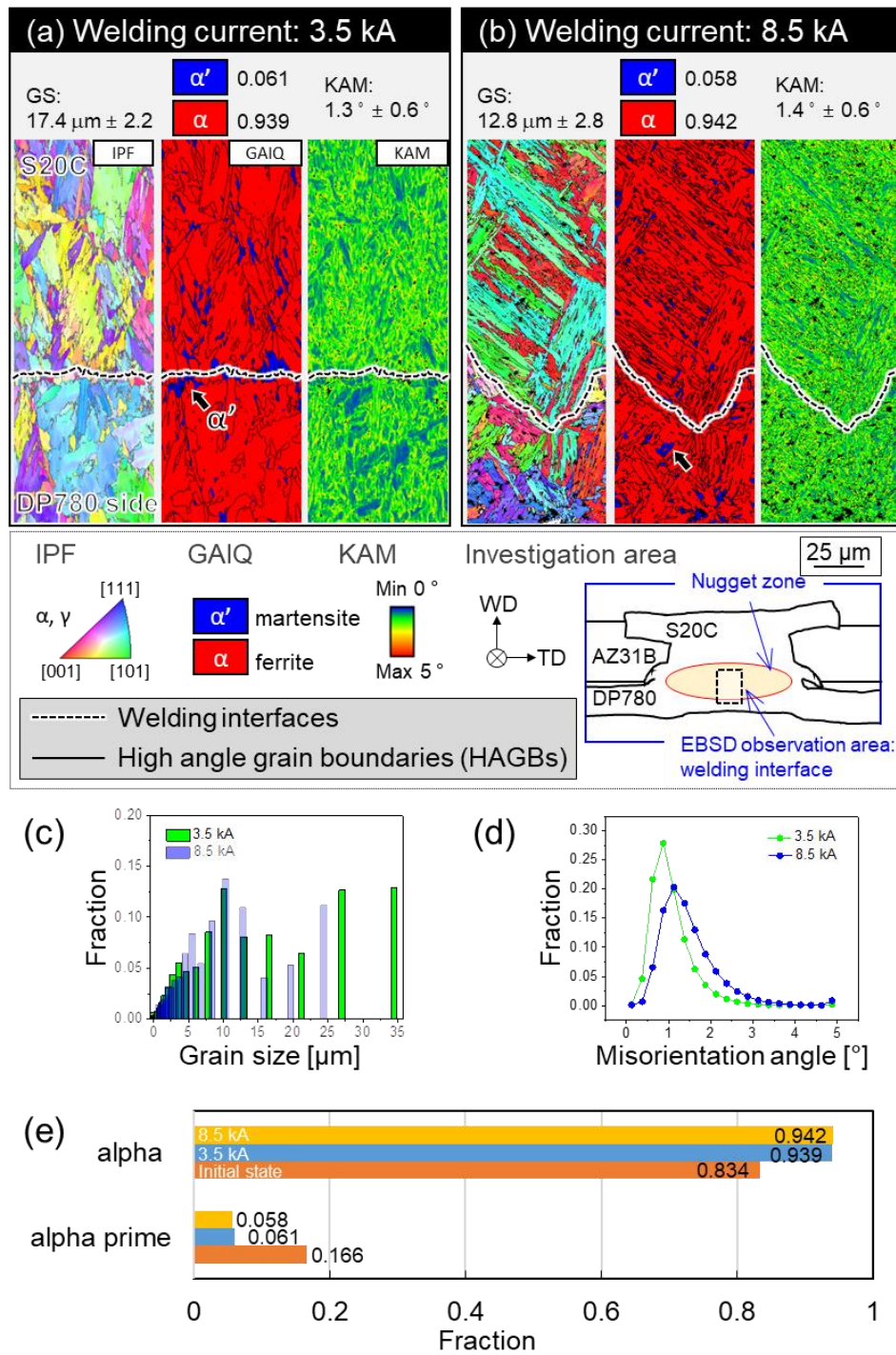


Fig. 5-5 EBSD observation results of welding interfaces between S20C and DP780 steel. (a) the welding interface of S20C/DP780 with the 3.5 kA current condition, (b) welding interface with 8.5 kA, and (c) grain size distribution plot, (d) KAM plot and (e) phase fraction plot.

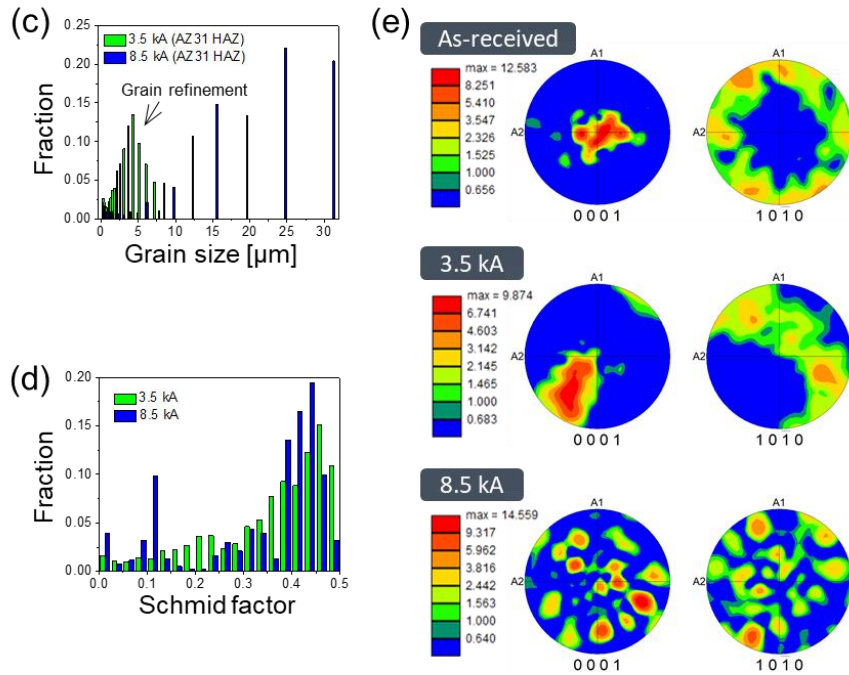
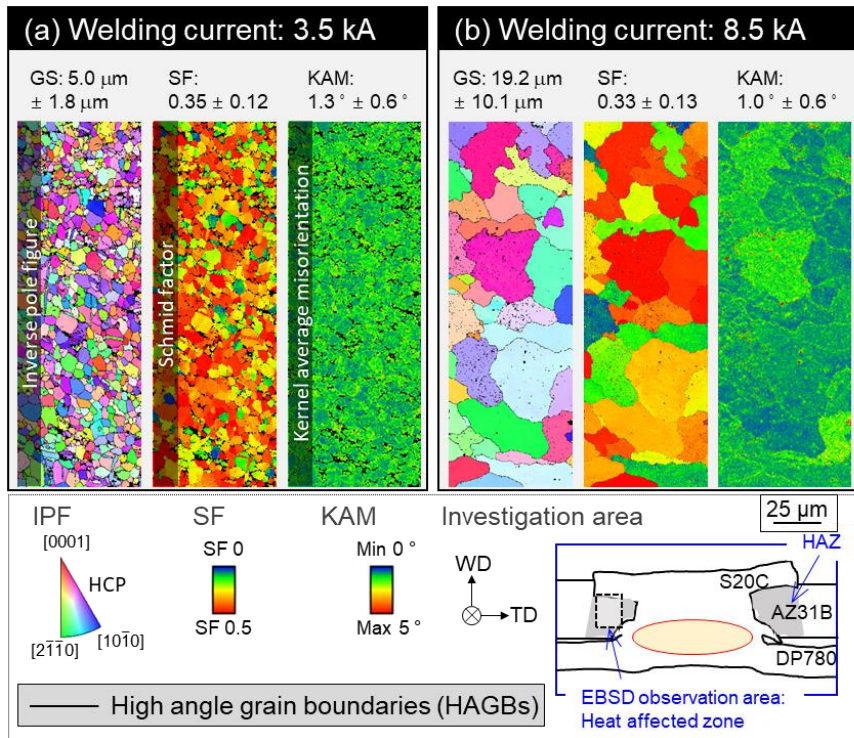


Fig. 5-6 EBSD observation results of AZ31B HAZ. (a) AZ31B HAZ with the 3.5 kA current condition, (b) AZ31B HAZ with the 8.5 kA, (c) grain size distribution plot, (d) Schmid factor plot and (e) pole figures.

5.3.3 Mechanical properties

5.3.3.1 Hardness distributions

Hardness change of a weld metal originated from microstructure developments. Fig. 5-7 presents micro-Vickers hardness distributions according to welding current conditions. Here, a smaller indentation means harder, and a larger indentation means softer. The welding current of 2.5 kA showed overall low hardness distribution, which means that this heat input did not cause significant phase transformation in the welding interface of the steel part. AZ31B parts showed no significant changes in hardness distributions according to the change of welding currents. On the other hand, as the heat input exceeded 3.5 kA, the maximum hardness value of the welding interface exceeded about 430 Hv, and as the heat input increased, the area where the hardness was further increased showed a tendency to expand. This is clearly supported by the evidence for α' -martensite transformation mentioned in the session 3.2.2.

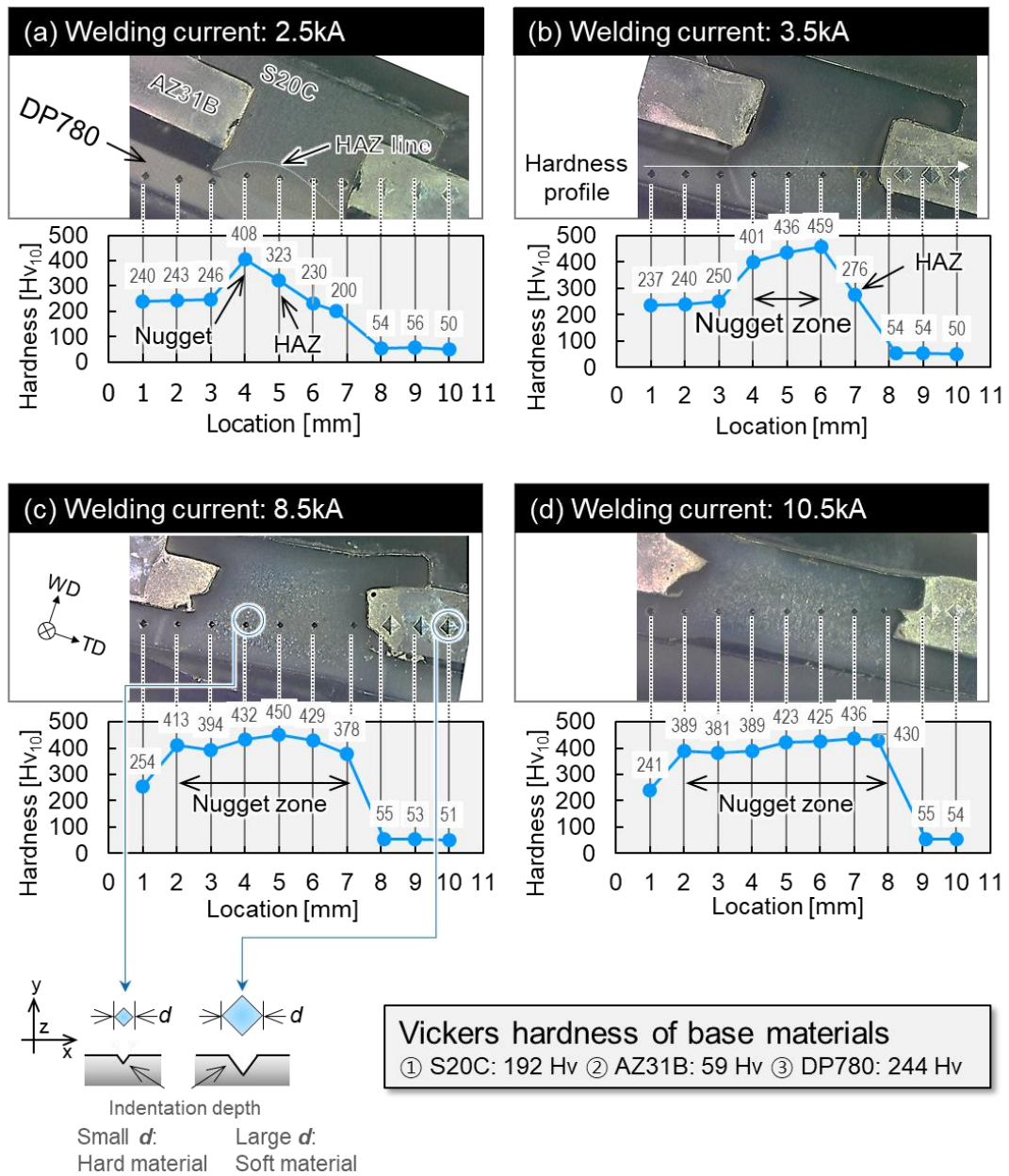


Fig. 5-7 Vickers-microhardness distributions. (a) the 2.5 kA current condition, (b) 3.5 kA, (c) 8.5 kA and (d) 10.5 kA.

5.3.3.2 Tensile-shear properties

Tensile-shear tests were performed to investigate how changes in microstructures affect mechanical properties. The mechanical behavior occurring during tensile-shear testing was visualized by DIC method. A welding current of 2.5 kA obtained peak loads

of less than 3,000 N with a displacement of less than 1 mm, which caused an interfacial fracture. A moment of the failure shows that the maximum strain was recorded on the S20C element as displayed in Fig. 5-8(a). However, with a welding current of 3.5 kA, the increased displacements and peak loads approaching about 5,000 N were noticeable as shown in Fig. 5-8(b). The fracture mode changed dramatically with the ripped AZ31B sheet. As confirmed in the microstructure session, it can be seen that the deformation of Mg alloys can be more actively performed than the initial state due to the increase of grain boundary systems. Fig. 5-8(c) presents the tensile-shear testing results of 8.5 kA welding conditions. When the welding current reached 8.5 kA, the peak loads exceeded 6000 N, but a relatively small displacement with plug failure mode was observed. The welding current of 10.5 kA caused similar tendency of the mechanical behavior and fracture mode with 8.5 kA current. The displacement was further reduced, and traces of a ripped Mg element were observed around S20C. Fig. 5-8(e) summaries the relationship between peak loads and displacements depending on the welding currents. The peak load of tensile-shear testing was gradually increased when the welding currents from 2.5 kA to 8.5 kA, but when the welding current exceeded 8.5 kA, the maximum load was decreased. However, the change of the displacement showed the largest value at about 13.5 mm at the REWeld joint of 3.5 kA, and then decreased linearly.

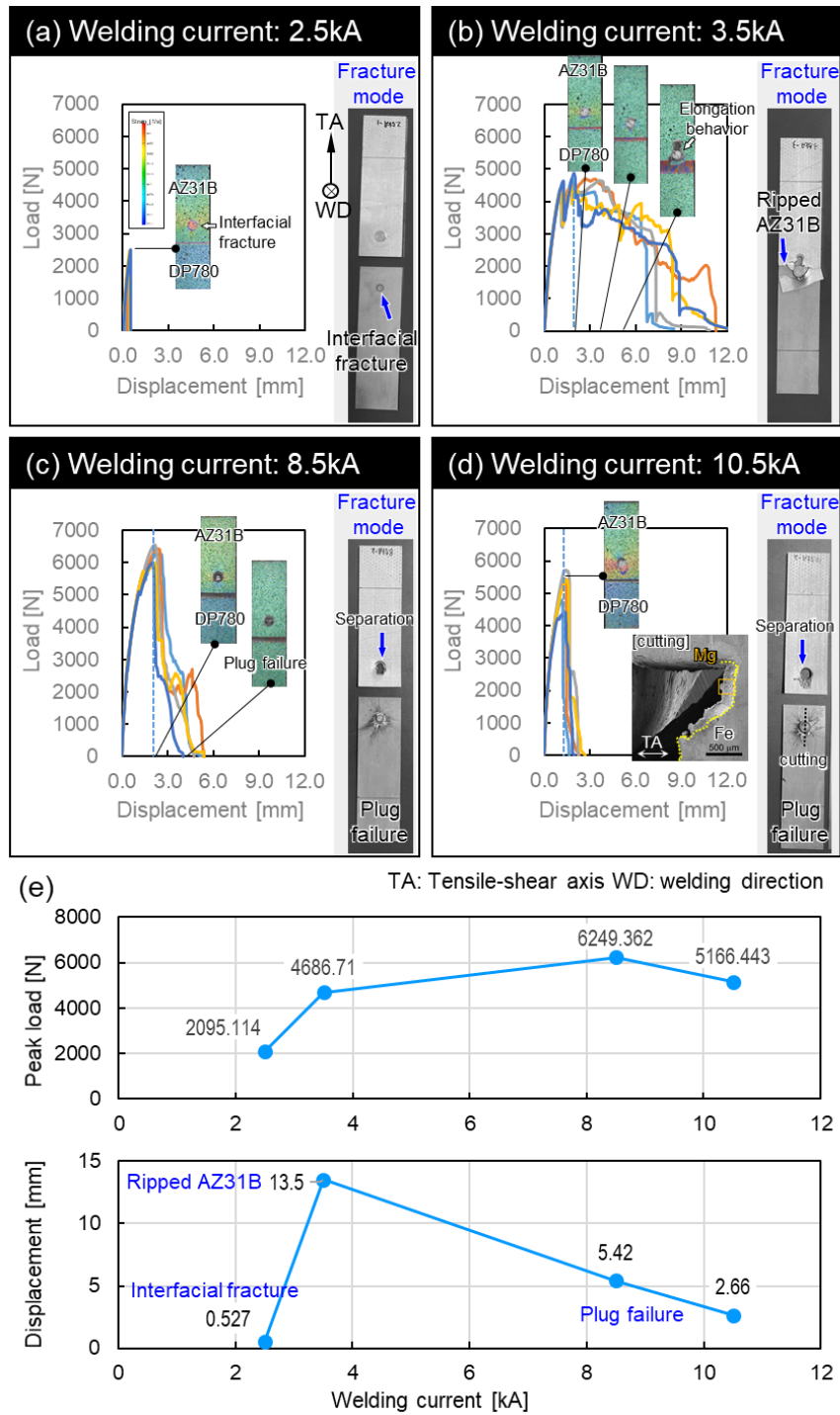


Fig. 5-8 Results of tensile-shear tests. (a) the 2.5 kA current condition, (b) 3.5 kA, (c) 8.5 kA and (d) 10.5 kA. (e) plot of change of peak load and displacement by welding current parameters.

5.3.3.3 Fatigue performances

Results of fatigue tests conducted are plotted in Fig. 5-9(a) as load amplitude (N) vs number of cycles to failure (N_f) plots. Failure modes corresponding to each life cycle are also provided. The fatigue load was applied from 80% to 20% of the tensile-shear load. In Fig. 5-9(b), specimens welded at 2.5 kA had a lifetime of 105 cycles with an interfacial fracture at about 1,747 N (pink X sign). The fracture occurred at the weld interface even at a fatigue load lower than the tensile-shear load, which was attributed from the insufficient weld penetration. The high-cycle fatigue fracture of the specimen welded to 2.5 kA withstood up to 1,030,020 cycles at 499 N, which was the crack propagation fracture of the AZ31B sheet as presented in Fig. 5-9(c). Fatigue characteristics of joints welded by 3.5 kA currents (red squares) withstood 18,670 cycles at about 2,500 N. In addition, when the fatigue load over 1,000N was applied, it exceeded 10^5 cycles, which showed a significant improvement in fatigue strength compared to the welding condition of 2.5 kA (see Fig. 5-9 (d, e)). The condition of 8.5 kA (sky blue dots) displayed the highest tensile shear load, which shows excellent fatigue life withstanding 3,010 cycles under applied load of over 4,700 N (Fig. 5-9(f)). This is an exceptional performance to the previously reported results of Mg/steel lap joint fatigue studies[19–21]. Furthermore, this specimen endured 147,803 cycles with the fatigue load of 1,371 N as shown in Fig. 5-9(g). The joint at condition 10.5 kA caused the plug failure of Mg alloys at 45 cycles with 4,021 N (Fig. 5-9(h)). This means that it could be related to significant defects formed in the HAZ of the AZ31B. Fig. 5-9(i) exhibits the fatigue failure mode of the specimen bonded with 10.5 kA. A lifetime of 10^5 cycles at a load of 1,100N was shown with crack propagation in the AZ31B sheet. Fig. 5-10 summaries the fatigue loading histories. It has been clearly confirmed that the

reference cycle for determining the fatigue failure mode was 10^3 cycles. An interfacial failure (IF) of welding interfaces, and plug failure (PF) of Mg alloys were common features that did not exceed 10^3 cycles. The crack propagation failure modes of Mg alloys commonly exceeded 10^3 cycles. The origins of these phenomena are discussed in detail in the next section.

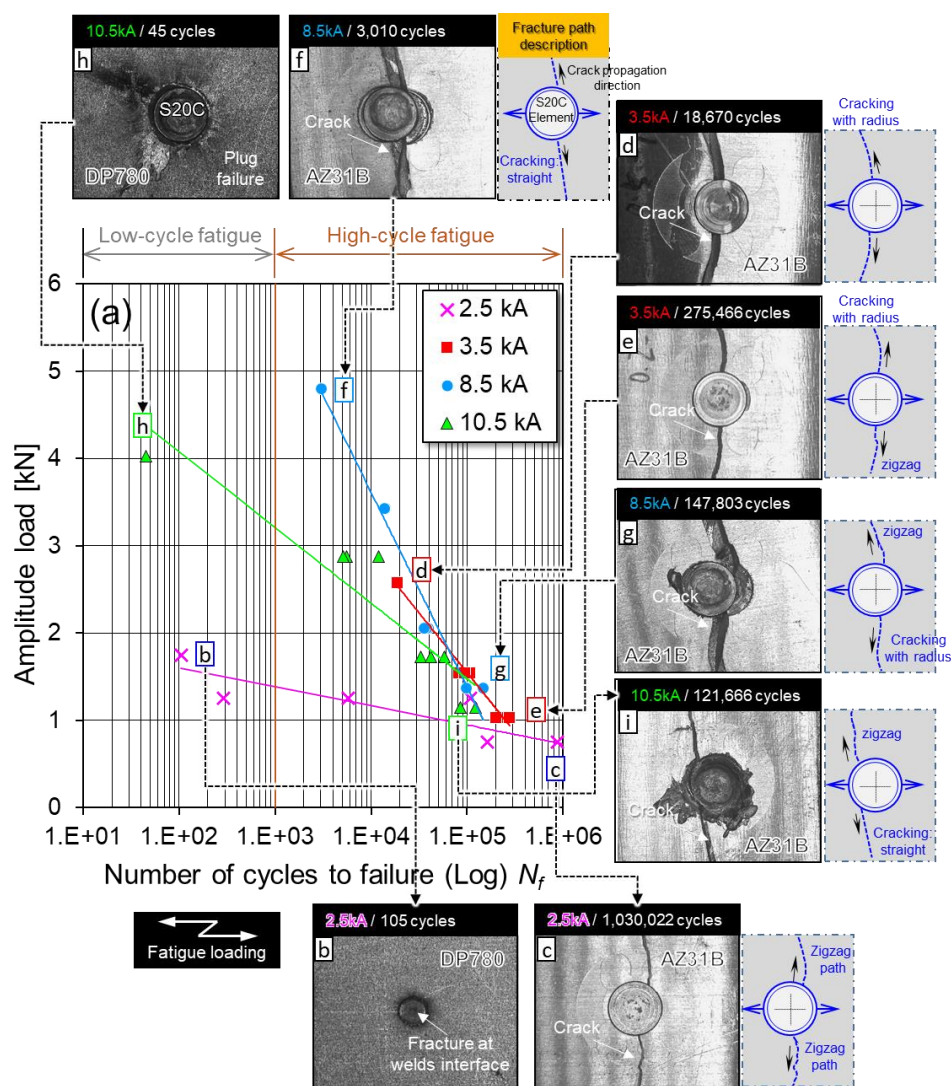


Fig. 5-9 Results of fatigue tests and fracture modes. (a) fatigue duration diagram, (b, c) fracture modes for weld joints with the 2.5 kA current; pink color, (d, e) fracture modes of weld joints with 3.5 kA; red color, (f, g) fracture modes with 8.5 kA; sky blue, and (h, i) fracture modes of weld joints with the 10.5 kA welding current; green color.

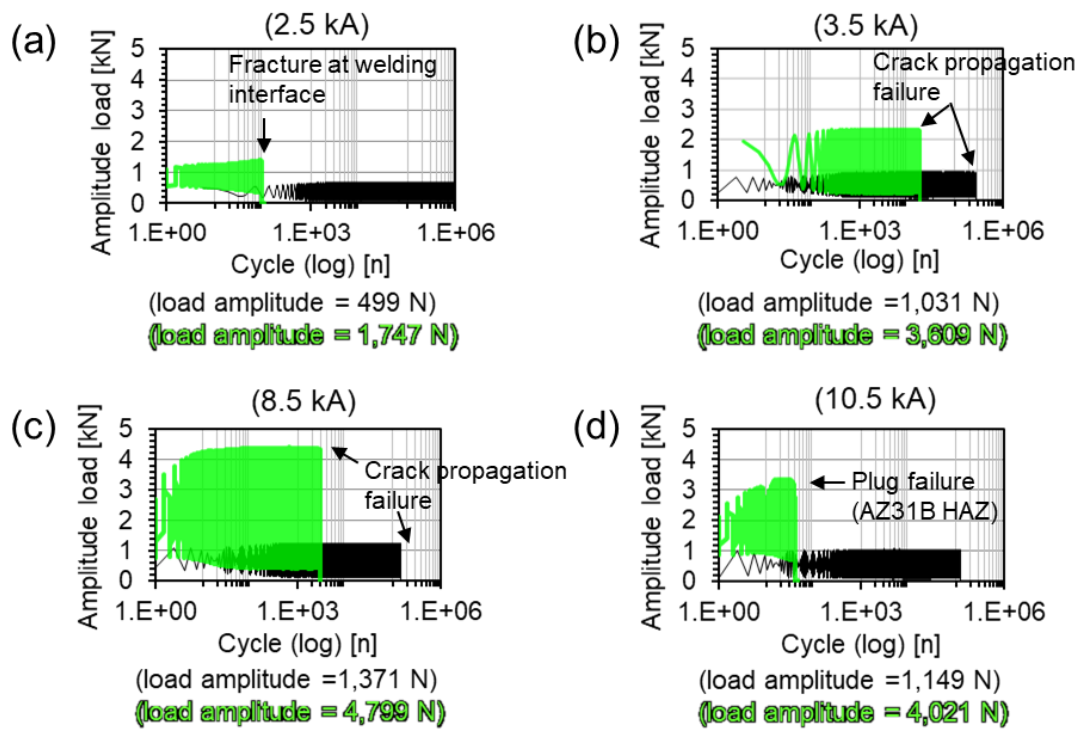


Fig. 5-10 Fatigue loading histories. (a) 2.5 kA, (b) 3.5 kA, (c) 8.5 kA and (d) 10.5 kA. The lifetime exceeding 10^3 cycles was the crack propagation fatigue failure mode of Mg alloys, and the fatigue life below 10^3 cycles was either plug failure or S20C/DP780 interfacial failure.

5.3.3.4 Fracture surfaces

This section focuses on the relationship between fatigue properties and microstructures through fracture surface analysis. Fig. 5-11 represents the FESEM micrographs of the fracture surface at 105 cycles tested at 1,747 N of AZ31B/DP780 welded joint with the 2.5 kA current. There was a significant portion of the un-bonded portion, and traces of resistance to the fatigue load were observed around the welded zone. A fatigue fracture occurred the interface between S20C and DP780, ripped areas and cracking are noticeable as shown in Fig. 5-11(a). In the magnified image of the ripped area at a higher magnification, traces of resistance to the fatigue load can be observed, and dimples were observed (Fig. 5-11(b, c, d)). This mean that, as explained in

the schematic description (Fig. 5-11(e)), the fatigue load was concentrated only in the narrowly welded area. In the AZ31B/DP780 REWeld joint where the fatigue load of less than 1,000 N was applied, a crack propagation occurred in the AZ31B up to 10^6 cycles. In Fig. 5-12(a), there were no conspicuous defects, and most of the area was occupied by crack propagation areas. In here, three main characteristics were observed, consisting of the crack propagation region, the fatigue chevron region, and the dimple zone. In Fig. 5-12(b), a fracture surface characterized by a cleavage facet with fatigue striations was observed in the crack initiation zone. The high magnification image of the clear chevron mark is shown in the Fig. 5-12(c). The cleavage facet was also present in this area, these type of fractures are considered brittle fractures. Z. Han et al.[22] also have been reported similar fatigue fracture morphological characteristics. This feature is considered a typical fatigue failure form of magnesium alloy extrusions. A dimple zone, a trace of the eventual fracture resistance of the decreased section, was visible near the tip of the welded specimen as crack propagations advanced as displayed in Fig. 5-12(d). This type of the fatigue fracture specimen was a zigzag fracture morphology (Fig. 5-12(e)).

2.5 kA / 105 cycles:
Fatigue fractured at welding interface (DP780 side)

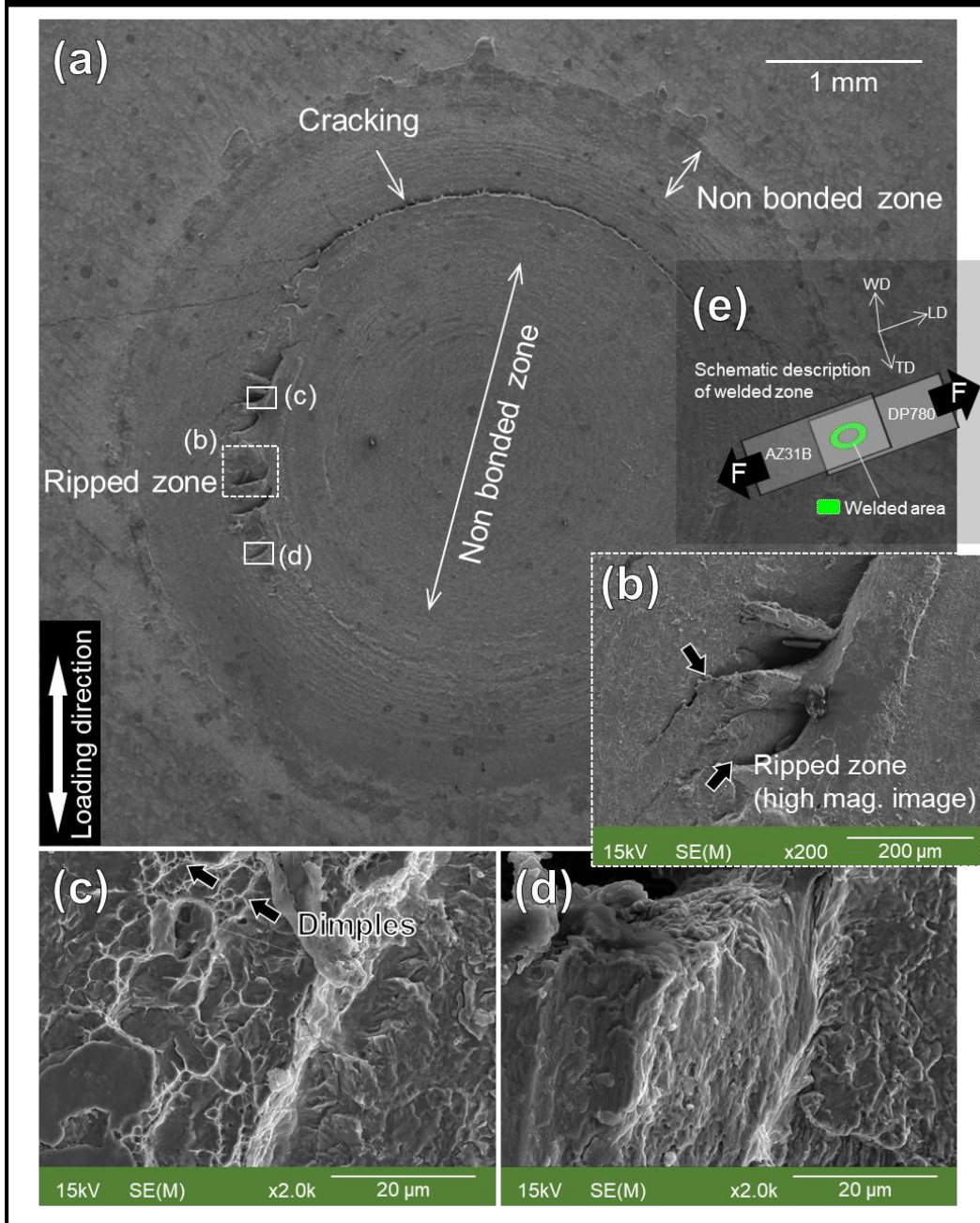


Fig. 5-11 Fracture surface analysis results of the welding joint with the 2.5 kA which failure at 105 cycles. (a) interfacial fractured surface at the DP780 side, (b) high magnification image of traces that resist destruction, and (c) dimple zone, (d) high magnification image of ripped zone, (e) a schematic description of fractured zone.

When the welding current was 8.5 kA, the low-frequency fatigue fracture surface of the weld joint with the sufficient penetration and mechanical hook formation is displayed in Fig. 5-13. As seen in Fig. 5-13(a), porosities with a size of approximately 0.39 mm in diameter was observed in the S20C silhouette. This is considered a defect resulting from the welding process. And it can be clearly divided into the crack propagation area and the ductile area. The crack propagation area with secondary cracking is considered to be rougher than that of the specimen withstanding up to 10^6 cycles (see Fig. 5-13(b, c)). This may be related to the development of the heat-affected zone of the AZ31B sheet. Fig. 5-13(d) displays the dimple zone attributed from the overloading during fatigue tests. Fig. 5-13(e) illustrates the measured cracking path, the fracture path where crack propagation has mainly progressed was a zigzag path, whereas the area with many ductile fractures shows a straight fracture path, respectively. Fig. 5-14 shows high-frequency fatigue fracture surface of the AZ31B/DP780 lap joint with the 8.5 kA welding current. Porosities were still detected in the S20C silhouette, which are believed to have formed during the welding process. It is considered to be due to S20C and DP780 being heated above the melting point of Mg alloys during the welding process. Fig. 5-14(b, c) exhibits FESEM images of the crack initiation and crack propagation zone, respectively. The secondary crack was not found and it was not rough as the low-frequency fatigue fracture. This area is a direct comparison to the fracture surface subjected to a high fatigue load. In Fig. 5-14(d), as with the previous conditions, the final stage of fatigue shows failure by overloading with the dimple zone. Fig. 5-14(e) summaries the crack propagation path, which can be seen that the crack developed in the shape of a zigzag and radius shape. The result of the low cycle fatigue test of 10.5 kA reached failure in 45 cycles due to the plug failure which

showed a pattern similar to that of the tensile-shear test. SFig. 5-1 illustrates the fracture surface FESEM image of the AZ31B/DP780 lap joint with 10.5 kA, it withstood up to 1.21×10^5 cycles.

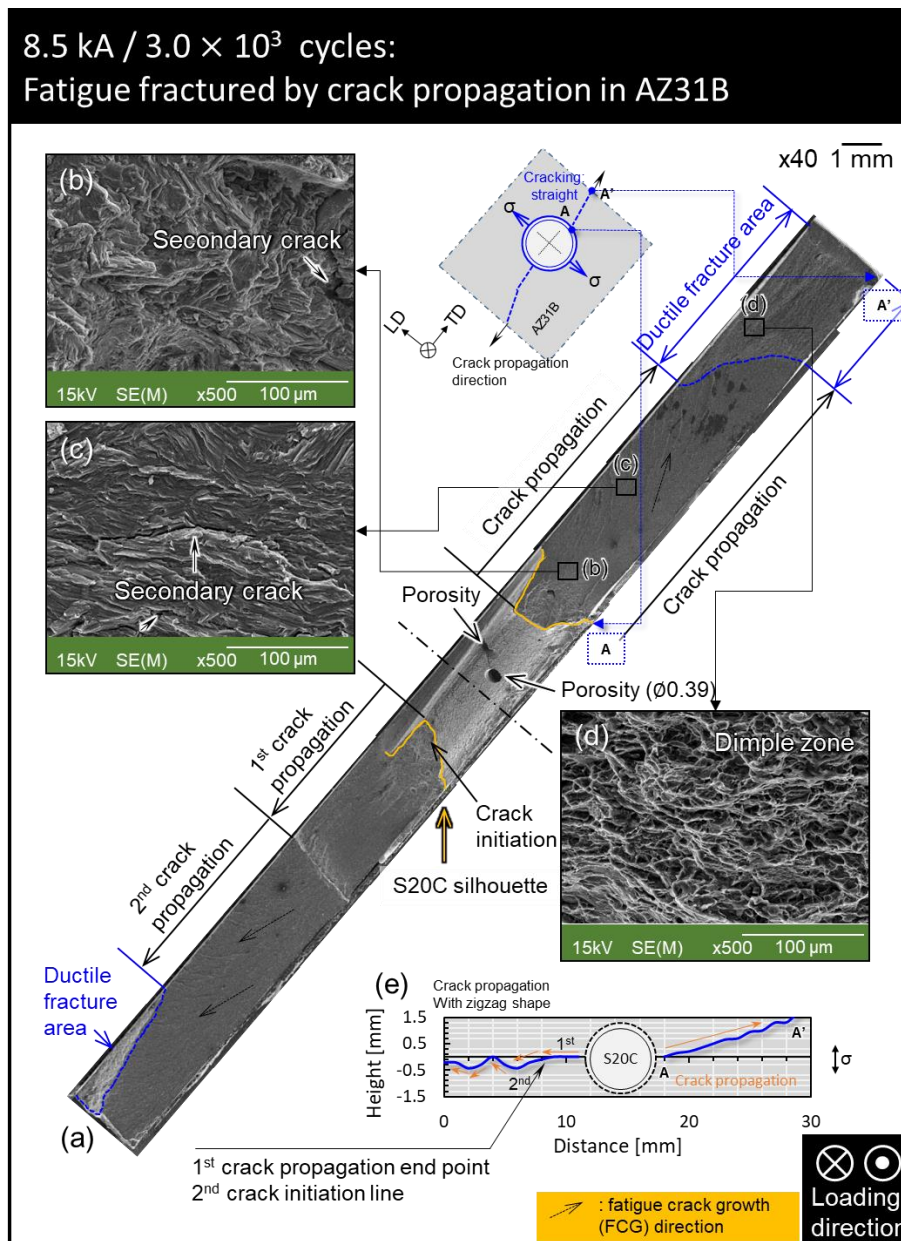


Fig. 5-13 Fracture surface analysis results of the welding joint with the 8.5 kA which failure at 3×10^3 cycles. (a) AZ31B side fractured surface with crack propagation, (b) high magnification image of cracking initiation zone; secondary cracking, (c) fractured surface of crack propagation zone, (d) dimple zone, and (e) crack propagation of zigzag type path.

8.5 kA / 1.47×10^5 cycles:
Fatigue fractured by crack propagation in AZ31B

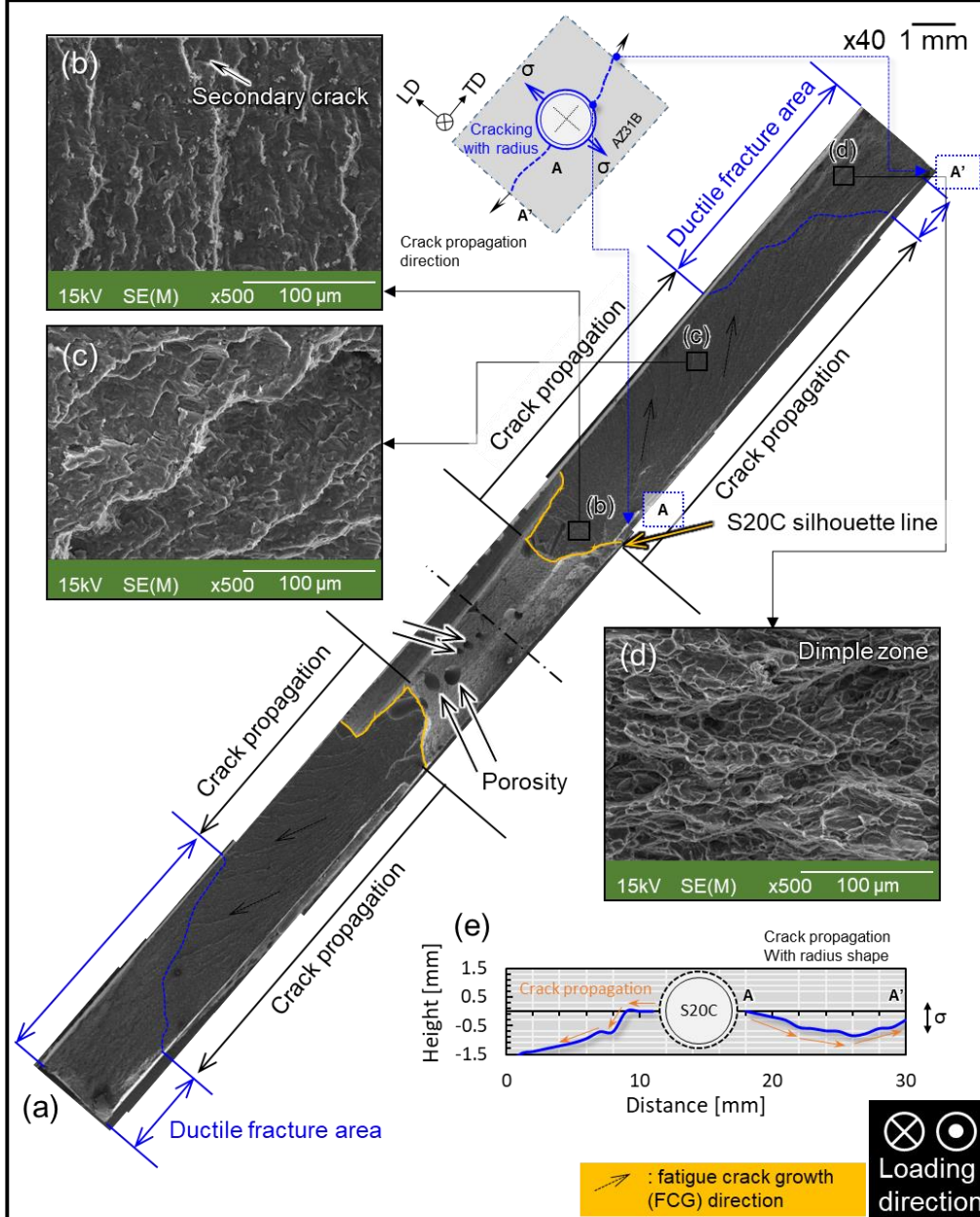
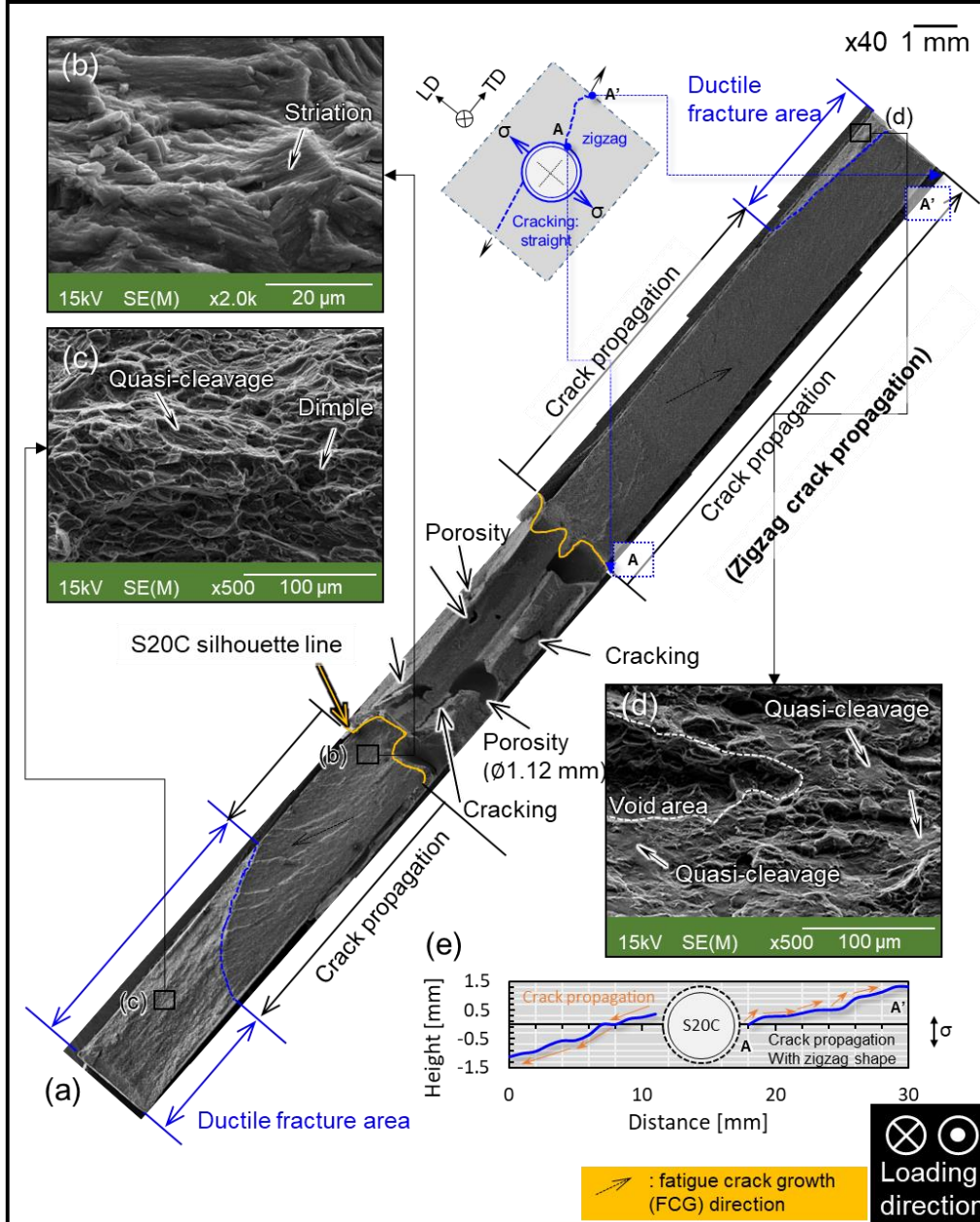


Fig. 5-14 Fracture surfaces of the welding joint with the 8.5 kA which failure at 1.47×10^5 cycles. (a) AZ31B side fractured surface with crack propagation, (b) cracking initiation zone with secondary cracking, (c) fractured surface of crack propagation zone, (d) dimple zone, and (e) crack propagation of radius type path.

10.5 kA / 1.21×10^5 cycles:
Fatigue fractured by crack propagation in AZ31B



SFig. 5-1 Fracture surfaces of the welding joint with the 8.5 kA which failure at 1.47×10^5 cycles. (a) AZ31B side fractured surface with crack propagation, (b) cracking initiation zone with secondary cracking, (c) fractured surface of crack propagation zone, (d) dimple zone, and (e) crack propagation of radius type path.

5.4 Discussion

5.4.1 Phase transformation of S20C/DP780 welding interfaces

Welds in DP780 steel are focused in this section as they are the main factor determining mechanical strength, leading to loss of martensite fractions. Fig. 5-15(a) illustrates the schematic description of the prior austenite grain boundary (PAGB). When steel is welded, it is transformed into austenite at high temperature and then transformed into martensite, bainite, or ferrite depending on cooling speeds. Namely, the grain boundary that was austenite at high temperature is called PAGB. It is well known that the PAGB range is $20 \leq \theta \leq 50^\circ$ in structural steels[23]. Fig. 5-15(b) presents PAGBs of base materials on the IPF maps. Herein the black lines mean PAGBs. Fundamentally, the PAGES of low carbon steel and DP steel showed a significant difference. PAGES grown more than doubled after welding as shown in Fig. 5-15(c). The prior austenite grain size (PAGS) of S20C was larger than DP780 steel. Fig. 5-15(d) summaries changes in PAGES from the base metals to the changes in welding currents. PAGES also has a significant effect on phase transformation. Moreover, phase transformation of fusion zone of low carbon steel after RSWs mainly depends on the austenite stability and cooling rate[24–26]. Namely, lower austenite stability and higher cooling rate drive more active α' -martensitic transformation during cooling after RSW. Regarding the austenite stability, it can be evaluated quantitatively by means of α' -martensite start temperatures. The effect of alloying elements on the martensite start temperature of α' -martensite phases has been suggested by previous studies[27,28]:

$$M_s^0 (C) = 576 \pm 539 - 423C - 30.4Mn - 7.5Si + 30Al \quad (4)$$

where Mn, Si, Al, and C denote the concentration of the Mn, Si, Al, and C in weight percent. The effect of PAGS on the M_s^0 temperature was derived by Yang and Bhadeshia et al.[29] and Yen et al.[30], as follow:

$$M_s^0 - M_s = \frac{1}{b} \ln \left[\frac{1}{\bar{V}_\gamma} \left\{ \exp \left(-\frac{\ln(1-f)}{m} \right) - 1 \right\} + 1 \right] \quad (5)$$

where M_s means α' -martensite start temperatures reflecting the effects of both alloying elements and prior austenite grain size. b denotes the fitting parameters (0.2689 for α' -martensite), \bar{V}_γ is the austenite grain volume_{avg} of (unit: mm³), related to the PAGS, m is the aspect ratio of the martensite plate (0.05 for α' -martensite), and f is the first detectable fraction of martensite which is assumed to be 0.01. For the present S20C (Fe-0.47Mn-0.2Si-0.2C-0.012P) steel, the M_s^0 values of α' -martensite was calculated as 438.612 °C. Namely, based on these temperature ranges, martensite phase can be formed at the M_s^0 temperature of the S20C near the top of the nugget.

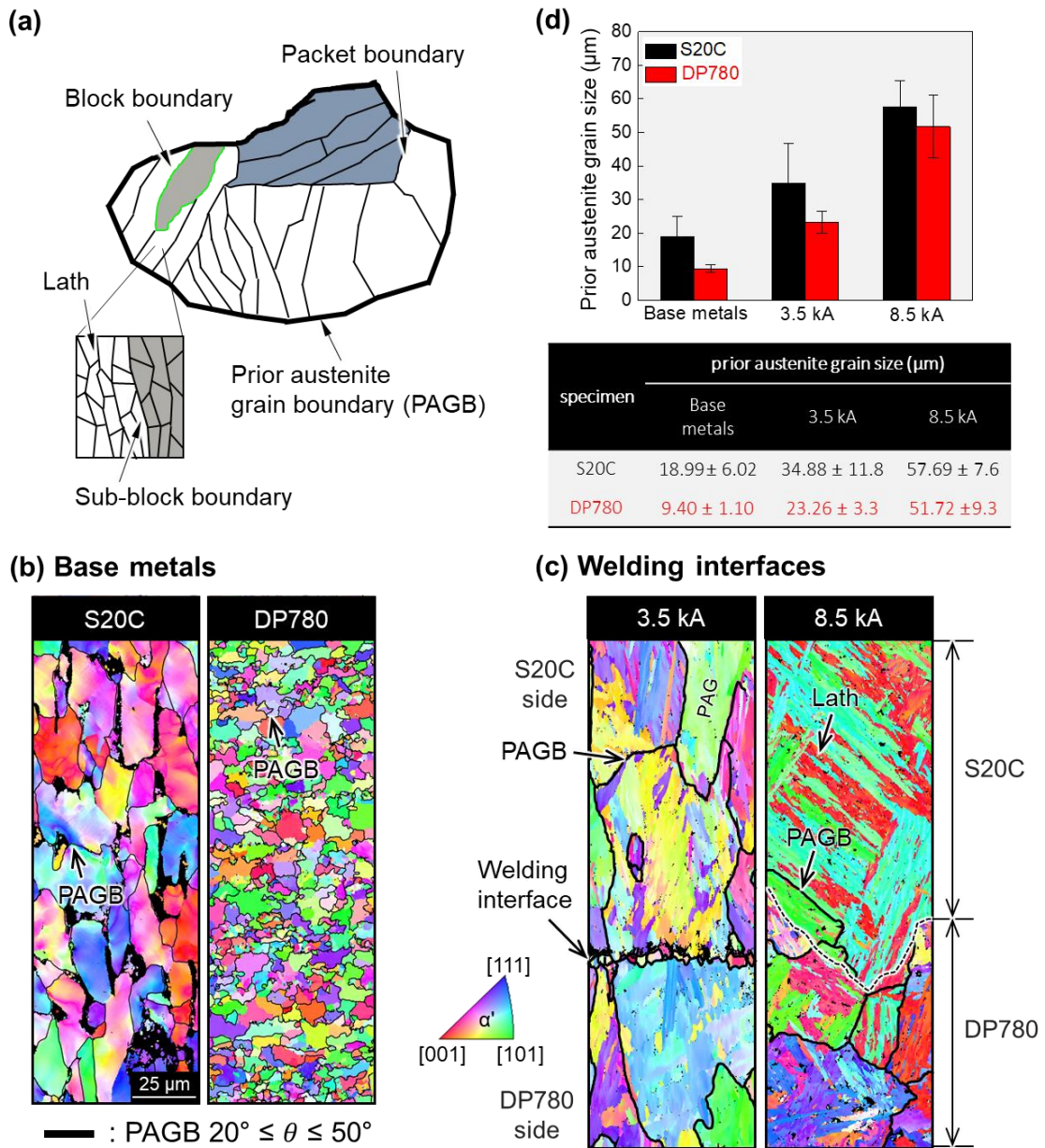


Fig. 5-15 An evidence of martensite transformation; change of prior γ grain boundaries depending on welding currents in detail. (a) a description of PAGB, (b) IPF map with PGABs of initial state materials, (c) PAGS change after resistance element welding, and (d) plot for prior austenite grain size change. PAGB: prior austenite grain boundary.

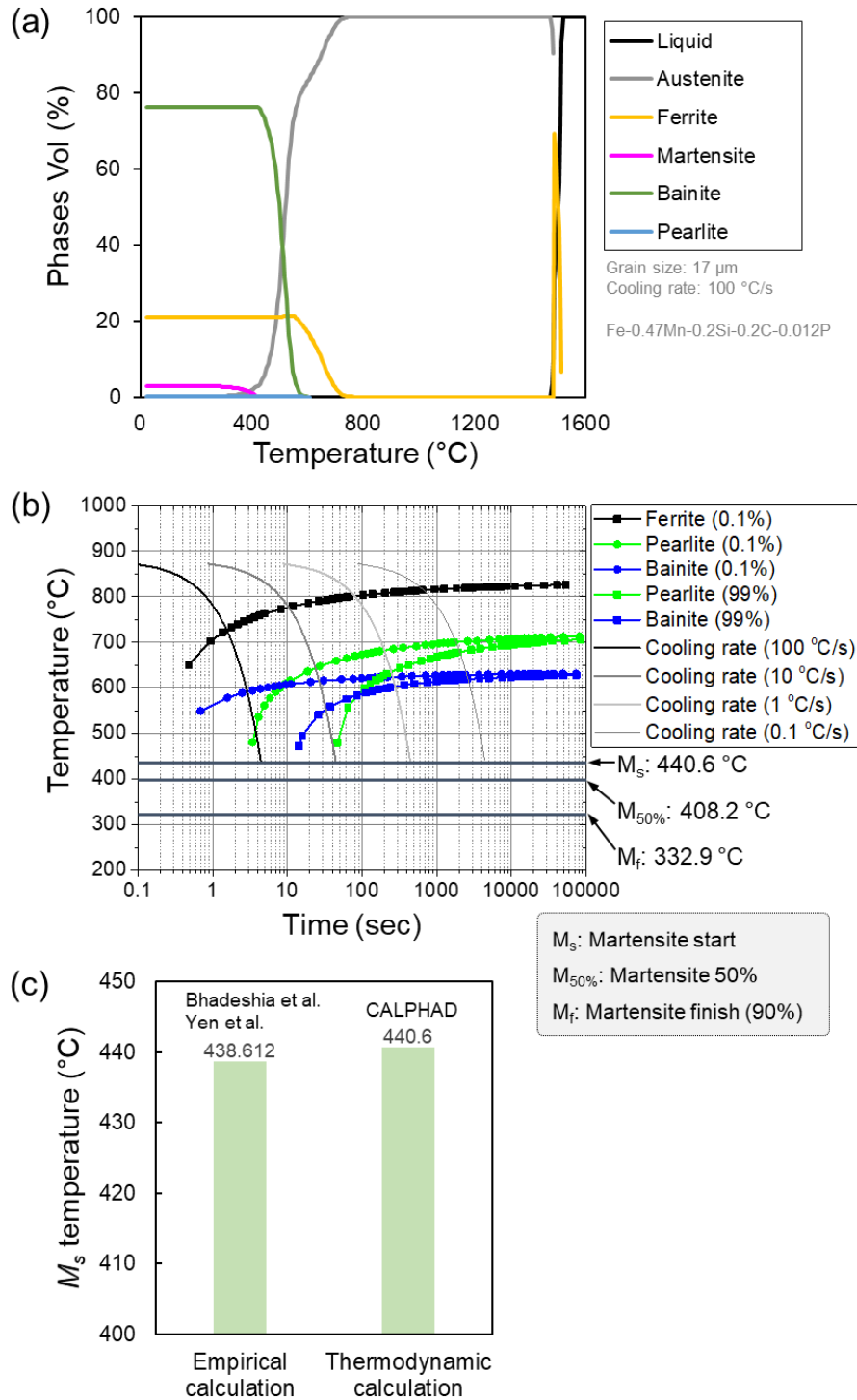


Fig. 5-16 Thermodynamic calculation results for S20C (Fe-0.47Mn-0.2Si-0.2C-0.012P) steel; exploring martensite potential. (a) solidification diagram, (b) CCT curve plot, and (c) a comparison of empirical calculation and thermodynamic calculation. CCT: continuous cooling transformation.

To further clarify the origin of the martensite development after welding in S20C rivet elements, phase fraction simulation was performed through thermodynamic calculations as well. Fig. 5-16(a) exhibits the result of solidifications on the S20C element. A cooling rate of 100 °C/s in the molten state was assumed, and the grain size of the base metal was selected with 17 μm based on EBSD results as displayed Fig. 5-4(b). As a result of thermodynamic calculations, the 100% austenite point of S20C was found to be over 785 °C. In addition, assuming solidification under these conditions, it was found that about 2.85% of martensite can be produced on the S20C side and about 76.13% of the bainite phase can be formed in theoretically. Fig. 5-16(b) presents continuous cooling transformation (CCT) curve of the S20C element, the temperature of martensite start (M_s^0) was 440.6 °C and the temperature of martensite finish (M_f) was 332.9 °C, respectively. As a result, M_s^0 by empirical formula and the result by thermodynamic calculations are summarized in the Fig. 5-16(c). The difference between the empirical formula and the thermodynamic calculations was only 0.45%, which seems very reliable results. This martensite transformation can be contributed to high strength with maintaining the dual phase. For this reason, it can be concluded that the combination of elements of DP steels and S20C by REW process can realize dual phase properties in steel parts.

5.4.2 The mechanism for microstructures evolutions of AZ31B HAZ

The condition of AZ31B near the weld interface is a very important factor in determining the elongation and strength when subjected to mechanical loading. In this study, it was observed that the HAZ of AZ31B caused by a relatively low welding current and the HAZ induced by a high welding current were different (Fig. 5-6).

Moreover, it was observed that the mechanical behavior was significantly different. The mechanism for the HAZ development of AZ31B depending on the welding current is displayed in Fig. 5-18. The outline of the welds with the current of 3.5 kA is shown in Fig. 5-17(a). The welding joint has constraint at bottom and top side with electrodes, respectively. Fig. 5-17(b) presents the schematic description in detail. The compression force with this constraint caused deformed HAZ of the AZ31B. When the welding current was 3.5 kA, the tolerance between S20C and AZ31B was not reduced because the S20C and DP780 steel did not melt sufficiently with each other, which occurred insufficient heat transfer. For this reason, as can be seen from the SEM image, 785 μm left an incomplete defect near the welding interface. Thus, the grain refinement was promoted because only the compressive force was applied to the AZ31B without thermal loading (see Fig. 5-17(c)). The macrograph of the joint welded with the current of 8.5 kA is presented in Fig. 5-17(d). The welding interface between S20C and DP780 was completely melted each other, which caused extruded hook with compressed forcing. Due to this phenomenon, the tolerance between S20C and AZ31B was disappeared, and heat of the welding interface formed the AZ31B HAZ as shown in Fig. 5-17(e). The grain of AZ31B by heat transfer was grown as presented in Fig. 5-17(f). The degradation of AZ31B due to welding heat transfer was confirmed in the OM macrograph as displayed in Fig. 5-17(g). Based on the black dotted line, the difference between the grain boundary (G.B.) and the HAZ can be clearly distinguished. Dendrites were detected in HAZ as well. This suggests that there was solidification after melting. These considerations are further explored through simulation works. A possible mechanism illustrates in the schematic diagram in Fig. 5-17(h). In the case of the joint with 8.5 kA, it is considered that the heat generated by the nugget is transferred directly to the

AZ31B without tolerance. Since the melting point of the weld interface between S20C and DP780 steels is approximately 1,600 °C, the heat-affected zone of AZ31B may have been in a molten state. Therefore, dendrite is considered to be due to rapid solidification of grains after melting. Consequently, the HAZ of AZ31B can be a solidified structure after melting or a partially melted zone (PMZ). The thermal resistance map in the case of 8.5 kA processing condition can be described as follow:

$$R_{th} = R_{Mg} + R_{Fe} \quad (6)$$

Thermal resistance is a heat property and a measurement of a temperature difference by which an object or material resists a heat flow. Thermal resistance is the reciprocal of thermal conductance. where R_{th} is total summation of thermal resistance [K/W], R_{Mg} is the thermal resistance term of Mg alloys and R_{Fe} is the term of thermal resistance of Fe. The reason why HAZ development of AZ31B is impossible in the case of a relatively low current of 3.5 kA welding condition can be explained by the following the modified thermal resistance equation.

$$R_{th} = R_{Mg} + R_{Air} + R_{Fe} \quad (7)$$

In general, the tolerance is filled with air. The thermal resistance term of air has been added in Eq (6). It is well known that thermal conductivity of air is about 0.025 W/mK[31], which is a significantly low value with AZ31 alloys (85~100 W/mK)[32,33] and Fe system steels (30~60 W/mK)[34,35].

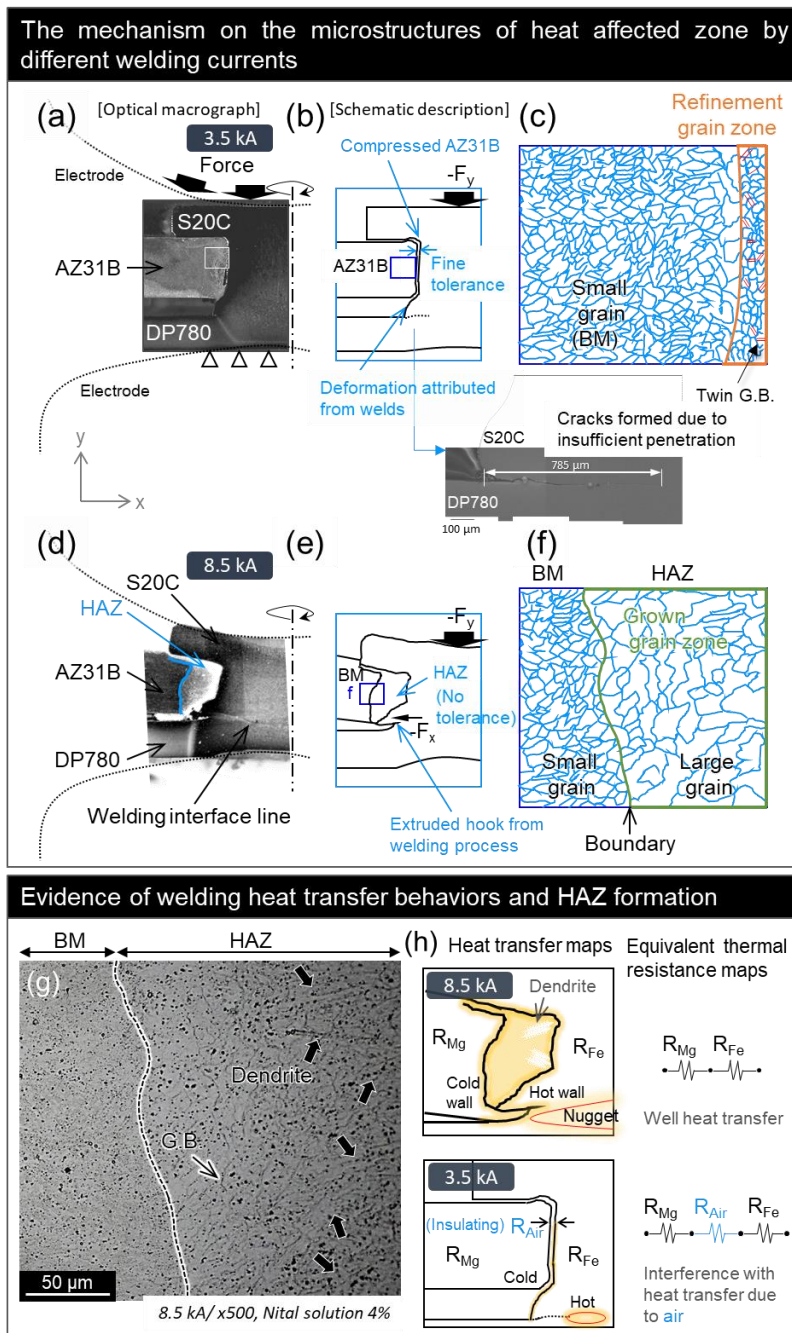


Fig. 5-17 The mechanism of formation AZ31B heat affected zone depending on various welding currents. (a) optical macrograph and welding boundary condition of the weld joint with the 3.5 kA, its schematic description (b), (c) schematic description for a grain refinement mechanism by compression force, and (d) description for welding boundary condition of 8.5 kA, its schematic illustration (e), (f) schematic sketch for grown grain by heat conduction from weld nugget, (g) OM picture of the molten zone and dendrite with grain boundaries, (h) possible heat transfer maps and equivalent thermal resistance maps.

5.4.3 Thermodynamic calculations of AZ31B HAZ

To reveal the origin of the HAZ evolution on the AZ31B, a thermodynamic calculation and finite element method (FEM) simulation were conducted. Fig. 5-18(a, b) depicts the simulation results of thermodynamic calculation (CALPHAD) for AZ31B alloys, respectively. The liquid composition path is shown for an alloy with bulk composition of AZ31B, the reaction taking place assuming the Scheil-Gulliver model as follows:

$$(C_i^{\bar{s}} - C_i^L)df_L = f_L dC_i^L \quad (8)$$

$$C_i^{\bar{s}} = \sum \left(\frac{C_i^L}{\sum f^i} \cdot C_i^k \right) \quad (9)$$

$$\frac{dC_i^L}{dC_{i+1}^L} = \frac{C_i^L - C_i^{\bar{s}}}{C_{i+1}^L - C_{i+1}^{\bar{s}}} \quad (10)$$

where f_L is the liquid fraction (the solid fraction f_S can be obtained by using $f_S = 1 - f_L$); the superscripts denote the phase, whereas the subscripts indicate a specific component (Mg, Al or Zn in this study). $C_i^{\bar{s}}$ is the local concentration of solid, C_i^L is the local composition of liquid. Element mole fraction in each phase was balanced with local thermodynamic equilibrium at the interface[36]. Thermodynamic calculations showed a liquid phase mixing zone from 517.058 °C to about 630°C, which is called the partially melted zone (PMZ). The phase completely transitioned to the liquid phase form 630 °C. Information on the phases that can be formed at the heated temperature is provided. In the solidification simulation, the solid fraction was decreased starting with 357 °C

around, which can exist that combinations of α -Mg and intermetallic compounds phase + liquid phase up to 630 °C (see Fig. 5- 18(a, b)). It is perfectly transitioned to solid phase from 357 °C. Fig. 5- 18(c) presents the 3D FEM simulation result of the thermal distribution of welds. Fig. 5- 18(d) exhibits the cross section image of the thermal distribution and the corresponding OM macrograph of the 8.5 kA welding current. It was clearly found that the heat of the welding interface could sufficiently melt the HAZ of the AZ31B. This result was also the result corresponding to the phase diagram of Mg alloy in the Fig. 5- 18(e). Therefore, the area considered as HAZ in OM was the molten region, and it can be seen through numerical calculations that PMZ exists together. All phase information that can be generated as the molten part solidifies is summarized in Fig. 5- 19. $Mg_{17}Al_{12}$, τ -AlCuMgZn, Mg_2Si and Φ -AlMgZn phases can be formed in AZ31B during solidification processes. The formation of these IMCs in AZ31 alloys has been reported numerically in previous studies as well[37].

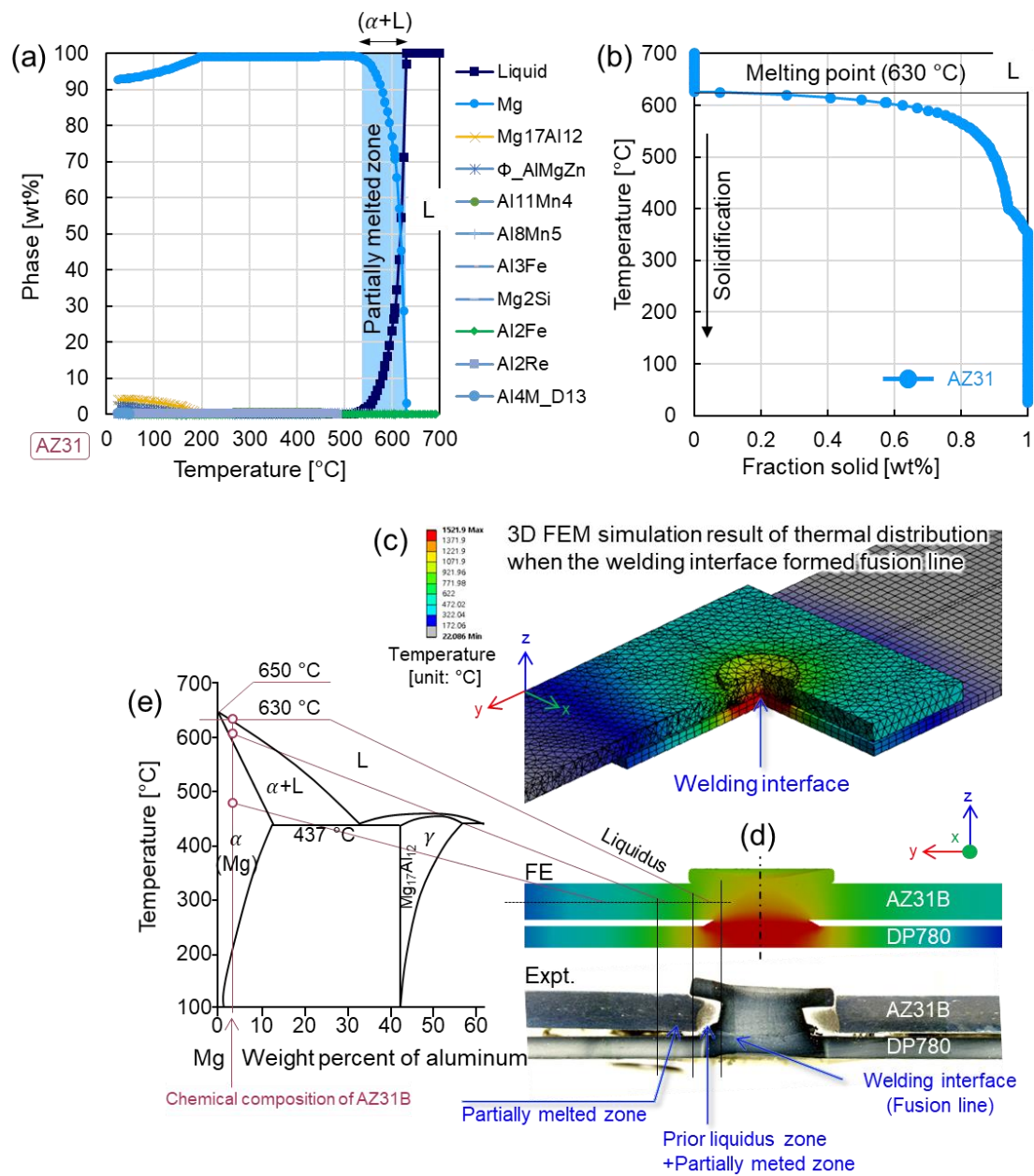


Fig. 5-18 Computer simulation results of thermodynamic calculations and thermal distribution simulations. (a) equilibrium phase diagram of AZ31B, its solidification map(b), (c) thermal distribution at the resistance element welding process, its cross-sectional view(d), and phase diagram of AZ31B corresponding to the temperature range.

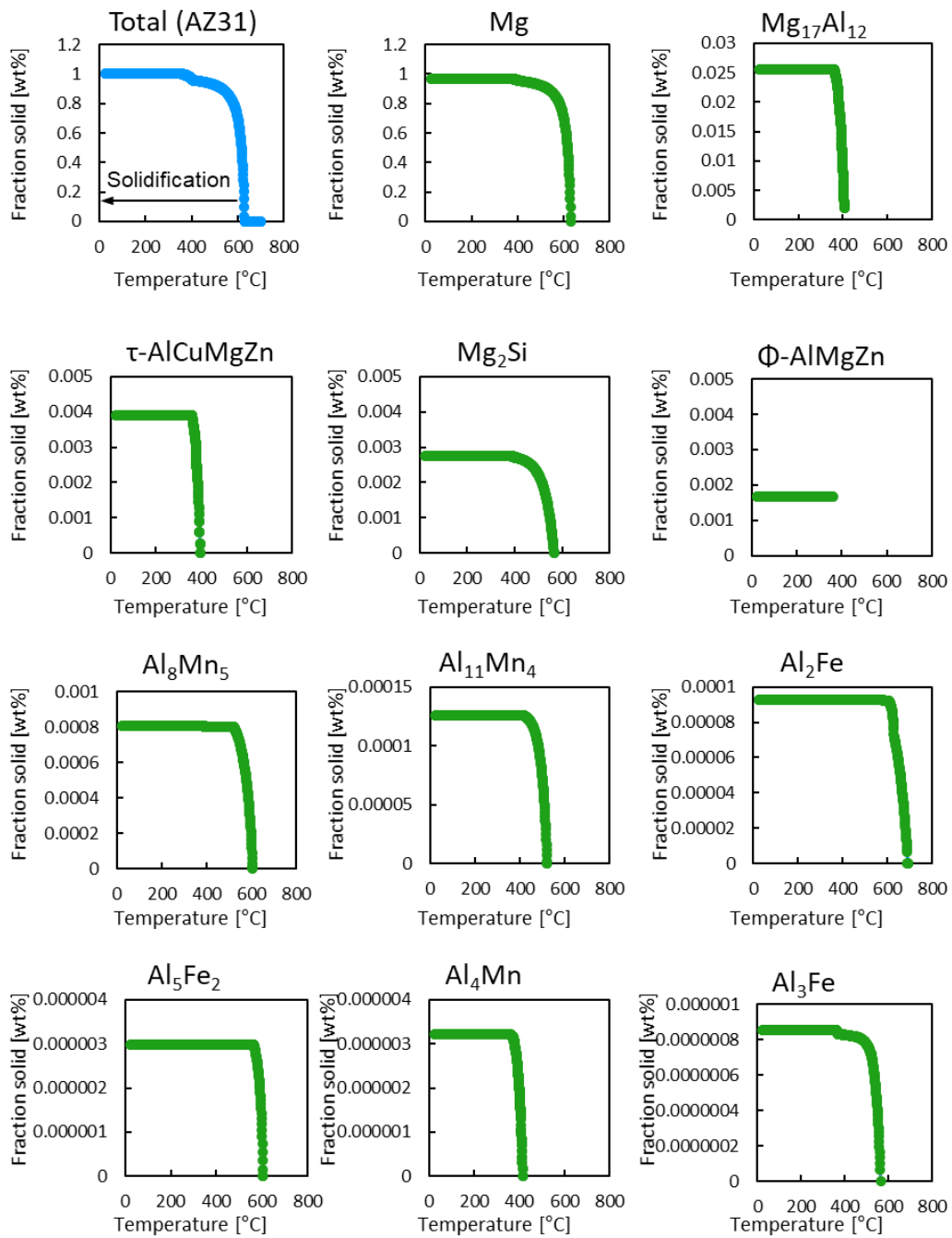


Fig. 5-19 Numerical prediction results for possible all phases from the solidification.

5.4.4 Microstructures determining mechanical properties in AZ31B

It has been confirmed that in the tensile-shear tests and fatigue tests in results section that the failure mode changes dramatically depending on the welding conditions. Except for welded specimens that fractured at the S20C/DP780 interface due to insufficient penetration, fractures were the dominant mode of failure in the AZ31B under all conditions. AZ31B may elongate and sometimes cause plug failure according to the welding conditions. As discussed in the previous section, $Mg_{17}Al_{12}$, Mg_2Si , $\tau-AlCuMgZn$, $\Phi-AlMgZn$ phases that may be formed during the solidification process can also be critical factors in determining mechanical properties in AZ31B alloys. In particular, J. Zhang et al. mentioned that these intermetallic compounds are brittle due to their inherent characteristics, their mechanical strength is negatively affected[38–40]. In addition, the formation of voids or cracks identified on the fracture surface is a phenomenon that can occur during the solidification process of Mg alloys and negatively affects mechanical properties[36]. SFig. 5-2 shows the grain boundary map of the AZ31B HAZ. The green line is low angle grain boundaries (LAGBs), the grey line is high angle grain boundaries (HAGBs), and the red line is $\{10\bar{1}2\}$ twin boundaries.

In SFig. 5-2(a), most of the base material appeared as equiaxed grains composed of HAGBs with complete recrystallizations. However, the AZ31B HAZ with a welding condition of 3.5 kA, which caused that the grains were further refined more than initial state, the $\{10\bar{1}2\}$ twin grain boundaries increased noticeably (SFig. 5-2(b)). These microstructural features are mechanisms to accommodate the deformation that can significantly improve elongation in HCP structures[41–43]. Most of the grain boundary of AZ31B HAZ welded with the condition of 8.5 kA was occupied by HAGBs, but the grains were larger than the base material and twin boundaries were not observed as 3.5

kA conditions (see SFig. 5-2(c)). Intermetallic compounds presumed to be $Mg_{17}Al_{12}$ were observed inside grains, which is considered to have been formed during the solidification process after melting. This type of microstructure may make the area brittle and cause deterioration of elongation. SFig. 5-2(d) illustrates the plot for mean twin boundary length per unit area depending on welding currents. Namely, the combination with grain refinements and higher twin fractions can induce the higher elongation. In previous studies[44,45], since Mg has an hexagonal close-packed (HCP) structure, it has been reported that a $\langle c+a \rangle$ slip surface or mechanical twinning is required for deformation. In contrast, the combination with large grains, low twin fractions, and compound growth was insufficient for contributions of the enhance elongation.

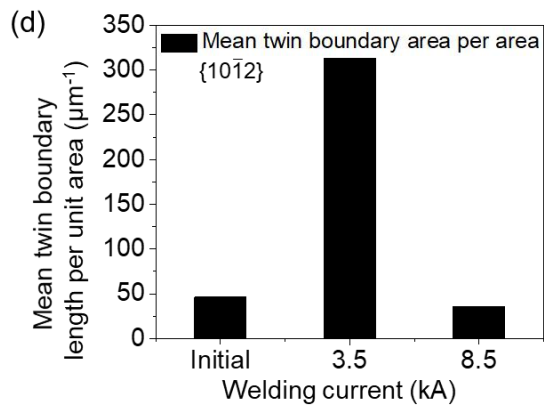
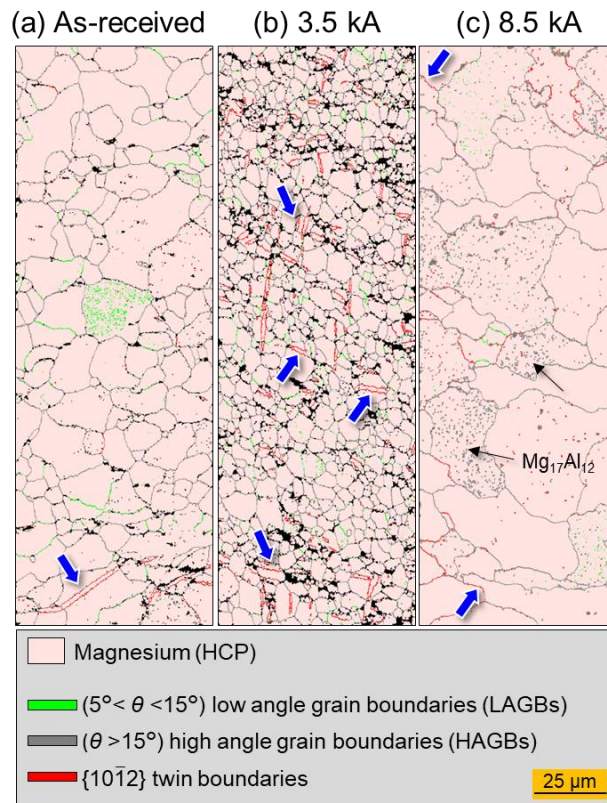


Fig. 5-2 Phase and misorientation angle maps of AZ31B HAZ. (a) as-received state, (b) 3.5 kA, and (c) 8.5 kA, (d) mean twin boundary length per unit area plot.

5.4.5 Mechanical factors determining the fracture mode

In this section, we focus on the revealing of fracture mechanism in terms of failure modes. Finding the cause of the failure mode is one of the important steps to ensure a robust welded joint. (3-D) FEM simulation was performed for a deeper understanding of

the fracture modes that appear differently depending on the geometries and characteristics of the joint. To realize the tensile-shear force applied to the joint, Johnson–Cook (J-C) model has a simpler mathematical expression for crystal structure materials and large deformations. Thus, the J-C constitutive model was widely implemented soon after it was proposed. To quantitatively analyze the stress experienced by the REWed joint during tensile-shear tests, the empirical rate-sensitivity J-C model as follow:

$$\sigma_{eq} = [A + B\varepsilon_p^n] \left[1 + C \ln \left(\frac{\dot{\varepsilon}}{\dot{\varepsilon}_0} \right) \right] \quad (11)$$

where σ_{eq} is equivalent stress; ε_p is plastic strain; $\dot{\varepsilon}$ denotes the equivalent plastic strain rate; $\dot{\varepsilon}_0$ is the reference strain rate. A, B, C, and n, represent the initial yield stress, hardening modulus, strain-rate sensitivity coefficient, strain hardening coefficient, respectively. Fig. 5- 20 illustrates the finite element (FE) model for simulations. The boundary condition constrained one side ($U_x=U_y=U_z=0$) as in the experiment, and applied a displacement to the opposite side of the constraint part ($\delta_x = 5$). In order to examine how the shape of the interface which varies depending on welding currents, affects the failure mode, FE models of the welding interfaces were established as shown in Fig. 5- 21(a, c). Based on the results of OM, the 3D model was reconstructed. The failure mode of the weld at 2.5 kA was interface failure (IF), and the failure mode of the specimen welded at 8.5 kA was plug failure (PF) in AZ31B. The interface of the specimen under the welding condition of 2.5 kA reached fracture within a short time at a shear stress of about 200 MPa as displayed in Fig. 5- 21(b). The failure mode was interfacial failure consistent with the experiment. In contrast, welds under

the condition of 8.5 kA that plug failure was accurately simulated by elongation with shear stress approaching about 400 MPa as shown in Fig. 5- 21(d). These results are well consistent with the experimental results. Fig. 5- 21(e) exhibits the stress distribution on the joint specimen with welding condition of 2.5 kA during the mechanical loading. Concentrated stresses around the weld interface where the weld is not done properly is conspicuous. On the other hand, the stress was not concentrated at the welding interface when the mechanical load was applied to the weld with the 8.5 kA welding condition where penetration was completed based on extruded hook formation into AZ31B. In summary, it can be seen that the penetration degree of the weld interface and the formation of hooks are critical factors in determining the mechanical performance and failure mode of REWed AZ31B/DP780 lap joints. Therefore, it can be concluded that sufficient penetration of S20C/DP780 and the formation of mechanical hooks that can secure the martensite fraction in a range that does not melt the HAZ of AZ31B can contribute to a significant improvement in mechanical performances of REWed AZ31B/DP780 lap joints.

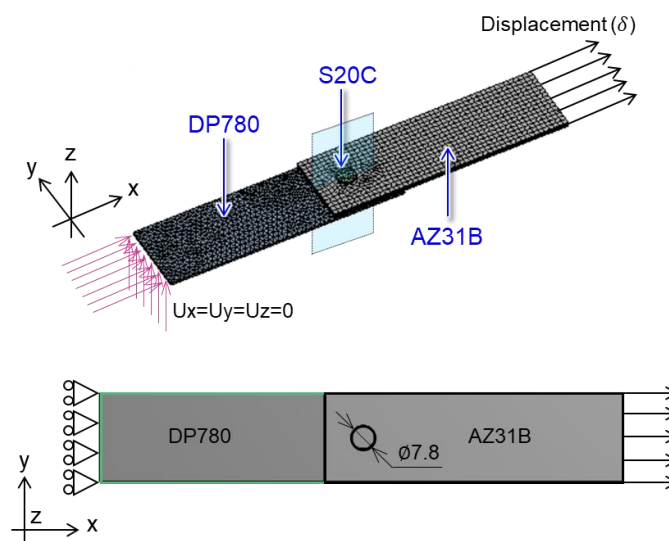


Fig. 5-20 Finite element modeling and boundary condition for the fracture mode simulation.

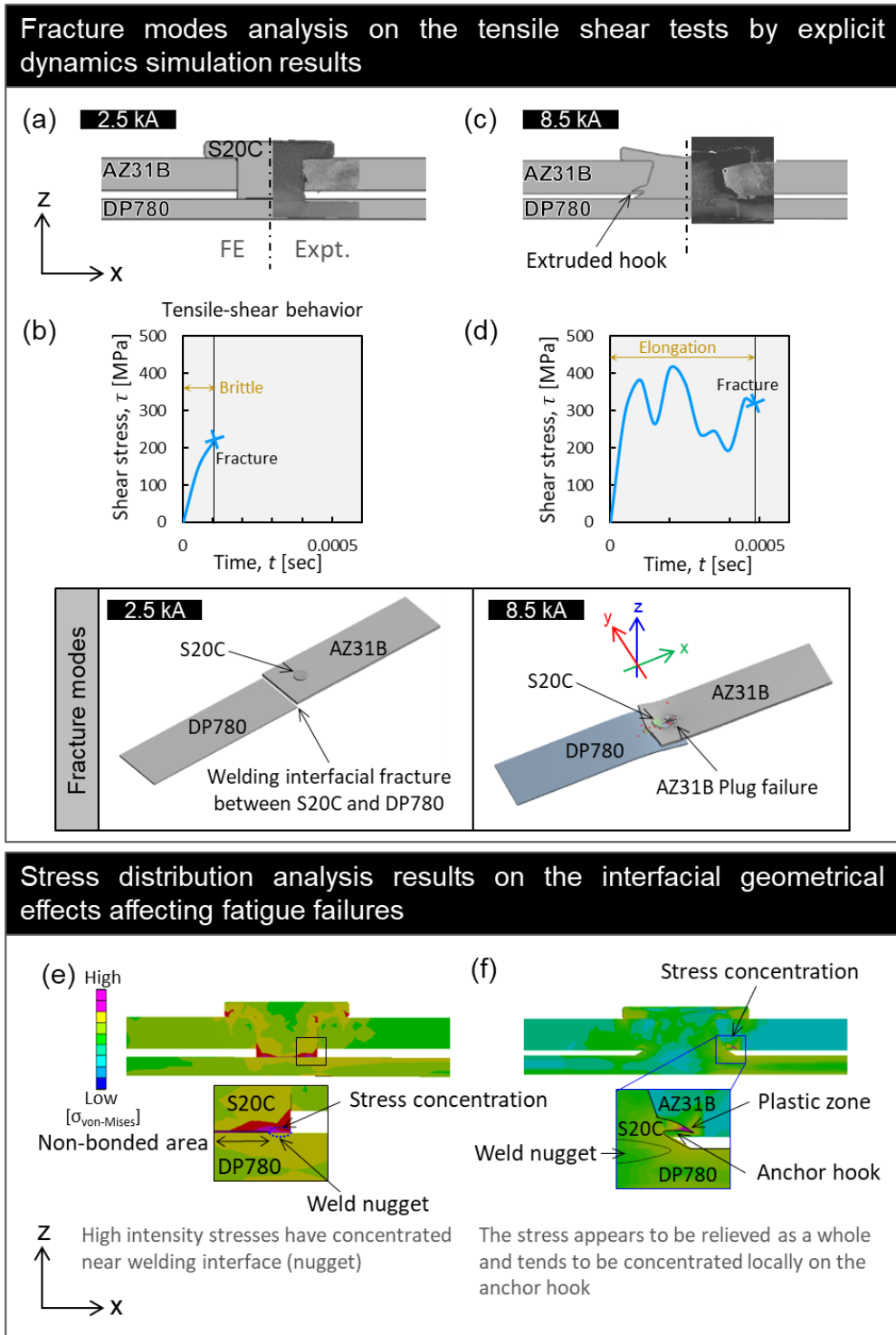


Fig. 5-21 Fracture mode simulation results. (a) simulation model for the weld joint with 2.5 kA, its tensile-shear behavior (b), and (c) simulation model of the joint with the 8.5 kA welding current, (d) tensile-shear simulation result of 8.5 kA, and (e) stress distribution map for 2.5 kA welding current, (f) stress distribution map of the weld joint with the 8.5 kA.

5.5 Conclusions

The resistance element welded (REWEd) lap joint in assembling AZ31B and DP780 plates with the S20C rivet had superior mechanical performances, which showed potential to realize the lightweight vehicle for response in the value of future mobility (CASE). The easy workability and stable interface of the REWEd joint can use the existing RSW equipment as it is and showed the possibility of mass-production as well. The main results obtained in this work are as follows:

1. Sufficient welding currents can generate α' -martensite phase even in S20C, enabling dual phases of the weld joint, which was effective for superior mechanical performances. In addition, the evidence of melting of Mg alloy was experimentally and numerically revealed, and the formation of phases of $Mg_{17}Al_{12}$, $t-AlCuMgAn$, Mg_2Si , $\Phi-AlMgZn$, Al_xMn_x systems and Al_xFe_x systems during solidification were thoroughly discussed.
2. Surprisingly, the failure mode of the REWEd joint whose fatigue life did not exceed 10^3 cycles was interfacial failure or plug failure, and the failure mode of the joint that exceeded 10^3 cycles was induced by crack propagation of the AZ31B.
3. When the welding current exceeds a certain range (up to 8.5 kA), the HAZ of AZ31B deteriorated and a void with a diameter of about 0.39 mm was formed. When the welding current reached 10.5 kA, the diameter of the void grew to about 1.12 mm, several cracks were also observed. In particular, the massive voids and cracks of AZ31B induced by the welding current of 10.5 kA were

fatal to tensile-shear performances and fatigue performances.

4. The welding current of 3.5 kA caused no degradation of the HAZ of AZ31B, accelerated grain refinements and dramatically increased the twin fractions. Therefore, the optimal welding conditions of REW can induce dual phase at the welding interface and increase the twin fraction without melting AZ31B which can sufficiently improve the mechanical performance.
5. The critical factors determining the mechanical properties such as the tensile-shear strength and fatigue duration, were the penetration of the weld interface of the steel and the degradation of the Mg alloys.

References

- [1] Iftikhar CMA, Brahme A, Inal K, Khan AS. An evolution of subsequent yield loci under proportional and non-proportional loading path of 'as-received' extruded AZ31 magnesium alloy: Experiments and CPFEM modeling. *Int J Plast* 2022;151:103216. <https://doi.org/10.1016/j.ijplas.2022.103216>.
- [2] Vaishakh K V., Narasimhan R, Yazar KU, Suwas S. Mixed-mode (I and II) fracture behavior of a basal-textured magnesium alloy. *Acta Mater* 2020;193:99–114. <https://doi.org/10.1016/j.actamat.2020.03.023>.
- [3] Tam KJ, Vaughan MW, Shen L, Knezevic M, Karaman I, Proust G. Modelling dynamic recrystallisation in magnesium alloy AZ31. *Int J Plast* 2021;142:1–22. <https://doi.org/10.1016/j.ijplas.2021.102995>.
- [4] Zhang W, Xu J. Materials & Design Advanced lightweight materials for Automobiles : A review. *Mater Des* 2022;221:110994. <https://doi.org/10.1016/j.matdes.2022.110994>.
- [5] Gao S, Li Y, Yang L, Qiu W. Microstructure and mechanical properties of laser-welded dissimilar DP780 and DP980 high-strength steel joints. *Mater Sci Eng A* 2018;720:117–29. <https://doi.org/10.1016/j.msea.2018.02.057>.
- [6] Ismail K, Perlade A, Jacques PJ, Pardoën T. Outstanding cracking resistance of fibrous dual phase steels. *Acta Mater* 2021;207:116700. <https://doi.org/10.1016/j.actamat.2021.116700>.
- [7] Tian C, Ponge D, Christiansen L, Kirchlechner C. On the mechanical heterogeneity in dual phase steel grades: Activation of slip systems and deformation of martensite in DP800. *Acta Mater* 2020;183:274–84. <https://doi.org/10.1016/j.actamat.2019.11.002>.

- [8] Kasai H, Morisada Y, Fujii H. Dissimilar FSW of immiscible materials: Steel/magnesium. *Mater Sci Eng A* 2015;624:250–5.
<https://doi.org/10.1016/j.msea.2014.11.060>.
- [9] Cheng J, Hu X, Sun X, Vivek A, Daehn G, Cullen D. Multi-scale characterization and simulation of impact welding between immiscible Mg/steel alloys. *J Mater Sci Technol* 2020;59:149–63. <https://doi.org/10.1016/j.jmst.2020.04.049>.
- [10] Farabi N, Chen DL, Zhou Y. Microstructure and mechanical properties of laser welded dissimilar DP600/DP980 dual-phase steel joints. *J Alloys Compd* 2011;509:982–9. <https://doi.org/10.1016/j.jallcom.2010.08.158>.
- [11] Wang J, Yang L, Sun M, Liu T, Li H. Effect of energy input on the microstructure and properties of butt joints in DP1000 steel laser welding. *Mater Des* 2016;90:642–9.
<https://doi.org/10.1016/j.matdes.2015.11.006>.
- [12] Han S-C, Chaudry UM, Yoon J-Y, Jun T-S. Investigating local strain rate sensitivity of the individual weld zone in the friction stir welded DP 780 steel. *J Mater Res Technol* 2022;20:508–15. <https://doi.org/https://doi.org/10.1016/j.jmrt.2022.07.125>.
- [13] Mostaan H, Saeedpour P, Ahmadi H, Nouri A. Laser welding of dual-phase steels with different silicon contents: Phase evolutions, microstructural observations, mechanical properties, and fracture behavior. *Mater Sci Eng A* 2021;811:140974.
<https://doi.org/10.1016/j.msea.2021.140974>.
- [14] Soomro IA, Pedapati SR, Awang M. Optimization of postweld tempering pulse parameters for maximum load bearing and failure energy absorption in dual phase (DP590) steel resistance spot welds. *Mater Sci Eng A* 2021;803:140713.
<https://doi.org/https://doi.org/10.1016/j.msea.2020.140713>.
- [15] Ryde L. Application of EBSD to analysis of microstructures in commercial steels.

- Mater Sci Technol 2006;22:1297–306. <https://doi.org/10.1179/174328406X130948>.
- [16] Atreya V, Van Dokkum JS, Bos C, Santofimia MJ. Effect of the anisotropy of martensitic transformation on ferrite deformation in Dual-Phase steels. *Mater Des* 2022;219:110805. <https://doi.org/10.1016/j.matdes.2022.110805>.
- [17] Mahmoudiniya M, Kestens LAI. Microstructural development and texture evolution in the stir zone and thermomechanically affected zone of a ferrite-martensite steel friction stir weld. *Mater Charact* 2021;175:111053. <https://doi.org/10.1016/j.matchar.2021.111053>.
- [18] Atreya V, Bos C, Santofimia MJ. Understanding ferrite deformation caused by austenite to martensite transformation in dual phase steels. *Scr Mater* 2021;202:114032. <https://doi.org/10.1016/j.scriptamat.2021.114032>.
- [19] Shen Z, Ding Y, Chen J, Gerlich AP. Comparison of fatigue behavior in Mg/Mg similar and Mg/steel dissimilar refill friction stir spot welds. *Int J Fatigue* 2016;92:78–86. <https://doi.org/10.1016/j.ijfatigue.2016.06.033>.
- [20] Liu L, Xiao L, Chen DL, Feng JC, Kim S, Zhou Y. Microstructure and fatigue properties of Mg-to-steel dissimilar resistance spot welds. *Mater Des* 2013;45:336–42. <https://doi.org/10.1016/j.matdes.2012.08.018>.
- [21] Song G, Li T, Yu J, Liu L. A review of bonding immiscible Mg/Steel dissimilar metals. *Materials (Basel)* 2018;10:1–25. <https://doi.org/10.3390/ma11122515>.
- [22] Han Z, Luo H, Sun C, Li J, Papaalias M, Davis C. Acoustic emission study of fatigue crack propagation in extruded AZ31 magnesium alloy. *Mater Sci Eng A* 2014;597:270–8. <https://doi.org/10.1016/j.msea.2013.12.083>.
- [23] Han J, da Silva AK, Ponge D, Raabe D, Lee SM, Lee YK, et al. The effects of prior austenite grain boundaries and microstructural morphology on the impact toughness

- of intercritically annealed medium Mn steel. *Acta Mater* 2017;122:199–206.
<https://doi.org/10.1016/j.actamat.2016.09.048>.
- [24] Baek S, Song J, Lee H chul, Park S yeon, Song KH, Lee S, et al. Robust bonding and microstructure behavior of aluminum/high-strength steel lap joints using resistance element welding process for lightweight vehicles: Experimental and numerical investigation. *Mater Sci Eng A* 2022;833:142378.
<https://doi.org/10.1016/j.msea.2021.142378>.
- [25] Gould JE, Khurana SP, Li T. Predictions of microstructures when welding automotive advanced high-strength steels. *Weld J (Miami, Fla)* 2006;85.
- [26] Goodarzi M, Marashi SPH, Pouranvari M. Dependence of overload performance on weld attributes for resistance spot welded galvanized low carbon steel. *J Mater Process Technol* 2009;209:4379–84. <https://doi.org/10.1016/j.jmatprotec.2008.11.017>.
- [27] Mahieu J, Maki J, De Cooman BC, Claessens S. Phase transformation and mechanical properties of Si-free CMnAl transformation-induced plasticity-aided steel. *Metall Mater Trans A Phys Metall Mater Sci* 2002;33:2573–80.
<https://doi.org/10.1007/s11661-002-0378-9>.
- [28] Yang HS, Jang JH, Bhadeshia HKDH, Suh DW. Critical assessment: Martensite-start temperature for the $\gamma \rightarrow \epsilon$ transformation. *Calphad Comput Coupling Phase Diagrams Thermochem* 2012;36:16–22.
<https://doi.org/10.1016/j.calphad.2011.10.008>.
- [29] Yang HS, Bhadeshia HKDH. Austenite grain size and the martensite-start temperature. *Scr Mater* 2009;60:493–5.
<https://doi.org/10.1016/j.scriptamat.2008.11.043>.
- [30] Yen HW, Ooi SW, Eizadjou M, Breen A, Huang CY, Bhadeshia HKDH, et al. Role of

- stress-assisted martensite in the design of strong ultrafine-grained duplex steels. *Acta Mater* 2015;82:100–14. <https://doi.org/10.1016/j.actamat.2014.09.017>.
- [31] Liu H, Zhao X. Thermal Conductivity Analysis of High Porosity Structures with Open and Closed Pores. *Int J Heat Mass Transf* 2022;183:122089. <https://doi.org/10.1016/j.ijheatmasstransfer.2021.122089>.
- [32] Oh GY, Kim YK, Kim SK, Lim HK, Kim YJ. Effects of grain size and texture on thermal conductivity of AZ31 during static recrystallization. *Mater Trans* 2017;58:1241–3. <https://doi.org/10.2320/matertrans.M2017126>.
- [33] Lee S, Ham HJ, Kwon SY, Kim SW, Suh CM. Thermal conductivity of magnesium alloys in the temperature range from -125 C to 400 C. *Int J Thermophys* 2013;34:2343–50. <https://doi.org/10.1007/s10765-011-1145-1>.
- [34] Hajbarati H, Zajkani A. A novel finite element simulation of hot stamping process of DP780 steel based on the Chaboche thermomechanically hardening model. *Int J Adv Manuf Technol* 2020;111:2705–18. <https://doi.org/10.1007/s00170-020-06297-4>.
- [35] Chen L, Zhang Y, Xue X, Wang B, Yang J, Zhang Z, et al. Investigation on shearing strength of resistance spot-welded joints of dissimilar steel plates with varying welding current and time. *J Mater Res Technol* 2022;16:1021–8. <https://doi.org/10.1016/j.jmrt.2021.12.079>.
- [36] Zhang Y, Zhou Z, Fu Y, Li H, Li Z, Mariusz B, et al. Effects of Al/Zn interlayer on the solidification path and liquation cracking susceptibility of AZ31/ZK61 dissimilar magnesium alloy resistance spot welding joints. *J Manuf Process* 2022;75:60–71. <https://doi.org/10.1016/j.jmapro.2021.12.017>.
- [37] Peng Z, Zhou T, Li Y, Cui Z, Wu Z, Yan J. Microstructure and mechanical performance of AZ31/2024 dissimilar alloy joints using a multi-interlayer of Ni/Al/Zn

- via ultrasonic-assisted transient liquid phase bonding. *Mater Des* 2021;197:109218.
<https://doi.org/10.1016/j.matdes.2020.109218>.
- [38] Zhang J, Ma L, Zhao G, Cai Z, Zhi C. Effect of annealing temperature on tensile fracture behavior of AZ31 / 6061 explosive composite plate. *J Mater Res Technol* 2022;19:4325–36. <https://doi.org/10.1016/j.jmrt.2022.06.142>.
- [39] Guo W, Wang Q, Ye B, Zhou H. Enhanced microstructure homogeneity and mechanical properties of AZ31-Si composite by cyclic closed-die forging. *J Alloys Compd* 2013;552:409–17. <https://doi.org/10.1016/j.jallcom.2012.11.067>.
- [40] Gan WM, Wu K, Zheng MY, Wang XJ, Chang H, Brokmeier HG. Microstructure and mechanical property of the ECAPed Mg2Si/Mg composite. *Mater Sci Eng A* 2009;516:283–9. <https://doi.org/10.1016/j.msea.2009.03.034>.
- [41] Jiang MG, Xu C, Yan H, Fan GH, Nakata T, Lao CS, et al. Unveiling the formation of basal texture variations based on twinning and dynamic recrystallization in AZ31 magnesium alloy during extrusion. *Acta Mater* 2018;157:53–71.
<https://doi.org/10.1016/j.actamat.2018.07.014>.
- [42] Azghandi SHM, Weiss M, Arhatari BD, Adrien J, Maire E, Barnett MR. A rationale for the influence of grain size on failure of magnesium alloy AZ31: An in situ X-ray microtomography study. *Acta Mater* 2020;200:619–31.
<https://doi.org/10.1016/j.actamat.2020.09.016>.
- [43] Dudamell N V., Ulacia I, Gálvez F, Yi S, Bohlen J, Letzig D, et al. Twinning and grain subdivision during dynamic deformation of a Mg AZ31 sheet alloy at room temperature. *Acta Mater* 2011;59:6949–62.
<https://doi.org/10.1016/j.actamat.2011.07.047>.
- [44] Khosravani AN and propagation of $\{10\bar{1}2\}$ twins in A magnesium alloy, Fullwood

DT, Adams BL, Rampton TM, Miles MP, Mishra RK. Nucleation and propagation of $\{10\bar{1}2\}$ twins in AZ31 magnesium alloy. *Acta Mater* 2015;100:202–14.

<https://doi.org/10.1016/j.actamat.2015.08.024>.

[45] Knezevic M, Levinson A, Harris R, Mishra RK, Doherty RD, Kalidindi SR.

Deformation twinning in AZ31: Influence on strain hardening and texture evolution.

Acta Mater 2010;58:6230–42. <https://doi.org/10.1016/j.actamat.2010.07.041>.

Chapter 6 Conclusions

In the present study, the author has investigated the bonding mechanism of resistance element welding for robust lap joints of lightweight alloys and ultra-high strength steels. As a result, the following conclusions have been derived.

Chapter 1

The author has introduced an overview of the resistance element welding (REW) process, focusing on the bonding process for dissimilar materials between lightweight alloys and steel, followed by the purpose of the present thesis.

Chapter 2

Chapter 2 presents the present the REW process as a novel alternative to Al(AA5052)/Fe(SPFC980) joints for the automotive structural assembly process. The resistance element welded test specimens with 3.5 kA and 4.5 kA welding currents were not sufficiently melted to achieve robust bonding. Gaps and micro-cracks at the bonding interface were identified as the main causes for inducing the brittle failure of the bonding interfaces. As the welding current increases, the tensile-shear strength gradually increases, reaching a peak load exceeding 9000 N. However, when the welding current exceeds 10.5 kA, the tensile-shear strength gradually decreases. The ϵ phase was detected at the interface under the 10.5 kA current condition. Additionally, the cooling rate was numerically confirmed to be within the critical region where the ϵ phase could be sufficiently realized through theoretical calculations and transient welding thermal simulations. Remarkably, these results demonstrated exceptional

mechanical properties of robust bonding between Al and Fe while utilizing the RSW facility. Consequently, REW can be adopted as a substantial alternative for robust bonding and mass production of automotive lightweight structures.

Chapter 3

Chapter 3 reports the study investigates a fatigue property and its microstructural and interface geometrical effect on the REWed Al/Fe lap joint. In the AA5052/SPFC980 lap joint welded with a welding current of 3.5-4.5 kA, joint interface fracture occurred in both low cycle and high cycle fatigue. Conversely, joints welded under the condition of 10.5-12 kA resulted in AA5052 base material fracture under all conditions. Fatigue properties also had the highest fatigue strength at 10.5 kA. However, in the case of the AA5052/SPFC980 joints welded with welding currents of 10.5-12 kA, fatigue cracks initiated and propagated at the HAZ of AA5052, leading to a rapid decrease in fatigue strength in high fatigue cycles. These results were attributed to the development of the heat-affected zone (HAZ) of AA5052, including factors such as grain size growth and grain recrystallization.

Chapter 4

In Chapter 4, HAZ-less technologies, necessary to minimize the risk associated with the formation of Heat-Affected Zones (HAZs) considered as welding defects, are investigated on AA5052/SPFC980 specimens. In the condition of hot wall joints, the presence of a dendrite-like Al HAZ was consistently observed across all welding current parameters. In contrast, in the cold wall condition, a finer microstructure devoid of dendritic Al HAZ formations was identified at welding current of 8.5 kA and 10.5 kA.

There existed a significant disparity in the hardness between the Al HAZ of hot wall conditions and the Al present in the cold wall conditions without a HAZ. The hardness of cold wall Al was slightly lower than that of the base material (BM) and hot wall Al HAZ. This was attributed to the dissipation of work hardening in AA5052-H32 resulting from the elevated process temperatures. The presence of Al HAZ exerted a noticeable impact on the hardness characteristics of the molten steel portion. In the case of the cold wall configuration without Al HAZ, hardness values exceeding those of the hot wall by approximately 100 Hv or more were observed, and these originated from variations in the Prior austenite grain structures (PAGS). The underlying cause for the incidence of interfacial failure (IF) in the cold wall conditions was not attributed to microstructural disparities. It was related to the formation of an inherent notch root when S20C melted due to the absence of Al HAZ.

Chapter 5

In chapter 5, the fatigue fracture response and microstructure behavior of a REW in assembling AZ31B Mg alloy and DP780 plates are focused. Sufficient welding currents can generate a α' -martensite phase even in S20C steel element, enabling dual phases in the weld joint, which was effective for superior mechanical performance. In addition, evidence of the melting of the magnesium (Mg) alloy was experimentally and numerically revealed. The failure mode of the REW joint, whose fatigue life did not exceed 10^3 cycles, was an interfacial failure or plug failure. On the other hand, the failure mode of the joint that exceeded 10^3 cycles was induced by crack propagations in the AZ31B. The massive voids and cracks in AZ31B induced by the welding current of 10.5 kA were fatal to both tensile-shear and fatigue performances. The welding current

of 3.5 kA caused no degradation of the HAZ of AZ31B, accelerated grain refinements, and dramatically increased the twin fractions. Therefore, the optimal welding conditions of REW can induce dual-phase at the welding interface and increase the twin fraction without melting AZ31B, which can sufficiently improve the mechanical performance. The critical factors determining the mechanical properties, such as the tensile-shear strength and fatigue duration, were the penetration of the weld interface of the steel and the degradation of the Mg alloys.

Through this study, the REW bonding mechanism for robust bonding of lightweight metals and ultra-high-strength steel was revealed. The experimentally and numerically investigated research content has been thoroughly examined for bonding and fracture mechanisms, and guidelines for obtaining excellent mechanical properties have been elucidated. Achieving excellent mechanical properties through the use of lightweight materials and ultra-high-strength steel while circumventing the challenges with joining dissimilar materials using REW is a significant accomplishment.

Finally, the scope of ongoing follow-up research is explained. The author's findings underline that, while it is possible to effectively develop an Al Heat-Affected Zone (HAZ)-less AA5052/1GPa-class steel lap joint, it is imperative to consider the thermal behavior during the process and its effects due to the geometric characteristics of the joint. These drawbacks can be mitigated through post-treatment strategies such as heat treatment. The results obtained in this study are expected to contribute to the advanced discussion on lightweight components for next-generation automobiles.

List of Publications

1. Seungyeop Baek, Jongho Song, Hyun-chul Lee, Seung-yeon Park, Kuk-Hyun Song, Sangmin Lee, Seung-Joon Lee, Chuantong Chen, Dongjin Kim*
Robust bonding and microstructure behavior of aluminum/high-strength steel lap joints using resistance element welding process for lightweight vehicles: Experimental and numerical investigation
Material Science & Engineering A, 833(2022)142378.
2. Seungyeop Baek, Gun Yung Go, Jong-Wook Park, Jongho Song, Hyun-chul Lee, Seung-Joon Lee, Sangmin Lee, Chuantong Chen, Min-Su Kim, Dongjin Kim*
Microstructural and interface geometrical influence on the mechanical fatigue property of aluminum/ high-strength steel lap joints using resistance element welding for lightweight vehicles: experimental and computational investigation
Journal of Materials Research and Technology, 17(2022)658-678.
3. Seungyeop Baek, Ninshu Ma**, Jongho Song, Dong-Kyu Kim, Seung-Joon Lee, Chuantong Chen, Min-Su Kim, Dongjin Kim*
Effect of Mg remelting and mechanical hooks of steel on the mechanical and fatigue responses of resistance element welded AZ31/DP780 joints: Experimental, FEM and thermodynamic calculation studies
Journal of Materials Research and Technology, 22(2023)1210-1237.
4. Seungyeop Baek, Junyeong Kim, Taeyang Kwak, Taejin Lee, Hyun-chul Lee, Chuantong Chen, Peihao Geng, Ninshu Ma*, Seung-Joon Lee, Dongjin Kim*
Al heat affected zone-less resistance element welded lap joints of Al alloy and 1 GPa class steel: Transition of microstructure of microstructure and fracture with heat transfer
Journal of Materials Research and Technology, 28(2024)3541-3565.

5. Junyeong Kim, Jong-Hun Kim, Jungsoo Park, Seungyeop Baek, Ninshu Ma, Seung-Joon Lee**, Dongjin Kim*

Continuous tempering effect induced PWHT alternative technology using wire arc additive manufacturing for application in replacing nuclear pressurized water reactor system repairing: CALPHAD, FEM simulation, and EBSD investigation

Journal of Materials Research and Technology, 25(2023)2961-2988.

6. Dongjin Kim*, Seungyeop Baek, Masahiko Nishijima, Hyun-chul Lee, Peihao Geng, Ninshu Ma, Zheng Zhang, Hyunsu Park, Chuantong Chen, Seung-Joon Lee, Katsuaki Suganuma

Toward defect-less and minimized work-hardening loss implementation of work-hardened Al alloy/high-purity Cu dissimilar lap joints by refill friction stir spot welding for battery tab-to-busbar applications

Material Science & Engineering A, 892(2024)146089.

Presentations

International conferences

1. Seungyeop Baek, Ninshu Ma, Peihao Geng, Jongho Song, Seung-Joon Lee, Min-Su Kim, Dongjin Kim
Effect of magnesium remelting and weld interface geometry on fatigue properties of resistance element welded Mg/DP steel
9th International Conference on Welding Science and Engineering 2023, Harbin, China, July, 2023
2. Seungyeop Baek, Ninshu Ma, Jongho Song, Seung-Joon Lee, Min-Su Kim, Dongjin Kim
Phase Transformation on the Heat Affected Zone in Aluminum/High Strength Steel Lap Joints using Resistance Element Welding for Lightweight Vehicles
3rd MRM2023/IUMRS-ICA2023, Kyoto, Japan, December, 2023

Acknowledgements